

UNIVERSITY OF ZULULAND



Solventless Synthesis of Nanostructured Spinel Ferrite Solid Solutions for Supercapacitance and Electrochemical Water Splitting Applications

By:

Nyemaga Masanje Malima

201945446

B.Ed.Sc. (UDOM); M.Sc. Chemistry (UDSM)

THESIS

Submitted in fulfilment of the requirements for the degree

DOCTOR OF PHILOSOPHY

In the field of

CHEMISTRY

Faculty of Science and Agriculture

University of Zululand

Supervisor: Prof. N. Revaprasadu

Co-supervisor: Dr. M. D. Khan

December 2021

DECLARATION

I hereby declare that the work described in this thesis entitled “**Solventless Synthesis of Nanostructured Spinel Ferrite Solid Solutions for Supercapacitance and Electrochemical Water Splitting Applications**” is my own work and has not been submitted in any form for another degree or qualification of the University of Zululand or any other University/Institution for tertiary education. Information derived from the published or unpublished work of others has been acknowledged in the text and a list of references is given.

Name: Nyemaga Masanje Malima

Signature: 

Date: 08th December 2021

CERTIFICATION BY SUPERVISOR

This is to certify that this work was carried out by Mr. Nyemaga Masanje Malima in the Department of Chemistry, University of Zululand and is approved for submission in fulfilment of the requirements for the degree of Doctor of Philosophy in Chemistry.



.....
Supervisor

N. Revaprasadu (Ph.D)

Professor of Inorganic Chemistry

Department of Chemistry, University of Zululand,

Kwa-Dlangezwa, South Africa.



.....
Co-Supervisor

M.D. Khan (Ph.D)

Postdoctoral Researcher

Department of Chemistry, University of Zululand,

Kwa-Dlangezwa, South Africa.

ACKNOWLEDGEMENT

My profound gratitude goes first to Almighty God, for his abundant blessings and protection throughout my studies, without which this thesis would not have been possible.

I owe a deep sense of gratitude to my supervisors, Prof. Neerish Revaprasadu and Dr. Malik Dilshad Khan for their constant support, guidance and mentorship throughout my Ph.D studies. It is through their expertise and unwavering enthusiasm for nanoscience that made this thesis gain the required standard and shape. A debt of gratitude is also owed to the late Prof. Egid Beatus Mubofu who introduced me to Prof. Revaprasadu, and hence playing a huge role in my academic life.

The National Research Foundation (NRF-Grantholder-linked student support) is highly acknowledged for the financial support. The Kansas polymer research center and the polymer chemistry program of the Pittsburg State University, USA are also acknowledged for providing research support.

Further, yet importantly, special thanks are extended to my doting parents, Mr. Malima Nyemaga and Ms. Moshi Masinde for their unconditional and unequivocal support, endless love and prayers. I am similarly grateful to my brothers, sisters and other relatives for their encouragement, love and support. I equally place on record my heartfelt gratitude to my fiancée, Rehema Elias, for her support, encouragement and prayers. I am also indebted to the members of Dodoma Central Seventh-Day Adventist Church for their spiritual support.

I thank profusely the Chemistry Staff of the University of Zululand, my colleagues, and friends. A special mention goes to Dr. S. Mlowe, Dr. C. Masikane, Dr. Shesan J.O, Dr. E. Ayom, Dr. C. Gervas, Dr. G. Shombe, Mr. W. Zibane, Mr. S. Khoza, Mr. Z. Mzimela, Mr. Z. Ncanana, Mr. L. Nene, Mr. G. Tigwere, Mr. A. Koffee, Mr. M. Khumalo, Mr. M. Sifundo, Ms. A. Nhlapo, and Ms. J. Govender. Their personal generosity helped me in striking a balance with life outside the dark depths of the lab, and made my time at Unizulu enjoyable.

My appreciation also extends to the academic and administrative personnel of the University of Dodoma, Tanzania, and my colleagues at both the College of Education, and College of Natural and Mathematical Sciences, for their constant cooperation.

My joy knows no bounds in expressing my cordial gratitude to all my friends from Tanzania, and all people who directly or indirectly, have lent their hand in this venture.

DEDICATION

It is with genuine gratitude and warm regard that I dedicate this work to my parents whose value to me grows with age.

ABSTRACT

Metal oxide nanocrystals that adopt the spinel crystal structure, such as spinel ferrites exhibit a variety of interesting electronic, magnetic, and optical properties, which render them suitable for numerous technologically relevant applications. Interestingly, tuning the composition of spinel nanoferrites via the design of solid solutions is recognized as an effective way to improve their electrochemical properties towards supercapacitance and water splitting. In this regard, achieving synthetic control over the composition is critical to tuning the properties of spinel ferrite nanocrystals. Efforts to find sustainable approaches to nanoparticle synthesis have focused on green chemistry principles, including reducing waste, improving yield and atom economy, and minimizing auxiliaries and reaction steps. The solventless approach, in which the synthesis of nanomaterials proceed by thermal decomposition of precursors has attracted considerable research interest and proven to be simple, economical, time-effective, scalable, and eco-friendly. The work described in this thesis demonstrates the suitability of the solventless thermolysis route for the fabrication of a series of nanostructured spinel ferrite solid solutions using metal acetylacetonate precursors. Investigation on the efficacy of the synthesized ferrite solid solutions for supercapacitance and water splitting applications is also described. The thesis is organized into seven chapters as described hereunder.

The first chapter presents the introduction and literature review which are the foundations upon which the entire research work is based. This chapter gives insight into electrochemical energy systems with a special focus on the theory behind electrocatalytic water splitting and the mechanism of hydrogen production in both acidic and alkaline electrolytes. Similarly, the description, classification and working principles of supercapacitors are described. It also shades light into the concept and potential applications of spinel ferrites and their corresponding solid solutions. The first chapter is culminated by highlighting the research justification and establishes the working scope and objectives of the study.

The work described in chapter two entails the scalable synthesis of nanostructured $\text{Ni}_{1-x}\text{Co}_x\text{Fe}_2\text{O}_4$ solid solutions via a solventless thermolysis method. The physicochemical analysis of the as-prepared solid solutions is established by a suite of characterization techniques, while the procedures of materials fabrication and electrochemical analysis are also presented. The p-XRD analysis confirmed the formation of a series of monophasic cubic spinel ferrites with space group $Fd3m$. Investigation of the synthesized materials for

supercapacitance revealed that the nanospinel $\text{Ni}_{0.4}\text{Co}_{0.6}\text{Fe}_2\text{O}_4$ electrode demonstrated a longer charge-discharge time, signifying superior charge storage capacity. For efficient HER electrocatalysis, the $\text{Ni}_{0.6}\text{Co}_{0.4}\text{Fe}_2\text{O}_4$ electrode showed high performance manifested by low overpotential of 168 mV and Tafel slope of 120 mV/dec. Similarly, $\text{Ni}_{0.8}\text{Co}_{0.2}\text{Fe}_2\text{O}_4$ exhibited a lower overpotential of 320 mV with a low Tafel slope of 79 mV/dec, indicating enhanced OER activity.

Chapter three describes scalable nanofabrication of composition-tuneable spinel $\text{Co}_{1-x}\text{Zn}_x\text{Fe}_2\text{O}_4$ solid solutions via a solvent-free thermolysis approach. The discussion of the experimental results regarding the materials' structural, compositional, morphological and optical properties is provided. Experimental results revealed that incorporation of diamagnetic Zn^{2+} in the crystal lattice of CoFe_2O_4 significantly enhanced both the physicochemical and electrochemical properties of the resultant material. Higher discharge time displayed by $\text{Co}_{0.4}\text{Zn}_{0.6}\text{Fe}_2\text{O}_4$ is indicative of higher specific capacitance of the material compared to the pristine CoFe_2O_4 . For OER, the $\text{Co}_{0.8}\text{Zn}_{0.2}\text{Fe}_2\text{O}_4$ solid solution exhibited higher performance reflected by low overpotential of 317 mV along with a small Tafel slope of 56 mV/dec. As for HER in alkaline electrolyte, $\text{Co}_{0.6}\text{Zn}_{0.4}\text{Fe}_2\text{O}_4$ displayed decent performance with a low overpotential of 169 mV and Tafel slope of 136 mV/dec compared to other electrode compositions.

Chapter four demonstrates that by regulating the molar composition of Mg and Ni in the preparation of $\text{Ni}_{1-x}\text{Mg}_x\text{Fe}_2\text{O}_4$ solid solutions, the physicochemical and the electrochemical performance of the material were tuned. The $\text{Ni}_{1-x}\text{Mg}_x\text{Fe}_2\text{O}_4$ ($x = 0.6$) nanoparticles exhibited the best electrocatalytic activity for HER with an overpotential of only 121 mV which is much smaller compared to its analogues, at current density of 10 mA/cm^2 and the electrode exhibits good stability during long-term electrolysis. Meanwhile, $\text{Ni}_{0.2}\text{Mg}_{0.8}\text{Fe}_2\text{O}_4$ showed the best OER activity, requiring an overpotential of 284 mV to deliver the same current density within the window of potential examined.

In chapter five, a series of $\text{Ni}_{1-x}\text{Zn}_x\text{Fe}_2\text{O}_4$ ($0 \leq x \leq 1$) solid solutions with varying amounts of zinc and nickel have been efficaciously fabricated via a solventless pyrolysis method. The p-XRD and EDX analyses confirmed the formation of homogeneous phase-pure $\text{Ni}_{1-x}\text{Zn}_x\text{Fe}_2\text{O}_4$ ($0 \leq x \leq 1$) nanoparticles. In comparison, the incorporation of zinc in the crystal lattices of nickel ferrite endowed a larger benefit on HER and OER than on supercapacitance. Specifically, the $\text{Ni}_{1-x}\text{Zn}_x\text{Fe}_2\text{O}_4$ ($x = 0.8$) nanocatalyst displays excellent HER performance with superior activity which is manifested by a small overpotential of 87

mV, whereas $\text{Ni}_{1-x}\text{Zn}_x\text{Fe}_2\text{O}_4$ ($x = 1$) catalyst exhibited superior OER performance with a small overpotential of 330 mV.

The main aim of the sixth chapter was to employ the same solventless pyrolysis approach to afford uniform $\text{Co}_{1-x}\text{Mg}_x\text{Fe}_2\text{O}_4$ ($0 \leq x \leq 1$) nanoparticles using metal acetylacetonate precursors. Structural analysis showed that all samples exhibited a cubic spinel ferrite structure with space group $Fd3m$. All samples showed the same morphology irrespective of the amount of Mg being incorporated in the CoFe_2O_4 system. Considering the band gap value of pristine cobalt ferrite, a blue shift was observed for all compositions except for $x = 0.2$ and 1, which were red shifted. The results and findings of this chapter are of profound significance for the design of novel electronic and optoelectronic devices.

Chapter 7 culminates the entire research project by presenting a brief summary of the work and possible areas to be considered for future work.

Overall, it was observed in this study that compared to the parent spinel ferrites, their corresponding solid solutions demonstrated improved physicochemical and electrochemical activity, except for $\text{Ni}_{1-x}\text{Zn}_x\text{Fe}_2\text{O}_4$ where the parent ZnFe_2O_4 exhibited higher OER activity than the solid solutions.

Table of contents

DECLARATION	i
CERTIFICATION BY SUPERVISOR	ii
ACKNOWLEDGEMENT	iii
DEDICATION	iv
ABSTRACT	v
Table of contents	viii
List of figures	xiv
List of tables	xix
List of abbreviations and symbols	xxi
CHAPTER 1. Introduction and Literature Review.....	1
1.1 General introduction	2
1.2 Literature review	4
1.2.1 Electrochemical energy storage and conversion systems	4
1.2.1.1 Supercapacitors	4
1.2.1.2 Design, classification and mechanism of energy storage in supercapacitors	5
1.2.1.3 Electrochemical water splitting.....	7
1.2.2 Introduction to ferrites	10
1.2.2.1 The ferrite's spinel structure and cation site occupation	10
1.2.3 Solid solutions	12
1.2.4 Classification of semiconductor solid solutions	14
1.2.4.1 Classification of solid solutions based on the type of ion occupancy.....	14
1.2.4.2 Classification of solid solutions based on the number of component elements	15
1.2.5 Progress on the synthesis of crystalline solid solutions.....	15
1.2.5.1 Binary solid solutions	16

1.2.5.2	Ternary solid solutions.....	16
1.2.5.2.1	Ternary cationic solid solutions	17
1.2.5.2.2	Ternary anionic solid solutions.....	30
1.2.5.3	Quaternary solid solutions	37
1.2.5.3.1	Quaternary cationic solid solutions	38
1.2.5.3.2	Quaternary anionic solid solutions	50
1.2.5.3.3	Pseudobinary quaternary solid solutions	51
1.2.6	Fabrication approaches of crystalline solid solutions	55
1.2.6.1	Solventless thermolysis (Melt) method	55
1.2.7	Statement of the research problem.....	56
1.2.8	Aim and objectives.....	58
References.....		59

CHAPTER 2. Solventless synthesis of nanospinel $\text{Ni}_{1-x}\text{Co}_x\text{Fe}_2\text{O}_4$ ($0 \leq x \leq 1$) solid solutions for efficient electrochemical water splitting and supercapacitance75

2.1	Introduction	76
2.2	Experimental	78
2.2.1	Chemicals.....	78
2.2.2	Solventless synthesis of $\text{Ni}_{1-x}\text{Co}_x\text{Fe}_2\text{O}_4$ ($x = 0, 0.2, 0.4, 0.6, 0.8, 1$) solid solutions	78
2.3	Characterization techniques for $\text{Ni}_{1-x}\text{Co}_x\text{Fe}_2\text{O}_4$ ($0 \leq x \leq 1$) solid solutions.....	79
2.3.1	Powder X-ray diffraction (p-XRD) analysis.....	79
2.3.2	Scanning electron microscopy (SEM) and Energy dispersive X-ray (EDX) analyses	79
2.3.3	X-ray photoelectron spectroscopy (XPS)	79
2.3.4	Transmission electron microscopy (TEM) and High resolution TEM analyses	79
2.3.5	Ultraviolet-visible (UV-Vis) spectroscopy.....	80
2.4	Electrochemical studies	80

2.5	Results and discussion	80
2.5.1	Powder X-ray diffraction analysis	80
2.5.2	EDX composition analysis	82
2.5.3	XPS Analysis	84
2.5.4	SEM, TEM and HRTEM analyses	86
2.5.5	Analysis of optical properties	88
2.5.6	Electrochemical performance of $\text{Ni}_{1-x}\text{Co}_x\text{Fe}_2\text{O}_4$ ($0 \leq x \leq 1$) solid solutions	90
2.5.6.1	Supercapacitance.....	90
2.5.6.2	Hydrogen evolution reaction (HER)	95
2.5.6.3	Oxygen evolution reaction (OER)	98
2.6	Conclusion	101
References.....		102

CHAPTER 3. Composition-tuneable synthesis of $\text{Co}_{1-x}\text{Zn}_x\text{Fe}_2\text{O}_4$ ($0 \leq x \leq 1$) solid solutions by melt pyrolysis for electrochemical energy conversion and storage.....108

3.1	Introduction	109
3.2	Experimental.....	111
3.2.1	Chemicals	111
3.2.2	Synthesis of $\text{Co}_{1-x}\text{Zn}_x\text{Fe}_2\text{O}_4$ ($x = 0, 0.2, 0.4, 0.6, 0.8, 1$) solid solutions	111
3.3	Instrumentation	112
3.3.1	Scanning electron microscopy (SEM) and Energy dispersive X-ray (EDX) analyses	112
3.3.2	Transmission electron microscopy (TEM) and High resolution TEM analyses....	112
3.3.3	UV-visible spectroscopy.....	112
3.4	Electrochemical characterization.....	112
3.5	Results and discussion	113
3.5.1	Structural analysis of $\text{Co}_{1-x}\text{Zn}_x\text{Fe}_2\text{O}_4$ ($0 \leq x \leq 1$) solid solutions.....	113
3.5.2	EDX analysis	115
3.5.3	SEM, TEM and HRTEM analyses	118

3.5.4	UV-vis analysis	120
3.6	Electrochemical evaluation of $\text{Co}_{1-x}\text{Zn}_x\text{Fe}_2\text{O}_4$ ($0 \leq x \leq 1$) nanoparticles	122
3.6.1	Supercapacitance	122
3.6.2	Electrocatalytic water splitting	124
3.7	Conclusion	130
References		131
CHAPTER 4. Direct solid-state synthesis of nanometric $\text{Ni}_{1-x}\text{Mg}_x\text{Fe}_2\text{O}_4$ ($0 \leq x \leq 1$) solid solutions as eco-friendly electrode materials for water splitting and supercapacitance		137
4.1	Introduction	138
4.2	Experimental	140
4.2.1	Chemicals	140
4.2.2	Synthesis of $\text{Ni}_{1-x}\text{Mg}_x\text{Fe}_2\text{O}_4$ ($0 \leq x \leq 1$) solid solutions	140
4.3	Characterization techniques	141
4.3.1	Powder X-ray diffraction (p-XRD) analysis	141
4.3.2	Scanning electron microscopy (SEM) and Energy dispersive X-ray (EDX) analyses	141
4.3.3	Transmission electron microscopy (TEM), High resolution TEM (HRTEM) and Selected area electron diffraction (SAED) analyses	141
4.3.4	UV-visible spectroscopy	141
4.4	Electrochemical characterization	141
4.5	Results and discussion	142
4.5.1	Structural analysis of $\text{Ni}_{1-x}\text{Co}_x\text{Fe}_2\text{O}_4$ ($0 \leq x \leq 1$) solid solutions	142
4.5.2	Elemental compositional analysis	144
4.5.3	Microstructure and morphological studies	147
4.5.4	UV-Vis analysis	150
4.5.5	Electrocatalytic water splitting studies of $\text{Ni}_{1-x}\text{Mg}_x\text{Fe}_2\text{O}_4$ solid solutions	151
4.5.6	Supercapacitance	157

4.5.7	Conclusion	160
References.....		161
CHAPTER 5. Electrochemical investigation of uncapped $\text{Ni}_{1-x}\text{Zn}_x\text{Fe}_2\text{O}_4$ ($0 \leq x \leq 1$) solid solutions prepared by a solventless thermolytic approach		166
5.1	Introduction	167
5.2	Experimental	169
5.2.1	Chemicals	169
5.2.2	Synthesis of $\text{Ni}_{1-x}\text{Zn}_x\text{Fe}_2\text{O}_4$ ($x = 0, 0.2, 0.4, 0.6, 0.8, 1$) solid solutions.....	169
5.3	Characterization of nanostructured $\text{Ni}_{1-x}\text{Zn}_x\text{Fe}_2\text{O}_4$ ($0 \leq x \leq 1$) solid solutions	170
5.3.1	Powder X-ray diffraction (p-XRD) analysis	170
5.3.2	Scanning electron microscopy (SEM) and Energy dispersive X-ray (EDX) analyses	170
5.3.3	Transmission electron microscopy (TEM), High resolution TEM (HRTEM) and Selected area electron diffraction (SAED) analyses	170
5.3.4	UV-visible spectroscopy	170
5.4	Electrochemical evaluation of $\text{Ni}_{1-x}\text{Zn}_x\text{Fe}_2\text{O}_4$ ($0 \leq x \leq 1$) solid solutions.....	170
5.5	Results and discussion.....	171
5.5.1	Powder X-ray diffraction (p-XRD) study	171
5.5.2	Compositional studies	174
5.5.3	Analysis of microstructure and morphology	176
5.5.4	Analysis of optical properties	179
5.5.5	Evaluation of the potential of $\text{Ni}_{1-x}\text{Zn}_x\text{Fe}_2\text{O}_4$ nanospinels for energy applications	181
5.5.5.1	Electrochemical water splitting	181
5.5.5.2	Supercapacitance application.....	185
5.6	Conclusion	188
References.....		189
CHAPTER 6. Facile solventless synthesis and physicochemical properties of nanostructured $\text{Co}_{1-x}\text{Mg}_x\text{Fe}_2\text{O}_4$ ($0 \leq x \leq 1$) solid solutions		193

6.1	Introduction.....	194
6.2	Experimental.....	196
6.2.1	Chemicals.....	196
6.2.2	Solventless synthesis of $\text{Co}_{1-x}\text{Mg}_x\text{Fe}_2\text{O}_4$ ($0 \leq x \leq 1$) solid solutions.....	196
6.3	Instrumentation	197
6.3.1	Powder X-ray diffraction (p-XRD) analysis.....	197
6.3.2	Scanning electron microscopy (SEM) and Energy dispersive X-ray (EDX) analyses	197
6.3.3	Transmission electron microscopy (TEM) and High resolution TEM analyses....	197
6.3.4	UV-visible spectroscopy.....	197
6.4	Results and discussion	197
6.4.1	Phase and structure analysis	197
6.4.2	EDX analysis	198
6.4.3	SEM, TEM, HRTEM and SAED analyses	200
6.4.4	Optical absorbance and band gap tuning	202
6.5	Conclusion	204
	References.....	205
	CHAPTER 7. Summary and future work	208
7.1	Summary of the work	209
7.2	Future work	210
	List of publications	212
	List of conferences	212

List of figures

Fig. 1.1 (a). Diagrams of the two and three-electrode configurations, (b) types of supercapacitors (EDLC, pseudocapacitor and hybrid), (c) mechanism of charge storage in EDLCs, ion adsorption and desorption on the surface. ⁵⁵	6
Fig. 1.2. Mechanism of capacitive energy storage via double-layer capacitance established at electrodes containing (a) carbon particles and (b) porous carbon. Pseudocapacitive mechanisms; (c) redox pseudocapacitance, as in metal oxides, and (d) intercalation pseudocapacitance, where Li ⁺ ions are intercalated into the host material.	6
Fig. 1.3. Scheme of conventional water electrolyzer.....	8
Fig. 1.4. (a) The crystal structure of spinel ferrite (AB ₂ O ₄ = MFe ₂ O ₄ , where A or M = divalent metals and B = Fe) (b) tetrahedral sites (c) octahedral sites.	12
Fig. 1.5. Representation of: (a) substitutional solid solution, (b) interstitial solid solution.	15
Fig. 1.6. HRTEM images of the synthesized (Bi _{1-x} Sb _x) ₂ S ₃ (0 ≤ x ≤ 1) nanorods (Reproduced from ref. 84).	18
Fig. 1.7. TEM images showing the as synthesized (Bi _{1-x} Sb _x) ₂ S ₃ (0 ≤ x ≤ 1) nanorods (Reproduced from ref. 84).	18
Fig. 1.8. TEM images of PbS _x Se _(1-x) obtained at x _{Se} values of (a) 0, (b) 0.3, (c) 0.5, (d) 0.8, (e) 1. (f).UV-Vis-NIR spectra of PbS _{1-x} Se _x (0 ≤ x ≤ 1) nanoparticles. (Reproduced from ref. 67).	35
Fig. 1.9. p-XRD pattern of SnS _{1-x} Se _x (0 ≤ x ≤ 1) prepared by (i) hot injection method in OLA at 200 °C, (ii) the solvent-less route at 330 °C (Reproduced from ref. 68).	36
Fig.1.10. SEM images of SnS _{1-x} Se _x (0 ≤ x ≤ 1) (i) synthesized by the hot injection method, (ii) synthesized by solventless method (Reproduced from ref. 68).	36
Fig. 1.11 (a) p-XRD pattern of Ni _{1-x} Co _x Fe ₂ O ₄ (0 ≤ x ≤ 1) series, (b) variation of lattice constant (left y-axis) and the optical band gap (right y-axis) of Ni _{1-x} Co _x Fe ₂ O ₄ (0 ≤ x ≤ 1) solid solutions (Reproduced from ref. 199).	45
Fig.1.12 (a) GCD graphs of the x = 0.6 electrode for various current densities (1-20 Ag ⁻¹) (b) HER polarization curves, (c) OER polarization curves, for Ni _{1-x} Co _x Fe ₂ O ₄ (0 ≤ x ≤ 1) (Reproduced from ref. 199).	45
Fig. 2.1. (a) p-XRD pattern of Ni _{1-x} Co _x Fe ₂ O ₄ (0 ≤ x ≤ 1) series. (b) variation of lattice constant (left y-axis) and the optical band gap (right y-axis) with cobalt content.	81

Fig. 2.2. EDX spectra for the prepared $\text{Ni}_{1-x}\text{Co}_x\text{Fe}_2\text{O}_4$ ($0 \leq x \leq 1$) nanoparticles.	83
Fig. 2.3. EDX elemental mapping of NiFe_2O_4 ($x = 0$) and CoFe_2O_4 ($x = 1$) showing a uniform distribution of elements.....	83
Fig. 2.4. EDX elemental mapping of $\text{Ni}_{1-x}\text{Co}_x\text{Fe}_2\text{O}_4$ ($0.2 \leq x \leq 0.8$) solid solutions showing a uniform distribution of elements.	84
Fig. 2.5: (a) Survey spectra for $\text{Ni}_{1-x}\text{Co}_x\text{Fe}_2\text{O}_4$: (i) $x = 0.2$, (ii) $x = 0.4$, (iii) $x = 0.6$. (b) High resolution core-level spectra of Fe 2p for $x = 0.6$. XPS high resolution core-level spectra of (c) O 1s and (d) C 1s of the ternary $\text{Ni}_{1-x}\text{Co}_x\text{Fe}_2\text{O}_4$ ($x = 0.4$).....	85
Fig. 2.6. SEM images of $\text{Ni}_{1-x}\text{Co}_x\text{Fe}_2\text{O}_4$ ($0 \leq x \leq 1$) solid solutions.....	87
Fig. 2.7. TEM images of $\text{Ni}_{1-x}\text{Co}_x\text{Fe}_2\text{O}_4$ ($0 \leq x \leq 1$) solid solutions.....	87
Fig. 2.8. HRTEM images of $\text{Ni}_{1-x}\text{Co}_x\text{Fe}_2\text{O}_4$ ($0 \leq x \leq 1$) solid solutions.	88
Fig. 2.9. UV-Vis absorption spectrum of $\text{Ni}_{1-x}\text{Co}_x\text{Fe}_2\text{O}_4$ ($0 \leq x \leq 1$) solid solutions.	89
Fig. 2.10. Tauc plots of $(\alpha h\nu)^2$ versus energy for $\text{Ni}_{1-x}\text{Co}_x\text{Fe}_2\text{O}_4$ ($0 \leq x \leq 1$) solid solutions.	89
Fig. 2.11. CV graphs of $\text{Ni}_{1-x}\text{Co}_x\text{Fe}_2\text{O}_4$ ($0 \leq x \leq 1$) electrodes at various scan rates (2mV/s – 300mV/s)	90
Fig. 2.12. (a) Specific capacitance versus scan rate, (b) Specific capacitance versus current density, (c) Variation of energy and power density, for $\text{Ni}_{1-x}\text{Co}_x\text{Fe}_2\text{O}_4$ ($0 \leq x \leq 1$) samples.....	93
Fig. 2.13. GCD characteristics of $\text{Ni}_{1-x}\text{Co}_x\text{Fe}_2\text{O}_4$ ($0 \leq x \leq 1$) electrodes at various current densities (1A/g – 20 A/g).....	94
Fig. 2.14. Capacitance retention and columbic efficiency of $\text{Ni}_{1-x}\text{Co}_x\text{Fe}_2\text{O}_4$ ($0 \leq x \leq 1$) electrodes.	94
Fig. 2.15. (a) HER polarization curves, (b) Tafel slopes for $\text{Ni}_{1-x}\text{Co}_x\text{Fe}_2\text{O}_4$ ($0 \leq x \leq 1$) samples.....	97
Fig. 2.16. HER polarization curves at various cycles for $\text{Ni}_{1-x}\text{Co}_x\text{Fe}_2\text{O}_4$ ($0 \leq x \leq 1$) samples.....	97
Fig. 2.17. (a) OER polarization curves, (b) Tafel slopes for various samples (c) Electrochemical impedance spectroscopic spectra of all the samples at various potentials (vs. SCE) at 0.5V.....	99
Fig. 2.18. Chronoamperometry characteristics of the various samples in 1 M KOH (inset) OER polarization curves at various cycles for the various samples.	100
Fig.3.1. (a) Powder-XRD pattern of $\text{Co}_{1-x}\text{Zn}_x\text{Fe}_2\text{O}_4$ ($0 \leq x \leq 1$) nanoparticles, (b) Variation of lattice constants as a function of zinc composition.	114

Fig.3.2. EDX spectra of $\text{Co}_{1-x}\text{Zn}_x\text{Fe}_2\text{O}_4$ ($0 \leq x \leq 1$) nanoparticles.	116
Fig.3.3. Change in the amount of zinc and cobalt as a function of mole fraction of [Zn]/[Zn+ Co] in precursor feed.	117
Fig.3.4. EDX elemental mapping of CoFe_2O_4 ($x = 0$) and ZnFe_2O_4 . ($x = 1$) nanoparticles.	117
Fig.3.5. EDX elemental mapping of $\text{Co}_{1-x}\text{Zn}_x\text{Fe}_2\text{O}_4$ ($0.2 \leq x \leq 0.8$) solid solutions.	117
Fig.3.6. SEM images of $\text{Co}_{1-x}\text{Zn}_x\text{Fe}_2\text{O}_4$ ($0 \leq x \leq 1$) samples prepared by solventless method.	118
Fig.3.7. The typical TEM images of $\text{Co}_{1-x}\text{Zn}_x\text{Fe}_2\text{O}_4$ ($0 \leq x \leq 1$) nanospinels.	119
Fig.3.8. The typical HRTEM images of $\text{Co}_{1-x}\text{Zn}_x\text{Fe}_2\text{O}_4$ ($0 \leq x \leq 1$) nanospinels.	120
Fig.3.9 (a). UV-Vis absorption spectra, (b) Tauc plot of $(\alpha h\nu)^2$ versus photon energy, for $\text{Co}_{1-x}\text{Zn}_x\text{Fe}_2\text{O}_4$ ($0 \leq x \leq 1$) solid solutions.	122
Fig.3.10. Cyclic voltammograms of $\text{Co}_{1-x}\text{Zn}_x\text{Fe}_2\text{O}_4$ ($0 \leq x \leq 1$) electrodes.	123
Fig.3.11. GCD of $\text{Co}_{1-x}\text{Zn}_x\text{Fe}_2\text{O}_4$ ($0 \leq x \leq 1$) electrodes.	124
Fig.3.12. Variation of specific capacitance with current density for $\text{Co}_{1-x}\text{Zn}_x\text{Fe}_2\text{O}_4$ ($0 \leq x \leq 1$) electrodes.	124
Fig.3.13: (a) OER polarization curves, (b) OER Tafel slopes, (c) HER polarization curves, (d) HER Tafel slopes, (e) Nyquist plots at 0.5 V, and (f) CA measurement at 0.55 V, for $\text{Co}_{1-x}\text{Zn}_x\text{Fe}_2\text{O}_4$ ($0 \leq x \leq 1$) electrodes.	126
Fig.3.14. Comparison of OER polarization curve between LSV 1 curve and LSV 1k curve for $\text{Co}_{1-x}\text{Zn}_x\text{Fe}_2\text{O}_4$ ($0 \leq x \leq 1$) electrodes.	128
Fig.3.15. Comparison of HER polarization curve between LSV 1 curve and LSV 1k curve for $\text{Co}_{1-x}\text{Zn}_x\text{Fe}_2\text{O}_4$ ($0 \leq x \leq 1$) electrodes.	128
Fig. 4.1. (a) Powder-XRD patterns (b) Variation of lattice constant (left y-axis) and cell volume (right y-axis) with Mg^{2+} content for $\text{Ni}_{1-x}\text{Mg}_x\text{Fe}_2\text{O}_4$ ($0 \leq x \leq 1$) solid solutions	143
Fig. 4.2. EDX pattern of $\text{Ni}_{1-x}\text{Mg}_x\text{Fe}_2\text{O}_4$ ($0 \leq x \leq 1$) solid solution nanoparticles.	145
Fig. 4.4. EDX elemental mapping of $\text{Ni}_{1-x}\text{Mg}_x\text{Fe}_2\text{O}_4$ ($x = 0$ and 1) nanoparticles.	146
Fig. 4.5. EDX elemental mapping of $\text{Ni}_{1-x}\text{Mg}_x\text{Fe}_2\text{O}_4$ ($0.2 \leq x \leq 0.8$) nanoparticles.	147
Fig. 4.6. SEM images of $\text{Ni}_{1-x}\text{Mg}_x\text{Fe}_2\text{O}_4$ ($0 \leq x \leq 1$) samples prepared by solid state pyrolysis of metal acetylacetonates precursors with different mole fractions of magnesium.	148
Fig. 4.7. TEM images of $\text{Ni}_{1-x}\text{Mg}_x\text{Fe}_2\text{O}_4$ ($0 \leq x \leq 1$) nanoparticles.	148
Fig. 4.8. HRTEM images of $\text{Ni}_{1-x}\text{Mg}_x\text{Fe}_2\text{O}_4$ ($0 \leq x \leq 1$) nanoparticles.	149

Fig. 4.9. SAED images of $\text{Ni}_{1-x}\text{Mg}_x\text{Fe}_2\text{O}_4$ ($0 \leq x \leq 1$) nanoparticles.....	149
Fig. 4.10. UV-Vis absorption spectra of $\text{Ni}_{1-x}\text{Mg}_x\text{Fe}_2\text{O}_4$ ($0 \leq x \leq 1$) solid solutions.	151
Fig. 4.11. Tauc plots of $(\alpha h\nu)^2$ versus energy for $\text{Ni}_{1-x}\text{Mg}_x\text{Fe}_2\text{O}_4$ ($0 \leq x \leq 1$) solid solutions.	151
Fig. 4.12. (a) HER polarization curves, (b) HER Tafel slopes, (c) OER polarization curves, (d) OER Tafel slopes, (e) Nyquist plots at 0.5 V, and (f) CA measurement at 0.55 V, for $\text{Ni}_{1-x}\text{Mg}_x\text{Fe}_2\text{O}_4$ ($0 \leq x \leq 1$) electrodes.	153
Fig. 4.13. Comparison of HER polarization curve between LSV 1 curve and LSV 1k curve for $\text{Ni}_{1-x}\text{Mg}_x\text{Fe}_2\text{O}_4$ ($0 \leq x \leq 1$) electrodes.....	154
Fig. 4.14. Comparison of OER polarization curve between LSV 1 curve and LSV 1k curve for $\text{Ni}_{1-x}\text{Mg}_x\text{Fe}_2\text{O}_4$ ($0 \leq x \leq 1$) ($0 \leq x \leq 1$) electrodes.....	155
Fig. 4.15. Cyclic voltammograms of $\text{Ni}_{1-x}\text{Mg}_x\text{Fe}_2\text{O}_4$ ($0 \leq x \leq 1$) electrodes.....	158
Fig. 4.16. GCD of $\text{Ni}_{1-x}\text{Mg}_x\text{Fe}_2\text{O}_4$ ($0 \leq x \leq 1$) electrodes.....	159
Fig. 4.17. Specific capacitance versus current density for $\text{Ni}_{1-x}\text{Mg}_x\text{Fe}_2\text{O}_4$ ($0 \leq x \leq 1$) electrodes.	160
Fig.5.1.(a) p-XRD patterns of $\text{Ni}_{1-x}\text{Zn}_x\text{Fe}_2\text{O}_4$ ($0 \leq x \leq 1$) nanoparticles. (b) Variation of lattice constant (left y-axis) and cell volume (right y-axis) as a function of Zn^{2+} concentration.....	172
Fig.5.2. EDX pattern of $\text{Ni}_{1-x}\text{Zn}_x\text{Fe}_2\text{O}_4$ ($0 \leq x \leq 1$) solid solution nanoparticles.	175
Fig.5.3. EDX elemental mapping of $\text{Ni}_{1-x}\text{Zn}_x\text{Fe}_2\text{O}_4$ ($x = 0$ and 1) showing uniform distribution of elements.....	175
Fig.5.4. EDX elemental mapping of $\text{Ni}_{1-x}\text{Zn}_x\text{Fe}_2\text{O}_4$ ($0.2 \leq x \leq 0.8$) solid solutions showing uniform distribution of elements.	176
Fig.5.5. SEM images of $\text{Ni}_{1-x}\text{Zn}_x\text{Fe}_2\text{O}_4$ ($0 \leq x \leq 1$) samples.	177
Fig.5.6. TEM images of $\text{Ni}_{1-x}\text{Zn}_x\text{Fe}_2\text{O}_4$ ($0 \leq x \leq 1$) nanoparticles.....	177
Fig.5.7. HRTEM images of $\text{Ni}_{1-x}\text{Zn}_x\text{Fe}_2\text{O}_4$ ($0 \leq x \leq 1$) nanoparticles.	178
Fig.5.8. SAED images of $\text{Ni}_{1-x}\text{Zn}_x\text{Fe}_2\text{O}_4$ ($0 \leq x \leq 1$) nanoparticles.....	178
Fig.5.9. UV-Vis of $\text{Ni}_{1-x}\text{Zn}_x\text{Fe}_2\text{O}_4$ ($0 \leq x \leq 1$) nanoparticles at different zinc contents. .	179
Fig. 5.10. Tauc plot of $\text{Ni}_{1-x}\text{Zn}_x\text{Fe}_2\text{O}_4$ ($0 \leq x \leq 1$) nanoparticles at different zinc content.	180
Fig.5.11. Variation of band gap of $\text{Ni}_{1-x}\text{Zn}_x\text{Fe}_2\text{O}_4$ ($0 \leq x \leq 1$) as a function of Zn^{2+} ions concentration.....	180

Fig. 5.12. (a) HER polarization curves, (b) HER Tafel slopes, (c) OER polarization curves, (d) OER Tafel slopes, (e) Nyquist plots at 0.5 V, and (f) CA measurement at 0.55 V, for $\text{Ni}_{1-x}\text{Zn}_x\text{Fe}_2\text{O}_4$ ($0 \leq x \leq 1$) electrodes.	183
Fig. 5.13. Comparison of HER polarization curve between LSV 1 curve and LSV 1k curve for $\text{Ni}_{1-x}\text{Zn}_x\text{Fe}_2\text{O}_4$ ($0 \leq x \leq 1$) electrodes.	183
Fig. 5.14. Comparison of OER polarization curve between LSV 1 curve and LSV 1k curve for $\text{Ni}_{1-x}\text{Zn}_x\text{Fe}_2\text{O}_4$ ($0 \leq x \leq 1$) electrodes.	184
Fig. 5.15. CV curves of $\text{Ni}_{1-x}\text{Zn}_x\text{Fe}_2\text{O}_4$ ($0 \leq x \leq 1$) electrodes at different scanning rates.	186
Fig. 5.16. GCD curves $\text{Ni}_{1-x}\text{Zn}_x\text{Fe}_2\text{O}_4$ ($0 \leq x \leq 1$) ($0 \leq x \leq 1$) electrodes at a current densities.	187
Fig. 5.17. Specific capacity of $\text{Ni}_{1-x}\text{Zn}_x\text{Fe}_2\text{O}_4$ ($0 \leq x \leq 1$) electrodes at different current densities.	187
Fig. 6.1. (a) p-XRD pattern of $\text{Co}_{1-x}\text{Mg}_x\text{Fe}_2\text{O}_4$ ($0 \leq x \leq 1$), (b) variation of lattice constant (left y-axis) and cell volume (right y-axis) of as a function of magnesium content. .	198
Fig. 6.2. EDX spectrum for the prepared $\text{Co}_{1-x}\text{Mg}_x\text{Fe}_2\text{O}_4$ ($0 \leq x \leq 1$) nanoparticles.	199
Fig. 6.3. EDX elemental mapping of $\text{Co}_{1-x}\text{Mg}_x\text{Fe}_2\text{O}_4$ ($0 \leq x \leq 1$) solid solutions showing a uniform distribution of elements.	199
Fig. 6.4. SEM images of $\text{Co}_{1-x}\text{Mg}_x\text{Fe}_2\text{O}_4$ ($0 \leq x \leq 1$) solid solutions.	201
Fig. 6.5. TEM images of $\text{Co}_{1-x}\text{Mg}_x\text{Fe}_2\text{O}_4$ ($0 \leq x \leq 1$) solid solutions.	201
Fig. 6.6. HRTEM images of $\text{Co}_{1-x}\text{Mg}_x\text{Fe}_2\text{O}_4$ ($0 \leq x \leq 1$) solid solutions.	202
Fig. 6.7. Representative SAED images of $\text{Co}_{1-x}\text{Mg}_x\text{Fe}_2\text{O}_4$ ($x = 0, 0.8$ and 1) nanoparticles.	202
Fig. 6.8. UV-Vis absorption spectrum of $\text{Co}_{1-x}\text{Mg}_x\text{Fe}_2\text{O}_4$ ($0 \leq x \leq 1$) solid solutions. ...	203
Fig. 6.9. Tauc plots of $(\alpha h\nu)^2$ versus energy for $\text{Co}_{1-x}\text{Mg}_x\text{Fe}_2\text{O}_4$ ($0 \leq x \leq 1$) solid solution.	204

List of tables

Table 1.1. Electrochemical water splitting reactions under alkaline and acidic electrolytes	8
Table 1.2. The electrochemical mechanism for HER.	9
Table 1.3. The preferred structure of spinel ferrites and its dependence on the type of cation.....	12
Table 1.4. Pseudobinary quaternary solid solutions of (III-V) _{1-x} (II-VI) _x systems	52
Table 2.1. Lattice parameter (a), crystallite size (d), unit cell volume (V), band gap (E_g), and EDX compositions of Ni _{1-x} Co _x Fe ₂ O ₄ solid solutions at different cobalt contents (x).....	84
Table 2.2. A comparison of the specific capacitance of Ni _{0.4} Co _{0.6} Fe ₂ O ₄ electrode with other metal oxide-based electrodes.	95
Table 2.3. Comparison of HER performance of the synthesized Ni _{0.6} Co _{0.4} Fe ₂ O ₄ and CoFe ₂ O ₄ with other reported Ni/Co-based electrocatalysts in alkaline electrolyte.	97
Table 2.4. Comparison of OER performance of the synthesized Ni _{0.8} Co _{0.2} Fe ₂ O ₄ with other reported Ni/Co-based electrocatalysts in alkaline electrolyte.	100
Table 3.1. Lattice parameter (a), crystallite size (d), unit cell volume (V), band gap (E_g) and EDX composition of Co _{1-x} Zn _x Fe ₂ O ₄ solid solutions at different zinc contents (x).	115
Table 3.2. Theoretical and actual elemental composition of Co _{1-x} Zn _x Fe ₂ O ₄ (0 ≤ x ≤ 1) solid solutions.	117
Table 3.3. Comparison of OER activities of Co _{0.8} Zn _{0.2} Fe ₂ O ₄ with previously reported electrocatalyst electrodes in alkaline solution.....	128
Table 3.4. Comparison of HER activities of Co _{0.6} Zn _{0.4} Fe ₂ O ₄ with previously reported electrocatalyst electrodes in alkaline solution.....	129
Table 4.1. Lattice parameter (a), crystallite size (d), unit cell volume (V), and EDX composition of nanospinel Ni _{1-x} Mg _x Fe ₂ O ₄ solid solutions at various magnesium contents (x).....	143
Table 4.2. Summary of the theoretical and experimental atomic % for Ni _{1-x} Mg _x Fe ₂ O ₄ solid solutions obtained from EDX analysis.....	146
Table 4.3. The optical band gaps for Ni _{1-x} Mg _x Fe ₂ O ₄ (0 ≤ x ≤ 1) nanoparticles.	150

Table 4.4. Comparison of HER performance of $\text{Ni}_{0.4}\text{Mg}_{0.6}\text{Fe}_2\text{O}_4$ with previously reported electrocatalysts in alkaline electrolyte.	155
Table 4.5. Comparison of OER performance of $\text{Ni}_{0.2}\text{Mg}_{0.8}\text{Fe}_2\text{O}_4$ with previously reported electrocatalysts in alkaline electrolyte.	156
Table 5.1: Lattice parameter (a), unit cell volume (V) , crystallite size (d), and EDX composition of $\text{Ni}_{1-x}\text{Zn}_x\text{Fe}_2\text{O}_4$ ($0 \leq x \leq 1$) solid solutions.	172
Table 5.2. Summary of $\text{Ni}_{1-x}\text{Zn}_x\text{Fe}_2\text{O}_4$ ($0 \leq x \leq 1$) compositions obtained from EDX analysis.....	174
Table 5.3. The optical band gaps for $\text{Ni}_{1-x}\text{Zn}_x\text{Fe}_2\text{O}_4$ ($0 \leq x \leq 1$) nanoparticles.....	180
Table 5.3. Comparison of HER performance of $\text{Ni}_{0.2}\text{Zn}_{0.8}\text{Fe}_2\text{O}_4$ with previously reported electrocatalysts in alkaline electrolyte.	184
Table 5.4. Comparison of OER performance of ZnFe_2O_4 with previously reported electrocatalysts in alkaline electrolyte.	185
Table 6.1. Lattice parameter (a), crystallite size (d), unit cell volume (V), and EDX composition of $\text{Co}_{1-x}\text{Mg}_x\text{Fe}_2\text{O}_4$ ($0 \leq x \leq 1$) solid solutions.	199
Table 6.2. Expected and experimental atomic percentage for $\text{Co}_{1-x}\text{Mg}_x\text{Fe}_2\text{O}_4$ ($0 \leq x \leq 1$) solid solutions.	200
Table 6.3. The optical band gaps for $\text{Co}_{1-x}\text{Mg}_x\text{Fe}_2\text{O}_4$ ($0 \leq x \leq 1$) nanoparticles obtained at different magnesium content.....	204

List of abbreviations and symbols

Å	Angstrom
b	Tafel slope
CA	Chronoamperometry
CV	Cyclic voltammetry
CVD	Chemical vapor deposition
DDT	1-dodecanethiol
Ddtc	Diethyldithiocarbamate
DMF	Dimethylformamide
EDLCs	Electric double layer capacitors
EDX	Energy dispersive X-ray analysis
EIS	Electrochemical impedance spectroscopy
eV	Electron volt
FESEM	Field emission scanning electron microscopy
GCD	Galvanostatic charge-discharge
HAD	Hexamethylenediamine
HER	Hydrogen evolution reaction
HRTEM	High-resolution transmission electron microscopy
ICDD	International centre for diffraction data
LSV	Linear sweep voltammetry
MOCVD	Metal organic chemical vapor deposition
N ₂	Nitrogen gas
nm	Nanometer
NMP	N-methyl pyrrolidinone
OA	Oleic acid
OAc	Acetate
ODE	1-octadecene
OER	Oxygen evolution reaction
OLA	Oleylamine
PVDF	Polyvinylidene difluoride
p-XRD	Powder X-ray diffraction
SAED	Selected area electron diffraction
SCE	Saturated calomel electrode

SEM	Scanning electron microscopy
STEM	Scanning transmission electron microscopy
TEM	Transmission electron microscopy
TOP	Trioctylphosphine
TPR	Temperature-programmed reduction
UV/Vis	Ultraviolet visible
XPS	X-ray photoelectron spectroscopy
θ	Theta
λ	Lambda (wavelength)
η_{10}	Overpotential at current density of 10 mA/cm ²

CHAPTER 1

Introduction and Literature Review

1.1 General introduction

Energy security and environmental sustainability are fundamental inputs for sustainable social and economic development in the modern world. However, the development of modern society is confronting the conflict between the growing energy demand and realizing a low-carbon economy.¹ Due to population and economic growth, the global energy demand is estimated to rise by 50% in 2030 and is likely to double by the year 2050.² Ideally, this demand could be realized from fossil fuels, namely, natural gas, coal, and petroleum oil. However, growing concerns about their non-renewability, rapid depletion and the associated myriad of environmental problems cannot be ignored.³ In the move towards a sustainable world, renewable sources of energy, including wind, tidal solar, and hydro-powers are undoubtedly playing a pivotal role in overcoming fossil fuel exhaustion and global pollution and assure the generation of clean energy.⁴ However, these renewable energy sources suffer from seasonal and intermittent issues, making them difficult to satisfy the demands of daily life. If they are to be used as primary energy sources, they must be harvested, stored and dispatched on demand to the ultimate user.⁵ Therefore, to meet the future energy needs and low-carbon lifestyle, there is a dire need to develop efficient technologies for renewable energy harvesting and storage.

Electrochemical energy storage (supercapacitors and batteries) and conversion (fuel and electrolytic cells) technologies play fundamental roles in the sustainable development of human society. They are essential components that facilitate electrification of transportation, proficient exploitation of renewable energies, and the rapid development of portable electronics.⁶⁻¹¹ In recent decades, supercapacitors and rechargeable batteries have demonstrated great potential as dominant power sources for electric automobiles, portable electronics, and large-scale electric grids.¹²⁻¹⁴ Supercapacitors have continued to draw widespread promise owing to their fast charge-discharge rate, long cycling capability, and eco-friendliness. They, however, exhibit inferior energy density compared to batteries, necessitating intervention for improvement.¹⁵ Similarly, the production of hydrogen has been recognized as a highly efficient energy storage/conversion process to exploit renewable energy resources. Molecular hydrogen gas (H_2) stands out as an exceptionally appealing fuel with the highest energy content, making it an excellent renewable energy carrier.¹⁶ However, most of the H_2 is presently generated via steam reforming of fossil resources, a route which proceeds at a low conversion rate and emits pollutants, such as CO_2 and CO . Thus, successful realization of a green hydrogen economy requires clean and efficient routes for H_2

production. Electrochemical water splitting to yield hydrogen (H_2) and oxygen (O_2) is regarded as a clean and proficient solution for a sustainable energy system. It is viewed as a sustainable approach to substitute fossil fuels because, in the cycle of the hydrogen economy, water is used as both the starting precursor and by-product. The combustion of H_2 simultaneously liberates energy and reproduces pollution-free water as the only combustion by-product.¹⁷ The operational proficiency of water electrolysis is significantly influenced by the efficacy of electrocatalysts for the hydrogen evolution reaction (HER) and oxygen evolution reaction (OER). Principally, both HER and OER require catalysts to reduce the overpotentials, as well as electrical and transport-related resistances for effective H_2 and O_2 generation. Traditionally, platinum, ruthenium, and palladium and their hybrid materials have long been utilized as ideal HER catalysts, owing to their optimal hydrogen binding energy and low overpotential.¹⁸ Similarly, Ir/ Ru-based compounds including RuO_2 and IrO_2 have been known for OER catalysis. Unfortunately, the high price, insufficient reserves and poor stability of these noble metal-based catalysts restrict their yield of H_2 at a large scale equivalent to the global demand.¹⁹

Although electrochemical energy systems have advanced considerably over recent years, further improvements are still needed to meet the ever-growing power demand, lower overall cost and expand commercialization. In this context, the type of electroactive material plays a decisive role in determining their performance, stability, and cost.^{20, 21} Thus, the focus of new interventions in energy storage is to design state-of-the-art electrode materials capable of delivering high energy density without compromising the power density and cycling capability.²² Equally important, inexpensive, inexhaustible, efficient, and stable electrocatalysts operating at low overpotentials are needed for efficient energy conversion systems.^{23, 24} To date, low-cost materials based on transition metals, metal alloys, metal oxides, carbides, nitrides, phosphides, sulfides, borides, and metal-free composites have been explored for energy applications.²⁵⁻²⁸ Benefiting from their low cost, abundance, as well as structural and chemical stability, spinel nanoferrites have demonstrated a promising potential compared to their corresponding simple metal oxides. They have been further shown to exhibit remarkable electrochemical activity towards water splitting and supercapacitance due to their rich chemical composition, redox reversibility, high intrinsic conductivity, and superior ion transport.²⁹⁻³³

Beyond the nature of the material, effective tuning of its electronic property is a critical strategy for developing efficient energy devices as it provides additional opportunities to optimize electrochemical performance. Several approaches, including alloying, interfacing, doping, incorporating oxygen vacancies, and edge-defect engineering, have been selectively

used to tailor the electronic structure of diverse nanostructures.^{23, 34} Interestingly, the formation of solid solutions has recently been reported to induce substantial changes in the materials' electrical transport, redox reaction sites and energy band gap. Rational fabrication of nanoscopic solid solutions represents a robust approach towards obtaining materials with comparably high electrochemical performance than their pristine counterparts due to increased electrochemical sites and electroconductivity.³⁵⁻³⁸

To obtain homogeneous solid solutions, the rational design of a facile and efficient synthetic protocol is important.³⁹ This is because their formation may proceed with unforeseen events such as a rapid increase in enthalpy, the limited solubility of species involved, and slight structural disorder arising from vacancies or stacking faults.⁴⁰ These events, along with increased chemical complexity, may result in phase segregation and make the synthesis of these materials challenging. Recently, solventless thermolysis has been described as an alternative strategy for large-scale preparation of various nanomaterials because it is a self-capping, eco-friendly, scalable and straightforward protocol in which precursor(s) material undergo solid-state pyrolysis under thermal treatment.⁴¹ In comparison with the most frequently used wet-chemical synthesis and traditional solid-state techniques, this method guarantees a low-cost, efficient and low-temperature production of semiconductor materials with good control of crystallite size and stoichiometry, and it has not been utilized for the synthesis of nanostructured ferrite solid solutions from metal acetylacetonate precursors.^{42, 43} The choice of metal acetylacetonate precursors is based on their low melting points, eco-friendliness, cost-effectiveness, as well as low and clean decomposition.⁴⁴

1.2 Literature review

1.2.1 Electrochemical energy storage and conversion systems

Electrochemical technologies play a crucial role in realizing a sustainable future driven by the production, transformation as well as storage of clean energy from renewable sources. However, the scope of this literature review is confined to supercapacitors and water splitting as energy storage and conversion systems, respectively.

1.2.1.1 Supercapacitors

Supercapacitors (SCs) refers to energy storage devices in which the storage and release of electrochemical energy is achieved via reversible adsorption and desorption of ions at the electrode-electrolytes interface. They have attracted considerable research attention in

both academia and industry owing to their rapid rate capability, superior power density, pollution free operation, and long life cycle compared to batteries.^{45, 46} Owing to these fascinating properties, supercapacitors are regarded as highly desirable candidates for adoption as energy storage systems to narrow the gap between batteries and the traditional capacitors.⁴⁷ Presently, supercapacitors have found potential applications in transportation, grid balancing, consumer electronics, military and aerospace, and power backup by protecting, enhancing, and/or replacing batteries in these applications.¹⁵

1.2.1.2 Design, classification and mechanism of energy storage in supercapacitors

The design of a supercapacitor is composed of electrodes dipped in an electrolyte and separated by a permeable membrane, and their properties uniquely complement the overall device performance. In addition to non-toxicity and low-cost of the electroactive materials used in an electrode design, it should also be highly porous with higher electronic and ionic conductivity, higher specific surface area, and mechanical and thermal stability.⁴⁸ Likewise, for efficient working of the supercapacitor, the separator's shallow thickness, dielectric strength, permeability, and chemical inertness should be considered. On the basis of charge storage mechanism, electrochemical capacitors (supercapacitors) are classified into electrochemical double layer capacitors (EDLCs), pseudocapacitors, and hybrid capacitors (Fig. 1.1).⁴⁹

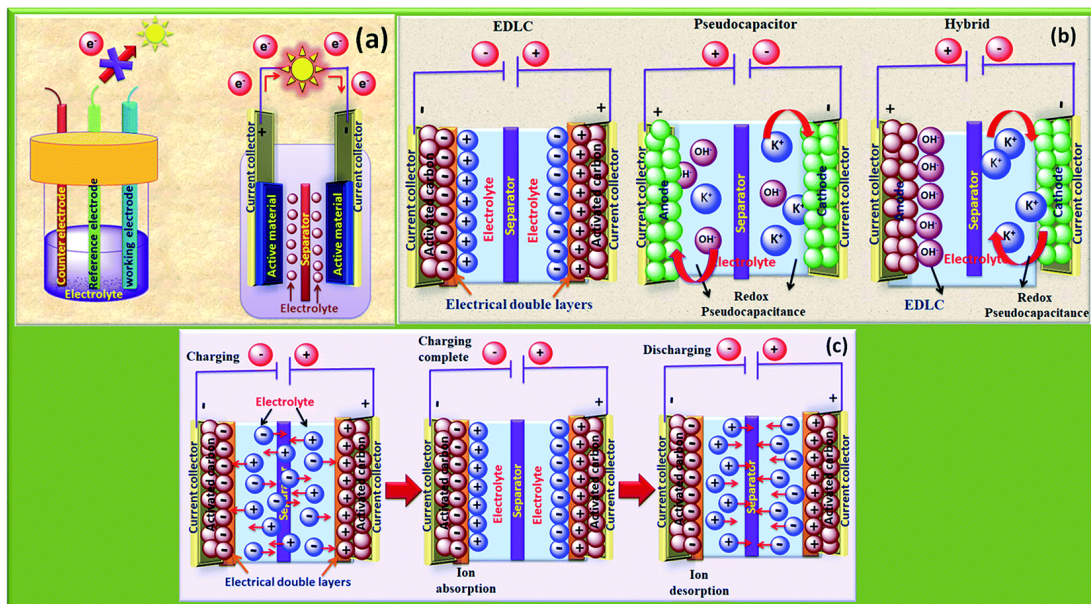


Fig. 1.1 Diagrams of (a) two and three-electrode configurations, (b) types of supercapacitors (EDLC, pseudocapacitor and hybrid), and (c) mechanism of charge storage in EDLCs, ion adsorption and desorption on the surface.⁵⁵

The EDLC relies on electrostatic accumulation of charges at the electrode-electrolyte interface, and therefore charge storage is done via physical adsorption of the electrolytic ions at the surface of electrode. When a potential is applied, an electric double layer consisting of cations and anions is formed at the interface between the electrodes and the electrolyte, and the charges get stored at the interface (Fig. 1.2(a & b)).

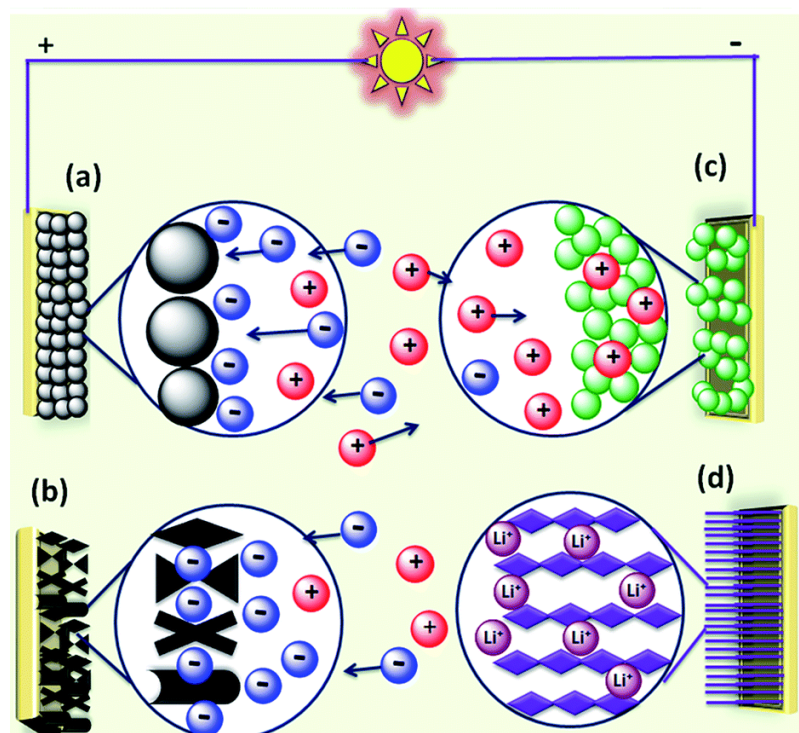


Fig. 1.2. Mechanism of capacitive energy storage via double-layer capacitance established at electrodes containing (a) carbon particles and (b) porous carbon. Pseudocapacitive mechanisms, (c) redox pseudocapacitance, as in metal oxides, and (d) intercalation pseudocapacitance, where Li^+ ions are intercalated into the host material.

The formed bilayer is due to physisorption of positively charged ions from the electrolyte on a negatively charged electrode and vice versa, when the potential is applied. The rapid ion diffusion between the electrode surface and the electrolyte solution accounts for their superior power density. Unlike rechargeable batteries, the charge-discharge process in DLCs is non-Faradic and therefore it shows high cyclability, which is significantly higher compared to rechargeable batteries. Nevertheless, EDLCs shows comparatively low energy

density than batteries. Owing to their porous nature, large surface area as well as high conductivity, carbon-based materials are preferably used as common electrodes for EDLCs.⁵⁰

⁵¹ In contrast, charge storage in pseudocapacitors rely not only on fast surface reversible redox reactions (Fig. 1.2(c)) which are Faradaic in nature but also on the creation of an electric double layer. Pseudocapacitive mechanisms deliver high capacitance compared to EDLC, and they arise from reversible reduction and oxidation processes like those occurring in metal oxides, adsorption or insertion of electrolytic ions at the electrode surface, and intercalation of ions, where Li^+ ions are introduced into the pristine material as displayed in Fig. 1.2(d). Common pseudocapacitive materials include metal oxides and conducting polymers.⁵² In hybrid supercapacitors, charge is stored both electrostatically and electrochemically. This type of supercapacitor benefits synergistically from the influence of EDLC (which enhances conductivity and stability) and pseudocapacitor (which offers capacitance), thus, increasing the overall device performance.⁵³ This can be realized through pairing a pseudocapacitor electrode with an EDLC electrode (forming asymmetric capacitor), incorporating metal oxides in carbon-based materials or conducting polymers in one electrode (composite capacitor), or coupling a supercapacitor electrode with a battery electrode (battery-type supercapacitor).^{53, 54}

1.2.1.3 Electrochemical water splitting

Water splitting (water electrolysis) is generally pictured as an appealing strategy for the production of clean hydrogen (H_2) and oxygen (O_2) from renewable resource. Electrochemical water splitting involves the chemical breakdown of water into hydrogen (H_2) and oxygen (O_2) at the separate electrodes by applying an electric current.⁵⁶ The water splitting process takes place in an electrolyzer consisting of anode and cathode electrode compartments immersed in an aqueous electrolyte (acidic, alkaline, or neutral) as displayed in Fig. 1.3. In order to mitigate the losses in charge transport in the course of electrochemical processes, conventional water electrolysis is commonly performed under either alkaline conditions with a diaphragm or acidic media with a proton exchange membrane.^{57, 58} Cathodic HER and anodic OER are two fundamental half-cell reactions of electrocatalytic water splitting, and they can be expressed in distinct ways subject to the reaction conditions (Fig. 1.3 and Table 1.1). When an external voltage is applied between the two electrode compartments, the HER yields H_2 at the cathode, whereas O_2 is formed at the anode by the OER.

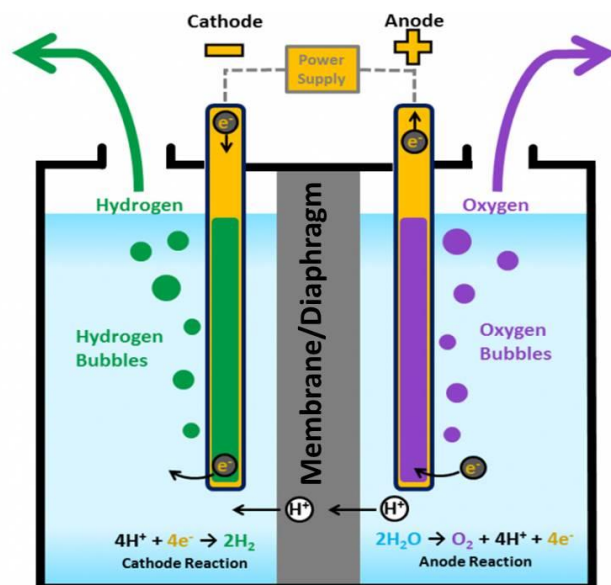


Fig. 1.3. Scheme of conventional water electrolyzer

Table 1.1. Electrochemical water splitting reactions under alkaline and acidic electrolytes.

Electrode reaction	Acidic medium	Alkaline medium
Anode	$2\text{H}_2\text{O} \rightarrow \text{O}_2 + 4\text{H}^+ + 4\text{e}^- \quad E^\theta = -1.23 \text{ V}$	$4\text{OH}^- \rightarrow \text{O}_2 + 2\text{H}_2\text{O} + 4\text{e}^- \quad E^\theta = -0.40 \text{ V}$
Cathode	$4\text{H}^+ + 4\text{e}^- \rightarrow 2\text{H}_2 \quad E^\theta = 0.00 \text{ V}$	$4\text{H}_2\text{O} + 4\text{e}^- \rightarrow 2\text{H}_2 + 4\text{OH}^- \quad E^\theta = -0.83 \text{ V}$
Overall	$2\text{H}_2\text{O} \rightarrow 2\text{O}_2 + 2\text{H}_2 \quad E^\theta = -1.23 \text{ V}$	$2\text{H}_2\text{O} \rightarrow 2\text{H}_2 + 2\text{O}_2 \quad E^\theta = -1.23 \text{ V}$

Under standard temperature (25 °C), and pressure (1 atm), the splitting of water into molecular H_2 and O_2 is not thermodynamically favourable, as it needs a thermodynamic potential of 1.23 V, equivalent to an energy supply of $\Delta G = 237.1 \text{ kJ/mol}$ to drive the process. Practically, during water electrolysis, a higher applied potential is needed to facilitate the intricate transfer of electrons and ions and overcome the slow kinetics and poor energy conversion efficiency.⁵⁹ It is also well established that, during water electrolysis, some unfavorable factors of electrode materials, including ion and gas diffusion and activation energy, can contribute to extra potential over the standard one, which is called an overpotential. Similarly, other factors related to a device, including heat release, electrolyte diffusion blockage, solution concentration, bubble formation, and wire and electrodes resistances, can equally contribute to the same effect.^{60, 61} Attempts have been made to elucidate the reaction pathway and improve electrolyzers, lowering the energy loss. The use

of proper electrocatalysts could significantly lower the overpotential and consequently promote the reaction rate and total cell efficiency. This is manifested by enormous efforts devoted to developing non-noble metal electrocatalysts with enhanced HER and OER activity. For instance, among many materials, carbides, metal alloys, sulfides, nitrides, tellurides, phosphides, selenides, and borides have been investigated as HER electrocatalysts in acidic medium, while several non-noble metal OER catalysts like metal oxides and (oxy)hydroxides have demonstrated excellent performance in alkaline condition.^{58, 62, 63}

In order to gain insights into some issues, such as determining the reaction rates, and designing and synthesizing electrocatalysts, a clear understanding of the HER mechanism is indispensable. The mechanism of HER process is greatly dependent on the pH of the electrolyte, and it takes place according to either the Volmer-Heyrovsky or Volmer-Tafel reaction mechanisms. In acidic solutions, the HER mechanism proceeds according to the following steps: The process begins with the Volmer reaction in which a proton (H^+) combines with an electron (e^-) on the surface of the catalyst (T), resulting in adsorption of a hydrogen atom on the surface. This is followed by the Heyrovsky reaction, which involves the combination of the adsorbed hydrogen atom (TH_{ads}) with a proton (H^+) and an electron (e^-) to produce a hydrogen molecule (H_2). Finally, the two adsorbed hydrogen atoms are combined to form a hydrogen molecule in the Tafel reaction. The mechanism of HER in alkaline media proceeds through a distinct Volmer and Heyrovsky reaction pathway due to high pH in alkaline conditions, hence the low concentration of protons. Therefore, in these two steps, molecular H_2O is used instead of H^+ . The HER mechanism in both acidic and alkaline electrolytes is described in Table 1.2.⁶³ On the other hand, the OER mechanism is a bit complex compared to that observed in HER, and will not be discussed here. Generally, the catalytic activity of an electrocatalyst can be examined using different factors such as overpotential, Tafel slope, Faradaic efficiency, turnover number, and catalyst stability.⁶⁴

Table 1.2. The electrochemical mechanism for HER.

HER step	In acidic medium	In alkaline medium
Volmer reaction	$T + H^+ + e^- \rightarrow TH_{ads}$	$H_2O + e^- + T \rightarrow TH_{ads} + OH^-$
Heyrovsky reaction	$TH_{ads} + H^+ + e^- \rightarrow H_2 + T$	$TH_{ads} + H_2O + e^- \rightarrow H_2 + OH^- + T$
Tafel reaction	$TH_{ads} + TH_{ads} \rightarrow H_2 + 2T$	$TH_{ads} + TH_{ads} \rightarrow H_2 + 2T$

1.2.2 Introduction to ferrites

Ferrites refer to a class of metal oxides consisting of iron as the main component in their structure. According to their structure, there are four broad ferrites categories: *ortho*-ferrites, garnets, hexagonal, and spinel ferrites. *Ortho*-ferrites is a category of ferrites exhibiting an orthorhombic crystal system with space group *Pbnm*. They are generally weak ferromagnetic materials designated by $RFeO_3$, where R is the rare-earth element. Common examples include $LaFeO_3$ and $DyFeO_3$. Garnets refer to a group of ferrites characterized by “hard magnetic” features and are represented by a general chemical formula $R_3(Fe_5O_{12})$, where R stands for the rare-earth element. Their crystal structure possesses tetrahedral, octahedral and dodecahedral sites. A good example is Yttrium garnet, $Y_3Fe_5O_{12}$. On the other hand, hexagonal ferrites or hexaferrites are ferrites with the chemical formula $MFe_{12}O_{19}$, where M can be barium, strontium, calcium or lead. They are an interrelated group of compounds having hexagonal and rhombohedral symmetry. These compounds exhibit complex crystal systems and are magnetically hard.^{65, 66} Spinel ferrites represent a large family of magnetic mixed-metal oxides having a stable crystal structure of the naturally occurring mineral spinel, $MgAl_2O_4$, and was determined for the first time by Bragg in 1915.⁶⁷ These semiconducting ferrites derive their name from their structural similarity with a naturally occurring mineral $MgAl_2O_4$. They are alternatively referred to as ferrospinels or cubic ferrites. Thus, spinel ferrites can simply be defined as closely packed cubic systems consisting of trivalent iron (Fe^{3+}) and divalent cations M^{2+} resulting in formula MFe_2O_4 (where M represents divalent metals including Mn, Ni, Fe, Co, Mg, Cu, Zn, Ca, etc., or their combinations). They are very stable compounds due to their stable crystal structure. Spinel ferrites provide important flexibility in modulating the materials’ electronic, magnetic and optical characteristics due to the proximal interaction between two distinct metal cations in the crystallographic sites, enabling synergistic effects not displayed in simple metal oxides.⁶⁸

1.2.2.1 The ferrite’s spinel structure and cation site occupation

Crystallographically, the ferrite spinel structure (Fig.1.4) is a cubic crystal system consisting of 32 closely packed oxygen atoms with 64 tetrahedral and 32 octahedral voids. The electrical neutrality of spinel ferrites formula, $(M^{2+})[Fe^{3+}]_2O_4$ is maintained by the corresponding divalent cation, M^{2+} and trivalent cation, Fe^{3+} in 8 tetrahedral and 16 octahedral positions, correspondingly.⁶⁹ The arrangement of metal cations and oxygen anions in the crystal lattice of spinel ferrites generates a variety of geometric configurations. Based

on M^{2+} and Fe^{3+} cation distribution in the tetrahedral and octahedral voids, normal, inverse and mixed spinel structures can be obtained. The normal spinel structure comprises divalent cation M^{2+} in the tetrahedral voids and Fe^{3+} in octahedral holes of the cubic cell. In contrast, the inverse spinel structure has both tetrahedral and octahedral positions harbored by an equal population of trivalent Fe^{3+} ions while the divalent M^{2+} ions fill the octahedral spaces. The mixed spinel system have both M^{2+} and Fe^{3+} distributed randomly in tetrahedral and octahedral voids.⁷⁰⁻⁷² The distribution of metal cations in the crystal structure depends on their affinity to occupy the crystallographic sites, which in turn is determined by the ionic size of metal cations, cation charge, crystal field stabilization energy, size of interstitial sites, fabrication route, and synthesis reaction parameters.⁷³⁻⁷⁵ It has also been established that, cation occupancy within the spinel system depends essentially on the elastic energy, which is the magnitude to which the crystal structure is deformed because of the differences in dimensions of different cations within the spinel. In general, trivalent metal ions should locate at the octahedral sites while divalent cations occupy the tetrahedral sites. Additionally, metal ion distribution in octahedral and tetrahedral sites also depends on electrostatic energy, which takes care of electrical charge distribution. Simply, metal ions with higher electrical charge occupy octahedral sites, while those with smaller charges are stable in the tetrahedral position.⁶⁶ Table 1.3 shows the preference of different cations in both tetrahedral and octahedral holes for different types of spinel ferrite structures. The existing difference in geometry and bonding energy of the cations and the neighboring oxygen ions can be utilized to modulate the physical and chemical properties of spinel ferrites via changes in cation arrangement, composition and oxidation state.⁷⁶

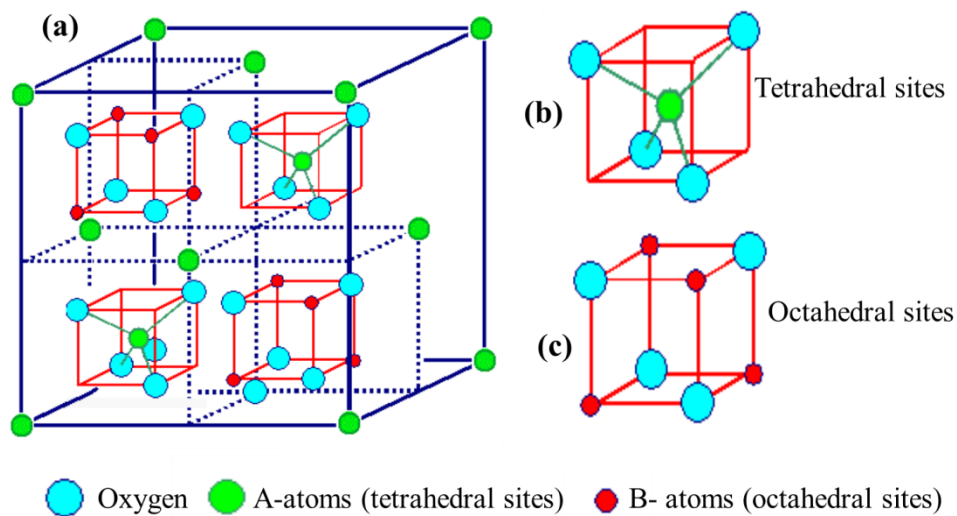


Fig. 1.4. (a) The crystal structure of spinel ferrite ($AB_2O_4 = MFe_2O_4$, where A or M = divalent metals and B = Fe) (b) tetrahedral sites (c) octahedral sites.

Table 1.3. The preferred structure of spinel ferrites and its dependence on the type of cation.

Spinel structure		Normal		Mixed	Inverse				
Cation		Zn ²⁺	Cd ²⁺	Mn ²⁺	Fe ²⁺	Mg ²⁺	Ni ²⁺	Co ²⁺	Cu ²⁺
Co-ordination	Tetrahedral	√	√	√					
	Octahedral				√	√	√	√	√

Spinel ferrites have been at the core of materials research ever since their discovery because of their fascinating optical, magnetic, electrical and catalytic properties. They also exhibit admirable mechanical hardness, chemical and structural stability.⁶⁶ Interestingly, these materials consist of highly abundant elements, and their low fabrication costs make them appealing for numerous use in different fields, including energy storage and conversion, gas sensors, photocatalysis, and magnetic drug delivery.⁷⁷⁻⁸⁰ It is worth noting that nanoengineering has given spinel ferrites a new lease of life, enabling them to unveil important properties that were still far from being realized in the bulk dimension. Moreover, their preparation by diverse synthetic routes and the possibility to fabricate a virtually infinite series of solid solutions unlock the means to tailor their properties for many advanced applications.

1.2.3 Solid solutions

The formation of crystalline solid solutions has long been considered an effective strategy for tailoring materials' structural and physicochemical properties. A number of these crystalline phases have been selectively applied in everyday life for many years. Consequently, these phases have become significant components of materials science. Basically, a solid solution refers to a homogeneous crystalline phase with variable composition. Solid solutions are formed when foreign atoms occupy available interstitial voids or substitute for atoms or ions in the parent lattice. Practically, the material is referred to as a solid solution when the concentration of foreign species rises above 0.1 - 1%.⁸¹ The foreign chemical specie(s) being introduced in the host material may not result in a significant change in the crystal symmetry of the host material leading to the formation of a primary solid solution. When the foreign atom causes a change in the host crystal structure, an intermediate solid solution is formed. The formation of solid solutions may sometimes

involve concurrent substitution of both cation and anion, yielding pseudobinary solid solutions. It is well established that slight distortions in the crystal lattice in the form of defects can be attributed to empty spaces or stacking faults, subject to the nature of the species being introduced and reaction parameters. These distortions in the crystal lattice may induce variation in lattice parameters, and hence causing the cell to shrink or expand.

The main hurdles in forming crystalline solid solutions emanate from the limited solubility of different components in the solid-state. The host and the foreign components may exhibit a partial or complete solubility at different concentration ranges, thus generating solid solutions with variable properties. This phenomenon, therefore, offers the ability to modify or enhance the optical, electrical, magnetic, electrochemical, or mechanical properties of the host material for various applications. In a perfect crystal, the inclusion of foreign chemical components may cause a swift rise in enthalpy, necessitating recrystallization so as to efficiently purify the compound. In practice, if the change in energy associated with the introduction of the foreign heteroatom/element/molecule is reasonably small, the crystal acts like a solution, and its composition can be adjusted over a wide range. Generally, for the lowest formation energy and composition tuning over an entire range during the formation of solid solutions, crystallographic parameters, cationic/anionic radius, chemical valence, and quantum properties of the components should be considered.⁸² Basically, the formation of solid solutions is guided by a set of principles according to the following Hume-Rothery rules.^{83, 84} (i) the two components should possess similar crystallographic structures and very close lattice parameters; a decent match of the two components in structure and lattice constants can assure their alloying over the whole composition range and avert phase segregation, and (ii) The two components must have comparable chemical properties to encourage their amalgamation into a monophasic compound. The corresponding chemical species should have comparable cationic/anionic size, electronegativity and valence. It is recommended that the difference in size between the two species should be 15% or less to enable a random substitution. If the difference in size between the two component exceeds 15%, then the size factor is said to be unfavorable, and the components' solubility becomes limited. In homogeneous multicomponent phases such as solid solutions, stoichiometry influences the material's physicochemical and structural properties in an incessant and predictable manner, the variation being often monotonic with composition. This behavior can be well demonstrated by Vegard's law,⁸⁵ which relates composition and unit cell dimensions. The law stresses that the sizes of the atoms, independent of the other parameters, have a considerable effect on the crystal structure. As a result, a linear relationship can be observed

between lattice constants and composition in systems of alloys or solid solutions.⁸⁶ Besides the size, other features such as thermal stability, electronic and optical properties also vary regularly with composition.

Nanostructuring of solid solutions is considered a promising strategy for realizing tailored properties and superior performance in numerous applications such as photodegradation of organic pollutants, clean energy harvesting and storage, optoelectronic nanodevices, and bio-related applications. Compared with the bulk materials, nanostructured solid solutions offers more advantages, which include large specific surface area, quantum confinement effect, and quantum size effect. A wide range of solid solutions both in bulk and nanoscale, including the selenides ($\text{PbS}_{1-x}\text{Se}_x$,⁸⁷ and $\text{SnS}_{1-x}\text{Se}_x$,⁸⁸), sulphides ($\text{Bi}_{2-2x}\text{Sb}_{2x}\text{S}_3$,⁸⁹ and $\text{Ni}_x\text{Co}_{3-x}\text{S}_4$),⁹⁰ oxides ($\text{Mn}_{1-x}\text{Co}_x\text{Fe}_2\text{O}_4$,⁹¹ and $\text{Zn}_{1-x}\text{Mn}_x\text{Fe}_2\text{O}_4$),⁹² tellurides ($\text{Zn}_x\text{Cd}_{1-x}\text{Te}$)⁹³ and phosphides ($\text{Al}_x\text{Ga}_{1-x}\text{P}$),⁹⁴ have been prepared.

1.2.4 Classification of semiconductor solid solutions

Solid solutions can be classified based on the number of component elements present in the system/compound and the nature of cation/anion occupancy in the host crystal structure.

1.2.4.1 Classification of solid solutions based on the type of ion occupancy

Depending on the type of cation/anion occupancy occurring in the host crystal system, there are two types of solid solutions namely, substitutional and interstitial solid solutions. Substitutional solid solutions are the most common type of solid solutions formed when two or more chemical species (cation/anion) with the same valence can mutually substitute each other within the same crystal system, hence taking up corresponding crystallographic sites.⁹⁵ Simply, it involves cationic and/or anionic substitutions in the same crystal. On the other hand, interstitial solid solutions are formed when the foreign atom/ion occupies an existing empty site/interstices/voids, and no species are left out in the crystal system.⁹⁶ For this kind of solid solution to be formed, the atomic size of the foreign atoms should be smaller than that of the host atoms. As a result, most interstitial solid solutions incorporate solute/foreign atoms such as hydrogen, boron, lithium, carbon or nitrogen, with atomic size very much less than one nanometer. However, due to limited interstitial sites and the likelihood of forming lattice distortions/stresses, only a few solute atoms can be accommodated. In the two basic types, a significant variety of many complex solid solution mechanisms may be derived, through the simultaneous formation of substitution and interstitial processes, by incorporating

ions of different valence to those in the host structure or by creating empty spaces. Fig. 1.5 illustrates the formation of both interstitial and substitutional solid solutions.

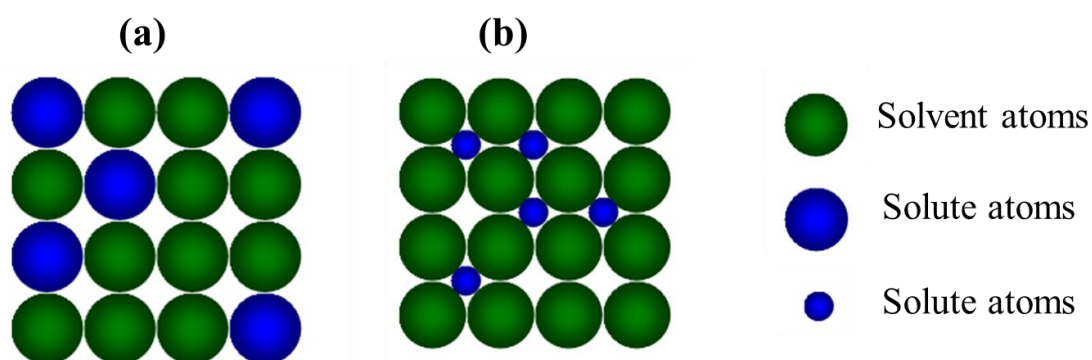


Fig. 1.5. Representation of (a) substitutional solid solution, and (b) interstitial solid solution.

1.2.4.2 Classification of solid solutions based on the number of component elements

On the basis of the number of component elements (i.e. cations or anions), crystalline solid solutions can be classified as binary (two elements), ternary (three elements) or quaternary (four elements). Even though all these solid solutions share a similar formation principle, there is a great disparity in their properties. Solid solutions under this category can also be considered as being cationic or anionic, subject to the chemical identity of the species undergoing substitution. If the substitution process involves metallic ions (cations), the resulting solid solution is called cationic solid solution, whereas an anionic solid solution involves substitution between non-metallic ions (anions).

1.2.5 Progress on the synthesis of crystalline solid solutions

With many years of research, the fabrication and applications of semiconductor solid solutions have achieved greater heights. With numerous synthetic strategies, a significant number of crystalline solid solutions of varying particle sizes, morphologies and composition have been rationally prepared in different material systems. Nevertheless, in all these years, there has been no systematic summary that covers diverse groups of solid solutions systems such as selenides, phosphides, sulfides, tellurides, oxides, and oxysulfides. Therefore, this work provides a systematic summary of the synthesis, characterization, properties, and possible applications of binary, ternary and quaternary solid solutions in various material systems such as selenides, sulfides, phosphides tellurides, oxides, nitrides, and oxysulfides.

1.2.5.1 Binary solid solutions

In this category, the $\text{Si}_x\text{Ge}_{1-x}$ system is the most popular and widely explored crystalline solid solution.⁹⁷ Ideally, the similarity in crystallographic structure and comparable lattice parameters between germanium, Ge (cubic, $a = 5.658 \text{ \AA}$), and silicon Si (cubic, $a = 5.431 \text{ \AA}$) permit a wide range of composition tuning and bandgap control from 0.66 to 1.12 eV. Based on nanostructured $\text{Si}_x\text{Ge}_{1-x}$ solid solution, numerous microelectronic and optoelectronic devices can be achieved via the accurate regulation of their physicochemical properties. The synthesis of $\text{Si}_{1-x}\text{Ge}_x$ nanoparticles having Ge concentration in the span of $0 \leq x \leq 0.31$, has been reportedly achieved by Takeoka *et al.* by depositing Si, Ge, and SiO_2 followed by annealing at 1100°C .⁹⁷ However, another study by Yang *et al.* employing SiH_4 and GeH_4 precursors in the chemical vapor deposition (CVD) process was found to extend the amount of Ge within the composition range of $0 \leq x \leq 1$.⁹⁸ The resulting nanosized $\text{Si}_{1-x}\text{Ge}_x$ displayed tuneable thermal conductivity, energy band-gaps, and good crystallinity. Further rational control of the starting materials (SiH_4 and GeH_4) in the course of the CVD process could yield composition programmed $\text{Si}_{1-x}\text{Ge}_x$ nanowires.^{99, 100} Selective and continuous adjustment of the ratio of Si and Ge in the precursor mixture permitted complete modification of the single nanowire's energy band-gap and optoelectronic behaviour. The fabrication of such individual $\text{Si}_{1-x}\text{Ge}_x$ nanowires with composition engineered energy-band gap paved new horizons in realizing high-performance photodetectors for selective wavelength detection over a wide range.¹⁰¹

Binary $\text{Co}_x\text{Cu}_{(100-x)}$ ($x = 10, 25, 50, 60, 75$, and 90) systems have been successfully prepared via mechanical alloying. XRD measurements showed that after 20 h of mechanical alloying, all the samples displayed an entirely face-centered cubic phase. HRTEM images demonstrated the formation of ultrafine-grained materials containing a high density of defects. The EDX studies revealed a homogeneous distribution of Co and Cu in the solid solutions at the nanometer scale.¹⁰²

1.2.5.2 Ternary solid solutions

Ternary solid solutions can be formed by combining two separate binary compounds, having an identical crystallographic system. The two compounds must be composed of either similar cation or anion. For example, alloying of $\text{A}'\text{B}$ and $\text{A}''\text{B}$ yields $(\text{A}'\text{B})_x(\text{A}''\text{B})_{1-x}$ or simply $\text{A}'_x\text{A}''_{1-x}\text{B}$, where A' and A'' are two unlike metallic ions, and B is the common non-metallic ion. Similarly, alloying AB' and AB'' gives $(\text{AB}')_x(\text{AB}'')_{1-x}$ or simply $\text{AB}'_x\text{B}''_{1-x}$.

Notable examples include $\text{Zn}_x\text{Cd}_{1-x}\text{Se}$ obtained from ZnSe and CdSe, and $\text{CdS}_x\text{Se}_{1-x}$ obtained by alloying CdS and CdSe. Alternatively, ternary solid solutions can be obtained from elemental doping process, wherein the cation or anion in the binary host compound is replaced by another cation or anion from the same group.¹⁰³ The presence of a large number of material systems able to form ternary solid solutions offer more opportunities to fine-tune their properties and more prospects to realize their potential uses in various fields.

1.2.5.2.1 Ternary cationic solid solutions

Ternary cationic solid solutions can be formed by combining two isostructural binary semiconductors having identical anions but different cations. On the other hand, ternary cationic solid solutions can be formed from elemental doping process, where a specific cation in the binary host compound is substituted by another cation of the same charge. A number of ternary cationic alloys or solid solutions have been reportedly prepared.

The use of xanthate complexes in the fabrication of ternary metal sulfide solid solutions has been reported. Alqahtani *et al.* reported the use of tris(*O*-ethylxanthate)bismuth(III) and tris(*O*-ethylxanthate)antimony(III) complexes for the preparation of $\text{Bi}_{2-2x}\text{Sb}_{2x}\text{S}_3$ ($0 \leq x \leq 1$) solid solutions by employing a facile melt method.⁸⁹ The synthesis was carried out by decomposition of stoichiometric mixtures of $\text{Bi}[\text{S}_2\text{COEt}]_3$ and $\text{Sb}[\text{S}_2\text{COEt}]_3$ complexes at 200, 250, and 300 °C under nitrogen for 1 h. The p-XRD peaks of the resulting solid solutions over the whole composition corroborated well with the orthorhombic crystal system. The inclusion of Sb into the Bi_2S_3 system led to a change in the materials' optical properties with an obvious rise in the band gap energy from 1.66 eV to 2.19 eV for $x = 0$ to $x = 1$, correspondingly.

Similarly, Kun *et al.* achieved the fabrication of $(\text{Bi}_{1-x}\text{Sb}_x)_2\text{S}_3$ ($0 \leq x \leq 1$) solid solutions via thermolysis of Bi and Sb piperidine dithiocarbamate complexes.¹⁰⁴ The typical hot injection procedure was carried out by dispersing a known amount of the two complexes in a mixture of 1-dodecanethiol and oleylamine and consequently injected into hot oleylamine at 230 °C under nitrogen supply. The amount of bismuth and antimony was varied throughout the synthesis process. The results indicated a near-linear expansion of the lattice constants as a function of antimony content in the precursor feed. A comparison between the particle composition and the lattice constants showed a slight deviation from Vegard's law. The HRTEM images and their SAED patterns showed the formation of highly polycrystalline powders exhibiting two-dimensional lattice fringes (Fig. 1.6). Additionally, TEM results showed the formation of nanorods over the whole composition range (Fig. 1.7).

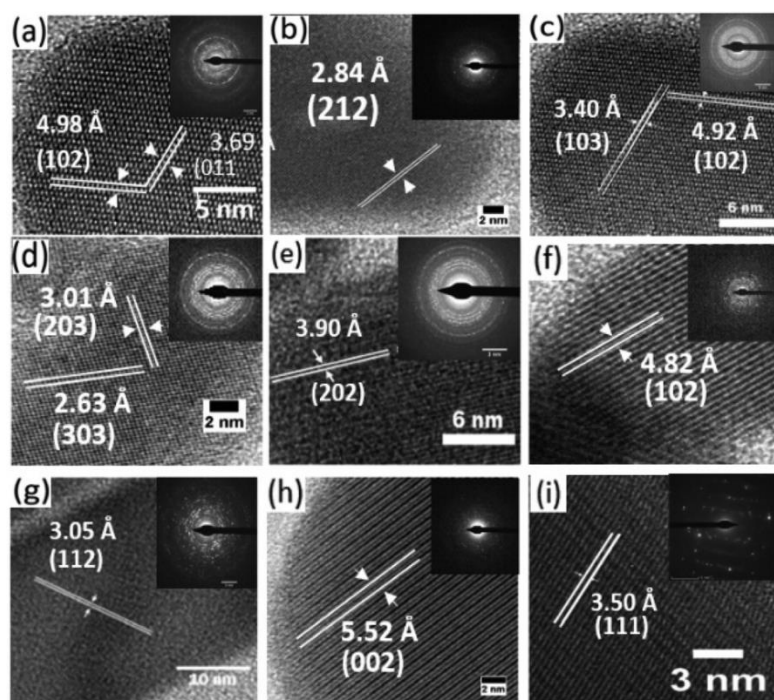


Fig. 1.6. HRTEM images of the synthesized $(\text{Bi}_{1-x}\text{Sb}_x)_2\text{S}_3$ ($0 \leq x \leq 1$) nanorods (Reproduced from ref. 104).

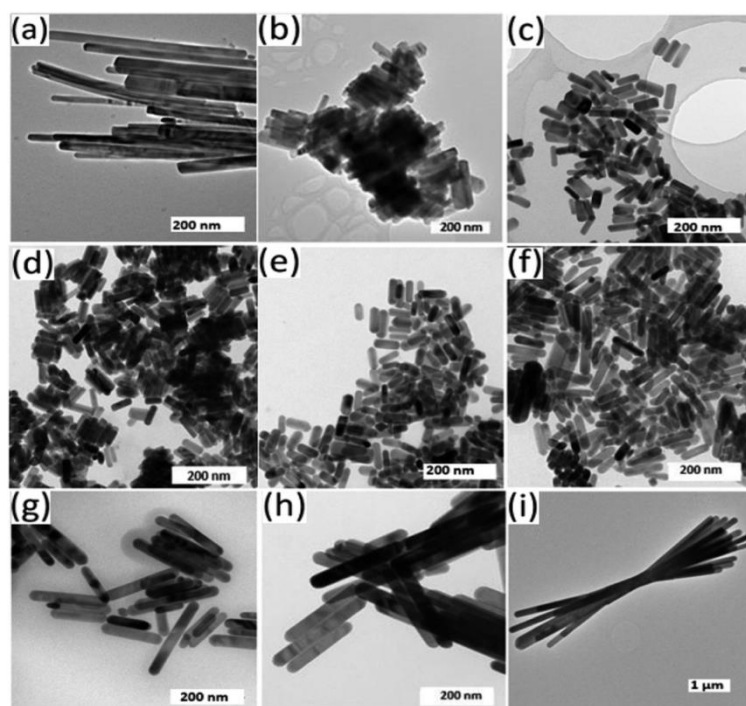


Fig. 1.7. TEM images showing the as synthesized $(\text{Bi}_{1-x}\text{Sb}_x)_2\text{S}_3$ ($0 \leq x \leq 1$) nanorods (Reproduced from ref. 104).

Likewise, Alqahtani *et al.* described the synthesis of $\text{M}_{2-2x}\text{In}_{2x}\text{S}_3$ ($\text{M} = \text{Bi/Sb}$) solid solutions by solventless thermolysis of a mixture of tris(O-ethylxanthato) bismuth (III),

tris(O-ethylxanthato) antimony (III) and tris(O-ethylxanthato) indium (III) complexes at 300 °C.¹⁰⁵ In the precursor mixture ($\text{In}(\text{S}_2\text{COEt})_3$ and $\text{M}(\text{S}_2\text{COEt})_3$), the mole fraction of indium was varied in the range of $0 \leq x \leq 1$. Structural analysis of the alloyed films by p-XRD revealed that the inclusion of In up to $x = 0.4$ into M_2S_3 system could not change the orthorhombic crystal system of the parent material. The SEM micrographs of the $\text{Bi}_{2-2x}\text{In}_{2x}\text{S}_3$ samples showed that their morphology changed considerably with variation in the amount of indium in the precursor mixture. In addition, the computed band gap of $\text{Bi}_{2-2x}\text{In}_{2x}\text{S}_3$ and $\text{Sb}_{2-2x}\text{In}_{2x}\text{S}_3$ films varied from 1.66 to 2.39 eV and 2.19 to 2.9 eV, respectively, and could still be modulated by changing the amount of indium.

Substitutional solid solutions of ternary sulfides containing cadmium and zinc have been reportedly prepared from thermolysis of xanthate complexes by using different methods. The study by Li *et al.* has successfully fabricated uniform $\text{Cd}_x\text{Zn}_{1-x}\text{S}$ ($0.13 \leq x \leq 1$) nanocrystals by thermal decomposition of cadmium (II) and zinc (II) ethylxanthate complexes.¹⁰⁶ The choice of ethyl xanthate precursors was due to their response to thermal decomposition at a fairly low-temperature range (180-210 °C) under the presence of hot coordinating solvents. The composition of the solid solutions was precisely attuned by regulating the molar ratio of Cd(II) and Zn(II) ethylxanthate complexes in the precursor feed. The alloyed $\text{Cd}_x\text{Zn}_{1-x}\text{S}$ nanoparticles prepared in coordinating solvents exhibited composition-dependent properties. With the decreasing amount of Zn in the mixture, the morphology of $\text{Cd}_x\text{Zn}_{1-x}\text{S}$ nanoparticles was observed to change from dot to single-armed rod and then to multi-armed rod. They also showed good optical properties with PL peak shift from 368 to 472 nm.

Wang *et al.* have synthesized nanoparticulate $\text{Zn}_x\text{Cd}_{1-x}\text{S}$ ($0.1 \leq x \leq 0.95$) solid solutions via a chemical reduction technique at ambient temperature.¹⁰⁷ In the typical synthesis, an appropriate amount of elemental sulfur was dissolved in 50 mL of tetrahydrofuran, agitated for 5 min at ambient temperature, followed by the addition of stoichiometric amounts of anhydrous ZnCl_2 , CdCl_2 salts, and KBH_4 powders for 12 h. After washing the precipitates using ethanol and water, the product was consequently dried to yield the highest quality monophasic $\text{Cd}_x\text{Zn}_{1-x}\text{S}$ nanoparticles. The size of the particles ranging from 4 to 8 nm was obtained. A gradual change of lattice structure from cubic to hexagonal was noted at a higher amount of zinc in the $\text{Cd}_x\text{Zn}_{1-x}\text{S}$ system. Moreover, the nanoparticles prepared by the chemical reduction method showed very broad emission peaks that shifted to lower wavelengths due to Zn content in $\text{Cd}_x\text{Zn}_{1-x}\text{S}$.

Zhong's group reported the synthesis of uniform wurtzite $\text{Zn}_x\text{Cd}_{1-x}\text{S}$ ($0.1 \leq x \leq 0.53$) quantum dots with good emission properties by employing a hot injection method.¹⁰⁸ The preparation procedure was carried out by reacting ZnO- and CdO-oleic acid precursors with sulfur at 300 °C in a non-coordinating octadecene solvent. The p-XRD analysis revealed the shift of diffraction patterns to higher diffraction angles with increasing zinc concentration. Additionally, the estimated lattice constant measured from p-XRD data showed a decreasing linear trend with respect to Zn concentration. This behavior was in line with Vegard's law and further proved the successful preparation of uniform solid solution nanoparticles. Moreover, increasing the amount of Zn in the solid solution resulted in systematic blue-shifting of the photoluminescence spectra from 474 to 391 nm, signifying the formation of the nanostructured alloyed crystals.

Thin films of $\text{Zn}_x\text{Cd}_{1-x}\text{S}$ ($0.1 \leq x \leq 0.53$) have been reportedly prepared by Barman *et al.* via the vacuum thermal evaporation method and the physicochemical properties evaluated as a function of zinc composition.¹⁰⁹ p-XRD studies showed that the prepared films exhibit diffraction patterns from both pristine CdS and ZnS systems. Investigation of optical properties of $\text{Zn}_x\text{Cd}_{1-x}\text{S}$ thin films confirmed the non-linearity of the optical band gap spanning from 2.42 to 3.49 eV with respect to zinc content from 0 to 1. Another study reported a novel ultrasonication-assisted hydrothermal route for the fabrication of $\text{Zn}_x\text{Cd}_{1-x}\text{S}$ ($0 \leq x \leq 1$) solid solution under visible light.¹¹⁰ XPS analysis confirmed the presence of Zn, Cd, and S in the samples. Also, the shift of the binding energies demonstrated the successful synthesis of solid solutions at different dopant levels. When the amount of Zn was increased, the UV-visible absorption spectra of $\text{Zn}_x\text{Cd}_{1-x}\text{S}$ solid solutions displayed a clear blue-shift from 576 to 343 nm, accompanied by changes in the color of samples from dark-orange to gray-white. Additionally, a gradual increase of the optical band gap of the solid solutions was noticed from 2.15 to 3.61 eV with respect to Zn content. The study demonstrated that $x = 0.3$ to $x = 0.5$ was the optimum composition of $\text{Zn}_x\text{Cd}_{1-x}\text{S}$, with $x = 0.3$ exhibiting superior photocatalytic activity for the degradation of a methyl orange solution under visible light. More reports are available on the synthesis of $\text{Zn}_x\text{Cd}_{1-x}\text{S}$ solid solutions from diverse precursors and by different synthetic methods.¹¹¹⁻¹¹⁹

Lehmann reported that solid solutions of $\text{Ca}_{1-x}\text{Cd}_x\text{S}$ existed over a mole ratio ranging from $x = 0$ to 0.55. The synthesis was achieved by firing the raw materials at temperatures up to 1525 K in sulfur-rich conditions. The resulting solid solutions displayed a linear relationship between the lattice constant and cadmium content.^{120, 121} Interestingly, the findings of Lehmann's work regarding the intense white cathodoluminescence for

composition x in the range of 0.05 - 0.10 triggered more interest in the $\text{Ca}_{1-x}\text{Cd}_x\text{S}$ system. Investigations conducted by Susa *et al.*¹²² and Kobayashi *et al.*¹²³ reported the possibility of extending the solid solubility range of $\text{Ca}_{1-x}\text{Cd}_x\text{S}$ at high pressures up to 2 GPa, to the extent that only a fairly slight miscibility gap in the range of $x = 0.8$ to 0.95 exist. The work by Ray,¹²⁴ and Viney,¹²⁵ reported the study of the photoluminescence of $\text{Ca}_{1-x}\text{Cd}_x\text{S}$ solid solution for composition (x) in the range of 0 - 0.40. Under 298 nm excitation at ambient temperature, their findings confirmed the occurrence of short wavelength luminescence extending into the ultraviolet region. Building on the work of Ray *et al.*,¹²⁴ solid solutions of $\text{Ca}_{1-x}\text{Cd}_x\text{S}$ with mole ratios ranging from 0.001 to 0.20 have also been synthesized by Barrett *et al.*¹²⁶ via sintering of the mixture of microcrystalline particles of CaS, CdS, and sulfur. In a study by Kobayashi *et al.*, rock salt type solid solution systems of $\text{Cd}_{1-x}\text{Sn}_x\text{S}$, $\text{Cd}_{1-x}\text{Pb}_x\text{S}$, $\text{Cd}_{1-x}\text{Ca}_x\text{S}$, $\text{Cd}_{1-x}\text{Sr}_x\text{S}$, and $\text{Cd}_{1-x}\text{Mg}_x\text{S}$ were also synthesized at high pressures by utilizing appropriate quantities of pure binary sulfides.¹²⁷ Measurements of their semiconductive properties revealed that $\text{Cd}_{1-x}\text{Ca}_x\text{S}$ solid solution exhibited a high electrical resistivity of more than $3 \times 10^{10} \Omega\text{-cm}$, compared to that of $\text{Cd}_{1-x}\text{Pb}_x\text{S}$ system, which was found in the span of 1 - $10 \Omega\text{-cm}$, and decreased with the increasing amount of substituent.

Thin films of $\text{Zn}_{1-x}\text{Mg}_x\text{S}$ ($0.1 \leq x \leq 0.9$) were prepared by Bashar *et al.* using radiofrequency (RF) magnetron co-sputtering from ZnS and MgS binary target materials under different applied RF power.¹²⁸ Variation of stoichiometric ratio of $\text{Zn}_{1-x}\text{Mg}_x\text{S}$ films was done by altering the RF power at 200 °C. Crystallographic studies showed that the as-prepared $\text{Zn}_{1-x}\text{Mg}_x\text{S}$ thin films exhibited a cubic phase corresponding to a zinc blende structure. The estimated optical bandgaps were obtained in the range of 4.39 to 3.25 eV, and they are appropriate for buffer or window layers of thin film photovoltaics.

Novel $\text{Cu}_{1-x}\text{Zn}_x\text{S}$ ($x = 0.01, 0.05, 0.1$) nanoparticles have been hydrothermally fabricated from pyrolysis of tris(thiourea)copper(I) sulphate and $\text{Zn}(\text{NO}_3)_2 \cdot 6\text{H}_2\text{O}$ precursors at 140 °C for 8 hours.¹²⁹ The p-XRD pattern of $\text{Cu}_{1-x}\text{Zn}_x\text{S}$ nanoparticles showed a well-ordered pure covellite phase exhibiting hexagonal crystal structure. FESEM showed that $\text{Cu}_{1-x}\text{Zn}_x\text{S}$ nanoparticles exhibited polyhedral shape with their size increasing with dopant concentration. Measurements of optical properties by diffuse reflectance spectra and photoluminescence showed that nanostructured samples with high zinc content ($\text{Cu}_{0.9}\text{Zn}_{0.1}\text{S}$) exhibited a small band gap value of 2.89 eV compared to 2.96 eV of CuS and 2.92 eV of $\text{Cu}_{0.99}\text{Zn}_{0.01}\text{S}$. Photocatalytic studies indicated that $\text{Cu}_{1-x}\text{Zn}_x\text{S}$ ($x = 0.1$) was able to remove 95% methylene blue in the presence of H_2O_2 under UV light in 90 min. Moreover, evaluation

of the materials' anticancer activity showed that the prepared nanoparticles ($x = 0.01 - 0.1$) had great capacity to remove of *Hep G2* cancer cells.

Kudo and Sekizawa described a precipitation reaction between a mixture of zinc and copper nitrates with an aqueous Na_2S solution which resulted into the formation of $\text{Zn}_{1-x}\text{Cu}_x\text{S}$ solid solution.¹³⁰ The p-XRD pattern of the synthesized material showed a cubic sphalerite (zinc blende) structure, indicating the successful incorporation of Cu in the ZnS lattice. Measurements of the ionic radii of Zn^{2+} and Cu^{2+} were found to be 0.60 and 0.63 Å, respectively. Measurements of the optical property indicated absorption of ZnS in the UV region only, whereas $\text{Zn}_{0.957}\text{Cu}_{0.043}\text{S}$ absorption edge extended to a visible light range of about 500 nm. The $\text{Zn}_{0.957}\text{Cu}_{0.043}\text{S}$ solid solution exhibited an optical band gap of 2.5 eV and the color was pale yellow. Conversely, absorption of CuS was observed in the whole UV range and visible light and without a distinct absorption edge. This observation further confirmed that $\text{Zn}_{0.957}\text{Cu}_{0.043}\text{S}$ solid solution was formed, ruling out the presence of a mixture of ZnS and CuS in the final product.

Ternary $\text{Ni}_x\text{Ru}_{1-x}\text{S}_2$ with different metal contents in the range of $0 \leq x \leq 1$ was reportedly prepared using step-by-step impregnation and sulfidation reactions.¹³¹ In the synthesis, $\text{RuCl}_3 \cdot 3\text{H}_2\text{O}$, NiCl_2 and H_2S were used as Ru, Ni and S sources, respectively. Through p-XRD, XPS, TPR, and STEM analyses, a series of ternary $\text{Ni}_x\text{Ru}_{1-x}\text{S}_2$ materials exhibiting a pyrite-like structure was confirmed to have been obtained up to mole ratio of $\text{Ni}/(\text{Ni} + \text{Ru})$ close to 0.7. It was further demonstrated by STEM measurements that the synthesized phases were stable under all test conditions. Compared with the pure ruthenium sulfide supported on alumina, the solid solution series displayed enhanced catalytic activity showing a thirty-fold rise in hydrogenation activity. The enhanced catalytic activity was due to the synergetic effect of mixed NiRu sites with a distinct electronic character from those of the individual Ni/Ru sites. Other ruthenium-based systems such as $\text{Fe}_x\text{Ru}_{1-x}\text{S}_2$,¹³² $\text{Cr}_x\text{Ru}_{1-x}\text{S}_2$ and $\text{Mn}_x\text{Ru}_{1-x}\text{S}_2$,¹³³ have also been reported.

In an effort to study the growth and optical behavior of ternary III-V nanowires, Berg *et al.* described the growth of metal-particle-free vertical pure wurtzite crystal $\text{In}_x\text{Ga}_{1-x}\text{P}$ ($0.26 \leq x \leq 0.54$) nanowire arrays synthesized by selective-area epitaxy.¹³⁴ Analysis of optical behaviour of the synthesized nanowires by cathodoluminescence spectroscopy revealed an emission wavelength ranging from 870 - 800 nm.

The synthesis of ternary $\text{Co}_{1-x}\text{Ni}_x\text{P}_3$ ($0 \leq x \leq 0.1$) nanoneedle arrays has been reported by Fu *et al.* via a simple hydrothermal treatment of $\text{Co}_{1-x}\text{Ni}_x(\text{OH})\text{F}$ precursors at 120 °C

followed by phosphidation reaction at 750 °C.¹³⁵ p-XRD studies showed that all samples exhibited the cubic system of the skutterudite-type CoP_3 , implying that the crystal structure was maintained upon incorporating Ni atoms in the range of $0 \leq x \leq 0.1$. Investigation of electrochemical properties of the synthesized samples showed that the electronic structure was modified by doping a suitable concentration of Ni, and the resulting $\text{Co}_{0.93}\text{Ni}_{0.07}\text{P}_3$ exhibited good HER performance with an overpotential of 87 mV at 10 mA/cm^2 in alkaline solution. Also, the $\text{Co}_{0.93}\text{Ni}_{0.07}\text{P}_3$ demonstrated an OER overpotential of 221 mV at 20 mA/cm^2 . The prepared skutterudite-based $\text{Co}_{1-x}\text{Ni}_x\text{P}_3$ nanocatalysts revealed hopeful potential for overall electrochemical water splitting in alkaline electrolyte.

Benefiting from the crystal structure similarity of both Ni_{12}P and MoP , Xiao *et al.* prepared a series of $\text{Ni}_{2-x}\text{Mo}_x\text{P}$ ($0 \leq x \leq 1$) and $\text{Ni}_x\text{Mo}_{2-x}\text{P}_{2-x}$ ($0 \leq x \leq 1$) solid solutions.¹³⁶ The reaction involved thermolyzing a pre-prepared solution comprising a mixture of $(\text{NH}_4)_6\text{Mo}_7\text{O}_{24} \cdot 4\text{H}_2\text{O}$ and $(\text{NH}_4)_2\text{HPO}_4$ and $\text{Ni}(\text{NO}_3)_2 \cdot 6\text{H}_2\text{O}$ solution at 383 K with constant stirring, followed by annealing of the product at 773 K in the air for 5 h. A gradual change in the lattice constant c was observed with respect to Mo and Ni content in the two sets of solid solution. This trend agreed well with Vegard's law, showing that Ni and Mo are likely to be uniformly substituted. HRTEM images of the two pristine members of solid solutions, Ni_{12}P and NiMoP , exhibited an Fe_2P crystal structure with unit cell constants comparable to those in the literature data.

Another study explored effective ways of developing bimetallic phosphides with tunable catalytic properties by making use of the electronic and synergistic contributions of multiple metal combinations. Thermolysis of a precursor mixture comprising $(\text{NH}_4)_2\text{HPO}_4$, $\text{FeNO}_3 \cdot 9\text{H}_2\text{O}$ and $(\text{NH}_4)_6\text{Mo}_7\text{O}_{24} \cdot 4\text{H}_2\text{O}$ afforded $\text{Fe}_x\text{Mo}_{2-x}\text{P}$ solid solutions via modulation of the composition of Fe and Mo in the range of $0.88 \leq x \leq 1.55$. Structural evaluation by p-XRD confirmed the formation of *iso*-structural series of FeMoP with orthorhombic structure at different compositions. Selected area electron diffraction (SAED) analysis showed a set of parallel lattice fringes corresponding to the [111] axis of FeMoP . In examining the influence of metal composition on the catalytic performance, it was generally revealed that catalysts containing a mole ratio of Fe in the range of 0.99 - 1.14 demonstrated high selectivity to C-O bond breaking of phenol with H_2 to form benzene.¹³⁷

In the quest for stable, earth-abundant, and efficient catalysts to replace the noble metals, a series of $\text{Ni}_{2-x}\text{Co}_x\text{P}$ ($0 \leq x \leq 1.3$) catalysts were prepared by Li *et al.* via solid-state phosphorization of $\text{Ni}_{1-0.5x}\text{Co}_{0.5x}(\text{OH})_2$ precursors by NaH_2PO_2 at elevated temperature.¹³⁸

The stoichiometric ratio of the total metal (nickel and cobalt) to P being 1:5. Structural investigation of the $\text{Ni}_{2-x}\text{Co}_x\text{P}$ catalysts by p-XRD showed the formation of monophasic hexagonal phosphide (Ni_2P -type) materials. Increasing Co levels resulted in the slight shifting of p-XRD patterns toward the high 2θ values, which further proved the successful inclusion of cobalt into the crystal lattice of Ni_2P . The HRTEM images of $\text{Ni}_{2-x}\text{Co}_x\text{P}$ catalysts revealed high crystallinity of the samples with a lattice spacing of $\approx 1.68 \text{ \AA}$, comparable to the interplanar spacing (1.69 \AA) of (300) facet of the Ni_2P . Elucidation of catalytic performance showed that increasing Co content in $\text{Ni}_{2-x}\text{Co}_x\text{P}$ effectively augments the HER performance. Among all compositions, the NiCoP ($x = 1$) catalyst yielded the best catalytic activity, recording a low overpotential of 59 mV at 10 mA/cm^2 , which is considerably smaller compared to 130, 119, 98, and 80 mV for Ni_2P , $\text{Ni}_{1.8}\text{Co}_{0.2}\text{P}$, $\text{Ni}_{1.4}\text{Co}_{0.6}\text{P}$, and $\text{Ni}_{1.2}\text{Co}_{0.8}\text{P}$, respectively, at the same current density.

The high-temperature rapid injection method has been extensively employed and is considered the most effective in yielding highly monodisperse colloidal nanomaterials. This method was adopted by Zhong *et al.*¹³⁹ in the fabrication of uniform $\text{Zn}_x\text{Cd}_{1-x}\text{Se}$ quantum dots. In the procedure, solutions composed of ZnEt_2 and TOP-Se precursors were rapidly injected into a hot solution of pre-prepared CdSe quantum dots in the presence of capping agents. With the increase in Zn, a composition-dependent emission across a large portion of the visible spectrum was manifested by a systematic blue-shift in emission wavelength. The photoluminescence characteristics of the as-prepared $\text{Zn}_x\text{Cd}_{1-x}\text{Se}$ nanoparticles was found in the range of 70 - 85%, which is comparable to other previously reported CdSe-based quantum dots. HRTEM micrographs confirmed the synthesis of the high monodisperse and crystalline nature of the resulting nanocrystals. The systematic change in the position of the diffraction peaks toward higher angles with the increasing Zn content indicated the reduction in lattice constant and agreed well with Vegard's law. This dismissed the possibility of phase segregation and served as proof for the formation of a uniform solid solution.

Similarly, the formation of $\text{Zn}_x\text{Cd}_{1-x}\text{Se}$ quantum dots have reportedly been prepared from ZnSe seeds or pre-prepared ZnSe quantum dots.^{140, 141} Moreover, the use of capping agents such as aminothiols have been used in the colloidal preparation of $\text{Zn}_x\text{Cd}_{1-x}\text{Se}$ nanocrystals.^{142, 143} With this strategy, the experiment is conducted at fairly low temperatures ($<100 \text{ }^\circ\text{C}$) by employing less harmful/less toxic starting materials of Zn salts such as ZnCl_2 . This approach can be easily extended to afford large-scale synthesis of biocompatible nanoalloys. Meanwhile, the use of stabilizing or capping agents has yielded nanocrystalline $\text{Zn}_x\text{Cd}_{1-x}\text{Se}$ with improved stability.¹⁴⁴ Apart from nanoparticles, thin films of $\text{Cd}_{1-x}\text{Zn}_x\text{Se}$ (0

$< x \leq 0.8$) have been synthesized by Bagade *et al.* via a self-organized arrested precipitation method.¹⁴⁵ p-XRD studies revealed the formation of nanocrystalline films exhibiting a cubic crystal structure and crystallite size in the range of 36.5 - 66.3 nm. Investigations on the effect of the mole ratio of Zn on the optical characteristics revealed an estimated direct band gap spanning from 1.77 - 1.98 eV corresponding to zinc concentration from $x = 0.0 - 0.8$. Reports are also available on the fabrication of $\text{Cd}_{1-x}\text{Zn}_x\text{Se}$ thin films via different methods, including chemo-mechanical synthesis,¹⁴⁶ thermal evaporation,^{147, 148} successive ionic layer adsorption and reaction,¹⁴⁹ closed space sublimation,¹⁵⁰ chemical bath deposition,¹⁵¹ and vacuum evaporation techniques.^{152, 153}

A single-step solvothermal procedure was used for the *in-situ* growth of $(\text{Ni}_x\text{Co}_{1-x})_9\text{Se}_8$ solid solutions on nickel foam by varying nickel content from $x = 0$ to 1.¹⁵⁴ Thermolysis of stoichiometric amounts of SeO_2 , $\text{Co}(\text{Ac})_2 \cdot 4\text{H}_2\text{O}$, and $\text{Ni}(\text{Ac})_2 \cdot 4\text{H}_2\text{O}$ at 180 °C for 15 h in the presence of benzyl alcohol yielded cubic solid solutions in the range of $0 < x \leq 0.2$. However, increasing Ni content beyond $x = 0.2$ resulted in impurity peaks corresponding to an intermediate phase of hexagonal CoSe. This indicated $x = 0.2$ as the maximum limit beyond which the formation of $(\text{Ni}_x\text{Co}_{1-x})_9\text{Se}_8$ could not be realized. When the amount of Ni was increased further, mixed cubic and hexagonal phases were observed, indicating that structure transformation from cubic to hexagonal phase occurs at higher nickel content. SEM images showed that all samples demonstrated a high coverage of several nanodendrites on the surface of nickel foam. Also, with the exception of pristine NiSe@NF, the SEM micrographs of the remaining samples displayed ordered morphology and fractal feature comprising various nanobranched and nanostems. The HRTEM images showed lattice fringes exhibiting interplanar spacing of 3.0 and 3.1 Å, corresponding to (222) and (311) planes of $(\text{Ni}_x\text{Co}_{1-x})_9\text{Se}_8$, respectively. Electrochemical studies showed that the optimized $(\text{Ni}_x\text{Co}_{1-x})_9\text{Se}_8$ nanodendrites produced a specific capacitance of 3762 F/g at 5 A/g and retained 94.8% of the initial capacitance after 5000 cycles.

The fabrication of uniform solid solution nanoparticles based on Pb chalcogenides have been reported. Arachchige and Kanatzidis have synthesized a set of $\text{Pb}_{1-x}\text{Sn}_x\text{Te}$ ($0.14 \leq x \leq 0.86$) nanoparticles via a low-temperature colloidal synthetic approach by reacting a mixture composed of $[(\text{Me}_3\text{Si})_2\text{N}]_2\text{Sn}$, Pb(II) oleate, and TOP-Te at 150 °C.¹⁵⁵ The reaction employed oleylamine as a stabilizing agent to assist the integration of Sn into the crystal lattice of PbTe. The as-prepared nanocrystals were found to be solid solutions crystallizing in a cubic rock salt structure that are virtually spherical in shape, and exhibiting band gap energy in the mid-IR range. EDX elemental mapping confirmed uniform dispersion of Sn in

the whole PbTe lattice, signaling the structural uniformity of the synthesized solid solutions. Contrary to the bulk counterpart, the band gap of the prepared solid solutions was not found to disappear at any Sn content but attains a lowest value of 0.28 eV for $x = 0.67$.

Ternary solid solutions of $(\text{Bi}_x\text{Sb}_{1-x})_2\text{Te}_3$ have also been prepared via the traveling heater method.¹⁵⁶ While the polycrystalline ingot was prepared via melting of Bi, Sb, and Te in a closed quartz ampoule, extra pure samples were obtained from single crystalline ingots by employing an annealing saturation method at temperatures in the range of 510 - 570°C. Thermoelectric measurements of these p-type solid solution samples was performed with respect to stoichiometric variations, and a maximum in the plot of merit value of $Z = 3.2 \times 10^{-3} \text{ K}^{-1}$ was recorded for the $\text{Bi}_9\text{Sb}_{31}\text{Te}_{60}$ solid solution. Zhang *et al.* demonstrated the controlled preparation of $\text{Bi}_x\text{Sb}_{2-x}\text{Te}_3$ ($0 \leq x \leq 2$) nanoplatelets by employing a modified solvothermal method. By means of the spark plasma sintering process, the synthesized nanoplatelets were successfully sintered into nanometric bulk pellets. P-XRD and raman spectroscopy studies revealed the synthesis of highly crystalline and phase-pure nanoplatelets. It was demonstrated from the composition dependent thermoelectric property of p-type $\text{Bi}_x\text{Sb}_{2-x}\text{Te}_3$ pellets that the optimized $\text{Bi}_{0.5}\text{Sb}_{1.5}\text{Te}_3$ sample exhibited $ZT \sim 0.51$ at 375K.¹⁵⁷ The synthesis and thermoelectric property of $\text{Bi}_x\text{Sb}_{2-x}\text{Te}_3$ have also been reported by Hong *et al.*¹⁵⁸

Acetate precursors have been employed in the solution based synthesis of oxide solid solutions. Naveen and Selladurai reported the synthesis and physicochemical properties of $\text{Mn}_x\text{Co}_{3-x}\text{O}_4$ ($0 \leq x \leq 0.2$) nanoparticles.¹⁵⁹ The typical synthesis was carried out by dissolving stoichiometric amounts of cobalt and manganese acetates in extra pure de-ionized water. The solution mixture was precipitated by using ammonia solution followed by calcination at 400 °C for 4 h, affording a mixed metal oxide. Structural and compositional analysis by p-XRD, FTIR and XPS techniques ruled out secondary phase formation, signifying successful inclusion of Mn ions into the crystal lattice of spinel cobalt oxide. It was also found that, with Mn addition, the crystallite size of the materials was reduced and was found in the range of 15.1-22.3 nm. Observation from SEM analysis revealed that compact agglomerates in pristine cubic cobalt oxide changed to loosely packed coalesced nanoparticles on Mn inclusion. Results from electrochemical tests demonstrated the improved performance of the Mn doped samples over the pristine cobalt oxide. Evidently, the electrode with 20% Mn showed the superior specific capacitance of 440 F/g compared to 343 F/g of pure cobalt oxide. Additionally, the addition of Mn improved the current density, columbic efficiency reversibility, and capacitance retention of $\text{Mn}_x\text{Co}_{3-x}\text{O}_4$ electrodes. In another study, Mn_{3-}

$x\text{Co}_x\text{O}_4$ nanoparticles with composition in the range of $0 \leq x < 1$ were obtained from the reaction of $\text{Mn}(\text{CH}_3\text{COO})_2 \cdot 4\text{H}_2\text{O}$ and $\text{Co}(\text{CH}_3\text{COO})_2 \cdot 4\text{H}_2\text{O}$ precursors at room temperature.¹⁶⁰ p-XRD measurements indicated that the prepared $\text{Mn}_{3-x}\text{Co}_x\text{O}_4$ solid solutions were monophasic and their peaks corresponded to the distorted spinel structure with the tetragonal structure. Analysis of particle morphology by TEM revealed the formation of isotropic nanoparticles exhibiting average particle sizes ranging from 15 - 17 nm. Investigation of the electrochemical property revealed a dramatic improvement of OER performance with an increase in the amount of Co in the precursor feed. Notably, higher specific OER activity (1700% of Mn_3O_4 at 1.76 V vs. RHE) was observed for $\text{Mn}_{2.1}\text{Co}_{0.9}\text{O}_4$ along with prolonged stability over 100 cycles.

A series of $\text{Ni}_x\text{Fe}_{3-x}\text{O}_4$ ($0 \leq x \leq 1.5$) solid solution have been prepared using the co-precipitation method and their electrochemical activity were evaluated in an alkaline medium.¹⁶¹ The substituted ferrites were prepared by precipitation of analytical grade $\text{Fe}(\text{NO}_3)_3 \cdot 9\text{H}_2\text{O}$ and $\text{Ni}(\text{NO}_3)_2 \cdot 6\text{H}_2\text{O}$ at 80 °C under NaOH solution as a precipitating agent. P-XRD and IR analyses showed the formation of phase-pure $\text{Ni}_x\text{Fe}_{3-x}\text{O}_4$ solid solution crystallizing in a cubic spinel system. The inclusion of Ni in the Fe_3O_4 crystal lattice enhanced the electrochemical activity, with $\text{Ni}_{1.5}\text{Fe}_{1.5}\text{O}_4$ exhibiting significantly higher current density (158.0 mA/cm^2) than that of pristine iron oxide (23.7 mA/cm^2), NiFe_2O_4 (107.0 mA/cm^2), and $\text{Ni}_{0.5}\text{Fe}_{2.5}\text{O}_4$ (89.4 mA/cm^2).

Pyrolysis of $\text{Mn}(\text{II})$ oleate and $\text{Co}(\text{II})$ stearate precursors at 578 K in the presence of 1-octadecene afforded the formation of $\text{Co}_y\text{Mn}_{1-y}\text{O}$ ($0 \leq x \leq 0.4$) solid solutions with tuneable composition.¹⁶² Structural studies by p-XRD analysis proved the formation of solid solutions crystallizing in a cubic rock salt crystal structure analogous to that of pristine MnO or CoO. The structural cell constants of the as-prepared $\text{Co}_y\text{Mn}_{1-y}\text{O}$ solid solutions were found to decrease linearly with the increasing amount of Co, satisfying Vegard's law. Examination of the catalytic performance of $\text{Co}_x\text{Mn}_{3-x}\text{O}_4$ nanoparticles towards O_2 evolution by linear sweep voltammetry showed an increase in the current density of $\text{Co}_x\text{Mn}_{3-x}\text{O}_4$ nanoparticles as a function of Co content. Notably, the $\text{Co}_x\text{Mn}_{3-x}\text{O}_4$ nanoparticles with 40 % Co demonstrated a high current density of 2.8 mA/cm^2 at 1.9 V (vs.RHE), which is relatively 3.9 times larger than that of pure Mn_3O_4 nanoparticles.

Since their discovery, the utility of most metal peroxides has been largely hampered by the corresponding pyrolytic temperatures, which are difficult to be tuned to fit the necessary reaction conditions. One approach to overcome this would have been to synthesize solid solutions between the two peroxides with different thermolytic temperatures (T_{dec}). To

address this, Lingampalli *et al.* demonstrated the formation of $\text{Zn}_x\text{Mg}_{1-x}\text{O}_2$ ($1 > x > 0$) solid solution in the entire solubility range by pyrolysis of peroxides of ZnO_2 and MgO_2 with decomposition temperatures, T_{dec} of ~ 200 °C and 300 °C, respectively.¹⁶³ The choice of using MgO_2 and ZnO_2 was due to their similarity in lattice constants, which is a prerequisite for forming a homogeneous solid solution exhibiting minimum lattice stress. The typical synthesis involved themolyzing a mixture of MgO and $\text{Zn}(\text{CH}_3\text{COO})_2 \cdot 2\text{H}_2\text{O}$ in ultrapure water 80 °C utilizing H_2O_2 as peroxidation reagent. The p-XRD diffractogram for the solid solution matched well with the parent MgO_2 and ZnO_2 , and their cubic structure was retained. Interestingly, decomposition temperatures of the resulting solid solutions were found between the parent phases and varied steadily with the composition.

Alloyed films of spinel $\gamma\text{-(Al}_x\text{Ga}_{1-x})_2\text{O}_3$ ($0 \leq x \leq 1$) were effectively stabilized on MgAl_2O_4 substrates by employing the molecular beam epitaxy method. The crystalline nature of the alloy films was significantly better compared with that of the parent $\gamma\text{-Ga}_2\text{O}_3$ film, showing more flexibility and sensitivity of the Al_2O_3 lattice to the epitaxial force exerted by the substrate than Ga_2O_3 crystal lattice. Deep-UV spectroscopy measurements showed direct and indirect energy gaps in the range of 4.96 - 6.97 and 4.80 - 6.86 eV, respectively.¹⁶⁴

Nanostructured $\text{Ce}_{1-x}\text{Y}_x\text{O}_{2-x/2}$ ($x \leq 0.35$) solid solutions were prepared via a novel carbonate co-precipitation of metal nitrate precursors utilizing ammonium carbonate as a precipitating agent.¹⁶⁵ In the typical procedure, carbonate solid solutions were directly formed during precipitation, enabling the direct formation of $\text{Ce}_{1-x}\text{Y}_x\text{O}_{2-x/2}$ solid solution at a low calcination temperature of ~ 301 °C for 2 h. p-XRD analysis showed that $\text{YO}_{1.5}$ could be soluble in CeO_2 in the composition range of 27 - 35 mol%, with Y_2O_3 -related type-C phase appearing in the final material. The results further indicated that the inclusion of Y^{3+} in the pristine CeO_2 materials facilitated the formation of nanospheres and slowed down the decomposition of the starting materials, which suppressed crystallite coarsening during calcination. A gradual increase in the activation energy for crystallite coarsening was observed from 68.7 to 138.6 kJ/mol for parent CeO_2 and CeO_2 doped with 35 mol% $\text{YO}_{1.5}$, respectively.

Owing to their special properties and chemical stability, nitride semiconductors are considered appealing materials for electronic applications. To further modulate their property and enhance their performance, composition-programmed synthesis of nitrides has been reported as a promising strategy. Bauers *et al.* described the fabrication of thin films of $\text{Mg}_x\text{Zr}_{2-x}\text{N}_2$ ($0.5 \leq x \leq 1.8$) by employing combinatorial co-sputtering in a nitrogen plasma.¹⁶⁶ Compositional analysis demonstrated that the formation of nitride solid solutions exhibiting

low oxygen content (<1%) could be achieved with magnesium content ≤ 1.0 , above which a higher oxygen content was detected. When magnesium content reached $x = 1.6$, the $\text{Mg}_x\text{Zr}_{2-x}\text{N}_2$ thin films crystallized in a rocksalt-derived crystal system, as disclosed by p-XRD results. With Mg content > 1.6 the films swiftly oxidized, making $x = 1.6$ the optimum mole ratio needed to yield a solid solution. The electrical conductivity of the as-synthesized films decreased with increasing Mg concentration. On the other hand, the conductivity of Mg-rich ($x \geq 1$) films increased with an increase in temperature, demonstrating the semiconducting property of Mg-rich $\text{Mg}_x\text{Zr}_{2-x}\text{N}_2$. Interestingly, evaluation of optical behaviour showed a clear absorption onset of the Mg-rich series at 1.8 eV, which is suggestive of semiconducting character.

Alloyed $\text{Al}_x\text{Sc}_{1-x}\text{N}$ films have been deposited directly on MgO substrates and were found stabilize in a uniform monophasic rock salt when $x < 0.51$.¹⁶⁷ The p-XRD pattern of the films grown straight on (100) MgO having mole ratio up to $x = 0.51$ were found to match well with a uniform monophasic rocksalt alloy. The uniformity range of the rocksalt phase was extended up to aluminum composition, $x = 0.82$ for a 120 nm thick film after introducing a 20 nm buffer layer of TiN between the MgO substrate and the $\text{Al}_x\text{Sc}_{1-x}\text{N}$ film. In the same range of homogeneity, the prepared material showed a modest direct bandgap bowing parameter of 1.41 ± 0.19 eV. On the other hand, the metastable rocksalt aluminium nitride recorded a direct bandgap of 4.70 ± 0.20 eV.

The decrease of carrier concentration in ScN and thin film alloys of p-type $\text{Sc}_x\text{Mn}_{1-x}\text{N}$ was described by Saha *et al.*¹⁶⁸ Nevertheless, a relatively large amount of manganese of about 11% Mn on Sc sites was needed to transform ScN into a p-type semiconductor. Also, very small hole mobility of $2 \text{ cm}^2/\text{Vs}$ was observed in p-type $\text{Sc}_{0.89}\text{Mn}_{0.11}\text{N}$, and in depth analyses of electronic character with respect to temperature were missing. Inspired by the desire to fabricate ScN based energy conversion devices, Saha *et al.*¹⁶⁹ conducted another study in which Mg_xN_y was incorporated in ScN to form $\text{Sc}_{1-x}\text{Mg}_x\text{N}$ solid solution alloys, diminishing its carrier concentration and transforming ScN into a p-type semiconductor at high amount of dopant. Evaluation of room temperature optical properties revealed a direct band gap of 2.21 eV for pristine ScN while that of $\text{Sc}_{1-x}\text{Mg}_x\text{N}$ thin-film alloys were found in the range of 2.21 - 2.24 eV at $0 < x < 0.04$. Notably, comparably higher absorption coefficients were displayed by the p-type than the n-type $\text{Sc}_{1-x}\text{Mg}_x\text{N}$ alloy films. Moreover, the pristine n-type ScN and the alloyed p-type $\text{Sc}_{0.962}\text{Mg}_{0.038}\text{N}$ thin films exhibited large thermoelectric power factors of $\sim 3.0 \times 10^{-3}$ and $\sim 0.8 \times 10^{-3} \text{ W/m-K}^2$, correspondingly, at elevated temperatures in the range of 600 - 850 K.

Wang *et al.* reported the deposition of epitaxial $\text{Ti}_{1-x}\text{Mg}_x\text{N}(001)$ ($0 \leq x \leq 0.49$) layers on $\text{MgO}(001)$ by employing reactive magnetron co-sputtering using Ti and Mg targets under pure N_2 supply at 600°C .¹⁷⁰ The substitution of Ti by Mg caused a red shift in the reflection edge from 2.0 to 0.8 eV where as the unscreened plasma energy varied in the range of 7.6 - 4.7 eV, indicating a linear decrease in the free carrier density with respect to composition, x . These results corroborated with XPS analysis, which showed a reduction of the density of filled conduction band states and about 0.9 eV reduction in the Fermi level with respect to Mg from 0 to 0.49. The screened plasma energy was successfully tuned from visible to infrared, exhibiting energy in the range of 2.64 - 1.33 eV for Mg composition in the range of 0 - 0.39, which is equivalent to wavelength in the range of 470 - 930 nm, indicating a tunable plasmonic activity.

In an attempt to modulate the band gap of molybdenum disulfide, Zhang *et al.* employed a chemical vapour deposition method to synthesize $\text{Mo}_{(1-x)}\text{W}_x\text{S}_2$ and $\text{MoS}_{2(1-x)}\text{Se}_{2x}$ alloy monolayers with good homogeneity and tunable composition. During the synthesis process, S powder was used as a chalcogenide source, while MoO_3 and WO_3 were used as Mo and W sources, respectively. The mixture of MoO_3 and WO_3 was heated at 750°C while S powder was subjected to 150°C . The morphological analysis confirmed the formation of triangular single-crystals. A composition-dependent band gap was obtained in the range of 1.83 (MoS_2) - 1.97 eV (WS_2).¹⁷¹ In another study, novel $\text{Mo}_x\text{W}_{1-x}\text{S}_2$ ($0 \leq x \leq 1$) inorganic fullerenes were synthesized via MOCVD setup using H_2S as a sulfur source. The particles exhibited an average size of 20.45 nm. Evaluation of the tribological performance of the prepared samples showed the best performance for samples with composition range $0.5 < x \leq 0.8$.¹⁷² Other $\text{Mo}_x\text{W}_{1-x}\text{S}_2$ alloyed systems have also been prepared via different approaches and investigated for their potential in energy conversion and storage applications.¹⁷³⁻¹⁷⁶

1.2.5.2.2 Ternary anionic solid solutions

Ternary anionic solid solutions or alloyed compounds are formed by combining two pristine binary systems composed of a common metallic ion. A good example is the alloying of AB' and AB'' to form $(\text{AB}')_x(\text{AB}'')_{1-x}$ or simply $\text{AB}'_xB''_{1-x}$ in which B' and B'' are two distinct anions and A is the common cation. A notable example is the alloying of binary CdS and CdSe to form $\text{CdS}_x\text{Se}_{1-x}$ solid solution. Alternatively, the ternary anionic solid solution can be obtained from the elemental doping process, where a particular anion in the binary host compound is replaced by another anion from the same group. Numerous studies have

reported the synthesis of ternary anionic solid solutions by employing different precursors and synthetic methods.

The growth of $\text{MoS}_{2(1-x)}\text{Se}_{2x}$ ($x = 0 - 1$) alloys with controlled morphology has been achieved by Feng *et al.* via physical vapor deposition.¹⁷⁷ The synthesis was achieved via evaporation of MoSe_2 powders and MoS_2 powders in addition to Se powders which were introduced upstream of the furnace at 300 °C. While representative TEM micrograph of $\text{MoS}_{0.78}\text{Se}_{1.22}$ showed the formation of triangle-shaped materials, SEM images indicated diverse shapes such as triangles, hexagons depending on the deposition temperature. The SAED pattern revealed only a single set of hexagon spots, signifying single-crystal nature of the $\text{MoS}_{0.78}\text{Se}_{1.22}$. The band gap photoluminescence was observed to be constantly tuned from 1.86 eV at $x = 0$ to 1.55 eV at $x = 1$.

Another report by Zhang *et al.* demonstrated the use of the chemical vapour deposition method to prepare uniform $\text{MoS}_{2(1-x)}\text{Se}_{2x}$ alloy monolayers exhibiting triangular single-crystalline shape. During the synthesis process, selenium and sulfur powders were utilized as chalcogenide sources, while the source of molybdenum was MoO_3 . The MoO_3 precursor was subjected at 680 °C, while the concoction of S and Se powders was placed at 280 °C because of the difference in the melting points of the precursors. Measurements of optical properties demonstrated that the bandgap could be extended from 1.55 (MoS_2) - 1.97 eV (MoSe_2).¹⁷¹

The fabrication of nanostructured $\text{CdE}'_x\text{E}''_{1-x}$ (in which E' and E'' are two dissimilar chalcogens) solid solutions have largely been dependent on similar synthetic protocols employed for binary cadmium chalcogenide nanoparticles. Mostly, the preparation protocol proceeds by the quick injection of a solution mixture comprising stoichiometric quantities of the chalcogen starting materials into a solution of cadmium (II) precursor in high boiling solvents at ~300 °C, followed by the growth stage. By employing this method, Swafford *et al.* produced uniform $\text{CdS}_x\text{Se}_{1-x}$ ($0 \leq x \leq 1$) solid solution nanocrystals in all proportions.¹⁷⁸ Typically, a mixture composed of known amounts of CdO, OA, and ODE in a 100 mL three-neck flask was thermally treated at 315 °C under an inert environment. A colourless solution was observed at a temperature range of 275 - 280 °C, representing the formation of cadmium oleate. To obtain $\text{CdS}_x\text{Se}_{1-x}$ nanocrystals, a solution consisting of stoichiometric proportions of sulfur and selenium was quickly injected into the flask by means of a needle after reaching 315 °C. The temperature was then reduced to 275 °C, leaving the nanoparticles to grow until the preferred size was obtained in less than 15 min. Elucidation of the relationship between the band gap and nanoparticle size and mole fraction revealed a bowing constant of 0.29,

which was consistent with bulk values. The same approach was successfully used by Bailey and Nie¹⁷⁹ in obtaining alloyed $\text{CdSe}_x\text{Te}_{1-x}$ quantum dots by varying the amount of selenium and sulfur in the reaction mixture. Another study by Al-Salim *et al.* has reportedly utilized organic solvents having distinct coordinating behavior in the fabrication of nanoscopic $\text{CdS}_x\text{Se}_{1-x}$ solid solutions.¹⁸⁰ Thermolysis of a mixture of cadmium acetate, selenium and sulfur powders at 230 - 300 °C in coordinating solvents slowed down the crystal growth, affording hexagonal phase. In contrast, non-coordinating solvents lead to faster crystal growth, enabling the formation of the cubic phase. It was observed that by choosing proper solvents, $\text{CdS}_x\text{Se}_{1-x}$ solid solutions could be selectively fabricated at temperatures as high as 300 °C. Studies on evolution of optical behavior revealed high photoluminescence properties of the nanocrystals which was modulated across the visible region by tuning the mole ratios of Se to S or changing the solvent. Aqueous synthesis of crystalline $\text{CdSe}_x\text{Te}_{1-x}$ nanoparticles has been reported by Piven *et al.* via concurrent injection of NaHSe and NaHTe in a solution of Cd-thiolate under the alkaline condition at ambient temperature.¹⁸¹ The growth of solid solution nanoparticles was observed to be faster compared to those of pristine CdSe and CdTe nanoparticles, yielding larger nanoparticles at particular reaction times. Also, the reactivity of the selenium source was comparably higher than that for the tellurium source, enabling adequate incorporation of Se content into the solid solution, in relation to the ratio of moles of Se and Te sources employed. Structural studies of the prepared solid solutions by p-XRD confirmed the successful synthesis of crystalline nanoparticles crystallizing in cubic zinc-blend structure, which is typical of thiol-capped water-soluble CdSe and CdTe nanomaterials. Monodisperse nanoparticles having sizes in the range of 3.6-4.9 nm were confirmed from TEM analysis. The shape of the nanoparticles was described to be edged within a truncated tetrahedral model. By varying the composition of $\text{CdSe}_x\text{Te}_{1-x}$ nanoparticles, the optical absorption spectra were tuned in the range of 550 - 690 nm. The solid solution nanoparticles demonstrated band-edge emission with relatively low intensity compared to the pristine CdTe nanoparticles. Similarly, Ouyang and co-workers synthesized uniformly $\text{CdS}_x\text{Se}_{1-x}$ nanoalloys via a scalable and reproducible non-injection approach.¹⁸² The formation of photoluminescent $\text{CdS}_x\text{Se}_{1-x}$ quantum dots was achieved by allowing air-stable precursors cadmium acetate dihydrate ($\text{Cd}(\text{OAc})_2 \cdot 2\text{H}_2\text{O}$), elemental Se and S to react at 240 °C under the presence of myristic acid, 2,2'-dithiobisbenzothiazole, and ODE. The p-XRD results showed that the fabricated $\text{CdS}_x\text{Se}_{1-x}$ nanocrystals assume a cubic crystal system. Additionally, their diffraction peaks shifted to large 2θ values with an increasing amount of S, serving as evidence of its successful inclusion into the CdSe lattice and

affording the formation of $\text{CdS}_x\text{Se}_{1-x}$ solid solution. Insights about the particle morphology and size revealed the formation of spherical shaped nanocrystals exhibiting high crystallinity and with a narrow size distribution in the range of 3.05 - 3.70 nm. It was further demonstrated that as the S content in the precursor feed increased, the particle size also increased. Moreover, the resultant ternary $\text{CdS}_x\text{Se}_{1-x}$ solid solutions could easily be tailored to emit in the visible region showing wavelength in the range of 470 - 550 nm, an emission window which is difficult to achieve with binary CdS and CdSe quantum dots.

Large scale synthesis of composition-tunable tetrapodal $\text{CdSe}_x\text{Te}_{1-x}$ nanocrystals were reported.¹⁸³ These alloyed tetrapods were prepared via thermolysis of a mixture of the organometallic Cd source and the pre-mixed (Se + Te) precursor in a mixed-ligand solution. The p-XRD diffractogram of the parent CdTe and CdSe as well as that of $\text{CdSe}_x\text{Te}_{1-x}$ tetrapods matched well with the wurtzite-phase structure, and the gradual peak shifting to larger diffraction angles rules out phase segregation or separated nucleation of CdTe/CdSe in the $\text{CdSe}_x\text{Te}_{1-x}$ system. Analysis of optical band properties revealed that the $\text{CdSe}_x\text{Te}_{1-x}$ tetrapodal nanoparticles display composition dependent absorption and emission characteristics, and exhibit a wide absorption spectra window of up to 100 nm and near-infrared emission.

The formation of $\text{CdS}_x\text{Se}_{1-x}$ ($0 \leq x \leq 1$) solid solutions via vacuum fusion of CdS and CdSe was reported by El-Nahass.¹⁸⁴ p-XRD results showed that the solid solution exhibited hexagonal wurtzite structure. A close structural investigation revealed a linear variation of the unit cell parameters with the sulfur mole ratio, corresponding to Vegard's law. In the same study, the deposition of thin films of $\text{CdS}_x\text{Se}_{1-x}$ ($0 \leq x \leq 1$) on glass substrates via conventional thermal evaporation of pre-prepared solid solution ingots was reported. Structural studies confirmed the formation of polycrystalline films with hexagonal structure, conforming to those of the solid solution ingots.

The preparation of solid solutions is considered a practical approach for tuning free carrier concentration in semiconductors. As a result, several researchers have synthesized solid solutions of IV-VI semiconductors, including lead chalcogenides, exhibiting a range of unusual properties that are not found in the parent materials. Building on the work of Kumar *et al.*¹⁸⁵ in which $\text{PbS}_{1-x}\text{Se}_x$, $\text{PbSe}_{1-x}\text{Te}_x$ and $\text{PbTe}_{1-x}\text{S}_x$ solid solutions with composition $x = 0.2$ and 0.8 was successfully prepared. Similar series of solid solutions with composition $x = 0.4$ and 0.6 were synthesized and investigated for their structural, optical and electrical properties.¹⁸⁶ The p-XRD measurements confirmed the formation of polycrystalline solid solutions exhibiting a rock salt (NaCl) structure. All samples displayed semiconducting

nature, which increased with an increase in temperature. The samples demonstrated a high absorption coefficient of about 10^4 cm^{-1} which increased abruptly below a particular wavelength. Analysis of optical band gap showed a linear variation of $(ah\nu)^2$ versus $h\nu$ over a broad spectrum of photon energies demonstrating the direct type of transitions.

Likewise, monodisperse $\text{PbS}_x\text{Se}_{1-x}$ nanoparticles have been obtained by rapid injection of a mixture of trioctylphosphine (TOP) and selenium (Se) solution, bis(trimethylsilyl) sulfide (TMS_2S), diphenylphosphine (DPP), ODE into a hot solution containing a mixture of PbO, ODE and oleic acid under inert atmosphere.¹⁸⁷ The well-regulated absorbance and reasonably fine PL peaks showed that the solid solution nanocrystals were monodisperse, ruling out the probability of the coexistence of separate phases of PbSe and PbS in $\text{PbS}_x\text{Se}_{1-x}$ system. Investigating the potential of ternary $\text{PbS}_x\text{Se}_{1-x}$ nanocrystals for application in photovoltaic devices demonstrated higher efficiency than binary PbSe and PbS based nanocrystal devices.

Bis(N,N-diethyl-N'-naphthoylthioureato)lead(II) and bis(N,N-diethyl-N'-naphthoylselenoureato)lead (II) complexes were successfully employed as single source precursors to afford the synthesis of nanocrystalline $\text{PbS}_{1-x}\text{Se}_x$ ($0 \leq x \leq 1$) solid solution via a hot injection method. The p-XRD analysis of the $\text{PbS}_{1-x}\text{Se}_x$ series showed that the diffraction peaks of the solid solutions were intermediate between the pristine PbS and PbSe. The solid solution nanoparticles displayed cubic shapes analogous to the parent binary materials (Fig. 1.8 (a-e)). The absorption band gap for the alloyed systems showed a linear shift from PbS to PbSe with respect to the mole fraction of Se (Fig. 1.8 (f)), and is attributed to the change in the lattice parameters.⁸⁷

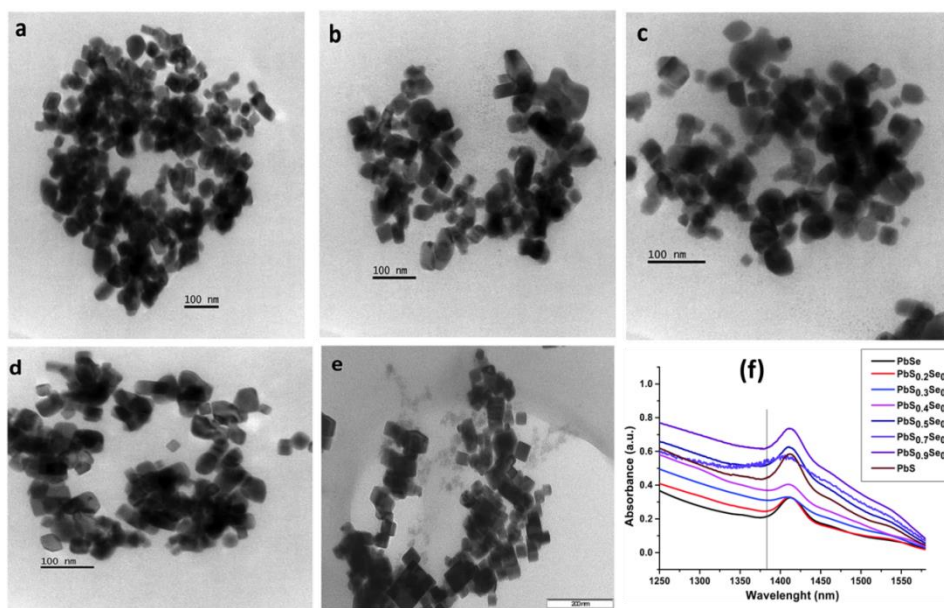


Fig. 1.8. TEM images of $\text{PbS}_x\text{Se}_{1-x}$ obtained at x_{Se} values of (a) 0, (b) 0.3, (c) 0.5, (d) 0.8, (e) 1. (f).UV-Vis-NIR spectra of $\text{PbS}_{1-x}\text{Se}_x$ ($0 \leq x \leq 1$) nanoparticles. (Reproduced from ref. 67).

The synthesis of polycrystalline thin films of $\text{ZnS}_x\text{Se}_{1-x}$ with composition in the range of $0 \leq x \leq 1$ have been achieved from pure ZnSe and ZnS powders by employing a close-spaced evaporation technique.¹⁸⁸ The deposition of the films onto glass substrates was performed at different substrate temperatures ranging from 200 - 400 °C. p-XRD measurements showed that the deposition of $\text{ZnS}_x\text{Se}_{1-x}$ films was achieved at a temperature range of 275 - 300 °C, and the films exhibited a cubic structure. Compositional analysis revealed the formation of nearly stoichiometric films at a deposition temperature range of 275 - 325 °C. The $\text{ZnS}_x\text{Se}_{1-x}$ films obtained at 300 °C exhibited an average surface roughness between 2 and 6 nm. The obtained optical transmittance of >85% suggested high transparency of the films. The films recorded energy band gaps in the range of 2.61 - 3.60 eV, which increased with respect to sulfur content. Another study by Nandkishor *et al.* demonstrated the preparation of zinc sulphoselenide, $\text{ZnS}_x\text{Se}_{1-x}$ ($0 \leq x \leq 1$) thin films crystallizing in a cubic zinc blende crystal system. A computerized chemical spray pyrolysis method was employed to grow the films on glass substrates. Changing the precursor composition in terms of varying the amount of S and Se in the $\text{ZnS}_x\text{Se}_{1-x}$ system resulted in the energy band gap from 2.84 eV to 3.57 eV. Overall, the prepared thin films exhibited semiconducting properties.¹⁸⁹ The synthesis of $\text{ZnS}_x\text{Se}_{1-x}$ films has also been reported by other researchers.¹⁹⁰⁻¹⁹⁵

The synthesis of $\text{SnS}_{1-x}\text{Se}_x$ ($0 \leq x \leq 1$) solid solution from chalcogeno-(thio/seleno) benzoate complexes of organotin, by both colloidal hot injection and solventless method, has been described.⁸⁸ Both methods afforded the formation of crystalline $\text{SnS}_{1-x}\text{Se}_x$ solid solutions over the whole composition range (Fig. 1.9 (i & ii)). The EDX results showed that the colloidal hot injection route offered better control over composition and a continuous change in lattice constants. In comparison, the change in lattice constants was not smooth for the product obtained by the solventless method and EDX analysis also demonstrated a broader deviation from the expected percentage. The morphology was independent of the method used, and a similar trend in size and shape was observed for both approaches (Fig. 1.10 (i & ii)). The band gap shows an increase in moving from SnSe to SnS.

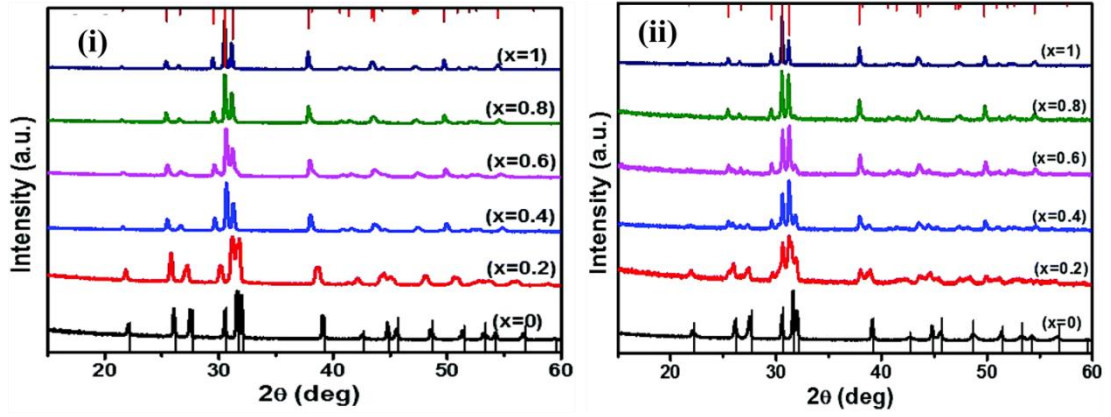


Fig. 1.9. p-XRD pattern of $\text{SnS}_{1-x}\text{Se}_x$ ($0 \leq x \leq 1$) prepared by (i) hot injection method in OLA at 200 °C, (ii) the solvent-less route at 330 °C (Reproduced from ref. 88).

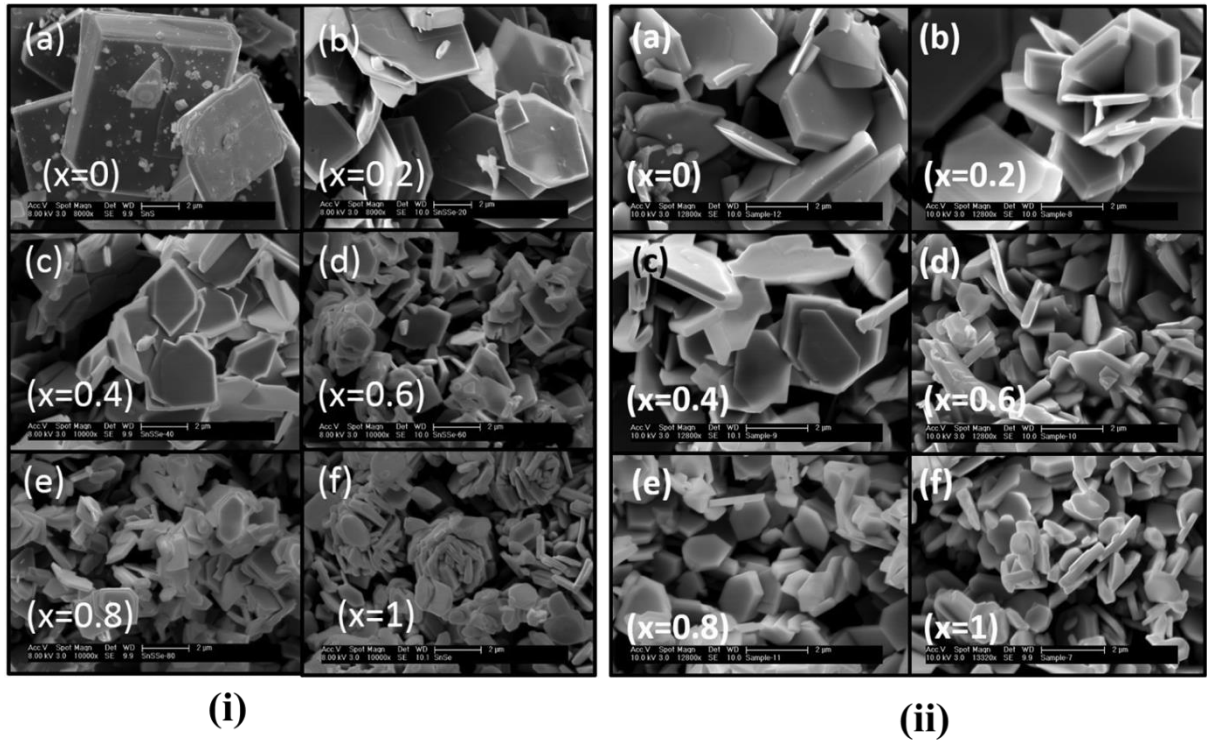


Fig.1.10. SEM images of $\text{SnS}_{1-x}\text{Se}_x$ ($0 \leq x \leq 1$) (i) synthesized by the hot injection method, (ii) synthesized by solventless method (Reproduced from ref. 88).

The preparation of $\text{ZnS}_x\text{Te}_{1-x}$ thin films has also been achieved by implanting sulfur into ZnTe obtained via molecular beam epitaxy, followed by pulsed laser melting. Optical analysis showed that after pulsed laser melting treatment with a laser fluence of 0.15 J/cm^2 , sulfur-induced states were formed above the valence band at 2.22 eV inside the bandgap of ZnTe for the $\text{ZnS}_x\text{Te}_{1-x}$ ($x = 3.2\%$).¹⁹⁶

A complete $\text{Sb}_2\text{S}_{3-x}\text{Se}_x$ ($0 \leq x \leq 3$) solid solution has been reportedly formed between Sb_2S_3 and Sb_2Se_3 by using elemental Sb, S and Se as precursors. The single-XRD measurements indicate that no phase change occurs throughout the solid solution range.¹⁹⁷

1.2.5.3 Quaternary solid solutions

In contrast to binary and ternary solid solutions, quaternary crystalline solid solutions with composition $\text{A}'_x\text{A}''_{1-x}\text{B}'_y\text{B}''_{1-y}$, are formed by alloying of two binary compounds that are composed of distinct cations and anions. Notable example involves the formation of $\text{Zn}_x\text{Cd}_{1-x}\text{S}_y\text{Se}_{1-y}$ ($0 \leq x, y \leq 1$) by alloying ZnS and CdSe. Combining ternary and binary compounds can also produce a quaternary alloyed system as revealed by the formation of $(\text{CuInS}_2)_x(\text{ZnS})_{1-x}$.¹⁹⁸ Quaternary solid solutions can alternatively be formed via concurrent doping or partial substitution of cations and anions in binary host compounds. For example, partial substitution of Co with Ni in CuCo_2S_4 by Ni yields a quaternary substitutional solid solution of $\text{CuCo}_{2-x}\text{Ni}_x\text{S}_4$ ($0 \leq x \leq 1$).³⁷ Compared to binary and ternary semiconductor solid-solutions, quaternary solid solutions provide a more powerful pathway to modify their properties. Nevertheless, despite all efforts, the formation of such materials remains challenging because their fabrication involves two individual spontaneous substitution or doping processes where anions and cations can be concurrently incorporated in the host system. During the nucleation and crystallization process, the anions and cations of the dopant substitute anions and cations of the host compound to afford a completely new solid phase. Unfortunately, the nucleation and crystallization dynamics in quaternary solid solutions are more complicated and the substitution takes place randomly and often incompletely. The growth conditions of a homogeneous crystallization of such solid solutions are strictly confined to local equilibrium.⁸³ Consequently, phase segregation and local elemental aggregation are difficult to avoid, along with the uniform composition regulation. Slight deviations in composition or temperature will result in a phase separation or might cause the formation of core-shell structures.¹⁹⁹ For that reason, quaternary solid solution nanostructures require rather critical growth conditions and elegant reaction procedures to guarantee phase purity. It is also crucial to authenticate the phase purity and composition uniformity by utilizing several characterization techniques.

Even though the synthesis of these multicomponent nanostructures presents a considerable challenge, numerous systems of anionic and cationic quaternary solid solutions have been reported. Above all, the growth conditions for forming pseudobinary solid

solutions proposed in different studies have been adopted and used as a general guideline in preparing diverse quaternary semiconductor systems.

1.2.5.3.1 Quaternary cationic solid solutions

Intentional doping or partial substitution of the parent material by foreign elements has been considered as an effective strategy to prepare quaternary cationic solid solutions with improved properties for numerous applications. In an attempt to improve the supercapacitive performance of the pristine CuCo_2S_4 , Gao *et al.* demonstrated the synthesis of monophasic $\text{CuCo}_{2-x}\text{Ni}_x\text{S}_4$ solid solution by a simple hydrothermal technique, where Ni partially replaced Co in CuCo_2S_4 .³⁷ The synthesis was carried out by the thermolysis of $\text{Ni}(\text{NO}_3)_2 \cdot 6\text{H}_2\text{O}$, $\text{Co}(\text{NO}_3)_2 \cdot 6\text{H}_2\text{O}$ and $\text{Cu}(\text{NO}_3)_2 \cdot 3\text{H}_2\text{O}$ precursors at 150 °C for 2 h, with subsequent washing and calcination at 80 °C for 12 h. The p-XRD results demonstrated that Co could be simply replaced with Ni in the composition range of $x = 0, 0.25, 0.5, 0.75$ and 1 without changing the crystalline phase and without the formation of a multi-phase composite at high content of Ni. The EDX elemental mappings confirmed homogeneous dispersion of Cu, Co, Ni and S in the solid solutions. SEM images showed the formation of spherical clusters consisting of a large number of nanorods which were observed to be much thinner and denser at higher nickel content. Further studies by TEM disclosed that the nanorods are made up of several small nanoparticulate crystals with sizes varying from 20 to 40 nm. Compared to the pristine CuCo_2S_4 and NiCo_2S_4 , the solid solution with composition $\text{CuCo}_{1.25}\text{Ni}_{0.75}\text{S}_4$ displayed a considerably high specific capacitance of 647 F/g at 1 A/g. Furthermore, asymmetric capacitors assembled by employing $\text{CuCo}_{1.25}\text{Ni}_{0.75}\text{S}_4$ and activated carbon as anode and cathode respectively produced a high energy density of 31.8 Wh/kg at the power density of 412.5 W/kg. These findings revealed that quaternary $\text{CuCo}_{2-x}\text{Ni}_x\text{S}_4$ solid solutions are hopeful electrode materials for high-performance electrochemical capacitors.

Similarly, Chen *et al.* prepared a set of $\text{Ni}_x\text{Cu}_{1-x}\text{Co}_2\text{S}_4$ solid solutions by a hydrothermal approach using $\text{Ni}(\text{NO}_3)_2 \cdot 6\text{H}_2\text{O}$, $\text{Cu}(\text{NO}_3)_2 \cdot 4\text{H}_2\text{O}$ and $\text{Co}(\text{NO}_3)_2 \cdot 6\text{H}_2\text{O}$ precursors and evaluated their potential for supercapacitor applications. These substitutional solid solutions were produced owing to similar atom occupation and comparable crystal size of Ni (0.69 Å) and Cu (0.71 Å) in the crystal lattice of metal sulfides. As inferred by p-XRD data, the crystal structures of all the samples conformed to the cubic NiCo_2S_4 and CuCo_2S_4 phases with the same $\text{Fd}\bar{3}\text{m}$ space group. Among all solid solution series, $\text{Ni}_{0.67}\text{Cu}_{0.33}\text{Co}_2\text{S}_4$

displayed excellent electrochemical activity recording the highest specific capacitance of 1340.48 F/g at 1 A/g, demonstrating an excellent rate capability.³⁶

Polycrystalline $\text{Co}_x\text{Zn}_{1-x}\text{In}_2\text{S}_4$ ($0 \leq x \leq 0.6$) solid solution has been prepared by heating stoichiometric mixture of the corresponding sulfides in a sealed quartz tube at 900°C. X-ray and spectroscopic investigations showed that the ZnIn_2S_4 -type structure existed up to $x = 0.6$, and the Co^{2+} ions were distributed in the tetrahedral and octahedral voids of the lattice.²⁰⁰ Spinel $\text{CdCr}_{2x}\text{In}_{2-2x}\text{S}_4$ ($0 \leq x \leq 1$) solid solutions were reportedly synthesized by mixing and annealing of the Cd, In and Cr sulfides. The spinel phase was found in the whole range of compositions. P-XRD analysis proved the formation of phase-pure spinels, and the lattice constants varied linearly as a function of substituent concentration.²⁰¹

Quaternary alloys have also been reportedly formed via alloying of ternary I-III-VI₂ semiconductors, famously known as chalcopyrites. The most prominent example includes the tetragonal $\text{CuIn}_x\text{Ga}_{1-x}\text{Se}_2$, which was synthesized by Tang *et al.* by alloying CuInSe_2 and CuGaSe_2 .²⁰² The solid solution was obtained from the high-temperature thermolysis reaction of analytical grade gallium, copper and indium salts, and Se powder in oleylamine. The resulting $\text{CuIn}_x\text{Ga}_{1-x}\text{Se}_2$ nanoparticles displayed strong UV-vis-NIR absorption around 1000 nm, conforming to band gap of 1.2 eV, which is the ideal value for single-junction solar cells.

Thermal decomposition of diisopropyldiselenophosphinato complexes of Ga(III), Cu(I) and In(III) in HDA/TOP at 250 °C has been employed by Malik *et al.* to afford $\text{CuIn}_{(1-x)}\text{Ga}_x\text{Se}_2$ solid solutions. The p-XRD patterns showed the formation of the tetragonal chalcopyrite crystallographic phase. The linear increase in the lattice parameters with the increasing indium composition confirmed the formation of a homogeneous alloy structure. TEM analysis of the tetragonal nanoparticles showed an average diameter of 14 nm.²⁰³

Arrested precipitation of chloride salts and elemental selenium as the metal and selenium sources, respectively, was employed by Panthani *et al.* to produce crystalline $\text{CuIn}_x\text{Ga}_{1-x}\text{Se}_2$ nanoparticles.²⁰⁴ In the quaternary $\text{CuIn}_x\text{Ga}_{1-x}\text{Se}_2$ solid solution, the In to Ga ratio could be monitored by changing the amount of their starting materials in the course of the reaction. Meanwhile, Guo *et al.* have successfully prepared a nanocrystal ink consisting of $\text{CuIn}_x\text{Ga}_{1-x}\text{S}_2$ through the rapid introduction of S solution into a solution composed of oleylamine and the metal chloride precursors at 225 °C.²⁰⁵ Evaluation of the photovoltaic performance revealed that a power conversion efficacy of 4.76% was exhibited by the solar cells fabricated by utilizing the $\text{CuIn}_x\text{Ga}_{1-x}\text{Se}_2$ absorber films.

Pan *et al.* prepared homogeneous nanocrystalline $(\text{CuInS}_2)_x(\text{ZnS})_{1-x}$ solid solutions by thermolysis of Zn, Cu and In dithiocarbamates in the presence of octadecene, oleic acid and

oleylamine as non-coordinating, capping and activation agents, respectively. TEM images showed nearly monodisperse nanoparticles having cubic and hexagonal structures of mean size in the range of 32.4 and 5.7 nm. The alloyed nanoparticles exhibited band gap tunability from 1.5 to 3.7 eV by varying the mole ratio of CuInS₂ and ZnS.¹⁹⁸ Similarly, solid solutions of CuGa_xIn_{2-x}S_{3.5} (0 ≤ x ≤ 2) and CuIn_xTl_{2-x}S_{3.5} (0 ≤ x ≤ 2) have also been obtained by Pan and co-workers via a wet chemical synthesis method by utilizing air-stable metal dithiocarbamate precursors.²⁰⁶ Thermal decomposition of the Cu, Ga and In dithiocarbamate complexes at 180 °C for 90 min in oleic acid, oleylamine and toluene led to the formation of CuGa_xIn_{2-x}S_{3.5} solid solutions. On the other hand, the formation of CuIn_xTl_{2-x}S_{3.5} was made possible by the injection of oleylamine into a hot solution of Cu, In, and TI dithiocarbamates in oleic acid and octadecene at 200 °C. TEM analysis indicated that the as-prepared quasi-spherical solid solution nanoparticles exhibited an average size of approximately 6.2 nm. It was also observed that the inclusion of Ga and TI permitted accurate regulation of the band gap energy in the range of 1.37 - 2.42 eV with respect to composition. Such bandgap tuneability in these materials may provide accurate control over the optical properties, which is of interest for optoelectronic applications.

Colloidal synthesis of rod-like (ZnS)_x(CuInS₂)_{1-x} nanoalloys was performed by employing a simple non-injection method. The preparation procedure involved thermolysis of metal dithiocarbamate precursors in a solution containing OA, DDT and ODE at 250 °C under argon atmosphere. p-XRD results showed that the prepared nanorods crystallize in the hexagonal wurtzite structure. Also, diffraction peaks were slightly shifted toward higher 2θ values, indicating the formation of a uniform solid solution. The bandgap of the quaternary alloyed nanorods was expediently adjusted by changing the stoichiometric amounts of ZnS and CuInS₂ in the alloyed system.²⁰⁷

Pyrolysis of a mixture of [Fe(S₂CNEt₂)₃], [Zn(S₂CNEt₂)₂], [ⁿBu₂Sn(S₂CNEt₂)₂] and [Cu(S₂CNEt₂)₂] precursors in oleylamine was reported to afford the formation of nanostructured Cu₂Zn_{1-x}Fe_xSnS₄ (0 ≤ x ≤ 1) semiconductor alloys.²⁰⁸ In depth structural studies according to p-XRD pattern indicated that the synthesized Cu₂Zn_{1-x}Fe_xSnS₄ material preserved a stannite structure. The morphology of Cu₂Zn_{1-x}Fe_xSnS₄ nanoparticles was identified to be rhombohedral as opposed to oblate spheroids of Cu₂FeSnS₄ nanostructures. This smooth evolution of morphology was evident through hexagonal crystals with composition, x = 0.5. TEM analysis showed smaller nanoparticles exhibiting particle sizes of about 9 ± 2 nm. Magnetic studies showed that the solid solutions were ferromagnetic at low temperatures. The photoluminescence properties using hexane as a dispersing solvent were

obvious in the range of 500 - 800 nm after excitation at 400 nm. The materials' band gap was found to be engineered within the visible region by adjusting the amount of Fe in the solid solution.

The formation of solid solutions from solvents with a small cation to anion ratio has also been confirmed as an effective approach to improve the thermoelectric properties of materials via the creation of vacancies. Owing to their smaller cation to anion ratio, binary compounds of In_2Te_3 and Ga_2Te_3 were reportedly used as molecular solvents for CuGaTe_2 to afford solid solutions of $(\text{CuGaTe}_2)_{1-x}(\text{In}_2\text{Te}_3)_x$ and $(\text{CuGaTe}_2)_{1-x}(\text{Ga}_2\text{Te}_3)_x$. The reactions were conducted by melting the stoichiometric quantity of highly pure precursors at 1183 K for 10 h, and subsequently quenched in cold water and annealed at 900 K for 72 h.²⁰⁹ High concentration vacancies exhibited by the solid solutions on the cation positions can serve as the phonon scattering hubs, enabling considerable decrease of the lattice thermal conductivity and consequently improving the thermoelectric activity to about ~75% in the whole temperature range.

In the search for active photocatalysts for hydrogen HER, Kato *et al.* reported the preparation of $(\text{CuGa})_{1-x}\text{Zn}_{2x}\text{S}_2$ ($0 \leq x \leq 1$) solid solution. The typical synthesis employed solid state reaction in which stoichiometric quantities of Cu_2S , Ga_2S_3 and ZnS were mixed and sealed in a quartz ampule after evacuation, followed by calcination at 1073 K for 10 h.²¹⁰ Structural analysis by p-XRD measurements indicated the formation of a monophasic chalcopyrite structure for all $(\text{CuGa})_{1-x}\text{Zn}_{2x}\text{S}_2$ solid solutions irrespective of zinc composition, x . Also, slight shifting of the p-XRD peaks to lower diffraction angles confirmed the successful formation of solid solutions between ZnS and CuGaS_2 . They also reported a slightly small band gap of 2.2 eV for $(\text{CuGa})_{1-x}\text{Zn}_{2x}\text{S}_2$ compared to 2.3 eV of CuGaS_2 . Moreover, the alloyed $(\text{CuGa})_{1-x}\text{Zn}_{2x}\text{S}_2$ displayed enhanced photocatalytic activity compared to CuGaS_2 , confirming the contribution of Zn in modifying the band structure of the pristine material.

Another solid solution of $(\text{CuIn})_x\text{Zn}_{2(1-x)}\text{S}_2$ with composition, $x = 0.01 - 0.5$ was reportedly synthesized by Tsuji *et al.*, and employed as photocatalysts for H_2 evolution under visible-light irradiation.²¹¹ The synthesis procedure involved precipitating a mixture of $\text{In}(\text{NO}_3)_3 \cdot 6\text{H}_2\text{O}$, $\text{Zn}(\text{NO}_3)_2 \cdot 6\text{H}_2\text{O}$ and CuCl precursors under inert conditions. H_2S gas was then bubbled through the aqueous solution and continuously agitated to yield the precipitates, which was then washed thoroughly and calcined at 1123 K for 5 h. The resulting solid solutions exhibited a zinc-blende structure, although some samples contained a negligible amount of a wurtzite phase. The photocatalytic properties were found to depend on the

energy structure with different compositions of the solid solutions. Notably, Pt (0.5 wt %)-loaded $(\text{CuIn})_{0.09}\text{Zn}_{1.82}\text{S}_2$ exhibiting a band gap of a 2.3 eV demonstrated the highest H_2 evolution activity and the apparent quantum yield at 420 nm was 12.5%.

Yuan *et al.* have successfully prepared $(\text{AgIn})_x\text{Zn}_{2(1-x)}\text{S}_2$ quantum dots by thermolysis of metal acetates i.e., $\text{In}(\text{CH}_3\text{COO})_3$, $\text{Ag}(\text{CH}_3\text{COO})$, and $\text{Zn}(\text{CH}_3\text{COO})_2 \cdot 2\text{H}_2\text{O}$ in the presence of oleylamine and 1-dodecanthiol at 250 °C under N_2 flow.²¹² It was evident from the p-XRD results that the diffraction patterns of $(\text{AgIn})_x\text{Zn}_{2(1-x)}\text{S}_2$ quantum dots with composition, $x > 0.5$ were similar to the pristine AgInS_2 while some peaks for samples with $x < 0.5$ matched with those for the pure ZnS . Clearly, the shifting of diffraction peaks to lower angles with respect to x values was an indication of the realization of a complete solid solution between the parent AgInS_2 and ZnS . Analysis of particle size and morphology by TEM revealed the formation of spherical quantum dots with an average diameter of 3.4 nm. However, the particle size was found to depend on the concentration of the metal acetates employed, and it changed from 3.4 nm with 20 mM metal acetate precursors to 2.1 and 4.4 nm when 10 and 60 mM metal acetate precursors were used, respectively. HRTEM images showed well-resolved lattice fringes with high crystallinity. Continuous composition tuning for $(\text{AgIn})_x\text{Zn}_{2(1-x)}\text{S}_2$ from $x = 0$ (ZnS) to $x = 1$ (AgInS_2) resulted to gradual modulation of bandgap from 3.55 eV to 1.80 eV. The highest photocatalytic performance of $(\text{AgIn})_x\text{Zn}_{2(1-x)}\text{S}_2$ further demonstrated the contribution of bandgap tuning on the efficiency of photocatalytic H_2 generation. With monochromatic irradiation at 450 nm, the photocatalytic system afforded a high apparent quantum yield of 8.2%.

A series of $\text{Cd}_{1-x}\text{Mn}_x\text{In}_2\text{S}_4$ solid solution with composition in the range of $0.5 \leq x \leq 1.0$ were reportedly prepared by the melt and annealing method, and grown by the chemical vapor transport method. p-XRD structure refinements employing the Rietveld method indicated the formation of a solid solution over an entire composition range, exhibiting a cubic structure and the space group of $\text{Fd}3\text{m}$. The linear relationship between the unit cell constants and composition revealed complete solid solubility in this system. All series of solid solution displayed a spinel structure with a random arrangement of Cd, Mn and In cations in the crystallographic positions.²¹³

With the use of iodine as a transport agent, single crystal of $\text{Cd}_{1-x}\text{Fe}_x\text{In}_2\text{S}_4$ ($x = 0.25, 0.5, 0.75$) systems were prepared via the chemical vapour transport method. In the typical synthesis, the growth of the crystals was done by introducing the ampoule in the furnace such that the source temperature was kept at 850 °C and the deposition temperature at 800 °C, respectively. The electron probe micro-analysis of the crystals showed that the actual Fe

content was lower compared to the nominal concentration. Room temperature XRD measurements revealed the formation of solid solutions exhibiting a cubic structure.²¹⁴

Khandale and Bhoga have synthesized $\text{Nd}_{2-x}\text{Ce}_x\text{CuO}_4$ ($x = 0 - 0.25$) solid solution nanoparticles by means of the acetate combustion method. The method employed cerium, neodymium and copper acetates as precursor materials, and it proceeded with a significant reduction of sintering temperature and reaction time. The p-XRD results confirmed the optimal solid solubility up to $x = 0.2$, and all the diffraction peaks matched with the tetragonal Nd_2CuO_4 phase. Studies on the variation of d.c conductivity as a function of temperature showed a transition from positive to negative temperature coefficient at 625 °C for $\text{Nd}_{2-x}\text{Ce}_x\text{CuO}_4$ within the solid solubility range.²¹⁵

Moussaoui *et al.* employed the co-precipitation method to carry out the synthesis of spinel $\text{Sn}_{1-x}\text{Mn}_x\text{Fe}_2\text{O}_4$ ($0 \leq x \leq 1$) nanoferrites from appropriate ratios of FeCl_3 , MnCl_2 and SnCl_2 salts.²¹⁶ The mixed metal hydroxides formed during the reaction were precipitated by using ammonia hydroxide at 80 °C for 30 min, and the product was washed and dried at 80 °C overnight to yield crystalline solid solutions. P-XRD confirmed the formation of monophasic cubic spinel structure for $\text{Sn}_{1-x}\text{Mn}_x\text{Fe}_2\text{O}_4$ solid solutions having crystallite sizes ranging from 3.91 - 4.61 nm. It was observed from TEM studies that the un-annealed ferrite nanoparticles exhibited ellipsoid morphology with particle sizes ranging from 9 - 10 nm. Also, for all $\text{Sn}_{1-x}\text{Mn}_x\text{Fe}_2\text{O}_4$ spinels over the entire composition range, the increase of magnetization and coercive fields as a function of manganese content was also obvious.

Zhao *et al.* elucidated the electrocatalytic activity of quaternary $\text{Ni}_x\text{Co}_{1-x}\text{Fe}_2\text{O}_4$ ($0 \leq x \leq 0.75$) nanospheres prepared hydrothermally from metal sulfates.²¹⁷ A stoichiometric mixture of $(\text{NH}_4)_2\text{Fe}(\text{SO}_4)_2 \cdot 6\text{H}_2\text{O}$, $\text{CoSO}_4 \cdot 7\text{H}_2\text{O}$ and $\text{NiSO}_4 \cdot 6\text{H}_2\text{O}$ in de-ionized water was thermolyzed at 160 °C in an autoclave for 24 h. Upon washing and annealing the product at 550 °C for 4 h, spherical nanoparticles exhibiting an average crystallite size ranging from 9 - 18 nm were produced. SEM studies show broken spherical nanoparticles with a characteristic hollow structure for all compositions. Their study found that partial replacement of Co by Ni in CoFe_2O_4 enhances the electrochemical activity toward ORR. In particular, the composition $\text{Ni}_{0.5}\text{Co}_{0.5}\text{Fe}_2\text{O}_4$ demonstrated more onset positive potential of -0.15 V compared to -0.18, -0.17, and -0.20 V of CoFe_2O_4 , $\text{Ni}_{0.25}\text{Co}_{0.75}\text{Fe}_2\text{O}_4$, and $\text{Ni}_{0.75}\text{Co}_{0.25}\text{Fe}_2\text{O}_4$, respectively. It also exhibited a diffusion-limited current density of -6.64 mA/cm^2 , comparably higher than other compositions. On the other hand, $\text{Ni}_{0.75}\text{Co}_{0.25}\text{Fe}_2\text{O}_4$ solid solutions exhibited excellent catalytic activity for OER, showing the highest current density of 36.0 mA/cm^2 , compared to

33.0, 29.2 and 30.7 mA/cm² of CoFe₂O₄, Ni_{0.25}Co_{0.75}Fe₂O₄, and Ni_{0.5}Co_{0.5}Fe₂O₄, correspondingly.

Maruthapandian *et al.* employed a sol-gel combustion method to synthesize nanoscale Co_xNi_{1-x}Fe₂O₄ (0 < x < 1) solid solution from their corresponding metal nitrate precursors and studied their electrochemical performance toward OER.²¹⁸ The nanoparticles exhibited crystallite size of 57.3, 57.3, 67.3, 72.9 and 69.4 nm for Co composition of x = 0, 0.25, 0.5, 0.75 and 1, correspondingly. The electrochemical measurements demonstrated that the pristine NiFe₂O₄ has superior catalytic activity manifested by a lower overpotential of 381 mV, surpassing Co_xNi_{1-x}Fe₂O₄ solid solutions, which exhibited overpotentials in the range of 450-470 mV at 10 mA/cm² in alkaline solution. The inclusion of Co in the crystal lattices of nickel ferrite was observed to inhibit the catalytic activity.

Our group recently synthesized homogeneous Ni_{1-x}Co_xFe₂O₄ (0 ≤ x ≤ 1) solid solution nanoparticles by solventless thermolysis of nickel, cobalt and iron acetylacetonates at 450 °C.²¹⁹ The p-XRD measurements revealed the formation of a series of monophasic cubic nanoferrites with space group *Fd3m* (Fig. 1.11(a)). The lattice parameters and band gap were observed to increase in a linear fashion with the increasing amount of cobalt, complying with Vegard's law (Fig. 1.11(b)). TEM images showed cubic and octahedron-shaped nanoparticles exhibiting an average size around 14-23.2 nm. Evaluation of the synthesized nanoparticles for supercapacitance showed that the spinel Ni_{0.4}Co_{0.6}Fe₂O₄ electrode exhibited a longer charge-discharge time (Fig. 1.12 (a)), suggesting excellent charge storage capacity compared to other samples. For efficient HER, the Ni_{0.6}Co_{0.4}Fe₂O₄ and CoFe₂O₄ electrodes demonstrated low overpotential of 168 and 169 mV (Fig. 1.12 (b)), correspondingly along with high stability, which suggests better catalytic activity. Likewise, Ni_{0.8}Co_{0.2}Fe₂O₄ showed a lower overpotential of 320 mV (Fig. 1.12(c)), indicative of improved OER activity.

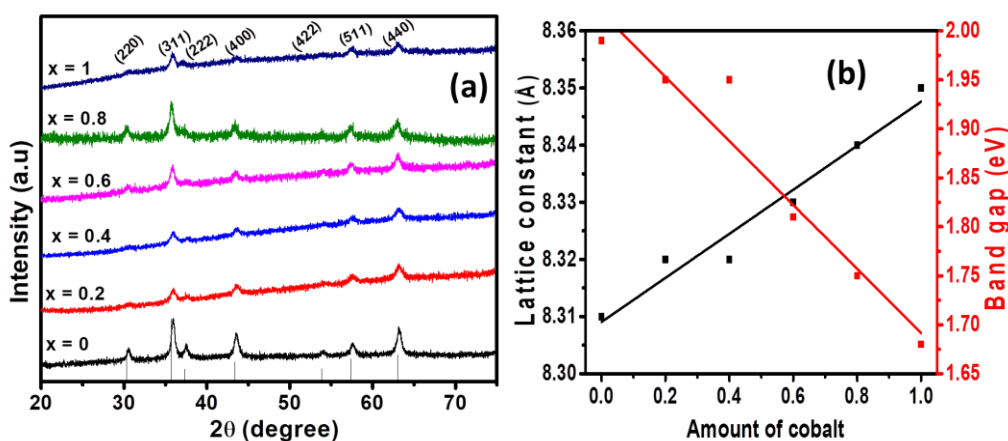


Fig. 1.11 (a) p-XRD diffractogram of $\text{Ni}_{1-x}\text{Co}_x\text{Fe}_2\text{O}_4$ ($0 \leq x \leq 1$) series, (b) variation of lattice constant (left y-axis) and the optical band gap (right y-axis) of $\text{Ni}_{1-x}\text{Co}_x\text{Fe}_2\text{O}_4$ ($0 \leq x \leq 1$) solid solutions (Reproduced from ref. 219).

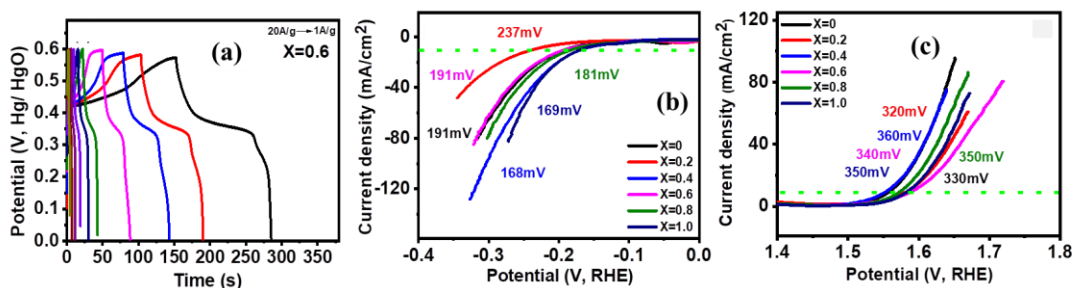


Fig.1.12 (a).GCD graphs of the $x = 0.6$ electrode for various current densities ($1\text{--}20 \text{ Ag}^{-1}$) (b) HER polarization curves, (c) OER polarization curves, for $\text{Ni}_{1-x}\text{Co}_x\text{Fe}_2\text{O}_4$ ($0 \leq x \leq 1$) (Reproduced from ref. 219).

The synthesis of spinel $\text{NiFe}_{2-x}\text{Cr}_x\text{O}_4$ ($0 \leq x \leq 1$) solid solutions have been achieved via the precipitation method, and their physicochemical and electrochemical properties evaluated.²²⁰ The $\text{NiFe}_{2-x}\text{Cr}_x\text{O}_4$ solid solutions were synthesized following hydroxide precipitation at 70°C , monitoring the solution pH at 11 and continuous O_2 bubbling. The SO_4^{2-} -free precipitate was then dried for 24 h at 100°C and subsequently annealed at 400°C for 24 h. Nickel sulfate, chromium chloride, and ferrous ammonium sulfate were used as precursors. p-XRD analysis showed that $\text{NiFe}_{2-x}\text{Cr}_x\text{O}_4$ nanoparticles crystallize in a cubic crystal and their crystal size was found in the range of 15-21 nm. The results showed the increased electrocatalytic activity towards OER upon Cr substitution in spinel matrix from $x = 0.2$ to 1.0. For example, for chromium composition $x = 0.8$ and 1, the overpotentials of 275, and 284 mV, respectively, were needed to yield a current density of 1.0 mA/cm^2 , while the base oxide demanded significantly higher overpotentials of 337 and 371 mV.

Kambale *et al.* synthesized a series of $\text{Ni}_{1-x}\text{Co}_x\text{Fe}_2\text{O}_4$ ($0.2 \leq x \leq 0.8$) solid solution via a standard ceramic route and examined their electric and magnetic properties.²²¹ The method involved milling and calcining a mixture of NiCO_3 , CoCO_3 and Fe_2O_3 at 1000°C and finally sintering the product at 1200°C . The method afforded highly crystalline monophasic ferrites crystallizing in the cubic structure. Measurements of resistivity at the ambient temperature indicated the reduction in resistivity with the increasing amount of cobalt in the spinel system. The studies further demonstrated that all the prepared polycrystalline solid solutions

over the entire range of cobalt concentration were characterized by semiconducting properties.

The chemical precipitation route was also used to prepare $\text{Zn}_x\text{Co}_{1-x}\text{Fe}_2\text{O}_4$ ($0 \leq x \leq 1$) ferrites by utilizing metal nitrate precursors.²²² The resulting spherical crystalline nanoparticles exhibited a cubic spinel structure and small crystallite size in the range of 6 -12 nm. Investigation of the magnetic behaviour of all ferrite samples at ambient temperature showed saturation magnetization ranging from 0.387 - 2.065, coercivity (60 - 1834 Oe), and remanence magnetization (0.057 - 1.282 emu/g). From the nature of the hysteresis loop, the solid solutions were considered to be soft magnetic materials.

Singh *et al.* prepared nanospinel $\text{CuFe}_{2-x}\text{Cr}_x\text{O}_4$ ($0 \leq x \leq 1$) solid solutions and investigated their electrocatalytic activity towards OER. Hydroxide-assisted co-precipitation of copper sulfate, chromium chloride and ferrous ammonium sulfate at 70 °C for 24 h yielded cubic nanospinels with crystallite size in the range of 13-19 nm.²²³ The results indicated that partial replacement of Fe by Cr in the CuFe_2O_4 spinel lattice enhanced both the geometrical and electronic characteristics of the material, contributing significantly to the high OER activity of the spinel oxide. It was observed that the inclusion of Cr in the crystal lattice of CuFe_2O_4 significantly increased the electrocatalytic activity of the oxide materials enabling to produce a high current density of 48.7 mA/cm² for $\text{CuFe}_{1.2}\text{Cr}_{0.8}\text{O}_4$ compared to 3.3 mA/cm² of the base CuFe_2O_4 .

Co-precipitation of stoichiometric ratios of cobalt sulfate, nickel sulfate, ferrous sulfate and ferric chloride has been reportedly employed by Archana *et al.* to yield $\text{Co}_x\text{Ni}_{(0.4-x)}\text{Fe}_{0.6}\text{Fe}_2\text{O}_4$ ($x = 0, 0.1, 0.2, 0.3, \text{ and } 0.4$) nanoparticles.²²⁴ The p-XRD pattern of the spinel ferrites at different metal compositions confirmed the formation of monophasic, pure and co-substituted ferrites, and the size of the particle was around 5 - 8 nm. Electrochemical investigation of the synthesized nanoparticles revealed that un-substituted $\text{Fe}^{\text{II}}\text{Fe}_2^{\text{III}}\text{O}_4$ material showed a high overpotential of about 450 mV at 10 mA/cm² compared to the substituted $\text{Co}_x\text{Ni}_{(0.4-x)}\text{Fe}_{0.6}\text{Fe}_2^{\text{III}}\text{O}_4$ ($x = 0.1, 0.2, 0.3, \text{ and } 0.4$). In particular, $\text{Co}_{0.2}\text{Ni}_{0.2}\text{Fe}_{0.6}\text{Fe}_2^{\text{III}}\text{O}_4$ demonstrated a low overpotential of 270 mV and 275 mV at 10 mA/cm², corresponding to substantially higher OER and HER activities, respectively. It was presumed that the monophasic $\text{Co}_x\text{Ni}_{(0.4-x)}\text{Fe}_{0.6}\text{Fe}_2^{\text{III}}\text{O}_4$ displayed superior HER and OER due to the synergistic influence of Co, Ni and Fe in the oxide structure.

Spinel $\text{Co}_x\text{Mg}_{1-x}\text{Fe}_2\text{O}_4$ ($0 \leq x \leq 1$) nanoferrites have been prepared from metal nitrates by using the sol-gel method.²²⁵ A cubic spinel system was authenticated from structural analysis by Raman spectroscopy, XRD, and the arrangement of cations and inversion degree

hinged on the composition, x . The crystallite size was observed to increase with respect to composition, from 34 nm for MgFe_2O_4 to 48 nm for CoFe_2O_4 . The SEM images showed multigrain coalesced nanoparticles in which the extent of agglomeration decreases with the substitution of the highly magnetic Co^{2+} with diamagnetic Mg^{2+} in the ferrite system. It was found that the magnitude of the maximal and remanent magnetization, and coercive field, increased with respect to the amount of diamagnetic Mg^{2+} replacing magnetic Co^{2+} ions. The coercive field augmented in the range of 74 - 1000 Oe corresponding to a transition between pure MgFe_2O_4 and CoFe_2O_4 , whereas magnetization in the field 10 kOe increased in the range of 27.4 - 75.7 emu/g. Analysis of optical property from UV/Vis DRS studies displayed a strong reliance of the band gap on the amount of cation and the size of crystallites, exhibiting a decreasing trend in the range of 2.09 - 1.42 eV for a transition between MgFe_2O_4 and CoFe_2O_4 .

Peng-peng *et al.* employed the sintering technique to prepare $\text{Ni}_x\text{Zn}_{1-x}\text{Fe}_2\text{O}_4$ ($0.2 \leq x \leq 0.8$) and examined their magnetic property.²²⁶ Increasing the amount of zinc led to the initial increase in saturation magnetization, which was then observed to decrease, reaching a minimum value of 43.8 Am/kg for $\text{Ni}_x\text{Zn}_{1-x}\text{Fe}_2\text{O}_4$ ($x = 0.6$). The residual magnetic flux density of $\text{Ni}_x\text{Zn}_{1-x}\text{Fe}_2\text{O}_4$ started to increase when zinc was introduced and then decreased, reaching a minimum magnitude of 0.31 T for $\text{Ni}_x\text{Zn}_{1-x}\text{Fe}_2\text{O}_4$ ($x = 0.2$), while the coercive force increased reaching 3.9 kA/m for $x = 0.6$.

An expedient and straightforward solvothermal method was adopted to synthesize Fe-doped $\text{Co}_3\text{V}_2\text{O}_8$, yielding a set of $\text{Co}_{3(1-x)}\text{Fe}_{3x}\text{V}_2\text{O}_8$ by varying the mole ratio of Fe in the system.²²⁷ Thermolysis of the mixture of $\text{FeCl}_3 \cdot 6\text{H}_2\text{O}$ and $\text{Co}(\text{CH}_3\text{COO})_2 \cdot 4\text{H}_2\text{O}$ in the presence of DMF and CH_3OH , sodium metavanadate and water at 180 °C for 24 h, followed by post-synthetic procedures afforded $\text{Co}_{3(1-x)}\text{Fe}_{3x}\text{V}_2\text{O}_8$ nanoparticles crystalizing in the orthorhombic structure. SEM analysis showed relatively uniform nanoparticles at low iron content, while the irregular blocky structure was observed at high iron content. The size of $\text{Co}_{1.5}\text{Fe}_{1.5}\text{V}_2\text{O}_8$ nanoparticle was obtained to be ~5 nm from a representative TEM image. HRTEM images showed lattice fringes with the spacing of 0.208 and 0.251 nm, which were assigned to (042) and (122) crystal planes, respectively. The electrochemical activity of $\text{Co}_{3(1-x)}\text{Fe}_{3x}\text{V}_2\text{O}_8$ towards OER was found to depend heavily on the amount of iron in the solid solution system, and among all, $\text{Co}_{1.5}\text{Fe}_{1.5}\text{V}_2\text{O}_8$ displayed a relatively low overpotential of 290 mV at 10 mA/cm². Additionally, the $\text{Co}_{1.5}\text{Fe}_{1.5}\text{V}_2\text{O}_8$ catalyst demonstrated strong durability for 10 h during the long-term stability test.

Solid solution of $\text{Ce}_{1-x}\text{Gd}_{x-y}\text{Y}_y\text{O}_{2-0.5x}$ with composition $x = 0.15$ and 0.2 , where $0 \leq y \leq x$, have been reportedly synthesized via glycine-nitrate strategy by employing metal nitrates as precursors.²²⁸ The p-XRD measurements indicated that the resulting ceria-based solid solutions exhibited fluorite-type structure with particle size ranging from 10 - 20 nm as estimated by TEM analysis. Compared with singly doped ceria, the doping of two cations resulted in significant improvement of the conductivity with the co-doped ceria exhibiting significantly higher ionic conductivities ranging from 673 - 973 K. Remarkably, the ionic conductivity of $\text{Ce}_{0.8}\text{Gd}_{0.05}\text{Y}_{0.15}\text{O}_{1.9}$ at 773 K increased threefold (0.013 S/cm) surpassing that of $\text{Ce}_{0.8}\text{Gd}_{0.2}\text{O}_{1.9}$. This indicated that $\text{Ce}_{1-x}\text{Gd}_{x-y}\text{Y}_y\text{O}_{2-0.5x}$ could serve as perfect electrolyte materials of intermediate temperature solid oxide fuel cells.

A novel solid solution of $\text{Cd}_x\text{Zn}_{2-x}\text{GeO}_4$ ($0 \leq x \leq 2$) have been synthesized via hydrothermal technique and its structural, morphological and photocatalytic activity was studied. The resulting product matched perfectly to the rhombohedral structure, as confirmed by p-XRD analysis. The solid solution exhibited a mixture of nanorods and nanosheets morphologies. Compared with pristine Zn_2GeO_4 , the $\text{Cd}_x\text{Zn}_{2-x}\text{GeO}_4$ solid solutions exhibited a narrower band gap and responded to a broad spectrum of sunlight. In addition, the hydrogen evolution activities of $\text{Cd}_x\text{Zn}_{2-x}\text{GeO}_4$ solid solutions were significantly higher than that of the pure Zn_2GeO_4 . Specifically, the highest H_2 production rate (15.00 mmol/gh) was obtained over the $\text{Cd}_{1.0}\text{Zn}_{1.0}\text{GeO}_4$, which was about 24.2 times higher than that of pure Zn_2GeO_4 (0.62 mmol/gh).²²⁹

A pulsed laser deposition approach has been utilized to deposit $\text{BaSn}_{1-x}\text{Ti}_x\text{O}_3$ ($0 \leq x \leq 1$) epitaxial films on $\text{LaAlO}_3(001)$ substrates. Prior to deposition, $\text{BaSn}_{1-x}\text{Ti}_x\text{O}_3$ targets were synthesized via a high-temperature pyrolysis of a mixture of pure BaCO_3 , SnO_2 , and TiO_2 precursors. High resolution XRD analysis showed a linear decrease in the film lattice constants with respect to Ti content, following Vegard's law. Assessment of optical property indicated that all films exhibit optical transmittance of >70% in the visible and infrared wavelength range. Remarkably, the bandgap nonlinearity of $\text{BaSn}_{1-x}\text{Ti}_x\text{O}_3$ films was noticed, and the film with Ti content of $x = 0.25$ exhibited the largest bandgap value of 4.04 eV.²³⁰

To study the change of magnetic behavior from ferromagnetic LaCo_2P_2 to paramagnetic LaFe_2P_2 , Kovnir *et al.*²³¹ synthesized a series of $\text{LaFe}_x\text{Co}_{2-x}\text{P}_2$ ($0 \leq x \leq 1$) solid solutions by adopting the tin flux synthetic method described by Reehuis and Jeitschko.²³² Stoichiometric amounts of finely dispersed cobalt, lanthanum, red phosphorus, iron powders and tin shots were mixed in 10 mm silica tubes enclosed under vacuum. The precursor mixture was heated at 1155 K for 10 days, allowed to cool to 875 K at 10 K/min. To remove

tin flux, the samples were soaked in dil. HCl, leaving behind single crystals which were selected from the final product for analysis. Powder XRD measurements confirmed the formation of phase pure $\text{LaFe}_x\text{Co}_{2-x}\text{P}_2$ solid solutions exhibiting a ThCr_2Si_2 type structure. The increase in the unit cell volume with respect to the amount of Fe, ratifies the bulk replacement of Fe for Co. Magnetic studies confirmed the presence of paramagnetic behavior in both $\text{LaFe}_{0.3}\text{Co}_{1.7}\text{P}_2$ and $\text{LaFe}_{0.5}\text{Co}_{1.5}\text{P}_2$ samples.

Jia *et al.* reported the fabrication, magnetic and structural characteristics of $\text{Ca}(\text{Fe}_{1-x}\text{Co}_x)_2\text{P}_2$ ($0 \leq x \leq 1$) and $\text{Ca}(\text{Ni}_{1-x}\text{Co}_x)_2\text{P}_2$ ($0 \leq x \leq 1$) solid solutions.²³³ The synthesis of these polycrystalline materials was carried out using elemental P, red, Ca, Fe, Co, and Ni powder. The process started by preparing FeP, CoP, and Ni_5P_4 according to the protocol described by McQueen *et al.*²³⁴ Then, CaFe_2P_2 and CaCo_2P_2 were prepared by mixing stoichiometric quantities of Ca, FeP, CoP, and P powders. On the other hand, the parent CaNi_2P_2 was synthesized from a mixture of stoichiometric amounts of Ca, Ni_5P_4 and P powders. The next step involved placing sample mixtures in alumina crucibles which were then introduced in silica tubes and annealed at 900 °C for 1 h. The resulting products were ground, mixed, pressed into pellets and sintered at 1000 °C to obtain $\text{Ca}(\text{Fe}_{1-x}\text{Co}_x)_2\text{P}_2$ ($0 \leq x \leq 1$) and $\text{Ca}(\text{Ni}_{1-x}\text{Co}_x)_2\text{P}_2$ ($0 \leq x \leq 1$). Magnetic results shows that both sets of solid solutions evolve from a Pauli paramagnetic CaFe_2P_2 and CaNi_2P_2 to antiferromagnetic CaCo_2P_2 as a function of Co content, through changes in the band structures.

The synthesis of $\text{TiCo}_{2-x}\text{Ni}_x\text{Se}_2$ solid solutions over entire range of compositions i.e., $0 \leq x \leq 2$ has also been described.²³⁵ p-XRD revealed that the as-prepared materials exist in ThCr_2Si_2 type tetragonal crystal structure. The synthesized materials were found to possess a high metallic character ($\delta \sim 10^{-4}$ - 10^{-5} Ω-cm). While the parent TiCo_2Se_2 shows Curie-Weiss characteristics from ~100-300 K and behaves as antiferromagnetic material at $T_N = 97$ K, the TiNi_2Se_2 counterpart is paramagnetic. Also, the solid solutions $\text{TiCo}_{2-x}\text{Ni}_x\text{Se}_2$ with composition ($0.25 \leq x \leq 1.5$) show antiferromagnetic behavior. The Neel temperature, T_N as a function of nickel composition, is maximum at $x = 0.5$, suggesting that incorporation of Ni at $x \leq 0.5$ improves antiferromagnetic interactions in these alloys.

Nanostructured alloys of $(\text{ZnSe})_x(\text{CuInSe}_2)_{1-x}$ and $\text{CuInSe}_x\text{S}_{2-x}$ have been reportedly prepared over the entire composition range using a hot injection approach. During the synthesis, CuCl, ZnCl_2 , $\text{InCl}_3 \cdot 4\text{H}_2\text{O}$, S powder, and Se powder were used as precursors, while oleylamine and oleic acid were respectively employed as dispersing solvent and capping agents. The p-XRD data showed that the zinc blende structure was conserved throughout the composition range. The alloyed nanostructures displayed narrow size distribution. The

average size of $(\text{ZnSe})_{0.5}(\text{CuInSe}_2)_{0.5}$ and $\text{CuInSe}_{1.0}\text{S}_{1.0}$ estimated from TEM was 17.1 and 15.0 nm, respectively. Modulation of the materials' band gaps was achieved in the range of 2.82 - 0.96 eV and 1.43 - 0.98 eV, for $(\text{ZnSe})_x(\text{CuInSe}_2)_{1-x}$ and $\text{CuInSe}_x\text{S}_{2-x}$, respectively. This broad band gap tunability in these alloyed nanocrystals renders them a high potential for photovoltaic and photocatalytic applications.²³⁶

$\text{CdCr}_{2-x}\text{In}_x\text{Se}_4$ and $\text{Cd}_{1-y}\text{In}_y\text{Cr}_2\text{Se}_4$ solid solutions were synthesized by Shabunina *et al.* using pure CdSe, Cr powder, OSCh 22-4 Se and In_2Se_3 precursors, and their composition ranges were explored. The solid solutions was prepared by pyrolysis of their respective precursors at 600°C in quartz tubes set at 10^{-2} Pa for one week, followed by re-grinding and re-firing the samples at 550 - 600°C for equilibration. P-XRD studies showed that the increase in the mole ratio of In in the solid solution system augmented the lattice constant while the Curie temperature decreased. Analysis of magnetic property revealed the existence of paramagnetic-ferromagnetic-spin-glass phase transition in both solid solution systems.²³⁷

1.2.5.3.2 Quaternary anionic solid solutions

Zhang and co-workers have declared large-scale fabrication of $\text{CuSb}(\text{S}_x\text{Se}_{1-x})_2$ nanosheets in a one-pot colloidal route.²³⁸ The synthesis was performed by reacting stoichiometric amounts of $\text{Cu}(\text{NO}_3)_2 \cdot 3\text{H}_2\text{O}$, SbCl_3 and SeO_2 precursors in a mixture of oleylamine and dodecanethiol at 200 °C. It was observed that when the temperature was increased, more S from the dodecanethiol was incorporated, yielding $\text{CuSb}(\text{S}_x\text{Se}_{1-x})_2$ nanosheets with high sulfur content. Morphological analysis by SEM indicated rectangle-shaped nanosheets. The resultant $\text{CuSb}(\text{S}_x\text{Se}_{1-x})_2$ solid solutions displayed composition-tunable band gaps in the range of 0.9 - 1.1 eV.

A facile hot-injection route towards the preparation of $\text{Cu}_2\text{Ge}(\text{S}_{3-x}\text{Se}_x)$ ($0 \leq x \leq 3$) nanocrystals was described by Yang *et al.*²³⁹ The preparation of $\text{Cu}_2\text{Ge}(\text{S}_{3-x}\text{Se}_x)$ was performed by injecting GeCl_4 in a solution of $\text{Cu}(\text{acac})_2$ in OLA at 125 °C under inert conditions. This was followed by injection a solution mixture of elemental S and Se pre-dissolved in OLA, at 160 °C, followed by heating the mixture to 280 °C for 2 h to produce $\text{Cu}_2\text{Ge}(\text{S}_{3-x}\text{Se}_x)$ nanocrystals. TEM results showed a narrow size distribution of 11 – 19 nm of the $\text{Cu}_2\text{Ge}(\text{S}_{3-x}\text{Se}_x)$ ($0 \leq x \leq 3$) solid solutions, and their size enlarged with increasing the amount of Se to some extent. The increase in Se contents in the $\text{Cu}_2\text{Ge}(\text{S}_{3-x}\text{Se}_x)$ ($0 \leq x \leq 3$) system was also found to cause a monotonous reduction of the band gaps.

1.2.5.3.3 Pseudobinary quaternary solid solutions

As mentioned earlier in this work, sometimes the formation of quaternary solid solutions may involve concurrent substitution of both cation and anion, pseudobinary solid solutions. For example, to obtain materials with enhanced insulating behavior, Ren *et al.* fabricated $\text{Bi}_{2-x}\text{Sb}_x\text{Te}_{3-y}\text{Se}_y$ solid solutions and studied the transport properties for a wide composition range and temperature. The synthesis of single crystals of $\text{Bi}_{2-x}\text{Sb}_x\text{Te}_{3-y}\text{Se}_y$ was achieved by melting stoichiometric quantities of pure Bi, Sb, Te and Se elements in closed quartz tubes at 850 °C for 48 h with occasional shaking to ensure uniformity of the melt. The melts were then cooled gradually to 550 °C and consequently annealed at the same temperature for 96 h. The p-XRD diffractogram of all the samples were similar and could be indexed with the rhombohedral structure, indicating that the solid solutions preserved the same crystal structure as their parent materials of Bi_2Te_3 , Bi_2Se_3 , and Sb_2Te_3 . Except for $\text{Bi}_{0.75}\text{Sb}_{1.25}\text{Te}_{0.5}\text{Se}_{2.5}$, all the $\text{Bi}_{2-x}\text{Sb}_x\text{Te}_{3-y}\text{Se}_y$ samples at the optimized mole ratios displayed large resistivity values beyond 1 Ωcm at low temperatures along with an activated behavior at elevated temperatures.²⁴⁰ Similar $\text{Bi}_{2-x}\text{Sb}_x\text{Te}_{3-y}\text{Se}_y$ system with a highly insulating bulk and tunable Dirac carrier was reported by Arakane *et al.*²⁴¹

Composition-tunable quantum dots of $\text{Zn}_x\text{Cd}_{1-x}\text{S}_y\text{Se}_{1-y}$ ($0 \leq x \leq 1$, $0 \leq y \leq 1$) exhibiting size tunability in the range of 4.0 - 10.0 nm have been reportedly prepared in paraffin liquid by Deng *et al.* via a colloidal route.²⁴² p-XRD results showed that all the $\text{Zn}_x\text{Cd}_{1-x}\text{S}_y\text{Se}_{1-y}$ alloyed compounds over the whole composition corresponded to a face-centered cubic phase. The gradual shifting of the diffraction peak positions toward smaller values was noted, inferring an increase in lattice parameters with steady replacement of Zn and S with the slightly large Cd and Se, respectively, and was found in compliance with Vegard's law. The band gap of the synthesized quantum solid solutions could also be tailored by adjusting either the material's composition or particle size.

Apart from the simultaneous substitution of both anions and cations in the host material, pseudobinary solid solutions can also be formed via alloying of two different binary compounds with distinct cations and anions. Studies have been conducted on the solid solubilities and physicochemical properties of a large number of pseudobinary systems. For example, investigations on the solid solubility and bandgap energy of several (III-V)-(II-VI) systems revealed the quaternary alloy systems of GaAs-ZnSe, GaP-ZnSe, and GaP-ZnS exhibited a wide spectrum of solid solubilities, enabling the formation of solid solutions across the whole system. For the GaAs-ZnSe system, the lattice parameters varied sublinearly

with composition, whereas an approximately linear variation was found in GaP-ZnSe and GaP-ZnS systems. Moreover, a sublinear reliance of optical bandgap on composition was revealed for the GaAs-ZnSe system. Likewise, the GaP-ZnSe and GaP-ZnS systems showed an anomalously sublinear relationship between composition and band gap, with the large variation occurring near the II-VI end component.²⁴³

Likewise, a pseudobinary solid solution of $(\text{GaP})_{1-x}(\text{ZnS})_x$, $(\text{ZnS})_{1-x}(\text{GaP})_x$ and $(\text{GaN})_{1-x}(\text{ZnO})_x$, were synthesized by Liu *et al.* by employing a vapor-liquid-solid process in the presence of Au nanoparticles as catalysts. The resulting nanowires exhibited a single phase with all four elements merged mutually and entirely in the studied composition range. With the aid of HRTEM and EDS analyses, it was revealed that the structural homogeneity and a lattice match between the two parent binary compounds were crucial in obtaining quaternary solid solution nanostructures. Studies of electrical transport on both GaP and $(\text{GaP})_{1-x}(\text{ZnS})_x$ systems showed that a small invasion of ZnS in the GaP host could result in a rapid increase in resistance, causing a transition between semiconductor and insulator.⁸³ Table 1.4 presents a list of quaternary $(\text{III-V})_{1-x}(\text{II-VI})_x$ solid solutions reported in the literature.

Table 1.4. Pseudobinary quaternary solid solutions of $(\text{III-V})_{1-x}(\text{II-VI})_x$ systems

Pseudobinary system	(III-V) compound	(II-VI) compound	Solubility (x)	Reference
$(\text{AlP})_{1-x}(\text{ZnS})_x$	AlP	ZnS	$x < 0.01$	244
$(\text{AlSb})_{1-x}(\text{CdTe})_x$	AlSb	CdTe	$0 \leq x \leq 1$	245
$(\text{AlSb})_{1-x}(\text{ZnTe})_x$	AlSb	ZnTe	$x < 0.18$	244
$(\text{GaN})_{1-x}(\text{ZnO})_x$	GaN	ZnO	$0.05 < x < 0.22$	246, 247
$(\text{GaP})_{1-x}(\text{ZnS})_x$	GaP	ZnS	$0 \leq x \leq 1$	83, 243, 248, 249
$(\text{GaP})_{1-x}(\text{ZnSe})_x$	GaP	ZnSe	$0 \leq x \leq 1$	243, 249-251
$(\text{GaAs})_{1-x}(\text{ZnS})_x$	GaAs	ZnS	$0 < x < 1$	245
$(\text{GaAs})_{1-x}(\text{ZnSe})_x$	GaAs	ZnSe	$0 \leq x \leq 1$	243, 252

$(\text{GaAs})_{1-x}(\text{ZnTe})_x$	GaAs	ZnTe	$x \leq 0.9$	245
$(\text{InP})_{1-x}(\text{CdS})_x$	InP	CdS	$0 < x < 1$	245, 253
$(\text{InP})_{1-x}(\text{ZnS})_x$	InP	ZnS	$x < 0.1, x > 0.94$	253
$(\text{InP})_{1-x}(\text{ZnSe})_x$	InP	ZnSe	$x < 0.06, x > 0.94$	253
$(\text{InAs})_{1-x}(\text{CdTe})_x$	InAs	CdTe	$x < 0.33, x > 0.7$	245, 253
$(\text{InAs})_{1-x}(\text{HgTe})_x$	InAs	HgTe	$0 \leq x < 1$	253
$(\text{InSb})_{1-x}(\text{CdTe})_x$	InSb	CdTe	$x < 0.05$	245, 253

Numerous pseudobinary solid solutions of rare-earth oxysulfides have been documented in the literature as appropriate phosphor materials. The oxysulfide phosphors are composed of a host compound (e.g., $\text{Y}_2\text{O}_2\text{S}$, $\text{La}_2\text{O}_2\text{S}$) and an activator (e.g., $\text{Eu}_2\text{O}_2\text{S}$, $\text{Tb}_2\text{O}_2\text{S}$) which together form a solid solution. Motivated by a desire to study new phosphors and unlock the subsolidus phase relations in the isostructural rare-earth oxysulfide series, Leskela and Niinisto investigated the solid solubility on the pseudobinary systems $\text{Ln}_2\text{O}_2\text{S}$ - $\text{La}_2\text{O}_2\text{S}$ (where $\text{Ln} = \text{Nd}, \text{Sm}, \text{Eu}, \text{Gd}, \text{Dy}, \text{Yb}, \text{Lu}, \text{and Y}$). From the results, only $\text{Nd}_2\text{O}_2\text{S}$ - $\text{La}_2\text{O}_2\text{S}$ and $\text{Sm}_2\text{O}_2\text{S}$ - $\text{La}_2\text{O}_2\text{S}$ showed complete solid solubility, while the remaining systems exhibited two phases. The solid solubility in the isostructural oxysulfide series could be explained by comparable ionic radii of the two rare-earth elements.²⁵⁴

The successful formation of diverse solid solutions from different groups and various systems offers compelling evidence for the pervasiveness of the solid solution nanosystems that are made of quaternary multicomponent. Therefore a vast array of multicomponent solid solution nanostructures are expected in diverse groups and systems as long as they have similar crystal structures and comparable lattice parameters. Basically, a set of requirements must be fulfilled to afford the formation of such complex nanostructures from two or more binary systems whose constituent elements belong to different groups:

(1) Structure compatibility: Crystallographically, in order to form a stable compound, the internal strains and higher long-range atomic ordering must be as few as possible. The formation of a single crystal requires the two components in a quaternary system to exhibit similar crystal structures and the same space group. Specifically, the lattice parameters of the two components should be fairly close to each other and their mismatch should be below

some threshold value. Consequently, the partial replacement of one component by another (substitution of cations/anions in the host material by the respective doped minor components) at the predefined sites becomes possible. It should be noted that such substitution is done without exceeding the solubility limit in favor of structural stability and avoiding phase separation.²⁵⁵ So far, it has been pointed out that sequential composition tuning has been a challenge in both bulk and nanostructured pseudobinary systems.²⁴⁹ The lower solubility in nanoscale quaternary compounds can be attributed to the self-generated processes in a confined space. It can also be caused by possible mismatches in lattice constants for each specific pseudobinary system. Nevertheless, it is also expected that the composition ratio in the quaternary nanosystems can be finely adjusted under some critical conditions.²⁴³

(2) Chemical similarity: As in the case of elemental doping, the solubility of a dopant/foreign component in the host matrix depends not only on the lattice matching but also the chemical similarity.²⁵⁶ The anions or cations of the host and foreign components are expected to be reasonably close and must display identical physical and chemical behavior to account for their complete solubility. As a result, the character of the new covalent bonds formed in a quaternary system is close to the character of those in the starting binary components. If the difference in their chemical behavior is too huge, the process of forming quaternary compounds becomes energetically costly and consequently implausible. Moreover, when more chemical elements are involved in the process, it results to the formation of more complex and new chemical bonds. This makes it challenging to obtain a phase-pure product and increases the chance of phase separation. In contrast to quaternary solid solution nanosystems, the preparation of both binary and ternary solid solutions is more favorable and has been reportedly achieved via different methods, as discussed in previous sections of this work.

(3) Proper growth conditions. A wide array of reaction conditions such as substrate type, growth temperature, nature of the catalyst, as well as pressure and flow rate of the gas may strongly determine the morphology, phase purity, size, and growth direction of the nanostructure. Thus, the synthesis of particular nanostructures exhibiting versatile properties and functions can be achieved via precise control of these variables during the reaction process. As an example, the preparation of quaternary $(\text{GaP})_{1-x}(\text{ZnS})_x$ nanowires was achieved on Au-coated Si substrate by employing a self-assembled protocol, during which the GaP substrate and elevated growth temperature were essential for in situ lattice penetration.⁸³

1.2.6 Fabrication approaches of crystalline solid solutions

Principally, the formation of crystalline solid solutions can simply be realized on the basis of the crystal structure and lattice parameter matching between the chemical components involved. Nevertheless, their nucleation and stoichiometry control, especially at nano regime, is quite difficult and challenging. In particular, the dynamics of nanoparticles growth and crystallization process varies vastly from one component to another, especially in multielement compounds.^{83, 257} Therefore, to get rid of probable phase separation and obtain uniform solid solution nanoparticles, a well-designed synthetic protocol along with accurate control of the reaction conditions is required. Virtually all strategies encompassing physical and chemical transformation can be employed to synthesize solid solutions. They are grouped into three general sets, namely, solution phase, solid-phase, and vapor-phase synthetic approaches. The solid-phase techniques include mechanochemical processing of precursors via traditional ball-milling (high-temperature solid phase) and thermochemical or thermal decomposition methods. On the other hand, the solution-based strategies comprise sol-gel, coprecipitation, heat-up, hot-injection, hydrothermal/ solvothermal, microwave-assisted heating, microemulsion methods, etc. Moreover, the vapor-phase transport methods include both chemical and physical vapour deposition techniques. In some cases, a modified technique or a blend of several reaction protocols is employed to obtain nanoparticulate solid-solutions having unique properties.³⁹ Although enormous efforts have been devoted towards developing robust and versatile synthetic protocols for the rational fabrication of a diverse range of nanoscale solid solutions, in this literature review only the solventless thermolysis approach will be briefly discussed.

1.2.6.1 Solventless thermolysis (Melt) method

Generally, solvent-free approaches are grouped into mechanochemical and thermochemical methods. Mechanochemical methods (e.g., ball milling and mortar-pestle grinding) are characterized by chemical changes caused by mechanical forces such as shear, compression, and friction. The thermochemical technique, on the other hand, involves thermolysis or decomposition of precursor(s) using microwave or traditional heating.²⁵⁸ In recent years, the solventless thermolysis or melt method has gained substantial interest.^{88, 89, 259-265} This method has been reportedly used to fabricate bulk and nanoscopic materials. In the solventless thermolysis method, fabrication of materials is achieved via thermal decomposition of organometallic precursors in the absence of any solvent. Thermolysis of

precursors takes place in a furnace either under oxygen or inert condition, subject to the nature of the material being synthesized. The reaction starts by melting the reactants to form reactive precursor melts, which then undergo thermolysis to yield the corresponding compound materials. A great deal of research conducted over the years has aided the fabrication of a wide array of metallic and compound (metal oxides, sulfides, tellurides) materials displaying diverse properties. The fascinating feature of the solventless thermolysis method is that the synthesis of materials is carried out in the absence of surfactants or capping agents because the stabilization of the resulting particles is done by the ligands produced in the course of precursor decomposition.^{259, 266, 267} Therefore, the approach is often referred to as the self-capping method. The level of surface stabilization and hence the size and/or morphology of the particles are largely influenced by the type of the precursor, mostly the length of the alkyl chain in organometallic precursors.²⁶³ There are, nevertheless, a few studies in which the fabrication of the nanomaterials has been conducted in the presence of capping agents.²⁶⁸⁻²⁷⁰ In some instances, catalysts are also utilized to permit reactions to proceed under mild conditions.²⁷¹

In the traditional solid-state methods, solid state reactions are carried out by heating a mixture of pure elements or simpler compounds at elevated temperatures. Consequently, the reactions take a very long time to complete, and because of the precursors' volatility at elevated temperatures, upscaling of the product and composition preservation becomes challenging. On the other hand, solventless thermolysis has proven to be a simple, economical, time-effective, and scalable approach.⁴¹ Moreover, the fabrication of nanomaterials in the absence of surface passivating ligands maximizes the probability of obtaining nanomaterials with copious exposed active sites for improved electrochemical performance.^{259, 267, 272} The selection of suitable precursors for the solventless synthesis of nanomaterials is guided by a set of general requirements: the precursor should possess a low melting point and decomposition temperature; the formed decomposition by-products should be highly volatile to ensure the synthesis of high purity materials; for industrial realization, the precursor should be stable, non-toxic, and cost-effective.²⁷³

1.2.7 Statement of the research problem

There have been significant developments of robust and reproducible methods for the synthesis of homogeneous inorganic nanomaterials over the past years. In the case of semiconductor spinel ferrites and their corresponding solid solutions, their synthesis has been predominantly based on wet-chemical syntheses, which offer versatile and robust routes of

obtaining nanomaterials with exceptional control of their properties. Notwithstanding the versatility and success of the wet-chemical synthetic protocols, their over-reliance on toxic and/or expensive chemicals and capping agents and the technical hitches causing hindrance in large-scale production, remain a challenge. Likewise, the presence of the bulky surfactants on the surface of the nanomaterials acts as insulating shells and impede the charge transfer behaviour of resulting nanomaterials. Therefore, there is a pressing need for the development of green, economical and scalable fabrication routes that avoid the use of expensive and/or injurious chemicals and insulating surface passivating ligands.

As a sustainable alternative to the solution-based routes, the solventless thermolysis route has recently been proven as a straightforward, cost-effective, self-capping and highly effective technique for the fabrication of nanoscale materials. It is worth noting that under the solventless thermolysis method, the synthesis proceeds in the absence of coordinating ligands because the ligands produced in the course of precursor thermolysis can then stabilize the synthesized nanoparticles. Notably, performing the synthesis in the absence of capping agents further increases the probability of obtaining nanomaterials with copious exposed active sites for improved electrochemical properties. Another advantage of the solventless thermolysis method is the absence of post-synthetic annealing procedures which are common in solution-based techniques. Moreover, in contrast to conventional solid-state strategies in which the syntheses are carried out under harsh conditions at high temperature and prolonged time, the solvent-free thermolysis method is time-efficient, requires low/mild temperature, and permits precise control over the stoichiometry of the precursors. Different organometallic precursor materials such as metal oleates, metal acetylacetonates, metal acetate, metal carbonyls, and metal oxalate, as well as metal salts such as nitrates, chlorides and sulfates, have been utilized in the synthesis of nanoparticulate ferrite materials of diverse morphologies and properties. Inspired by the above rationale, in this work, we describe the rational synthesis of nanostructured $\text{Ni}_{1-x}\text{Co}_x\text{Fe}_2\text{O}_4$, $\text{Co}_{1-x}\text{Zn}_x\text{Fe}_2\text{O}_4$, $\text{Ni}_{1-x}\text{Mg}_x\text{Fe}_2\text{O}_4$, $\text{Ni}_{1-x}\text{Zn}_x\text{Fe}_2\text{O}_4$, and $\text{Co}_{1-x}\text{Mg}_x\text{Fe}_2\text{O}_4$ solid solutions by solventless thermolysis of metal acetylacetonates. Investigation of the efficacy of the synthesized solid solution nanoparticles for supercapacitance, HER and OER is also presented. In comparison to other precursors available for the synthesis of spinel metal ferrites, the selection of metal acetylacetonates is based on their low melting points, eco-friendliness, affordability, and their clean decomposition. They also have low moisture sensitivity, making them less susceptible to hydrolysis, which is a common limitation of metal halides and alkoxides.

1.2.8 Aim and objectives

The aim of this research work is to employ the solventless thermolysis approach to synthesize nanostructured spinel ferrite solid solutions and investigate their performance for electrochemical energy conversion and storage.

The research objectives are:

- i. To employ solventless thermolysis method to synthesize nanostructured $\text{Ni}_{1-x}\text{Co}_x\text{Fe}_2\text{O}_4$, $\text{Co}_{1-x}\text{Zn}_x\text{Fe}_2\text{O}_4$, $\text{Ni}_{1-x}\text{Mg}_x\text{Fe}_2\text{O}_4$, $\text{Ni}_{1-x}\text{Zn}_x\text{Fe}_2\text{O}_4$, and $\text{Co}_{1-x}\text{Mg}_x\text{Fe}_2\text{O}_4$ solid solutions from their corresponding metal acetylacetonate precursors.
- ii. To characterize the synthesized nanoferrite solid solutions for their structural, compositional, morphological and optical properties.
- iii. To investigate the effect of substituent and the stoichiometric variation on the properties of the synthesized spinel ferrite solid solution nanoparticles.
- iv. To test the electrochemical performance of the synthesized nanospinel ferrite solid solutions towards supercapacitance, hydrogen evolution reaction and oxygen evolution reaction.

References

1. Chu, S.; Cui, Y.; Liu, N. *Nature Materials* **2017**, 16, (1), 16-22.
2. Lewis, N. S.; Nocera, D. G. *Proceedings of the National Academy of Sciences* **2006**, 103, (43), 15729-15735.
3. Güney, T. *International Journal of Sustainable Development & World Ecology* **2019**, 26, (5), 389-397.
4. Owusu, P. A.; Asumadu-Sarkodie, S. *Cogent Engineering* **2016**, 3, (1), 1167990.
5. Zsiborács, H.; Baranyai, N. H.; Vincze, A.; Zentkó, L.; Birkner, Z.; Máté, K.; Pintér, G. *Electronics* **2019**, 8, (7), 729.
6. Liu, T.; Zhang, Y.; Jiang, Z.; Zeng, X.; Ji, J.; Li, Z.; Gao, X.; Sun, M.; Lin, Z.; Ling, M. *Energy & Environmental Science* **2019**, 12, (5), 1512-1533.
7. Mackanic, D. G.; Chang, T.-H.; Huang, Z.; Cui, Y.; Bao, Z. *Chemical Society Reviews* **2020**, 49, (13), 4466-4495.
8. Raghavendra, K. V. G.; Vinoth, R.; Zeb, K.; Gopi, C. V. M.; Sambasivam, S.; Kummara, M. R.; Obaidat, I. M.; Kim, H. J. *Journal of Energy Storage* **2020**, 31, 101652.
9. Lu, J.; Tang, T.; Bai, C.; Gao, H.; Wang, J.; Li, C.; Gao, Y.; Guo, Z.; Zong, X. *Energy Sources, Part A: Recovery, Utilization, and Environmental Effects* **2020**, 1-22.
10. Lindorfer, J.; Rosenfeld, D. C.; Böhm, H., *Fuel cells: Energy conversion technology. In Future Energy, Elsevier: 2020*; pp 495-517.
11. Hauch, A.; Küngas, R.; Blennow, P.; Hansen, A. B.; Hansen, J. B.; Mathiesen, B. V.; Mogensen, M. B. *Science* **2020**, 370, (6513).
12. Liang, Y.; Zhao, C. Z.; Yuan, H.; Chen, Y.; Zhang, W.; Huang, J. Q.; Yu, D.; Liu, Y.; Titirici, M. M.; Chueh, Y. L. *InfoMat* **2019**, 1, (1), 6-32.
13. Liu, Y.; Sun, Z.; Tan, K.; Denis, D. K.; Sun, J.; Liang, L.; Hou, L.; Yuan, C. *Journal of Materials Chemistry A* **2019**, 7, (9), 4353-4382.
14. Kularatna, N.; Gunawardane, K., *Academic Press: 2021*.
15. Wang, F.; Wu, X.; Yuan, X.; Liu, Z.; Zhang, Y.; Fu, L.; Zhu, Y.; Zhou, Q.; Wu, Y.; Huang, W. *Chemical Society Reviews* **2017**, 46, (22), 6816-6854.
16. Zhu, J.; Hu, L.; Zhao, P.; Lee, L. Y. S.; Wong, K.-Y. *Chemical reviews* **2019**, 120, (2), 851-918.
17. Peng, L.; Wei, Z. *Engineering* **2020**.
18. Eftekhari, A. *International Journal of Hydrogen Energy* **2017**, 42, (16), 11053-11077.

19. Song, F.; Bai, L.; Moysiadou, A.; Lee, S.; Hu, C.; Liardet, L.; Hu, X. *Journal of the American Chemical Society* **2018**, 140, (25), 7748-7759.
20. Li, W.; Wang, D.; Zhang, Y.; Tao, L.; Wang, T.; Zou, Y.; Wang, Y.; Chen, R.; Wang, S. *Advanced Materials* **2020**, 32, (19), 1907879.
21. Yu, M.; Liu, F.; Li, J.; Liu, J.; Zhang, Y.; Cheng, F. *Advanced Energy Materials* **2021**, 2100640.
22. Tie, D.; Huang, S.; Wang, J.; Ma, J.; Zhang, J.; Zhao, Y. *Energy Storage Materials* **2019**, 21, 22-40.
23. Yang, W.; Wang, Z.; Zhang, W.; Guo, S. *Trends in Chemistry* **2019**, 1, (2), 259-271.
24. Jamesh, M.-I.; Sun, X. *Journal of Power Sources* **2018**, 400, 31-68.
25. Chen, Z.; Wei, W.; Ni, B.-J. *Current Opinion in Green and Sustainable Chemistry* **2021**, 27, 100398.
26. Chen, Z.; Duan, X.; Wei, W.; Wang, S.; Ni, B.-J. *Journal of Materials Chemistry A* **2019**, 7, (25), 14971-15005.
27. Shang, X.; Tang, J.-H.; Dong, B.; Sun, Y. *Sustainable Energy & Fuels* **2020**, 4, (7), 3211-3228.
28. Forouzandeh, P.; Kumaravel, V.; Pillai, S. C. *Catalysts* **2020**, 10, (9), 969.
29. Yuan, C.; Wu, H. B.; Xie, Y.; Lou, X. W. *Angewandte Chemie International Edition* **2014**, 53, (6), 1488-1504.
30. Zhao, Q.; Yan, Z.; Chen, C.; Chen, J. *Chemical reviews* **2017**, 117, (15), 10121-10211.
31. Zhang, Z.; Yan, X.; Liu, J.; Liu, B.; Gu, Z.-G. *Sustainable Energy & Fuels* **2021**.
32. Kennaz, H.; Harat, A.; Guellati, O.; Momodu, D.; Barzegar, F.; Dangbegnon, J.; Manyala, N.; Guerioune, M. *Journal of Solid State Electrochemistry* **2018**, 22, (3), 835-847.
33. Bhujun, B.; Tan, M. T.; Shanmugam, A. S. *Results in Physics* **2017**, 7, 345-353.
34. Zhu, Y.; Peng, L.; Fang, Z.; Yan, C.; Zhang, X.; Yu, G. *Advanced Materials* **2018**, 30, (15), 1706347.
35. Wongpratrat, U.; Tipsawat, P.; Khajonrit, J.; Swatsitang, E.; Maensiri, S. *Journal of Alloys and Compounds* **2020**, 831, 154718.
36. Chen, W.; Yuan, P.; Guo, S.; Gao, S.; Wang, J.; Li, M.; Liu, F.; Wang, J.; Cheng, J. *Journal of Electroanalytical Chemistry* **2019**, 836, 134-142.
37. Gao, S.; Zhang, P.; Guo, S.; Chen, W.; Li, M.; Liu, F.; Cheng, J. *Journal of colloid and interface science* **2019**, 555, 284-293.

38. Khan, M. D.; Awan, S. U.; Zequine, C.; Zhang, C.; Gupta, R. K.; Revaprasadu, N. *ACS Applied Energy Materials* **2020**, 3, (2), 1448-1460.
39. Liu, B.; Li, J.; Yang, W.; Zhang, X.; Jiang, X.; Bando, Y. *Small* **2017**, 13, (45), 1701998.
40. Lusi, M. *CrystEngComm* **2018**, 20, (44), 7042-7052.
41. Lewis, E.; Haigh, S.; O' Brien, P. *Journal of Materials Chemistry A* **2014**, 2, (3), 570-580.
42. Franco Junior, A.; Zapf, V.; Egan, P. *Journal of Applied Physics* **2007**, 101, (9), 09M506.
43. Franco Jr, A.; e Silva, F. *Journal of Applied Physics* **2013**, 113, (17), 17B513.
44. Sodhi, R. K.; Paul, S. *Catalysis Surveys from Asia* **2018**, 22, (1), 31-62.
45. Lukatskaya, M. R.; Dunn, B.; Gogotsi, Y. *Nature Communications* **2016**, 7, (1), 1-13.
46. Wang, Y.; Song, Y.; Xia, Y. *Chemical Society Reviews* **2016**, 45, (21), 5925-5950.
47. Abbas, Q. 2020.
48. Yu, Z.; Tetard, L.; Zhai, L.; Thomas, J. *Energy & Environmental Science* **2015**, 8, (3), 702-730.
49. Najib, S.; Erdem, E. *Nanoscale Advances* **2019**, 1, (8), 2817-2827.
50. Sato, T.; Marukane, S.; Morinaga, T.; Kamijo, T.; Arafune, H.; Tsujii, Y. *Journal of Power Sources* **2015**, 295, 108-116.
51. Sinha, P.; Kar, K. K., *Introduction to Supercapacitors. In Handbook of Nanocomposite Supercapacitor Materials II, Springer: 2020; pp 1-28.*
52. Chodankar, N. R.; Pham, H. D.; Nanjundan, A. K.; Fernando, J. F.; Jayaramulu, K.; Golberg, D.; Han, Y. K.; Dubal, D. P. *Small* **2020**, 16, (37), 2002806.
53. Muzaffar, A.; Ahamed, M. B.; Deshmukh, K.; Thirumalai, J. *Renewable and Sustainable Energy Reviews* **2019**, 101, 123-145.
54. Iro, Z. S.; Subramani, C.; Dash, S. *Int. J. Electrochem. Sci* **2016**, 11, (12), 10628-10643.
55. Pal, B.; Yang, S.; Ramesh, S.; Thangadurai, V.; Jose, R. *Nanoscale Advances* **2019**, 1, (10), 3807-3835.
56. Tee, S. Y.; Win, K. Y.; Teo, W. S.; Koh, L. D.; Liu, S.; Teng, C. P.; Han, M. Y. *Advanced Science* **2017**, 4, (5), 1600337.
57. Jiao, Y.; Zheng, Y.; Jaroniec, M.; Qiao, S. Z. *Chemical Society Reviews* **2015**, 44, (8), 2060-2086.
58. You, B.; Sun, Y. *ChemPlusChem* **2016**, 81, (10), 1045.

59. You, B.; Sun, Y. *Accounts of chemical research* **2018**, 51, (7), 1571-1580.
60. Fabbri, E.; Habereeder, A.; Waltar, K.; Kötz, R.; Schmidt, T. J. *Catalysis Science & Technology* **2014**, 4, (11), 3800-3821.
61. Zeng, M.; Li, Y. *Journal of Materials Chemistry A* **2015**, 3, (29), 14942-14962.
62. Zhu, Y. P.; Guo, C.; Zheng, Y.; Qiao, S.-Z. *Accounts of Chemical Research* **2017**, 50, (4), 915-923.
63. Li, X.; Hao, X.; Abudula, A.; Guan, G. *Journal of Materials Chemistry A* **2016**, 4, (31), 11973-12000.
64. Anantharaj, S.; Ede, S. R.; Sakthikumar, K.; Karthick, K.; Mishra, S.; Kundu, S. *Acs Catalysis* **2016**, 6, (12), 8069-8097.
65. Narang, S. B.; Pubby, K. *Journal of Magnetism and Magnetic Materials* **2020**, 167163.
66. Valenzuela, R. *Physics Research International* **2012**, 2012.
67. Bragg, W. H. *The London, Edinburgh, and Dublin Philosophical Magazine and Journal of Science* **1915**, 30, (176), 305-315.
68. Wang, R.; Wu, J., *Structure and basic properties of ternary metal oxides and their prospects for application in supercapacitors. In Metal Oxides in Supercapacitors, Elsevier: 2017*; pp 99-132.
69. Sickafus, K. E.; Wills, J. M.; Grimes, N. W. *Journal of the American Ceramic Society* **1999**, 82, (12), 3279-3292.
70. Dojcinovic, M. P.; Vasiljevic, Z. Z.; Pavlovic, V. P.; Barisic, D.; Pajic, D.; Tadic, N. B.; Nikolic, M. V. *Journal of Alloys and Compounds* **2021**, 855, 157429.
71. Henderson, C.; Charnock, J.; Plant, D. *Journal of Physics: Condensed Matter* **2007**, 19, (7), 076214.
72. Sharma, J.; Srivastava, P.; Singh, G.; Virk, H. S. *In Nanoferrites of transition metals and their catalytic activity, Solid State Phenomena, 2016*; Trans Tech Publ: pp 126-138.
73. Galvão, W. S.; Neto, D.; Freire, R. M.; Fachine, P. B. *In Super-paramagnetic nanoparticles with spinel structure: a review of synthesis and biomedical applications, solid state phenomena, 2016*; Trans Tech Publ: pp 139-176.
74. Carta, D.; Casula, M. F.; Falqui, A.; Loche, D.; Mountjoy, G.; Sangregorio, C.; Corrias, A. *The Journal of Physical Chemistry C* **2009**, 113, (20), 8606-8615.
75. Sanchez-Lievano, K. R.; Stair, J. L.; Knowles, K. E. *Inorganic Chemistry* **2021**, 60, (7), 4291-4305.
76. Šutka, A.; Gross, K. A. *Sensors and Actuators B: Chemical* **2016**, 222, 95-105.

77. Sakthivel, K.; Mani, G.; Chen, S.-M.; Lin, S.-H.; Muthumariappan, A.; Mani, V. *Journal of Electroanalytical Chemistry* **2018**, 820, 161-167.
78. Amiri, M.; Salavati-Niasari, M.; Akbari, A. *Advances in colloid and interface science* **2019**, 265, 29-44.
79. Malaie, K.; Ganjali, M. R. *Journal of Energy Storage* **2020**, 102097.
80. Odio, O. F.; Reguera, E. *Magnetic Spinels-Synthesis, Properties and Applications* **2017**, 185-216.
81. Wells, A. F., *Structural Inorganic Chemistry*. Oxford University Press: **2012**.
82. Liu, B.; Bando, Y.; Liu, L.; Zhao, J.; Masanori, M.; Jiang, X.; Golberg, D. *Nano letters* **2012**, 13, (1), 85-90.
83. Liu, B.; Bando, Y.; Liu, L.; Zhao, J.; Masanori, M.; Jiang, X.; Golberg, D. *Nano Letters* **2013**, 13, (1), 85-90.
84. Mizutani, U., *The Hume-Rothery rules for structurally complex alloy phases. In Surface Properties and Engineering of Complex Intermetallics*, World Scientific: **2010**; pp 323-399.
85. Bréger, J.; Jiang, M.; Dupré, N.; Meng, Y. S.; Shao-Horn, Y.; Ceder, G.; Grey, C. P. *Journal of Solid State Chemistry* **2005**, 178, (9), 2575-2585.
86. Denton, A. R.; Ashcroft, N. W. *Physical Review A* **1991**, 43, (6), 3161.
87. Saah, S. A.; Khan, M. D.; McNaughten, P. D.; Awudza, J. A.; Revaprasadu, N.; O'Brien, P. *New Journal of Chemistry* **2018**, 42, (20), 16602-16607.
88. Khan, M. D.; Aamir, M.; Murtaza, G.; Malik, M. A.; Revaprasadu, N. *Dalton Transactions* **2018**, 47, (30), 10025-10034.
89. Alqahtani, T.; Khan, M. D.; Kelly, D. J.; Haigh, S. J.; Lewis, D. J.; O'Brien, P. *Journal of Materials Chemistry C* **2018**, 6, (46), 12652-12659.
90. Gervas, C.; Khan, M. D.; Zhang, C.; Zhao, C.; Gupta, R. K.; Carleschi, E.; Doyle, B. P.; Revaprasadu, N. *RSC Advances* **2018**, 8, (42), 24049-24058.
91. Köseoğlu, Y.; Alan, F.; Tan, M.; Yilgin, R.; Öztürk, M. *Ceramics International* **2012**, 38, (5), 3625-3634.
92. Shyam, A. R.; Dwivedi, R.; Reddy, V.; Chary, K.; Prasad, R. *Green Chemistry* **2002**, 4, (6), 558-561.
93. Wang, Y.; Hou, Y.; Tang, A.; Feng, B.; Li, Y.; Liu, J.; Teng, F. *Journal of Crystal Growth* **2007**, 308, (1), 19-25.
94. Wang, X.-L.; Wakahara, A.; Sasaki, A. *Journal of Crystal Growth* **1993**, 129, (1-2), 289-296.

95. Kitaigorodsky, A. I., *Inorganic Solid Solutions. In Mixed Crystals*, Springer: **1984**; pp 181-199.
96. West, A. R., *Solid State Chemistry and its Applications*. John Wiley & Sons: **2014**.
97. Takeoka, S.; Toshikiyo, K.; Fujii, M.; Hayashi, S.; Yamamoto, K. *Physical Review B* **2000**, 61, (23), 15988.
98. Yang, J.-E.; Jin, C.-B.; Kim, C.-J.; Jo, M.-H. *Nano letters* **2006**, 6, (12), 2679-2684.
99. Yang, J.-E.; Park, W.-H.; Kim, C.-J.; Kim, Z. H.; Jo, M.-H. *Applied Physics Letters* **2008**, 92, (26), 263111.
100. Xia, M.; Han, J.; Cheng, Z.; Liang, C.; Zhang, S. *Applied Physics Letters* **2014**, 105, (10), 101902.
101. Kim, C. J.; Lee, H. S.; Cho, Y. J.; Yang, J. E.; Lee, R. R.; Lee, J. K.; Jo, M. H. *Advanced Materials* **2011**, 23, (8), 1025-1029.
102. Huang, J.; Yu, Y.; Wu, Y.; Li, D.; Ye, H. *Journal of Materials Research* **1997**, 12, (4), 936-946.
103. Regulacio, M. D.; Han, M.-Y. *Accounts of Chemical Research* **2010**, 43, (5), 621-630.
104. Kun, W. N.; McNaughter, P. D.; Nyamen, L. D.; Spencer, B. F.; O'Brien, P.; Ndifon, P. T.; Revaprasadu, N. *RSC Advances* **2019**.
105. Alqahtani, T.; Cernik, R. J.; O'Brien, P.; Lewis, D. J. *Journal of Materials Chemistry C* **2019**, 7, (17), 5112-5121.
106. Li, Y.; Ye, M.; Yang, C.; Li, X.; Li, Y. *Advanced Functional Materials* **2005**, 15, (3), 433-441.
107. Wang, W.; Germanenko, I.; El-Shall, M. S. *Chemistry of Materials* **2002**, 14, (7), 3028-3033.
108. Zhong, X.; Feng, Y.; Knoll, W.; Han, M. *Journal of the American Chemical Society* **2003**, 125, (44), 13559-13563.
109. Barman, B.; Bangera, K. V.; Shivakumar, G. *Materials Research Express* **2020**, 6, (12), 126441.
110. Yang, L.; Zhang, M.; Liu, M.; Fan, Y.; Ben, H.; Li, L.; Fu, X.; Chen, S. *Catalysts* **2020**, 10, (3), 276.
111. Abdelhady, A. L.; Malik, M. A.; O'Brien, P. *Journal of Inorganic and Organometallic Polymers and Materials* **2014**, 24, (1), 226-240.
112. Ramasamy, K.; Malik, M. A.; O'Brien, P.; Raftery, J. *MRS Online Proceedings Library (OPL)* **2008**, 1145.

113. Chu, T.; Chu, S. S.; Britt, J.; Ferekides, C.; Wu, C. *Journal of Applied Physics* **1991**, 70, (5), 2688-2693.
114. Kane, W. M.; Spratt, J. P.; Hershinger, L. W.; Khan, I. H. *Journal of The Electrochemical Society* **1966**, 113, (2), 136.
115. Reddy, D. S.; Kumar, K. S.; Reddy, N. K.; Reddy, B.; Gunasekhar, K.; Reddy, P. S. *Journal of the Electrochemical Society* **2008**, 155, (6), H407.
116. Xing, C.; Zhang, Y.; Yan, W.; Guo, L. *International Journal of Hydrogen Energy* **2006**, 31, (14), 2018-2024.
117. Li, Q.; Meng, H.; Zhou, P.; Zheng, Y.; Wang, J.; Yu, J.; Gong, J. *Acs Catalysis* **2013**, 3, (5), 882-889.
118. Liu, Y.; Zapien, J. A.; Shan, Y. Y.; Geng, C. Y.; Lee, C. S.; Lee, S. T. *Advanced Materials* **2005**, 17, (11), 1372-1377.
119. Kim, M. R.; Park, S.-Y.; Jang, D.-J. *The Journal of Physical Chemistry C* **2010**, 114, (14), 6452-6457.
120. Lehmann, W. *Journal of The Electrochemical Society* **1971**, 118, (7), 1164.
121. Lehmann, W. *Journal of Luminescence* **1972**, 5, (2), 87-107.
122. Susa, K.; Kobayashi, T.; Taniguchi, S. *Journal of Solid State Chemistry* **1980**, 33, (2), 197-202.
123. Kobayashi, T.; Susa, K.; Taniguchi, S. *Journal of Solid State Chemistry* **1980**, 33, (2), 203-207.
124. Ray, B.; Brightwell, J.; Allsop, D.; Green, A. *Journal of Crystal Growth* **1988**, 86, (1-4), 644-649.
125. Viney, I.; Ray, B.; Brightwell, J.; Arterton, B. *Journal of Crystal Growth* **1992**, 117, (1-4), 806-809.
126. Barrett, E.; Fern, G. R.; Ray, B.; Withnall, R.; Silver, J. *Journal of Optics A: Pure and Applied Optics* **2005**, 7, (6), S265.
127. Kobayashi, T.; Susa, K.; Taniguchi, S. *Journal of Physics and Chemistry of Solids* **1979**, 40, (10), 781-785.
128. Bashar, M. S.; Yusoff, Y.; Abdullah, S. F.; Rahaman, M.; Chelvanathan, P.; Gafur, A.; Ahmed, F.; Akhtaruzzaman, M.; Amin, N. *Coatings* **2020**, 10, (8), 766.
129. Alemi, A.; Sharabiyani, M. A. A.; Teymouri, E.; Sadeghi, L. *ChemistrySelect* **2019**, 4, (32), 9309-9316.
130. Kudo, A.; Sekizawa, M. *Catalysis Letters* **1999**, 58, (4), 241-243.

131. Delosreyes, J.; Vrinat, M.; Geantet, C.; Breysse, M.; Grimblot, J. *Journal of Catalysis* **1993**, 142, (2), 455-464.
132. Jaegermann, W. *The Journal of Physical Chemistry* **1984**, 88, (22), 5309-5313.
133. Bellaloui, A.; Mosoni, L.; Roubin, M.; Vrinat, M.; Lacroix, M.; Breysse, M. *ChemInform* **1987**, 18, (32), no-no.
134. Berg, A.; Caroff, P.; Shahid, N.; Lockrey, M. N.; Yuan, X.; Borgström, M. T.; Tan, H. H.; Jagadish, C. *Nano Research* **2017**, 10, (2), 672-682.
135. Fu, Q.; Wu, T.; Fu, G.; Gao, T.; Han, J.; Yao, T.; Zhang, Y.; Zhong, W.; Wang, X.; Song, B. *ACS Energy Letters* **2018**, 3, (7), 1744-1752.
136. Sergio, L.; Gobzalez-Cortes, S.; Serbia, M.; Rudolfo-Baecher, A.; Oliveros, A.; Oozco, J.; Fontal, B.; Mora, A.; Delgado, G. *Reac. Kinet. Catal. Lett* **2002**, 75, 3.
137. Rensel, D. J.; Kim, J.; Jain, V.; Bonita, Y.; Rai, N.; Hicks, J. C. *Catalysis Science & Technology* **2017**, 7, (9), 1857-1867.
138. Li, J.; Yan, M.; Zhou, X.; Huang, Z. Q.; Xia, Z.; Chang, C. R.; Ma, Y.; Qu, Y. *Advanced Functional Materials* **2016**, 26, (37), 6785-6796.
139. Zhong, X.; Han, M.; Dong, Z.; White, T. J.; Knoll, W. *Journal of the American Chemical Society* **2003**, 125, (28), 8589-8594.
140. Zhong, X.; Zhang, Z.; Liu, S.; Han, M.; Knoll, W. *The Journal of Physical Chemistry B* **2004**, 108, (40), 15552-15559.
141. Zhong, X.; Feng, Y.; Zhang, Y.; Gu, Z.; Zou, L. *Nanotechnology* **2007**, 18, (38), 385606.
142. Zheng, Y.; Yang, Z.; Ying, J. Y. *Advanced Materials* **2007**, 19, (11), 1475-1479.
143. Liu, F.-C.; Cheng, T.-L.; Shen, C.-C.; Tseng, W.-L.; Chiang, M. Y. *Langmuir* **2008**, 24, (5), 2162-2167.
144. Protière, M.; Reiss, P. *Small* **2007**, 3, (3), 399-403.
145. Bagade, C. S.; Mali, S. S.; Ghanwat, V. B.; Khot, K. V.; Patil, P. B.; Kharade, S. D.; Mane, R. M.; Desai, N. D.; Hong, C. K.; Patil, P. S. *RSC Advances* **2015**, 5, (69), 55658-55668.
146. Sutrave, D.; Shahane, G.; Patil, V.; Deshmukh, L. *Materials Chemistry and Physics* **2000**, 65, (3), 298-305.
147. Wahab, L.; Zayed, H.; Abd El-Galil, A. *Thin Solid Films* **2012**, 520, (16), 5195-5199.
148. Mahmood, A.; Shaista, R.; Shah, A.; Aziz, U.; Ahmed, E.; Ali, S.; Raza, Q. *Physica Scripta* **2011**, 83, (6), 065706.

149. Akaltun, Y.; Yıldırım, M. A.; Ateş, A.; Yıldırım, M. *Materials Research Bulletin* **2012**, 47, (11), 3390-3396.
150. Ali, I.; Iqbal, A.; Mahmood, A.; Shah, A.; Zakria, M.; Ali, A. *Mater. Sci* **2016**, 34, 828-833.
151. Prakshale, V.; Chavan, G.; Pawar, S.; Bangi, U.; Sikora, A.; Kamble, S.; Chaure, N.; Maldar, N.; Deshmukh, L. *AIP Conference Proceedings*, **2018**; AIP Publishing LLC: p 020037.
152. Rakesh, K.; Gulbir, S.; Singh, B. *Annals of Biology* **2015**, 31, (1), 122-125.
153. Rakesh, K.; Gulbir, S.; Singh, B. *Annals of Agri Bio Research* **2015**, 20, (1), 95-98.
154. Yang, P.; Wu, Z.; Jiang, Y.; Pan, Z.; Tian, W.; Jiang, L.; Hu, L. *Advanced Energy Materials* **2018**, 8, (26), 1801392.
155. Arachchige, I. U.; Kanatzidis, M. G. *Nano letters* **2009**, 9, (4), 1583-1587.
156. Caillat, T.; Carle, M.; Pierrat, P.; Scherrer, H.; Scherrer, S. *Journal of Physics and Chemistry of Solids* **1992**, 53, (8), 1121-1129.
157. Zhang, C.; Peng, Z.; Li, Z.; Yu, L.; Khor, K. A.; Xiong, Q. *Nano Energy* **2015**, 15, 688-696.
158. Hong, M.; Chen, Z. G.; Yang, L.; Zou, J. *Nano Energy* **2016**, 20, 144-155.
159. Naveen, A. N.; Selladurai, S. *Electrochimica Acta* **2014**, 125, 404-414.
160. Hirai, S.; Yagi, S.; Seno, A.; Fujioka, M.; Ohno, T.; Matsuda, T. *RSC advances* **2016**, 6, (3), 2019-2023.
161. Yadav, M. K.; Gangwar, C.; Singh, N. K. *Journal of New Materials for Electrochemical Systems* **2020**, 23(2), 78-86.
162. Yoshinaga, T.; Saruyama, M.; Xiong, A.; Ham, Y.; Kuang, Y.; Niishiro, R.; Akiyama, S.; Sakamoto, M.; Hisatomi, T.; Domen, K. *Nanoscale* **2018**, 10, (22), 10420-10427.
163. Lingampalli, S.; Dileep, K.; Datta, R.; Gautam, U. K. *Chemistry of Materials* **2014**, 26, (8), 2720-2725.
164. Oshima, T.; Kato, Y.; Oda, M.; Hitora, T.; Kasu, M. *Applied Physics Express* **2017**, 10, (5), 051104.
165. Li, J.-G.; Ikegami, T.; Wang, Y.; Mori, T. *Journal of Solid State Chemistry* **2002**, 168, (1), 52-59.
166. Bauers, S. R.; Hamann, D. M.; Patterson, A.; Perkins, J. D.; Talley, K. R.; Zakutayev, A. *Japanese Journal of Applied Physics* **2019**, 58, (SC), SC1015.
167. Saha, B.; Saber, S.; Naik, G. V.; Boltasseva, A.; Stach, E. A.; Kvam, E. P.; Sands, T. D. *physica status solidi (b)* **2015**, 252, (2), 251-259.

168. Saha, B.; Naik, G.; Drachev, V. P.; Boltasseva, A.; Marinero, E. E.; Sands, T. D. *Journal of Applied Physics* **2013**, 114, (6), 063519.
169. Biswas, B.; Saha, B. *Physical Review Materials* **2019**, 3, (2), 020301.
170. Wang, B.; Nawarat, P.; Lewis, K. M.; Patsalas, P.; Gall, D. *ACS Applied Materials & Interfaces* **2021**, 13, (19), 22738-22748.
171. Zhang, W.; Li, X.; Jiang, T.; Song, J.; Lin, Y.; Zhu, L.; Xu, X. *Nanoscale* **2015**, 7, (32), 13554-13560.
172. Tannous, J.; Dassenoy, F.; Bruhács, A.; Tremel, W. *Tribology Letters* **2010**, 37, (1), 83-92.
173. Lei, Y.; Pakhira, S.; Fujisawa, K.; Wang, X.; Iyiola, O. O.; Perea López, N. s.; Laura Elías, A.; Pulickal Rajukumar, L.; Zhou, C.; Kabius, B. *ACS nano* **2017**, 11, (5), 5103-5112.
174. Barik, G.; Pal, S. *The Journal of Physical Chemistry C* **2018**, 122, (45), 25837-25848.
175. Li, J.; Yan, H.; Wei, W.; Meng, L. *Dalton Transactions* **2018**, 47, (42), 15148-15154.
176. Meiron, O. E.; Kuraganti, V.; Hod, I.; Bar-Ziv, R.; Bar-Sadan, M. *Nanoscale* **2017**, 9, (37), 13998-14005.
177. Feng, Q.; Mao, N.; Wu, J.; Xu, H.; Wang, C.; Zhang, J.; Xie, L. *ACS nano* **2015**, 9, (7), 7450-7455.
178. Swafford, L. A.; Weigand, L. A.; Bowers, M. J.; McBride, J. R.; Rapaport, J. L.; Watt, T. L.; Dixit, S. K.; Feldman, L. C.; Rosenthal, S. J. *Journal of the American Chemical Society* **2006**, 128, (37), 12299-12306.
179. Bailey, R. E.; Nie, S. *Journal of the American Chemical Society* **2003**, 125, (23), 7100-7106.
180. Al-Salim, N.; Young, A. G.; Tilley, R. D.; McQuillan, A. J.; Xia, J. *Chemistry of Materials* **2007**, 19, (21), 5185-5193.
181. Piven, N.; Sussha, A. S.; Döblinger, M.; Rogach, A. L. *The Journal of Physical Chemistry C* **2008**, 112, (39), 15253-15259.
182. Ouyang, J.; Vincent, M.; Kingston, D.; Descours, P.; Boivineau, T.; Zaman, M. B.; Wu, X.; Yu, K. *The Journal of Physical Chemistry C* **2009**, 113, (13), 5193-5200.
183. Jiang, W.; Singhal, A.; Zheng, J.; Wang, C.; Chan, W. C. *Chemistry of Materials* **2006**, 18, (20), 4845-4854.
184. El-Nahass, M. *Journal of Materials Science: Materials in Electronics* **1992**, 3, (1), 71-76.

185. Kumar, S.; Lal, B.; Aghamkar, P.; Husain, M. *Journal of Alloys and Compounds* **2009**, 488, (1), 334-338.
186. Kumar, S.; Lal, B.; Rohilla, S.; Aghamkar, P.; Husain, M. *Journal of alloys and compounds* **2010**, 505, (1), 135-139.
187. Ma, W.; Luther, J. M.; Zheng, H.; Wu, Y.; Alivisatos, A. P. *Nano Letters* **2009**, 9, (4), 1699-1703.
188. Subbaiah, Y. V.; Prathap, P.; Reddy, K.; Mangalaraj, D.; Kim, K.; Yi, J. *Journal of Physics D: Applied Physics* **2007**, 40, (12), 3683.
189. Patil, N. M.; Nilange, S. G.; Yadav, A. A. *Thin Solid Films* **2018**, 664, 19-26.
190. Abo-Hassan, K. M.; Muhamad, M. R.; Radhakrishna, S. *Thin Solid Films* **2005**, 491, (1-2), 117-122.
191. Stutius, W. *Journal of Crystal Growth* **1982**, 59, (1-2), 1-9.
192. Wang, M.; Fei, G. T.; Zhang, Y. G.; Kong, M. G.; Zhang, L. *Advanced Materials* **2007**, 19, (24), 4491-4494.
193. Agawane, G.; Shin, S. W.; Vanalakar, S.; Moholkar, A.; Gurav, K.; Suryawanshi, M.; Lee, J. Y.; Yun, J. H.; Kim, J. H. *Materials Research Bulletin* **2014**, 55, 106-113.
194. Fujita, S.; Matsuda, Y.; Sasaki, A. *Journal of Crystal Growth* **1984**, 68, (1), 231-236.
195. Trubaieva, O. G.; Chaika, M. A.; Lalayants, A. I. *Lithuanian Journal of Physics* **2018**, 58, (3).
196. Zhang, X.; Xu, M.; Li, Q.; Wang, M.; Akhmadaliev, S.; Zhou, S.; Wu, Y.; Guo, B. *Nuclear Instruments and Methods in Physics Research Section B: Beam Interactions with Materials and Atoms* **2019**, 442, 24-27.
197. Atsushi, K.; Akinobu, H.; Mayumi, H. **2015**.
198. Pan, D.; Weng, D.; Wang, X.; Xiao, Q.; Chen, W.; Xu, C.; Yang, Z.; Lu, Y. *Chemical Communications* **2009**, (28), 4221-4223.
199. Ivanov, S. A.; Piryatinski, A.; Nanda, J.; Tretiak, S.; Zavadil, K. R.; Wallace, W. O.; Werder, D.; Klimov, V. I. *Journal of the American Chemical Society* **2007**, 129, (38), 11708-11719.
200. Fiorani, D.; Gastaldi, L.; Viticoli, S. *Solid State Communications* **1983**, 48, (10), 865-867.
201. Nogues, M.; Saifi, A.; Hamedoun, M.; Dormann, J.; Malmanche, A.; Fiorani, D.; Viticoli, S. *Journal of Applied Physics* **1982**, 53, (11), 7699-7701.
202. Tang, J.; Hinds, S.; Kelley, S. O.; Sargent, E. H. *Chemistry of Materials* **2008**, 20, (22), 6906-6910.

203. Malik, S. N.; Mahboob, S.; Haider, N.; Malik, M. A.; O'Brien, P. *Nanoscale* **2011**, 3, (12), 5132-5139.
204. Panthani, M. G.; Akhavan, V.; Goodfellow, B.; Schmidtke, J. P.; Dunn, L.; Dodabalapur, A.; Barbara, P. F.; Korgel, B. A. *Journal of the American Chemical Society* **2008**, 130, (49), 16770-16777.
205. Guo, Q.; Ford, G. M.; Hillhouse, H. W.; Agrawal, R. *Nano Letters* **2009**, 9, (8), 3060-3065.
206. Pan, D.; Wang, X.; Zhou, Z. H.; Chen, W.; Xu, C.; Lu, Y. *Chemistry of Materials* **2009**, 21, (12), 2489-2493.
207. Ye, C.; Regulacio, M. D.; Lim, S. H.; Xu, Q. H.; Han, M. Y. *Chemistry—A European Journal* **2012**, 18, (36), 11258-11263.
208. Kevin, P.; Malik, M. A.; Mcadams, S.; O'Brien, P. *Journal of the American Chemical Society* **2015**, 137, (48), 15086-15089.
209. Shen, J.; Zhang, X.; Lin, S.; Li, J.; Chen, Z.; Li, W.; Pei, Y. *Journal of Materials Chemistry A* **2016**, 4, (40), 15464-15470.
210. Kato, T.; Hakari, Y.; Ikeda, S.; Jia, Q.; Iwase, A.; Kudo, A. *The Journal of Physical Chemistry Letters* **2015**, 6, (6), 1042-1047.
211. Tsuji, I.; Kato, H.; Kobayashi, H.; Kudo, A. *The Journal of Physical Chemistry B* **2005**, 109, (15), 7323-7329.
212. Yuan, Y.-J.; Chen, D.-Q.; Xiong, M.; Zhong, J.-S.; Wan, Z.-Y.; Zhou, Y.; Liu, S.; Yu, Z.-T.; Yang, L.-X.; Zou, Z.-G. *Applied Catalysis B: Environmental* **2017**, 204, 58-66.
213. Delgado, G.; Betancourt, L.; Sagredo, V.; Morón, M. C. *Physica Status Solidi (a)* **2006**, 203, (15), 3627-3632.
214. Attolini, G.; Frigeri, C.; Sagredo, V.; Solzi, M.; Delgado, G. *Crystal Research and Technology* **2011**, 46, (8), 761-764.
215. Khandale, A.; Bhoga, S. *Journal of Power Sources* **2010**, 195, (24), 7974-7982.
216. El Moussaoui, H.; Mahfoud, T.; Habouti, S.; El Maalam, K.; Ali, M. B.; Hamedoun, M.; Mounkachi, O.; Masrour, R.; Hlil, E.; Benyoussef, A. *Journal of Magnetism and Magnetic Materials* **2016**, 405, 181-186.
217. Zhao, X.; Fu, Y.; Wang, J.; Xu, Y.; Tian, J.-H.; Yang, R. *Electrochimica Acta* **2016**, 201, 172-178.
218. Maruthapandian, V.; Mathankumar, M.; Saraswathy, V.; Subramanian, B.; Muralidharan, S. *ACS Applied Materials & Interfaces* **2017**, 9, (15), 13132-13141.

219. Malima, N. M.; Khan, M. D.; Choi, J.; Gupta, R. K.; Mashazi, P.; Nyokong, T.; Revaprasadu, N. *RSC Advances* **2021**, 11, (49), 31002-31014.
220. Singh, R.; Singh, J.; Lal, B.; Thomas, M.; Bera, S. *Electrochimica Acta* **2006**, 51, (25), 5515-5523.
221. Kambale, R.; Shaikh, P.; Kamble, S.; Kolekar, Y. *Journal of Alloys and Compounds* **2009**, 478, (1-2), 599-603.
222. Powar, R. R.; Phadtare, V. D.; Parale, V. G.; Park, H.-H.; Pathak, S.; Kamble, P. R.; Piste, P. B.; Zambare, D. N. *Ceramics International* **2018**, 44, (17), 20782-20789.
223. Singh, R.; Singh, J.; Lal, B.; Singh, A. *International journal of hydrogen energy* **2007**, 32, (1), 11-16.
224. Archana, V.; Rastogi, P. K.; Thoufeeq, S.; Vinayasree, S.; Shaji, S.; Reddy, V.; Navarro, M. A. G.; Thomas, S.; Narayanan, T. N.; Anantharaman, M. *Sustainable Energy & Fuels* **2020**.
225. Dojcinovic, M. P.; Vasiljevic, Z. Z.; Pavlovic, V. P.; Barisic, D.; Pajic, D.; Tadic, N. B.; Nikolic, M. V. *Journal of Alloys and Compounds* **2020**, 157429.
226. Wang, P.; Liu, X.; Jia, D.; Ruan, Z.; Cheng, C.-H. *Journal of Hefei University of Technology (Natural Science)* **2011**, 9, 009.
227. Xu, Q.; Qin, W.; Chu, J.-F. *Energy & Fuels* **2020**, 34, (11), 15019-15025.
228. Guan, X.; Zhou, H.; Liu, Z.; Wang, Y.; Zhang, J. *Materials Research Bulletin* **2008**, 43, (4), 1046-1054.
229. Geng, Y.; Hou, Z.; Zou, X.; Song, X.; Pu, X.; Wang, L. *Journal of Alloys and Compounds* **2020**, 830, 154391.
230. Gao, Q.; Li, K.; Zhang, K.; Zhang, J.; Liu, Q. *Applied Physics Letters* **2019**, 114, (8), 081901.
231. Kovnir, K.; Garlea, V. O.; Thompson, C. M.; Zhou, H.; Reiff, W. M.; Ozarowski, A.; Shatruk, M. *Inorganic Chemistry* **2011**, 50, (20), 10274-10283.
232. Reehuis, M.; Jeitschko, W. *Journal of Physics and Chemistry of Solids* **1990**, 51, (8), 961-968.
233. Jia, S.; Chi, S.; Lynn, J.; Cava, R. *Physical Review B* **2010**, 81, (21), 214446.
234. McQueen, T. M.; Regulacio, M.; Williams, A. J.; Huang, Q.; Lynn, J. W.; Hor, Y. S.; West, D. V.; Green, M. A.; Cava, R. J. *Physical Review B* **2008**, 78, (2), 024521.
235. Huan, G.; Greenblatt, M.; Ramanujachary, K. *Solid State Communications* **1989**, 71, (3), 221-228.

236. Li, S.; Zhao, Z.; Liu, Q.; Huang, L.; Wang, G.; Pan, D.; Zhang, H.; He, X. *Inorganic Chemistry* **2011**, 50, (23), 11958-11964.
237. Shabunina, G.; Sadykov, R.; Aminov, T. *Inorganic materials* **2000**, 36, (12), 1208-1212.
238. Zhang, Y.; Li, L.; Li, D.; Wang, Q. *The Journal of Physical Chemistry C* **2015**, 119, (3), 1496-1499.
239. Yang, C.; Zhou, B.; Miao, S.; Yang, C.; Cai, B.; Zhang, W.-H.; Xu, X. *Journal of the American Chemical Society* **2013**, 135, (16), 5958-5961.
240. Ren, Z.; Taskin, A.; Sasaki, S.; Segawa, K.; Ando, Y. *Physical Review B* **2011**, 84, (16), 165311.
241. Arakane, T.; Sato, T.; Souma, S.; Kosaka, K.; Nakayama, K.; Komatsu, M.; Takahashi, T.; Ren, Z.; Segawa, K.; Ando, Y. *Nature Communications* **2012**, 3, (1), 1-5.
242. Deng, Z.; Yan, H.; Liu, Y. *Journal of the American Chemical Society* **2009**, 131, (49), 17744-17745.
243. Yim, W. M. *Journal of Applied Physics* **1969**, 40, (6), 2617-2623.
244. Madelung, O.; Rössler, U.; Schulz, M., *Semiconductors·Group IV Elements, IV-IV and III-V Compounds. Part B-Electronic, Transport, Optical and Other Properties. Berlin, Springer: 2002.*
245. Glicksman, M.; Kraeft, W. *Solid-State Electronics* 1985, 28, (1-2), 151-161.
246. Maeda, K.; Teramura, K.; Takata, T.; Hara, M.; Saito, N.; Toda, K.; Inoue, Y.; Kobayashi, H.; Domen, K. *The Journal of Physical Chemistry B* **2005**, 109, (43), 20504-20510.
247. Yoshida, M.; Hirai, T.; Maeda, K.; Saito, N.; Kubota, J.; Kobayashi, H.; Inoue, Y.; Domen, K. *The Journal of Physical Chemistry C* **2010**, 114, (36), 15510-15515.
248. Liu, B.; Bando, Y.; Dierre, B.; Sekiguchi, T.; Golberg, D.; Jiang, X. *ACS Applied Materials & Interfaces* **2013**, 5, (18), 9199-9204.
249. Sonomura, H.; Uragaki, T.; Miyauchi, T. *Japanese Journal of Applied Physics* **1973**, 12, (7), 968.
250. Catalano, A.; Beaulieu, R.; Gregg, T.; Head, P.; Wold, A.; Glicksman, M. *Solid State Communications* **1974**, 14, (5), 421-425.
251. Yu, P. W.; Glicksman, M. *Journal of Applied Physics* **1972**, 43, (10), 4153-4163.
252. Wang, Y.; Xu, J.; Ren, P.; Zhang, Q.; Zhuang, X.; Zhu, X.; Wan, Q.; Zhou, H.; Hu, W.; Pan, A. *Physical Chemistry Chemical Physics* **2013**, 15, (8), 2912-2916.

253. Authors, C.; III/17A-22A-41A1b, E. o. t. L. V. Group IV Elements, IV-IV and III-V Compounds. Part b-Electronic, Transport, Optical and Other Properties **2002**, 1-3.
254. Leskelä, M.; Niinistö, L. *Journal of Solid State Chemistry* **1976**, 19, (3), 245-250.
255. Fukutani, K.; Tanji, K.; Motoi, T.; Den, T. *Advanced Materials* **2004**, 16, (16), 1456-1460.
256. Zhang, S. *Journal of Physics: Condensed Matter* **2002**, 14, (34), R881.
257. Yang, W.; Liu, B.; Yang, B.; Wang, J.; Sekiguchi, T.; Thorsten, S.; Jiang, X. *Advanced Functional Materials* **2015**, 25, (17), 2543-2551.
258. Landge, S.; Ghosh, D.; Aiken, K., *Solvent-free synthesis of nanoparticles. In Green Chemistry, Elsevier: 2018*; pp 609-646.
259. Shombe, G. B.; Khan, M. D.; Zequine, C.; Zhao, C.; Gupta, R. K.; Revaprasadu, N. *Scientific Reports* **2020**, 10, (1), 1-14.
260. Shombe, G. B.; Khan, M. D.; Alenad, A. M.; Choi, J.; Ingsel, T.; Gupta, R. K.; Revaprasadu, N. *Sustainable Energy & Fuels* **2020**, 4, (10), 5132-5143.
261. Khan, M. D.; Aamir, M.; Sohail, M.; Bhoyate, S.; Hyatt, M.; Gupta, R. K.; Sher, M.; Revaprasadu, N. *Dalton Transactions* **2019**, 48, (11), 3714-3722.
262. Ayom, G. E.; Khan, M. D.; Ingsel, T.; Lin, W.; Gupta, R. K.; Zamisa, S. J.; van Zyl, W. E.; Revaprasadu, N. *Chemistry–A European Journal* **2020**, 26, (12), 2693-2704.
263. McNaughten, P. D.; Saah, S. A.; Akhtar, M.; Abdulwahab, K.; Malik, M. A.; Raftery, J.; Awudza, J. A.; O'Brien, P. *Dalton Transactions* **2016**, 45, (41), 16345-16353.
264. Zeng, N.; Hopkinson, D. G.; Spencer, B. F.; McAdams, S. G.; Tedstone, A. A.; Haigh, S. J.; Lewis, D. J. *Chemical Communications* **2019**, 55, (1), 99-102.
265. Akram, R.; Khan, M. D.; Zequine, C.; Zhao, C.; Gupta, R. K.; Akhtar, M.; Akhtar, J.; Malik, M. A.; Revaprasadu, N.; Bhatti, M. H. *Materials Science in Semiconductor Processing* **2020**, 109, 104925.
266. Zhang, C.; Zhang, S.; Yu, L.; Zhang, Z.; Zhang, P.; Wu, Z. *Materials Letters* **2012**, 85, 77-80.
267. Lazell, M.; O'Brien, P. *Chemical Communications* **1999**, (20), 2041-2042.
268. Wang, Y.; Chen, J.; Chen, L.; Chen, Y.-B.; Wu, L.-M. *Crystal Growth & design* **2010**, 10, (4), 1578-1584.
269. Chen, J.; Chen, L.; Wu, L.-M. *Inorganic chemistry* **2007**, 46, (19), 8038-8043.
270. Ghezelbash, A.; Sigman, M. B.; Korgel, B. A. *Nano Letters* **2004**, 4, (4), 537-542.
271. Yamamoto, M.; Nakamoto, M. *Chemistry Letters* **2003**, 32, (5), 452-453.

272. Lazell, M.; Nørager, S. J.; O'Brien, P.; Revaprasadu, N. *Materials Science and Engineering: C* **2001**, 16, (1-2), 129-133.
273. Shombe, G. B.; Khan, M. D.; Revaprasadu, N.; Alenad, A. M.; Mahmood, R. F. *SPR Nanoscience*, **2021**; pp 213-250.

CHAPTER 2

**Solventless synthesis of nanospinel $\text{Ni}_{1-x}\text{Co}_x\text{Fe}_2\text{O}_4$ ($0 \leq x \leq 1$)
solid solutions for efficient electrochemical water splitting and
supercapacitance**

2.1 Introduction

In the wake of the increasing demand for clean and renewable energy supply coupled with rapid depletion and non-renewability of fossil fuels, innovative energy generation and storage technologies are highly desired.^{1, 2} Electrocatalytic water splitting represents an efficient and flexible pathway for hydrogen production, a non-carbon-based alternative energy source. However, water splitting reactions have sluggish kinetics, large overpotential, and poor energy efficiency resulting from intricate processes of electrons/ions transfer in oxygen evolution (OER) and hydrogen evolution (HER) reactions.³ Although precious-metal-based catalysts have reportedly been employed to overcome these hurdles, their scarcity and substantial cost restrict their use in large-scale industrial applications.^{4, 5} On the other hand, electrochemical capacitors are regarded as promising candidates for energy storage due to their long life cycle and high power density compared to rechargeable batteries.⁶ However, their relatively low energy density has prevented their widespread use in high-energy applications. In this regard, research endeavours are focused on developing earth-abundant, low-cost, and stable noble metal-free electrocatalysts for water splitting and supercapacitors.⁷

Spinel ferrites with a general formula AFe_2O_4 (where A is a divalent transition metal) are a fundamentally important class of semiconductor materials, primarily due to their attractive properties. They display superior ion transport, rapid electrode kinetics and high electrochemical behaviour towards water splitting and supercapacitance.^{8, 9} Additionally, owing to their complex and elegant chemical composition, low band gap, valence states and stability, spinel ferrites have demonstrated interesting electrical, magnetic, optical, and catalytic properties.¹⁰⁻¹⁵ Spinel ferrites, such as $NiFe_2O_4$ and $CoFe_2O_4$, are composed of inexpensive, environmentally benign and easily accessible materials.¹⁶⁻¹⁸ Studies have indicated their applicability as electrode material in supercapacitors,^{19, 20} lithium-ion batteries,^{21, 22} as well as catalysts for electrochemical water splitting.^{23, 24} Their electrochemical performance is ascribed to the presence of electrochemically active multivalent cations of Ni^{3+}/Ni^{2+} , Co^{3+}/Co^{2+} and Fe^{3+}/Fe^{2+} . Despite all the appealing properties, the practical applications of these spinels for supercapacitors and water splitting are still relatively limited. This is due to unsatisfactory capacitance and a significant amount of energy would be inevitably lost due to internal resistances.^{6, 17} Likewise, their use as bifunctional catalysts for overall water splitting is hampered by their limited activity,²⁵ and the electrochemical performance of these materials still necessitates further improvement.

A promising approach for the improvement of these spinel ferrite's electrochemical performance is to design a nanostructured solid solution. Consequently, the resultant solid solutions possess the additional composition-dependent synergistic effect of different elements, apart from properties emanating from the quantum confinement effects.²⁶ In preparation of the solid solution, the chemical valence, crystallographic parameters, and radius of the component ions should be greatly considered for minimum formation energy and composition tuning in continuum.²⁷ Interestingly, both NiFe_2O_4 and CoFe_2O_4 are isostructural and consist of isovalent Ni^{2+} and Co^{2+} , thus they are characterized by the ability to form a highly diverse range of substitutional solid solutions following Hume-Rothery rules.²⁸ The resultant effect is an enhancement of the overall properties as the mixed nickel-cobalt ferrite solid solution is an electrochemically efficient material compared to the pristine NiFe_2O_4 and CoFe_2O_4 .

Likewise, controlled preparation of solid solutions is likely to augment the number of exposed atoms, surface area, number of active sites and electrical conductivity,¹ which permit facile ion-diffusion and increased electrode-electrolyte interfacial interaction.^{18, 29, 30} This approach affords the fabrication of more sophisticated electrode materials for supercapacitors, HER and OER with enhanced activity.³¹ For example, nanospinel $\text{NiFe}_{2-x}\text{Cr}_x\text{O}_4$ ($0 \leq x \leq 1$), prepared by a simple precipitation approach, showed an increase in OER activity when Cr content was increased from 0.2 to 1.0 mol in the spinel lattice of NiFe_2O_4 .³² In addition, the synthesis of $\text{CuFe}_{2-x}\text{Cr}_x\text{O}_4$ ($0 \leq x \leq 1$) has been achieved by employing a precipitation route, and the improvement in electronic properties was found in favour of OER catalysis in basic media.³³

Nevertheless, for solid solutions, the composition control and nucleation in the nano regime are quite challenging. Particularly, the growth dynamics, solubility and crystallization process vary vastly when the component elements increase. In this regard, a well-designed reaction protocol and accurate control of the growth parameters are indispensable for obtaining homogeneous solid solution nanostructures and avoiding any probable phase segregation.³⁴ Recently, solventless thermolysis has emerged as an alternative method for the large-scale fabrication of diverse homogeneous nanostructures. It is an environmentally benign, scalable and straightforward approach in which precursor materials undergo solid-state decomposition by thermal treatment.^{35, 36} Compared with the most frequently used solution-based techniques, this approach ensures an inexpensive synthesis of nanoscopic oxide materials with surfaces free of any insulating surfactants. The surfactants adhere to the active surfaces of the catalyst and block/reduce the interaction of reactant molecules with the

active sites. Therefore, the synthesis of bare surface nanoparticles may show much enhanced catalytic activity due to exposed active sites. Moreover, it has not been extensively utilized to synthesize nanoferrite solid solutions from metal-organic precursors.

In this study, we have utilized the solventless thermolysis method to prepare uncapped solid solutions of $\text{Ni}_{1-x}\text{Co}_x\text{Fe}_2\text{O}_4$ ($0 \leq x \leq 1$) from the respective metal acetylacetonate precursors and examined their potential for electrochemical water splitting and supercapacitance. With reference to the review of existing published works, there is no report on the solventless synthesis of $\text{Ni}_{1-x}\text{Co}_x\text{Fe}_2\text{O}_4$ ($0 \leq x \leq 1$) solid solutions from metal acetylacetonates.

2.2 Experimental

2.2.1 Chemicals

Nickel (II) acetylacetonate (98%, Merck-Schuchardt), cobalt (II) acetylacetonate (98%, Merck-Schuchardt), and iron (III) acetylacetonate (97%, Sigma-Aldrich). All metal acetylacetonate complexes were used as received.

2.2.2 Solventless synthesis of $\text{Ni}_{1-x}\text{Co}_x\text{Fe}_2\text{O}_4$ ($0 \leq x \leq 1$) solid solutions

The $\text{Ni}_{1-x}\text{Co}_x\text{Fe}_2\text{O}_4$ ($0 \leq x \leq 1$) solid solutions of different stoichiometric compositions were prepared by solventless thermolysis of metal acetylacetonates. For the typical synthesis of ternary NiFe_2O_4 nanoparticles, 0.10 g (0.39 mmol) of nickel acetylacetonate and 0.27 g (0.78 mmol) of iron acetylacetonate were mixed and the solid mixture was grounded using pestle and mortar for ≈ 20 minutes to obtain a homogeneous mixture. The precursor mixture was then placed into a ceramic boat, which was placed in a reactor tube. The reactor tube was then introduced inside the carbolite tube furnace in such a way that the ceramic boat must be placed almost in the middle of the heating zone, followed by thermal treatment at 450 °C, at a heating rate of 20 °C per minute for 1 h. After 1 h of annealing, the heating was switched off, and the furnace was left to cool naturally to ambient temperature. The reactor tube was taken out of the furnace upon cooling, and the product was collected for analysis without any post-treatment. Likewise, the synthesis of CoFe_2O_4 nanoparticles was achieved by employing similar procedures except that cobalt acetylacetonate was used instead of nickel acetylacetonate and the amount of cobalt and iron complexes were maintained in the same mole ratio of 1:2.

For the synthesis of quaternary $\text{Ni}_{1-x}\text{Co}_x\text{Fe}_2\text{O}_4$ ($x = 0.2, 0.4, 0.6, 0.8$) solid solutions, a known quantity of nickel acetylacetonate was partially substituted by appropriate amounts of cobalt acetylacetonate by adjusting the mole ratios of Co and Ni in the intervals of 0.2, 0.4, 0.6, and 0.8, while keeping the amount of iron acetylacetonate unchanged in the reaction mixture. The reaction procedures for the entire series of solid solutions were similar to those employed to synthesize the ternary nickel and cobalt ferrites.

2.3 Characterization techniques for $\text{Ni}_{1-x}\text{Co}_x\text{Fe}_2\text{O}_4$ ($0 \leq x \leq 1$) solid solutions

2.3.1 Powder X-ray diffraction analysis

The crystalline phase of the spinel $\text{Ni}_{1-x}\text{Co}_x\text{Fe}_2\text{O}_4$ ($0 \leq x \leq 1$) solid solutions was ascertained by powder X-ray diffraction (p-XRD) analysis employing a Bruker AXS D8 Advance X-ray diffractometer. The instrument uses nickel-filtered $\text{Cu K}\alpha$ radiation ($\lambda=1.5418\text{\AA}$) at 40 kV, 40 mA. The analysis was performed in the values of 2θ ranging from 10 to 80° and the data obtained were also utilized to compute the structural parameters such as cell volume, lattice constants and crystallite size.

2.3.2 Scanning electron microscopy and energy dispersive X-ray analyses

Scanning electron microscopy (SEM) analysis was performed on a ZEISS-Auriga Cobra SEM while energy dispersive X-ray (EDX) elemental analysis was carried out on a Zeiss Ultra Plus Field Emission Gun Scanning Electron Microscope (FEG SEM).

2.3.3 X-ray photoelectron spectroscopy

X-ray photoelectron spectroscopy (XPS) analysis was conducted using Kratos Axis Ultra DLD X-ray Photoelectron spectrophotometer. For the experimental setup the emission was set at 10 mA, the anode (HT) at 15 kV, the pressure for the analysis chamber was 5×10^{-9} Torr, hybrid lens, and resolution to acquire survey scans was at 80 eV pass energy in slot mode centred at 597.5 with the width of 1205 eV, and steps at 1 eV and dwell time at 100 ms. High resolution core-level spectra were acquired at 40 eV pass energy in slot mode centred at 285 eV for C 1s, and the step size was 0.05 eV and dwell time at 500 ms.

2.3.4 Transmission electron microscopy (TEM) and High resolution TEM (HRTEM) analyses

The TEM and HRTEM imaging techniques were collectively used to determine the morphological and microstructural features of the $\text{Ni}_{1-x}\text{Co}_x\text{Fe}_2\text{O}_4$ ($0 \leq x \leq 1$) solid solutions.

TEM imaging was performed on a JEOL 1400 TEM while HRTEM images were captured on a JEOL 2100 HRTEM, at accelerating voltages of 120 kV and 200 kV, respectively.

2.3.5 Ultraviolet-visible (UV-Vis) spectroscopy

The optical absorbance measurements were conducted in the UV-Vis spectral range on a Varian Cary 50 UV/Vis spectrophotometer.

2.4 Electrochemical studies

The electrochemical behaviour of the synthesized $\text{Ni}_{1-x}\text{Co}_x\text{Fe}_2\text{O}_4$ ($0 \leq x \leq 1$) solid solutions was investigated by Gamry Potentiostat using a three-electrode system. A paste comprising $\text{Ni}_{1-x}\text{Co}_x\text{Fe}_2\text{O}_4$ sample (80 wt.%), polyvinylidene difluoride (PVDF, 10 wt.%) and acetylene black (10 wt.%) was prepared using N-methyl pyrrolidinone (NMP) as a solvent. This paste was then applied to pre-cleaned and weighted nickel foam. The paste was then dried under vacuum at 60 °C for 10 hours and used as a working electrode. A platinum wire and Hg/HgO were used as counter and reference electrodes, respectively. In all supercapacitance and water splitting experiments, 3M and 1M KOH were employed as the electrolyte, respectively. Measurements of charge storage capacity were performed by cyclic voltammetry (CV) at various scan rates as well as galvanostatic charge-discharge (GCD) at different current densities. Studies on the electrocatalytic activity of $\text{Ni}_{1-x}\text{Co}_x\text{Fe}_2\text{O}_4$ electrodes were carried out by linear sweep voltammetry (LSV), chronoamperometry (CA) and cyclic voltammetry. For both OER and HER measurements, LSV was carried out at a scan rate of 2 mV/s. Electrochemical impedance spectroscopy (EIS) was done in the frequency range of 0.05 Hz to 10 kHz with an applied AC amplitude of 10 mV.

2.5 Results and discussion

2.5.1 Powder X-ray diffraction analysis

Among different precursors for the preparation of metal oxides, the choice of metal acetylacetonate precursors is based on their low melting points, environmental benignity, commercial availability at affordable cost and their clean decomposition.³⁷ Although they have been used to prepare spinel ferrites, $\text{Ni}_{1-x}\text{Co}_x\text{Fe}_2\text{O}_4$ ($0 \leq x \leq 1$) solid solution has not been prepared from metal acetylacetonates.

The crystalline phase of $\text{Ni}_{1-x}\text{Co}_x\text{Fe}_2\text{O}_4$ ($0 \leq x \leq 1$) solid solutions was investigated using powder X-ray diffraction (p-XRD) analysis. Fig. 2.1 (a) indicates the p-XRD pattern of $\text{Ni}_{1-x}\text{Co}_x\text{Fe}_2\text{O}_4$ ($0 \leq x \leq 1$) solid solutions whose diffraction peaks are indexed to the (220),

(311), (222), (400), (422), (511) and (440) planes, confirming the formation of a single-phase cubic spinels with $Fd3m$ space group. The diffraction peaks of the pristine NiFe_2O_4 ($x = 0$) and CoFe_2O_4 ($x = 1$) were found to match well with the standard diffraction peaks of pure NiFe_2O_4 (ICDD # 00-044-1485) and CoFe_2O_4 (ICDD # 00-001-1121), respectively. Also, the diffraction peaks of the $\text{Ni}_{1-x}\text{Co}_x\text{Fe}_2\text{O}_4$ solid solutions with cobalt composition from $x = 0.2$ to $x = 0.8$ were consistent with those of the pristine materials and were found to lie in between the two pure ferrite systems of nickel and cobalt. Interestingly, no extra peaks associated with any impurity were present, suggesting the formation of a series of crystalline, monophasic solid solutions between pure NiFe_2O_4 and CoFe_2O_4 . The diffraction pattern was similar for pristine and the alloyed compositions, which indicates that the lattice symmetry was retained during the substitution of Ni^{2+} by Co^{2+} ions. It also indicates the successful inclusion of Co^{2+} into the NiFe_2O_4 lattice system. Additionally, the observed differences in peak intensities between the parent ferrites and the solid solutions are ascribed to the internal stresses and planar faults caused by different amount of Co^{2+} or uneven cation distribution at the tetrahedral and octahedral positions, respectively.³⁸ Furthermore, slight peak broadening is observed in alloyed compositions which could probably be caused by reduction in crystallite size or/and the increase in lattice strain arising from the presence of lattice defects or microstresses upon cobalt substitution in the pristine NiFe_2O_4 .^{38, 39}

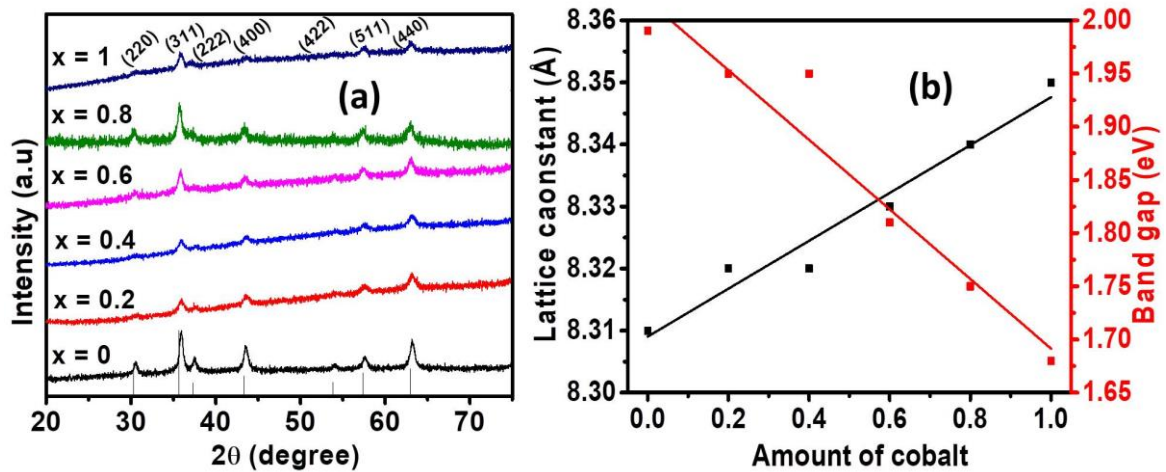


Fig. 2.1. (a) p-XRD patterns of $\text{Ni}_{1-x}\text{Co}_x\text{Fe}_2\text{O}_4$ ($0 \leq x \leq 1$) series. (b) variation of lattice constant (left y-axis) and the optical band gap (right y-axis) with cobalt content.

The lattice constants ($a = b = c$) of the synthesized nanospinels were calculated from the p-XRD data and their values presented in Table 2.1. The estimation of the average values was achieved by considering the mean values of a computed for each diffraction peak by employing the equation: $a = d\sqrt{h^2 + k^2 + l^2}$, where d is the inter-planer spacing obtained

from Bragg's law while h , k and l represents Miller indices.⁴⁰ The lattice parameters are observed to increase almost in a linear fashion with the increasing amount of cobalt. The linear increase in lattice parameters can be explained by the difference in the ionic sizes of the substituting cations. The small Ni^{2+} ions (0.69 Å) is replaced by slightly larger Co^{2+} ions (0.74 Å) in $\text{Ni}_{1-x}\text{Co}_x\text{Fe}_2\text{O}_4$ system, introducing strain and gradual expansion of the ferrite unit cell which in turn contributes to the observed increase in the lattice parameters while the lattice symmetry remains intact. The values of lattice parameters for the alloyed samples were found to lie within the range of the lattice parameters of the two pristine cubic phases.⁴¹ The experimental values for lattice constant (8.313 Å) for pure NiFe_2O_4 are consistent with the standard values (8.337 Å, ICDD #: 00-044-1485). However, a slight discrepancy between the standard and experimental lattice constant values is noted, which is due to the stresses and/or approximation which regards all ions to be rigid spheres spread in a rigid fashion.⁴² A plot of the lattice constants with respect to Co^{2+} content used in precursor mixture shows a linear relationship (Fig. 2.1(b)). In general, the observed linear dependence existing between the values of lattice constant is in compliance with Vegard's law.⁴³

The crystallite sizes of $\text{Ni}_{1-x}\text{Co}_x\text{Fe}_2\text{O}_4$ solid solutions were estimated from p-XRD data using Debye Scherrer's formula.⁴⁴ The estimation was done by considering the line broadening of the most intense peak (311) and the crystallite sizes of $\text{Ni}_{1-x}\text{Co}_x\text{Fe}_2\text{O}_4$ were found to be in the range of 8-19 nm (**Table 2.1**). In addition, the crystallite sizes were observed to decrease with increasing amount of cobalt from $x = 0$ to $x = 1$ due to slight peak broadening and micro-strain in the lattice structure. However, a non-uniform trend in the changes of crystallite sizes with respect to Co^{2+} content was noted.

2.5.2 EDX composition analysis

EDX analysis was performed to provide both qualitative and quantitative description of elemental composition in the synthesized $\text{Ni}_{1-x}\text{Co}_x\text{Fe}_2\text{O}_4$ ($0 \leq x \leq 1$) solid solutions (Fig. 2.2). The EDX spectra of pristine NiFe_2O_4 ($x = 0$) authenticated the presence of Ni, Fe and O while that of pure CoFe_2O_4 ($x = 1$) confirmed the presence of Co, Fe and O. The EDX patterns of $\text{Ni}_{1-x}\text{Co}_x\text{Fe}_2\text{O}_4$ solid solutions from $x = 0.2$ to $x = 0.8$ confirmed the presence of Ni, Co, Fe and O. Again, no impurity was observed in the EDX spectra of all samples, and hence these results corroborate well with the p-XRD results which shows the formation of a series of phase-pure spinel ferrites. The experimental elemental composition in terms of normalized atomic percentage confirmed the presence of all atoms in a good stoichiometric ratio as expected. This infers that the nominal stoichiometric ratio of different metal

components mixed at the time of preparation is consistent with the amount obtained in the final product (Table 2.1), suggesting that there is no unexpected chemical reaction or any significant loss of ingredients. EDX elemental mapping displayed in Figs. 2.3 and 2.4 indicate uniform distribution of the respective elements in all $\text{Ni}_{1-x}\text{Co}_x\text{Fe}_2\text{O}_4$ ($0 \leq x \leq 1$) nanospinel ferrites.

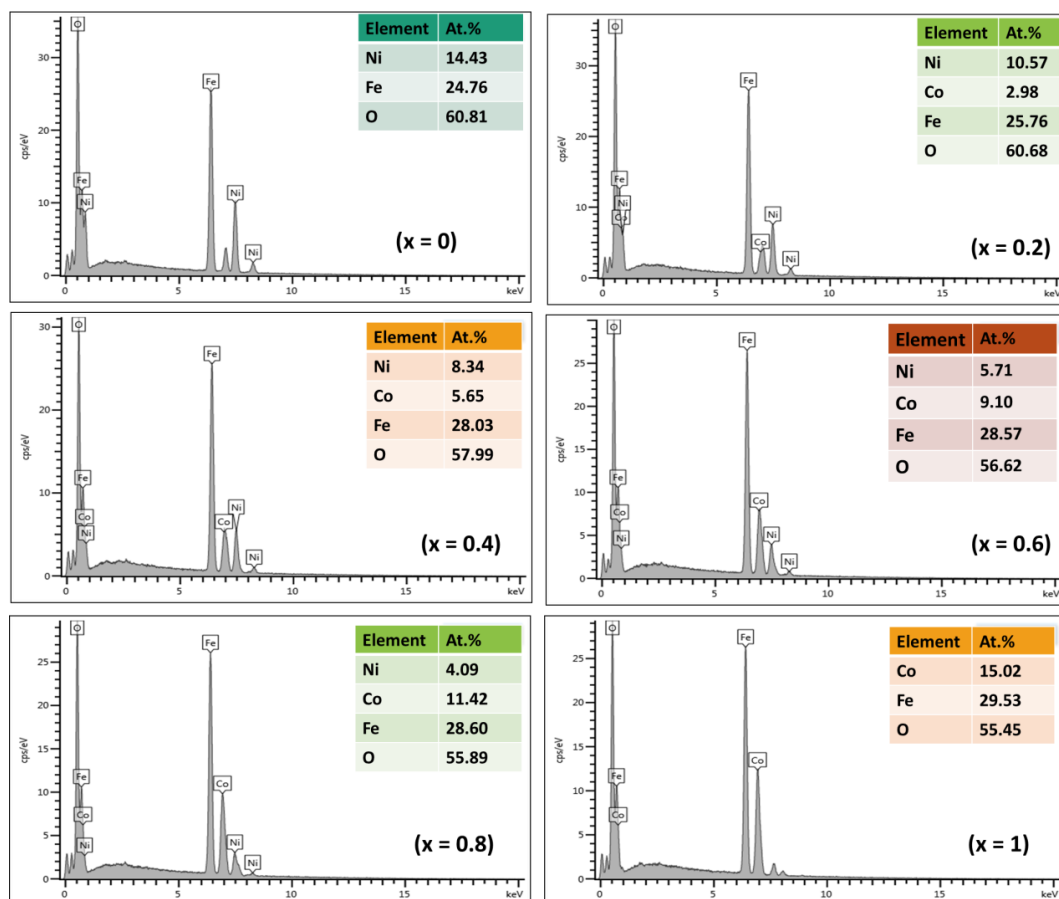


Fig. 2.2. EDX spectra for the prepared $\text{Ni}_{1-x}\text{Co}_x\text{Fe}_2\text{O}_4$ ($0 \leq x \leq 1$) nanoparticles.

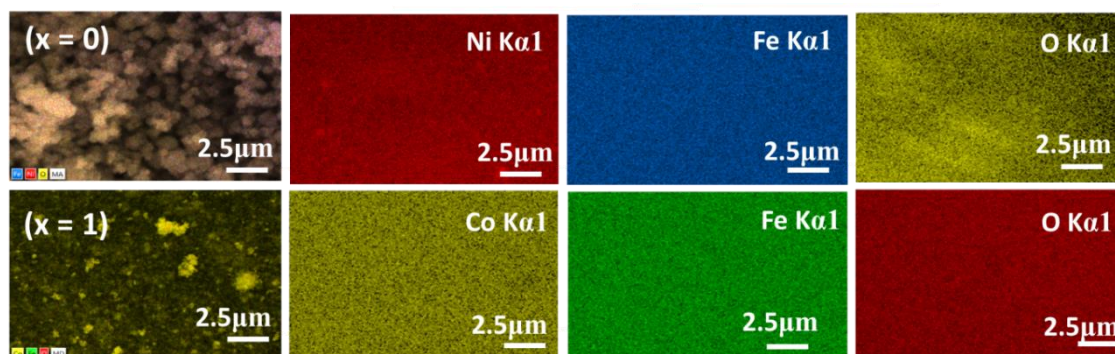


Fig. 2.3. EDX elemental mapping of NiFe_2O_4 ($x = 0$) and CoFe_2O_4 ($x = 1$) showing a uniform distribution of elements.

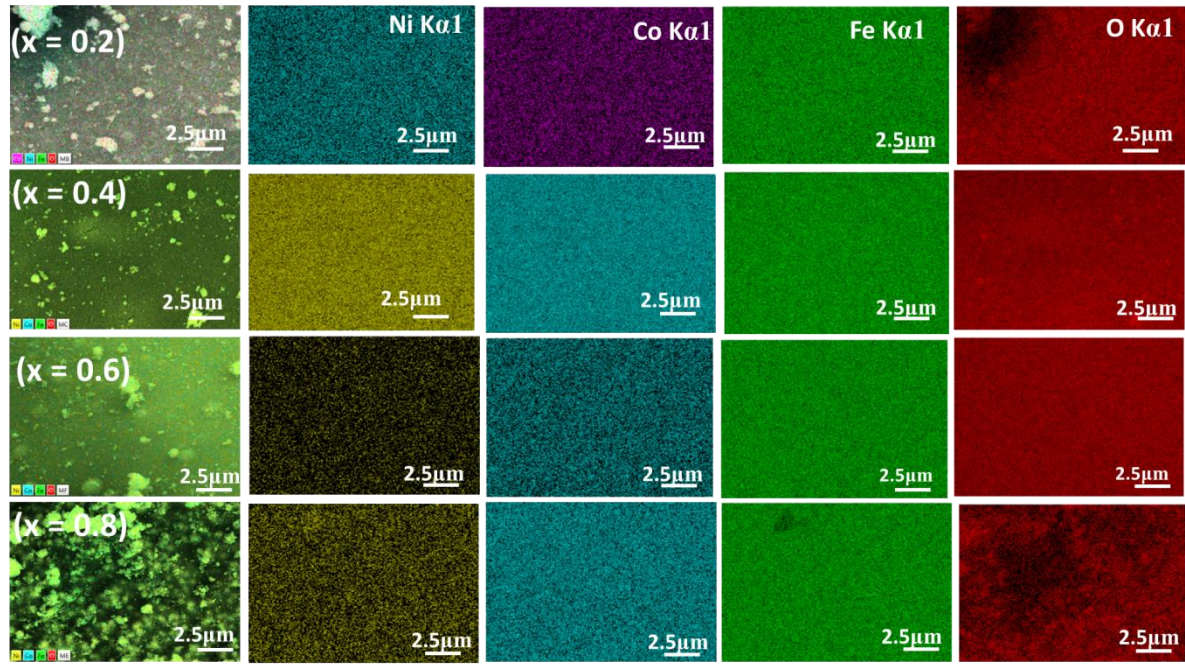


Fig. 2.4. EDX elemental mapping of $\text{Ni}_{1-x}\text{Co}_x\text{Fe}_2\text{O}_4$ ($0.2 \leq x \leq 0.8$) solid solutions showing a uniform distribution of elements.

Table 2.1. Lattice parameter (a), crystallite size (d), unit cell volume (V), band gap (E_g), and EDX compositions of $\text{Ni}_{1-x}\text{Co}_x\text{Fe}_2\text{O}_4$ solid solutions at different cobalt contents (x).

	Target ferrite composition	Stoichiometry obtained from EDX	a (Å)	d (nm)	V (Å ³)	E_g (eV)
(x)						
0	NiFe_2O_4	$\text{Ni}_{1.01}\text{Fe}_{1.73}\text{O}_{4.26}$	8.313	19.40	574.48	1.99
0.2	$\text{Ni}_{0.8}\text{Co}_{0.2}\text{Fe}_2\text{O}_4$	$\text{Ni}_{0.74}\text{Co}_{0.21}\text{Fe}_{1.80}\text{O}_{4.25}$	8.317	8.91	575.31	1.95
0.4	$\text{Ni}_{0.6}\text{Co}_{0.4}\text{Fe}_2\text{O}_4$	$\text{Ni}_{0.58}\text{Co}_{0.39}\text{Fe}_{1.96}\text{O}_{4.06}$	8.321	14.43	576.14	1.95
0.6	$\text{Ni}_{0.4}\text{Co}_{0.6}\text{Fe}_2\text{O}_4$	$\text{Ni}_{0.39}\text{Co}_{0.64}\text{Fe}_{1.99}\text{O}_{3.96}$	8.334	10.73	578.84	1.81
0.8	$\text{Ni}_{0.2}\text{Co}_{0.8}\text{Fe}_2\text{O}_4$	$\text{Ni}_{0.29}\text{Co}_{0.79}\text{Fe}_{2.0}\text{O}_{3.91}$	8.349	12.90	581.97	1.75
1	CoFe_2O_4	$\text{Co}_{1.05}\text{Fe}_{2.07}\text{O}_{3.88}$	8.351	9.68	582.39	1.67

2.5.3 XPS Analysis

The XPS was used to investigate the chemical states and to determine quantitative surface composition of $\text{Ni}_{1-x}\text{Co}_x\text{Fe}_2\text{O}_4$ nanoparticles. The analysis was performed on three representative samples with cobalt content, $x = 0.2$, 0.4 and 0.6 . The survey spectra shown in in Fig. 2.5(a) depict the presence of Ni 2p (854 eV), Co (783 eV), Fe 2p (710 eV), and O 1s (529 eV) as expected from the prepared samples for (i) $x = 0.2$, (ii) $x = 0.4$ and (iii) $x = 0.6$.

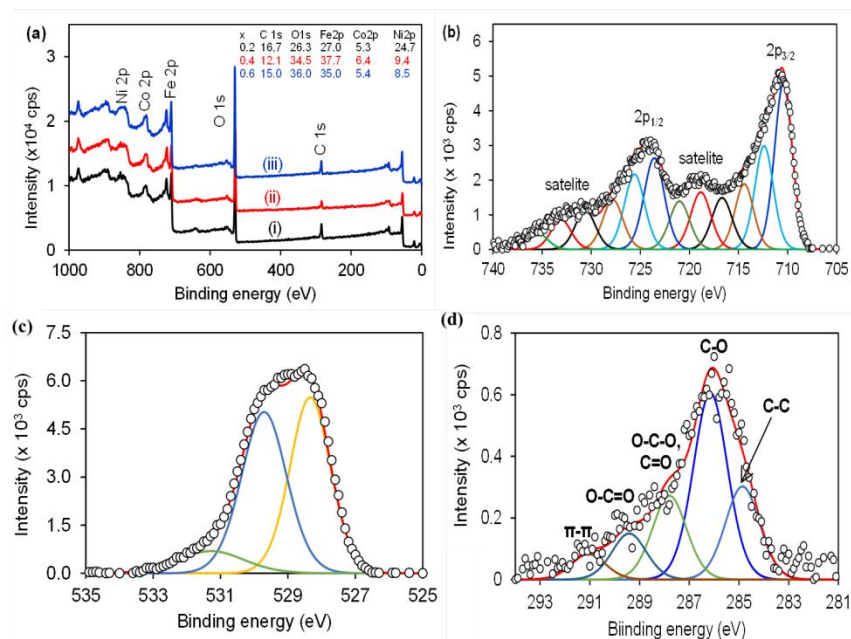


Fig. 2.5: (a) Survey spectra for $\text{Ni}_{1-x}\text{Co}_x\text{Fe}_2\text{O}_4$: (i) $x = 0.2$, (ii) $x = 0.4$, (iii) $x = 0.6$. (b) High resolution core-level spectra of Fe 2p for $x = 0.6$. XPS high resolution core-level spectra of (c) O 1s and (d) C 1s of the ternary $\text{Ni}_{1-x}\text{Co}_x\text{Fe}_2\text{O}_4$ ($x = 0.4$).

The presence of C 1s (284 eV) is probably ascribed to the surface ligands produced during decomposition of metal acetylacetonate precursors.³⁵ Additionally, carbon is the material which is always present in atmosphere, so it is likely to find some monolayers of contamination from environmental air, especially the ubiquitous 284eV signal. Also, although it is possible to minimize it under very restrictive circumstances during analysis, but CO will desorb from the walls of a steel ultra high vacuum chamber and there is potential backstreaming contamination from hydrocarbon pump oil depending on the system as well. Furthermore, the signal strength of C1s shows the possibility of adsorbed CO or CO₂ in which O1s contains C-O, C=O, O-C=O, O-C-O related binding energies between 532-536eV. The elemental composition of each sample is shown in the inset of Fig. 2.5(a). The XPS results further shows that the composition of Ni to Co designated by a subscript x for all samples was equivalent to the predicted values during the preparation. Evidently, the stoichiometric ratio was found to be 0.86 (Ni) vs 0.2 (Co), 0.61 (Ni) vs 0.4 (Co), and 0.42 (Ni) vs 0.6 (Co) for $x = 0.2$, 0.4 and 0.6, respectively. The results confirmed the increase in the amount of Co with the decreasing Ni content. The high resolution core-level spectra of Fe 2p in Fig. 2.5(b) is similar to the samples prepared. The fitting shows multiple oxidation states of Fe^0 , Fe^{2+} and Fe^{3+} . The high resolution of core-level spectra of Co 2p and Ni 2p could not be deconvoluted due to very small signals. The high resolution core-level spectra of

O 1s and C 1s shown Fig. 2.5 (c) and (d), respectively, for the ternary $\text{Ni}_{1-x}\text{Co}_x\text{Fe}_2\text{O}_4$ ($x = 0.4$) was similar for other samples ($x = 0.2$ and 0.4). The spectra were deconvoluted and multiple peaks were identified, corresponding to the material used for the synthesis of $\text{Ni}_{1-x}\text{Co}_x\text{Fe}_2\text{O}_4$ at 450°C .

2.5.4 SEM, TEM and HRTEM analyses

The analysis of surface morphology, microstructure and particle size is crucial since these parameters control the overall properties and hence the application of spinel nanoferrites. The SEM micrographs presented in Fig. 2.6 show the surface morphologies of $\text{Ni}_{1-x}\text{Co}_x\text{Fe}_2\text{O}_4$ solid solutions prepared from molecular precursors of metal acetylacetonates by using solventless thermolysis method. It is apparent from the SEM images that the formation of octahedron and cubic shaped particles, with some truncated edges, of monophasic $\text{Ni}_{1-x}\text{Co}_x\text{Fe}_2\text{O}_4$ solid solutions was achieved at different Co^{2+} stoichiometries. It can also be inferred from the SEM images that the uniformity of particles vary with different quantities of cobalt, incorporated in the crystal lattice of nickel ferrite. This variation in particle uniformity is due to the difference between the driving force responsible for particle boundary movement and the retarding force exerted by the pores during particle growth/formation.⁴⁵ The appearance of somewhat agglomerated $\text{Ni}_{1-x}\text{Co}_x\text{Fe}_2\text{O}_4$ nanoparticles is a result of interaction arising from the magnetic nature of the nanoparticles, which make them to be held together due to intensive Van der Waals attractive forces.⁴⁶ Particle agglomeration can also be ascribed to the absence of capping agents during thermolysis, as the method proceeds without the use of solvents or passivating agents. The average particle size estimated from SEM micrographs (47.8 nm) was larger than the value of crystallite size computed according to Scherrer formula from p-XRD data (12.7 nm). However, SEM analysis has its limitations in image magnifications and in addition, this disparity in particle size between p-XRD and SEM could probably be attributable to the aggregation of the nanoparticles.⁴⁶

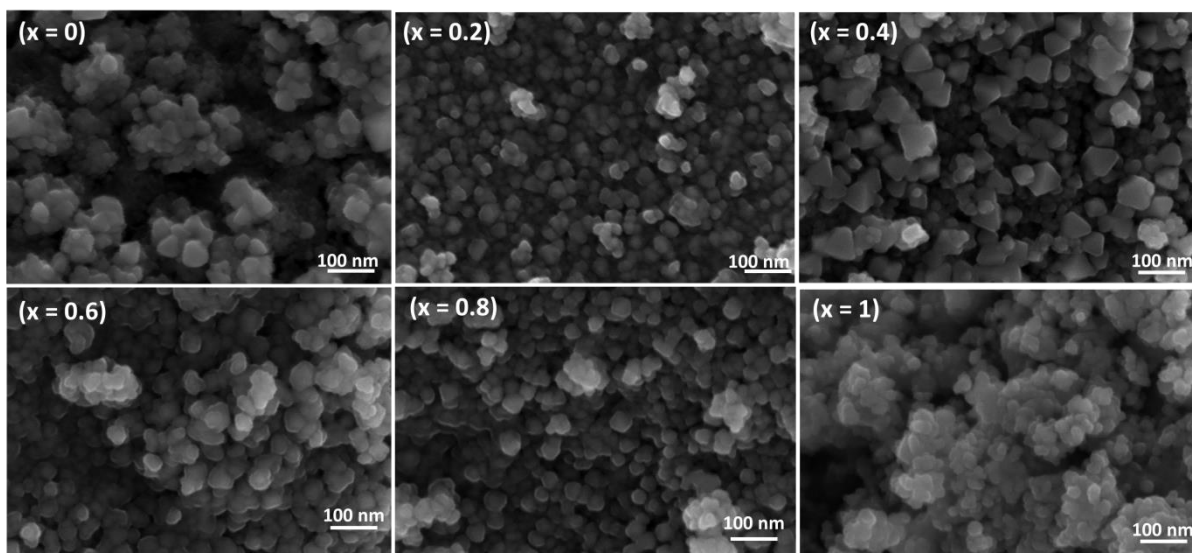


Fig. 2.6. SEM images of $\text{Ni}_{1-x}\text{Co}_x\text{Fe}_2\text{O}_4$ ($0 \leq x \leq 1$) solid solutions.

In order to have a better understanding of the size and morphology, the $\text{Ni}_{1-x}\text{Co}_x\text{Fe}_2\text{O}_4$ ($0 \leq x \leq 1$) solid solutions were also analysed by TEM analysis (Fig. 2.7). Well-separated cubic and octahedron-shaped nanoparticles are observed, having average size around 14 - 23.2 nm. Some particles are agglomerated possibly due to interfacial forces. Such aggregation of particles has also been reported in the literature.⁴⁷ The average particle sizes of $\text{Ni}_{1-x}\text{Co}_x\text{Fe}_2\text{O}_4$ ($0 \leq x \leq 1$) solid solutions observed in the TEM images are consistent with those estimated from p-XRD.

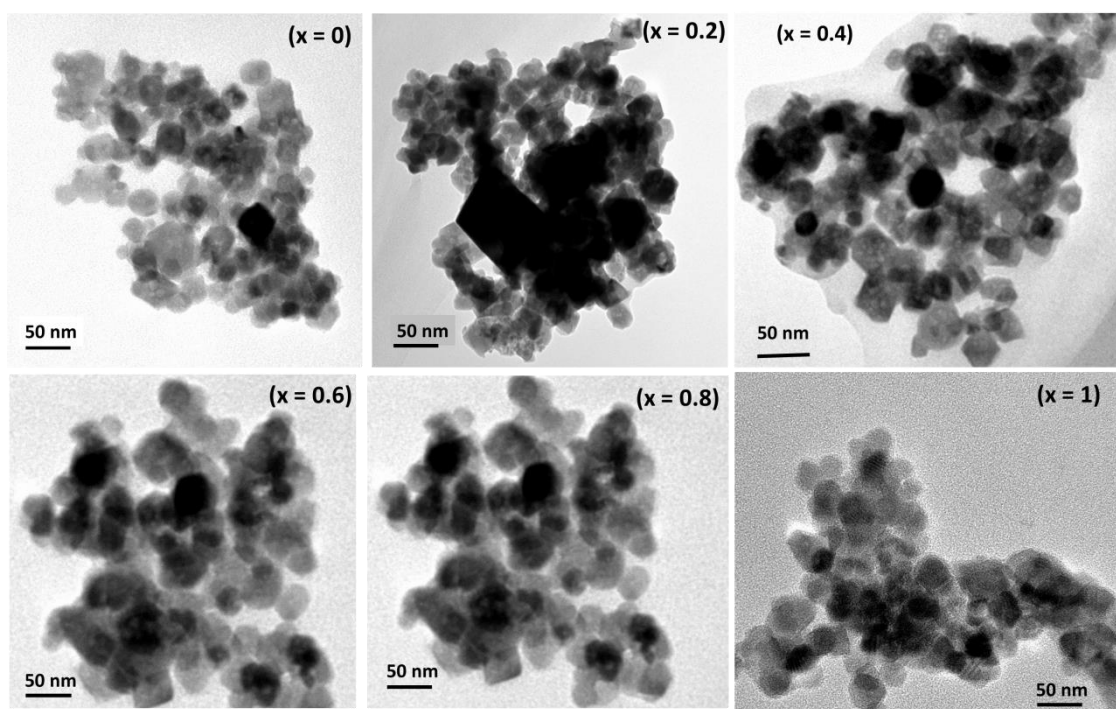


Fig. 2.7. TEM images of $\text{Ni}_{1-x}\text{Co}_x\text{Fe}_2\text{O}_4$ ($0 \leq x \leq 1$) solid solutions.

The HRTEM images presented in Fig. 2.8 clearly display the lattice interplanar spacing, which shows that extremely fine particles are properly crystallized into single crystals. The average d-spacing of 0.21, 0.25, 0.26, 0.29 and 0.30 nm were computed by profile of frame at different regions of image. The interplanar distances are in compliance with (400), (311) and (220) planes of the spinel NiFe_2O_4 and CoFe_2O_4 nanospinels.^{48, 49} The absence of secondary phase in HRTEM analysis suggests a good agreement with the p-XRD results.

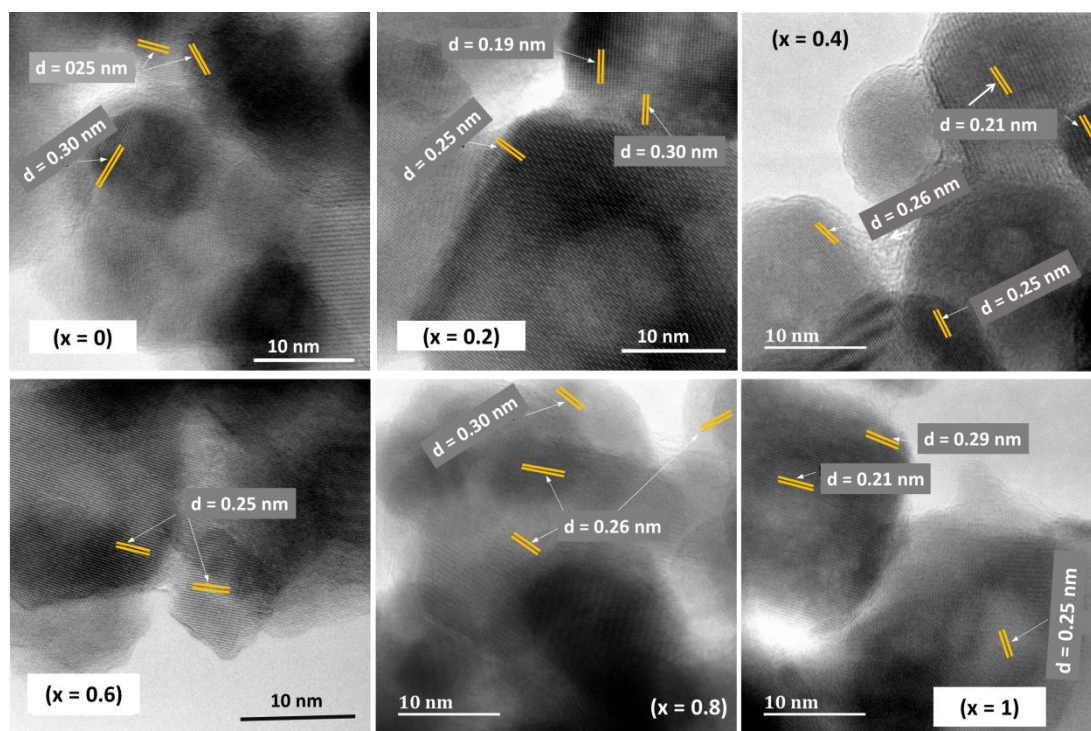


Fig. 2.8. HRTEM images of $\text{Ni}_{1-x}\text{Co}_x\text{Fe}_2\text{O}_4$ ($0 \leq x \leq 1$) solid solutions.

2.5.5 Analysis of optical properties

The optical properties of the synthesized $\text{Ni}_{1-x}\text{Co}_x\text{Fe}_2\text{O}_4$ solid solutions were studied by UV-Vis spectroscopy and the results obtained are displayed in Fig. 2.9. The absorption spectra of the prepared solid solution series show an absorption in the range of 400-800 nm. The values of band gap were computed from the Tauc plots of $(\alpha h\nu)^2$ vs photon energy, $h\nu$ (Fig. 2.10), where α stands for absorption coefficient, ν represents frequency of UV-Vis radiation and h is Planck's constant.⁵⁰ The estimated values of band gap were found to decrease slightly from 1.98 to 1.67 eV with the increase in cobalt content (Table 2.1 and Fig. 2.1(b)), and is related to the inclusion of slightly larger Co^{2+} ions in NiFe_2O_4 which creates less deep Co^{2+} states due to weaker electrostatic interaction, hence shortening the energy band gap. To a certain degree, the change in energy band gap might also be affected by

localized electronic states present in the material. In the present case, the red shift is attributed to the sp-d exchange interactions occurring between the band electrons and the localized d electrons of Co^{2+} replacing Ni^{2+} ions.⁵¹ A similar observation in the absorption edge was previously reported in copper substituted nickel ferrite.⁵² In general, it is worth noting that the range of band gap values obtained in this study suggests the applicability of the synthesized $\text{Ni}_{1-x}\text{Co}_x\text{Fe}_2\text{O}_4$ solid solutions in photocatalysis and optoelectronics.

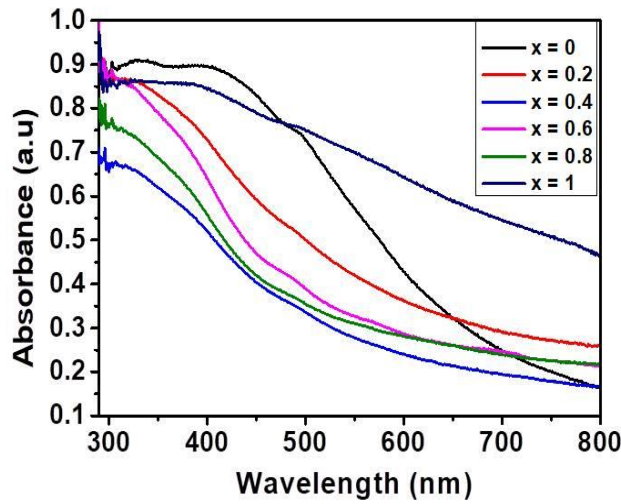


Fig. 2.9. UV-Vis absorption spectrum of $\text{Ni}_{1-x}\text{Co}_x\text{Fe}_2\text{O}_4$ ($0 \leq x \leq 1$) solid solutions.

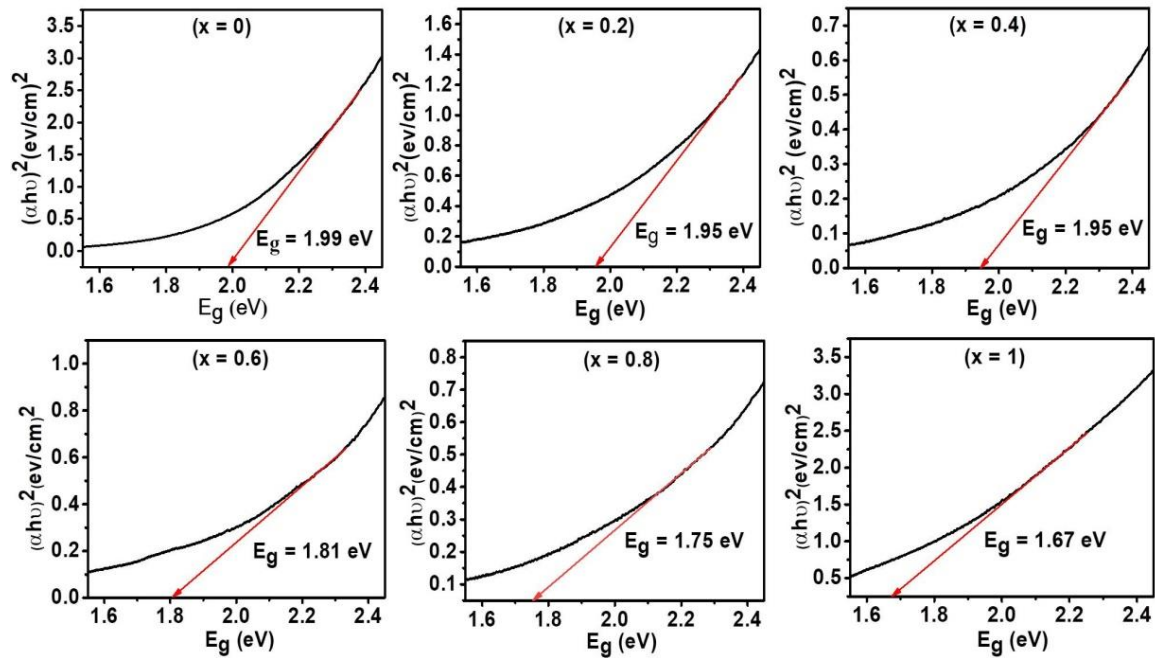


Fig. 2.10. Tauc plots of $(\alpha h\nu)^2$ versus energy for $\text{Ni}_{1-x}\text{Co}_x\text{Fe}_2\text{O}_4$ ($0 \leq x \leq 1$) solid solutions.

2.5.6 Electrochemical performance of $\text{Ni}_{1-x}\text{Co}_x\text{Fe}_2\text{O}_4$ ($0 \leq x \leq 1$) solid solutions

2.5.6.1 Supercapacitance

The supercapacitor characteristics of the $\text{Ni}_{1-x}\text{Co}_x\text{Fe}_2\text{O}_4$ ($0 \leq x \leq 1$) electrodes were evaluated using cyclic voltammetry (CV) and galvanostatic charge-discharge (GCD) curves in 3M KOH electrolyte within a potential range (0 – 0.6 V vs. Hg/HgO). Fig. 2.11 displays the CV graphs of $\text{Ni}_{1-x}\text{Co}_x\text{Fe}_2\text{O}_4$ samples with compositions $x = 0, 0.2, 0.4, 0.6, 0.8$ and 1 from a low scan rate (2 mV/s) to a high scan rate (300 mV/s). In all compositions of $\text{Ni}_{1-x}\text{Co}_x\text{Fe}_2\text{O}_4$ samples, two peaks generated by reversible redox reaction were observed in the CV plots, indicating the pseudocapacitive property of the synthesized solid solutions. Also, a shift in redox peak towards higher potential with a change in the scan rates was observed which suggests that a diffusion-controlled charge-transfer process is the predominant charge-transport process.⁵³ As seen in the graph, the shape of the CV curves remained unchanged even at a high scan rate, signifying excellent capacitive, stability, and charge storing properties of the electrodes even at the fast charge-transfer process.⁵⁴

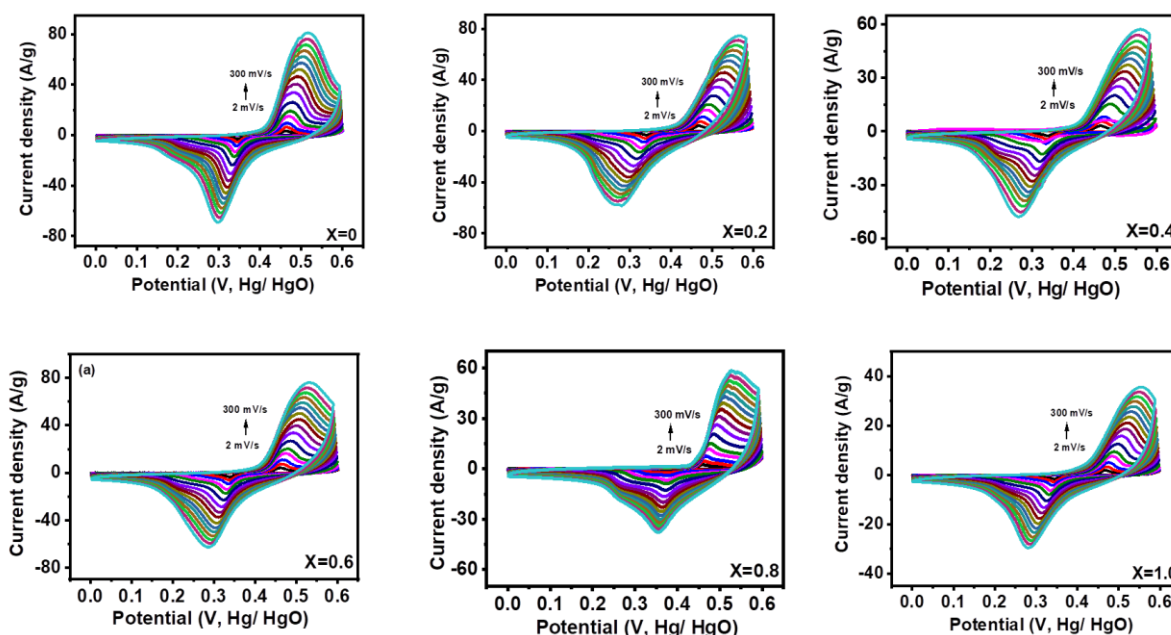


Fig. 2.11. CV graphs of $\text{Ni}_{1-x}\text{Co}_x\text{Fe}_2\text{O}_4$ ($0 \leq x \leq 1$) electrodes at various scan rates (2mV/s – 300mV/s) .

Quantitative analysis of the electrochemical performance of $\text{Ni}_{1-x}\text{Co}_x\text{Fe}_2\text{O}_4$ ($0 \leq x \leq 1$) working electrodes was carried out by deducing the specific capacitance from the CV data using equation (1) given below:

$$C\left(\frac{F}{g}\right) = \frac{A}{V \times \frac{\partial v}{\partial t} \times m} \quad (1)$$

Where A denotes the area under the CV curve, V stands for the potential window, $\frac{\partial v}{\partial t}$ is the scan rate, and m is the mass of the $\text{Ni}_{1-x}\text{Co}_x\text{Fe}_2\text{O}_4$ electrodes. Fig. 2.12(a) presents the voltammograms showing the variation of specific capacitance (F/g) with scan rates (mV/s). The trend of the results shows that the specific capacitance of all samples decreases as the scan rate is amplified from 2 to 300 mV/s. The observed high specific capacitance at lower scan rates can be explained by easy diffusion and high mobility of the electrolyte ions into the active material. At a lower scan rate, there is more time available to count for enhanced interaction between the electrolyte ions and the ions of deposited electrically active material. Increasing the scan rate to higher values leads to the reduction in the specific capacitance because there is not enough time for the ions in motion to fill the spaces of active material, resulting in limited interactions on the outer surfaces only. Consequently, at higher scan rates, some active parts of the surface areas become unavailable for charge storage.⁵⁵ The values of specific capacitance obtained at 2 mV/s are 388, 534, 332, 513, 470 and 254 F/g for $\text{Ni}_{1-x}\text{Co}_x\text{Fe}_2\text{O}_4$ electrodes with cobalt composition, x = 0, 0.2, 0.4, 0.6, 0.8 and 1, respectively. It is obvious that at the lowest scan rate of 2 mV/s, the compositions x = 0.2 and 0.6 recorded higher specific capacitance than other compositions, particularly the pristine NiFe_2O_4 . This might be caused by the appreciable content and uniform distribution of Co^{2+} ions in the NiFe_2O_4 lattice. The distribution of Co^{2+} ions in the octahedral sites causes a change in the lattice parameters and bond length due to the ionic size difference between Co^{+2} and Ni^{+2} ions. Consequently, stronger interaction between Co^{2+} and O^{2-} ions occurs, leading to the splitting of degenerate orbitals, and when there are more chances for the working electrode to react with the electrolyte, the increase in specific capacitance becomes obvious.⁵⁶

The variation of specific capacitance with respect to current density for $\text{Ni}_{1-x}\text{Co}_x\text{Fe}_2\text{O}_4$ solid solutions is displayed in Fig. 2.12(b). The obtained specific capacitance was derived from equation (2) below.

$$C\left(\frac{F}{g}\right) = \frac{I \times t}{V \times m} \quad (2)$$

Where I is the discharge current, t is the discharge time, V is the applied potential window, and m is the mass of $\text{Ni}_{1-x}\text{Co}_x\text{Fe}_2\text{O}_4$ samples. The specific capacitances of 178, 168, 140, 237, 121 and 93 F/g were obtained for electrodes with x = 0, 0.2, 0.4, 0.6, 0.8 and 1, respectively,

at the current density of 1 A/g. The specific capacitance of the $\text{Ni}_{1-x}\text{Co}_x\text{Fe}_2\text{O}_4$ electrodes decreased to 70, 68, 73, 105, 65 and 43 F/g for the electrodes with $x = 0, 0.2, 0.4, 0.6, 0.8$ and 1, respectively, at current density of 20 A/g. The electrodes retained 39.3, 40.5, 52.1, 44.3, 53.3, and 46.2% of their charge storage capacity on increase current density from 1 to 20 A/g. These results suggest that the synthesized electrodes have a good rate capability and could be used in fast-charging devices. The best performance was observed for $x = 0.6$, which exhibited a specific capacitance of 237 F/g at a current density of 1 A/g. The overall trend shows a decrease in specific capacitance with the increase in current density and is ascribed to the limits in diffusion movements of electrolyte ions.⁵⁷ At low current densities, the inner active sites of nanoscale $\text{Ni}_{1-x}\text{Co}_x\text{Fe}_2\text{O}_4$ electrodes are fully utilized due to low ohmic drop, which offers enough time for redox reactions, resulting in the high specific capacity. However, the high charge-discharge rate at high current densities presents an inevitable time constraint making it difficult to maintain high capacities. Also, at this point, the movement of ions in the electrolyte is dependent on diffusion, and the charge storage center is limited on the outer surface.⁵⁸ The superior supercapacitor performance of the $\text{Ni}_{1-x}\text{Co}_x\text{Fe}_2\text{O}_4$ ($x = 0.6$) sample was compared with other studies on binary and ternary metal oxides for supercapacitor applications. The Bhujun group employed a sol-gel method to synthesize ternary transition metal ferrites of $\text{NiCoFe}_2\text{O}_4$, $\text{NiCuFe}_2\text{O}_4$, and $\text{CuCoFe}_2\text{O}_4$, which acquired the maximum specific capacitance of 50, 44, 76.9 F/g, respectively at the current density of 1 A/g.¹⁶ In addition, binary transition metal oxide, NiMnO_3 synthesized via a hydrothermal route recorded a specific capacitance of 230 F/g at 1A/g.⁵⁹ When compared with other binary/ternary metal oxides, the nanospinel $\text{Ni}_{1-x}\text{Co}_x\text{Fe}_2\text{O}_4$ electrode with composition, $x = 0.6$ synthesized via solventless thermolysis method showed an excellent electrochemical performance. It is also believed that Co^{2+} tends to offer additional holes while Ni^{3+} provides extra electrons in the redox reactions, thus enhancing conductivity and capacitive performance. Table 2.2 presents a detailed comparison of the specific capacitance of $\text{Ni}_{0.4}\text{Co}_{0.6}\text{Fe}_2\text{O}_4$ electrode with other previously reported metal oxide-based electrodes.

The relationship between energy and power density for all the samples is shown in Fig. 2.12(c). The energy (E) and power (P) density was obtained from the GCD measurement by using equations (3) and (4), respectively, where C is the capacitance of the electrode (F/g), V is the applied window potential (Volt), and t is the time (seconds).

$$E = \frac{1}{2}CV^2 \quad (3)$$

$$P = \frac{E}{t} \quad (4)$$

Among all the samples examined, the nanoscopic $\text{Ni}_{1-x}\text{Co}_x\text{Fe}_2\text{O}_4$ electrode with $x = 0.6$ displayed a superior energy density of 10.3 Wh/kg while also showing a high power density with a peak value of 4208 (W/kg). The power density of $\text{Ni}_{1-x}\text{Co}_x\text{Fe}_2\text{O}_4$ ($x = 0.6$) obtained in this study by employing a solventless pyrolysis approach is much superior to the NiFe_2O_4 (62.64 W/kg), $\text{Co}_{0.5}\text{Ni}_{0.5}\text{Fe}_2\text{O}_4$ (60.45 W/kg), and CoFe_2O_4 (62.13 W/kg) nanoparticles prepared hydrothermally by Sharifi *et al.* Likewise, the energy density of 10.3 Wh/kg demonstrated by $\text{Ni}_{1-x}\text{Co}_x\text{Fe}_2\text{O}_4$ ($x = 0.6$) surpasses that of NiFe_2O_4 (6.64 Wh/kg), $\text{Co}_{0.5}\text{Ni}_{0.5}\text{Fe}_2\text{O}_4$ (7.43 Wh/kg), and CoFe_2O_4 (9.32 Wh/kg) nanoparticles.⁵⁶

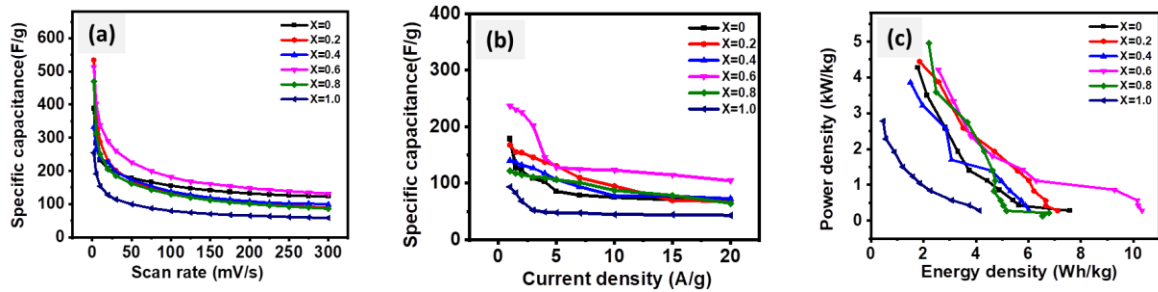


Fig. 2.12. (a) Specific capacitance versus scan rate, (b) Specific capacitance versus current density, (c) Variation of energy and power density, for $\text{Ni}_{1-x}\text{Co}_x\text{Fe}_2\text{O}_4$ ($0 \leq x \leq 1$) samples.

The galvanostatic charge-discharge studies of $\text{Ni}_{1-x}\text{Co}_x\text{Fe}_2\text{O}_4$ samples conducted at different charge-discharge current densities (1 - 20 A/g) are presented in Fig. 2.13. As seen in the charge-discharge curves at various current densities, an apparent plateau and nonlinearity were observed, suggesting pseudo-capacitance behaviour of the $\text{Ni}_{1-x}\text{Co}_x\text{Fe}_2\text{O}_4$ electrode materials with various stoichiometric compositions. Among all the compositions investigated, nanospinel ferrite electrodes with $x = 0.6$ demonstrated a longer charge-discharge time, signifying superiority in charge storage capacity.

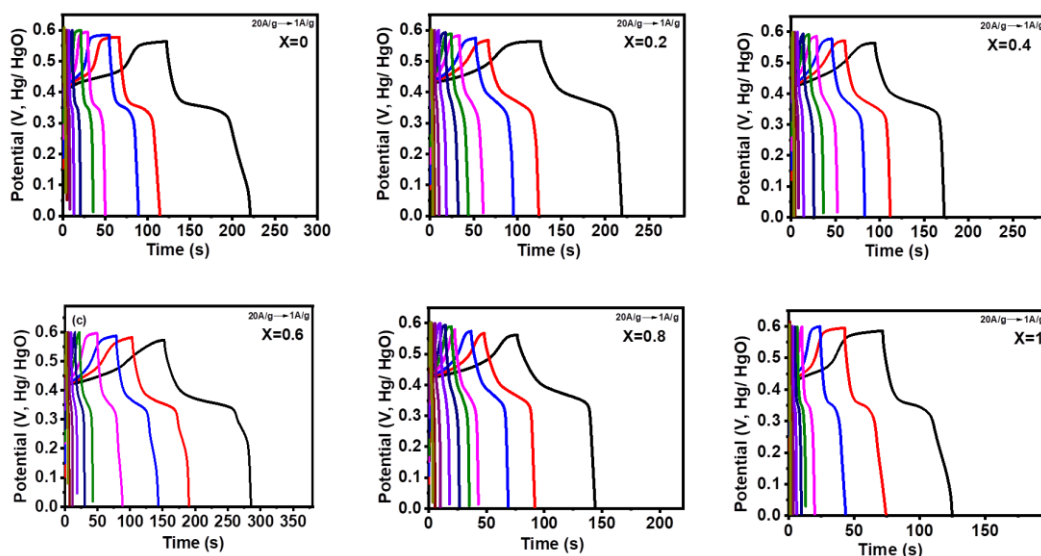


Fig. 2.13. GCD characteristics of $\text{Ni}_{1-x}\text{Co}_x\text{Fe}_2\text{O}_4$ ($0 \leq x \leq 1$) electrodes at various current densities (1A/g – 20 A/g).

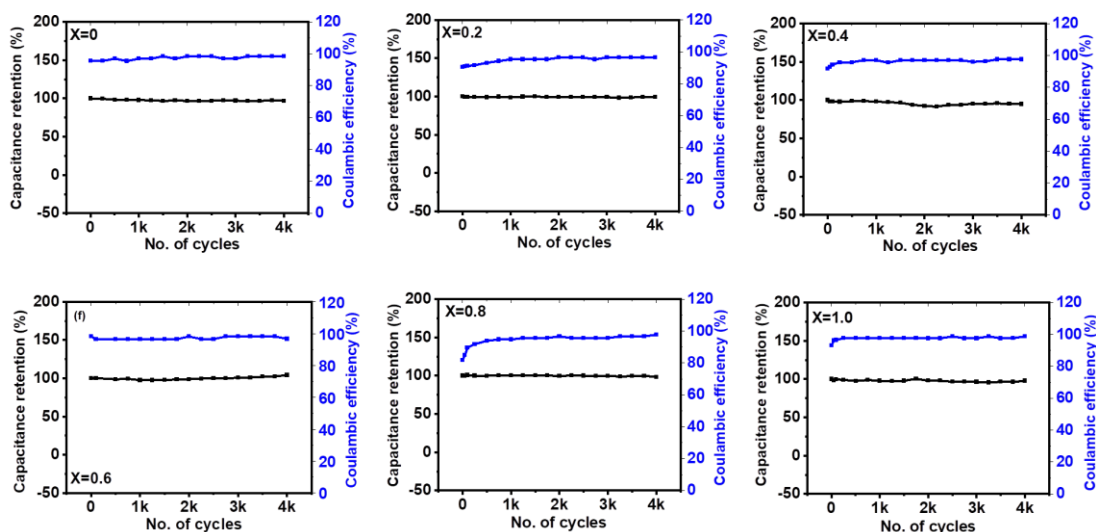


Fig. 2.14. Capacitance retention and columbic efficiency of $\text{Ni}_{1-x}\text{Co}_x\text{Fe}_2\text{O}_4$ ($0 \leq x \leq 1$) electrodes.

The long-term stability tests for all $\text{Ni}_{1-x}\text{Co}_x\text{Fe}_2\text{O}_4$ electrodes shown in Fig. 2.14 were conducted up to 4,000 cycles at current density 7 A/g. Compared to other samples, an electrode with $x = 0.6$ demonstrated about 100% retention in the charge storage capacity at the end of 4,000 cycles of charge-discharge study with about 97% Coulombic efficiency. Other compositions of $\text{Ni}_{1-x}\text{Co}_x\text{Fe}_2\text{O}_4$ ($x = 0, 0.2, 0.4, 0.8$ and 10) samples also showed high charge retention with high coulombic efficiency up to 4000 cycles of charge-discharge study.

Based on CV, GCD, and stability tests, the $x = 0.6$ electrode shows the highest performance for the supercapacitor electrode. These results might be due to the careful consideration of surface area, porosity, and conductivity of the electrode.

Table 2.2. A comparison of the specific capacitance of $\text{Ni}_{0.4}\text{Co}_{0.6}\text{Fe}_2\text{O}_4$ electrode with other metal oxide-based electrodes.

Electrode material	Synthesis route	Specific capacitance (F/g)	Current density (A/g)	Reference
$\text{Cu}_{0.5}\text{Co}_{0.5}\text{Fe}_2\text{O}_4$	Sol-gel	76.9	1	16
MnFe_2O_4	Co-precipitation	173	1	60
MgFe_2O_4	Sol-gel	61	0.5	61
$\text{Ni}_{0.5}\text{Co}_{0.5}\text{Fe}_2\text{O}_4$	Sol-gel	50	1	16
Fe_3O_4	Solvothermal	97	3	62
NiCo_2O_4	Sol-gel	217	1	63
$\text{Ni}_{0.5}\text{Cu}_{0.5}\text{Fe}_2\text{O}_4$	Sol-gel	44	1	16
MnFe_2O_4 /graphene	Solvothermal	120	0.1	64
CoMnFeO_4	Sol-gel	150	1	65
CdMn_2O_4	Electrospinning	210	1	66
$\text{Ni}_{0.25}\text{Mg}_{0.75}\text{Fe}_2\text{O}_4$	Hydrothermal	133.95	0.5	67
MgCr_2O_4	Sol-gel	21	0.5	68
$\text{Ni}_{0.4}\text{Co}_{0.6}\text{Fe}_2\text{O}_4$	Solventless	237	1	This study

2.5.6.2 Hydrogen evolution reaction (HER)

The electrocatalytic behaviour of the $\text{Ni}_{1-x}\text{Co}_x\text{Fe}_2\text{O}_4$ ($0 \leq x \leq 1$) electrodes for efficient HER were examined using linear sweep voltammetry (LSV) in 1 M KOH. As seen in Fig. 2.15(a), the low overpotentials of 191, 237, 168, 191, 181 and 169 mV were required for $x = 0, 0.2, 0.4, 0.6, 0.8$, and 1 electrodes, respectively to deliver the current density 10 mA/cm^2 . All results showed very low overpotential, but among them, $x = 0.4$ (168 mV) showed fairly low overpotential followed by $x = 1$ (169 mV), indicating better catalytic activity than other samples. There are many reports regarding the synthesis of efficient HER catalysts by using Ni, Fe, and Co, which are relatively cheap and abundant on earth, instead of expensive noble metal materials. For example, Adamson's group synthesized the Co-Fe binary metal oxide electrocatalyst which exhibited the overpotential value of 220 mV at current density 10 mA/cm^2 , signifying much higher activity than CoO (387 mV) and Fe_3O_4 (431 mV) at 10 mA/cm^2 .

mA/cm^2 .⁶⁹ Also, nanostructured flower-like nickel-cobalt oxide were synthesized by the Elakkiya group. It demanded the overpotential of 370 mV at $10 \text{ mA}/\text{cm}^2$, which is higher activity than NiO (400 mV) and Co_3O_4 (410 mV) comprising the nickel-cobalt oxide nanomaterials.⁷⁰ Compared with other group's work, the multicomponent $\text{Ni}_{1-x}\text{Co}_x\text{Fe}_2\text{O}_4$ ($x = 0.4$) electrode having low overpotential and high current density shows high electrocatalytic activity for hydrogen evolution. Table 2.3 shows a detailed comparison of HER performance of the synthesized $\text{Ni}_{1-x}\text{Co}_x\text{Fe}_2\text{O}_4$ ($x = 0.4$) with other reported Ni/Co-based electrocatalysts in alkaline electrolyte. Fig. 2.15(b) shows the Tafel slope, an indicator of electrocatalytic kinetics. It was plotted with the aid of the equation $\eta = a + b \log j$; where η is the overpotential, a is a constant, b is the Tafel slope, and j is the current density. The calculated Tafel slopes are 128, 157, 120, 135, 131 and 113 mV/dec for electrodes with compositions $x = 0, 0.2, 0.4, 0.6, 0.8$, and 1, respectively. Since the lower Tafel slope indicates the faster kinetics, thus electrodes with molar ratios $x = 0.4$ (120 mV/dec) and $x = 1$ (113 mV/dec) exhibit better reaction kinetics than other samples. In Fig. 2.16, stability tests of all samples were performed by comparing 1st polarization curve with the 1000th polarization curve. Even after 1000 cycles of cyclic voltammetry measurements, a little deviation was observed for both graphs, indicating high durability. For efficient electrocatalysis, it is essential for the electrode material to have low overpotential and Tafel slope, and high stability. Overall, the $\text{Ni}_{1-x}\text{Co}_x\text{Fe}_2\text{O}_4$ ($x = 0.4$) electrode prepared by the solventless method, possess these crucial elements and show favourable electrocatalytic properties for HER, outperforming other electrode compositions examined in this study. In addition, the effect of electronic push in cobalt substituent on the HER performance of Ni-based materials has been established in the literature, where partial electrons adjacent to nickel sites are pushed by cobalt substituent resulting in an increase in the number of lattice O^{2-} groups and consequently boosting H^+ adsorption and charge transfer for the HER.⁷¹

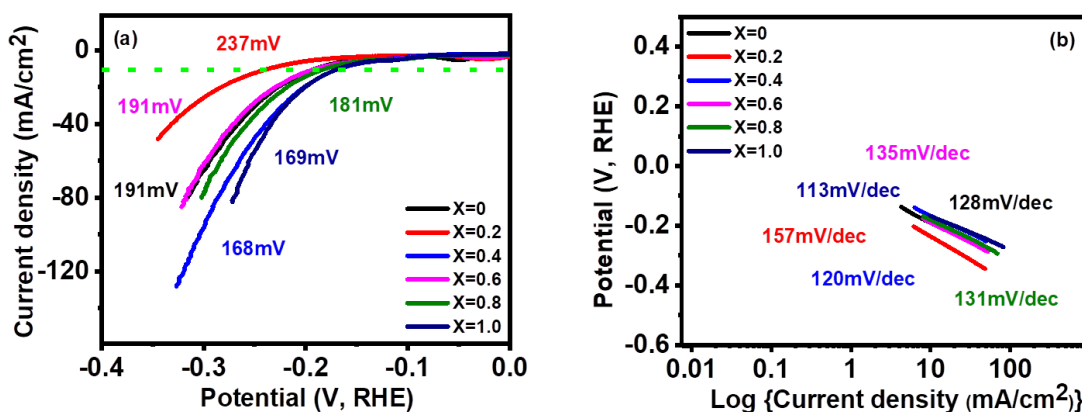


Fig. 2.15. (a) HER polarization curves, (b) Tafel slopes for $\text{Ni}_{1-x}\text{Co}_x\text{Fe}_2\text{O}_4$ ($0 \leq x \leq 1$) samples.

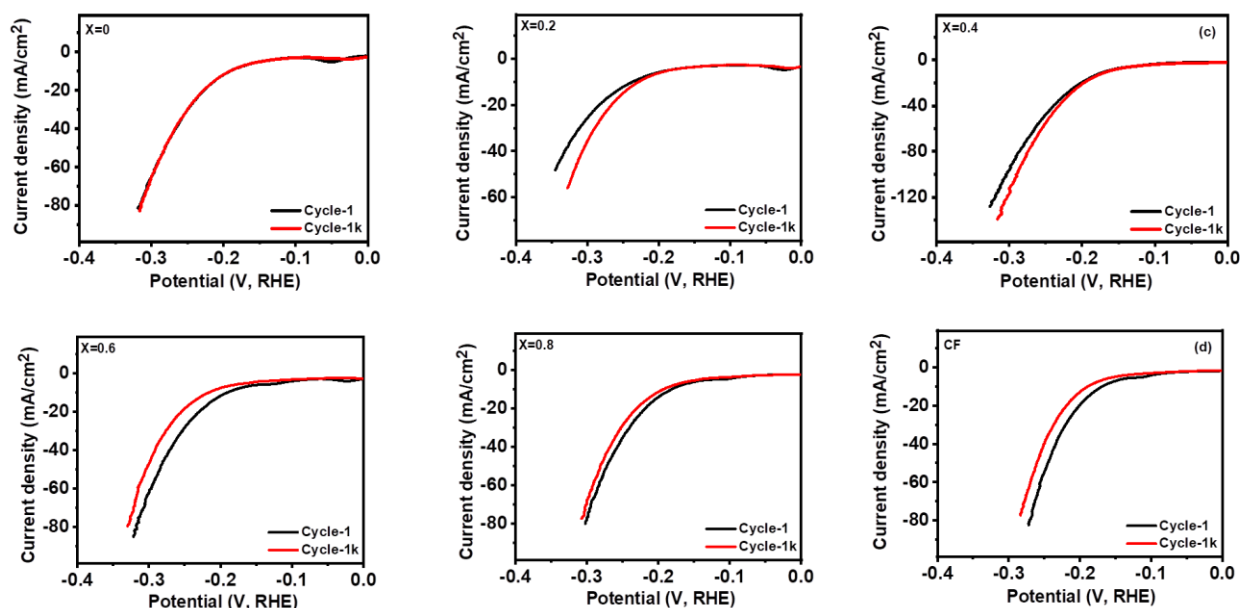


Fig. 2.16. HER polarization curves at various cycles for $\text{Ni}_{1-x}\text{Co}_x\text{Fe}_2\text{O}_4$ ($0 \leq x \leq 1$) samples.

Table 2.3. Comparison of HER performance of the synthesized $\text{Ni}_{0.6}\text{Co}_{0.4}\text{Fe}_2\text{O}_4$ and CoFe_2O_4 with other reported Ni/Co-based electrocatalysts in alkaline electrolyte.

Catalyst	Synthetic method	η_{10} (mV in 1 M KOH)	Tafel slope (mV/dec)	Reference
NiFe Sponges	Polyol-assisted chemical synthesis	190	82	72
NiCoP NW/CFP	Hydrothermal	170	73.0	73
$\text{Ni}_{1.5}\text{Co}_{1.5}\text{S}_4\text{NW/CFP}$	followed by sulfuration and phosphorization	237	112.9	73
$\text{CoFe}_2\text{O}_4/\text{SWNTs}$	Sonochemical	263	46	74
Ni-MoSe ₂	Hydrothermal	206	81	75
NiMnP	Colloidal	490	238	76
$\text{FeSe}_2/\text{CoFe}_2\text{O}_4$	Hydrothermal	231	88.76	77
CoCuZn/C	Electrodeposition	213	92	78
$\text{NiCo}_2\text{S}_4/\text{Ni foam}$	hydrothermal	210	-	79

CoSe ₂ /MoSe ₂	Solvothermal	218	76	80
NiCo ₂ O ₄ /NiCoP	Solvothermal	198	91	81
	followed by phosphorization			
CoFe₂O₄	Solventless	169	113	This study
Ni_{0.6}Co_{0.4}Fe₂O₄	Solventless	168	120	This study

2.5.6.3 Oxygen evolution reaction (OER)

The electrocatalytic activity of Ni_{1-x}Co_xFe₂O₄ ($0 \leq x \leq 1$) electrodes for OER was analyzed using LSV, electrochemical impedance spectroscopy (EIS) and chronoamperometric (CA) measurements in 1 M KOH. At the current density of 10 mA/cm², the overpotentials of 330, 320, 360, 340, 350 and 350 mV were observed along with low Tafel slopes of 66, 79, 97, 68, 67 and 90 mV/dec for $x = 0, 0.2, 0.4, 0.6, 0.8$ and 1, respectively as shown in Figs. 2.17(a-b). The values of Tafel slope give an insight into the kinetics of OER mechanism. The electrode with a lower Tafel slope is expected to display faster reaction kinetics that accelerates higher OER activity. The $x = 0.2$ electrode exhibited a lower overpotential of 320 mV with a low Tafel slope of 79 mV/dec. The greater OER activity demonstrated by Ni_{1-x}Co_xFe₂O₄ electrode with $x = 2$ can also be ascribed to the multicomponent structure and higher number of active sites because of the small crystallite size (8.91 nm) compared to other compositions. This surpasses the results of oxygen evolution activity obtained in other studies based on Co, Fe, Ni transition metal materials such as NiCo₂O₄ nanoneedles (565 mV @10 mA/cm² overpotential, 292 mV/dec Tafel slope), NiCo₂O₄ nanosheets (888 mV @10 mA/cm², 393 mV/dec),⁸² N-doped graphene -NiCo₂O₄ hybrid (434 mV @ 10 mA/cm², 156 mV/dec Tafel slope),⁸³ and Co_{0.5} Fe_{0.5} S@N-MC (410 mV @10 mA/cm², 159 mV/dec Tafel slope).⁸⁴ Table 2.4 shows a comparison of OER performance of the synthesized Ni_{0.8}Co_{0.2}Fe₂O₄ with other reported Ni/Co-based electrocatalysts in alkaline electrolyte. The Nyquist plots shown in Fig. 2.17(c), were studied from the electrochemical impedance spectroscopy in the frequency range of 0.05 Hz to 10 kHz with an applied AC amplitude of 10 mV. The intersection value of the real axis represents electrolyte resistance. The low electrolyte resistance of ~1.5 Ω/cm² was observed in the graph. Furthermore, all graphs appear semi-circle at 0.5 V potential (V vs. Hg/HgO). The semi-circle shown in the graph indicates the resistance of charge transfer at the interface between 1 M KOH electrolyte and the Ni_{1-x}Co_xFe₂O₄ electrodes. The lower the diameter of the semi-circle suggest the less charge transfer resistance. The observed values of

the resistance are $\sim 4.6, 3.5, 10, 5.8, 7.2, 7 \Omega/\text{cm}^2$ for $x = 0, 0.2, 0.4, 0.6, 0.8$ and 1 , respectively. Among the stoichiometric molar ratios of the spinel $\text{Ni}_{1-x}\text{Co}_x\text{Fe}_2\text{O}_4$ electrodes, an electrode with composition $x = 0.2$ displayed low charge transfer resistance ($3.5 \Omega/\text{cm}^2$), representing better OER catalytic properties than other compositions. Long-term stability and durability tests were conducted by 1000 cycles of CV measurements and chronoamperometry for all electrodes as presented in Fig. 2.18. All electrode materials delivered stable high current density over 20 h at a constant voltage of 0.55 V . In addition, the polarization curves of all electrode composition show a perfect match between the 1st cycle and the 1,000th cycle (inset). Although, all samples showed a nearly identical graph between the 1st and 1,000th cycle, and stable high current density over 20 h, a little fluctuation was observed in some graphs which indicate oxygen gas during oxygen evolution.

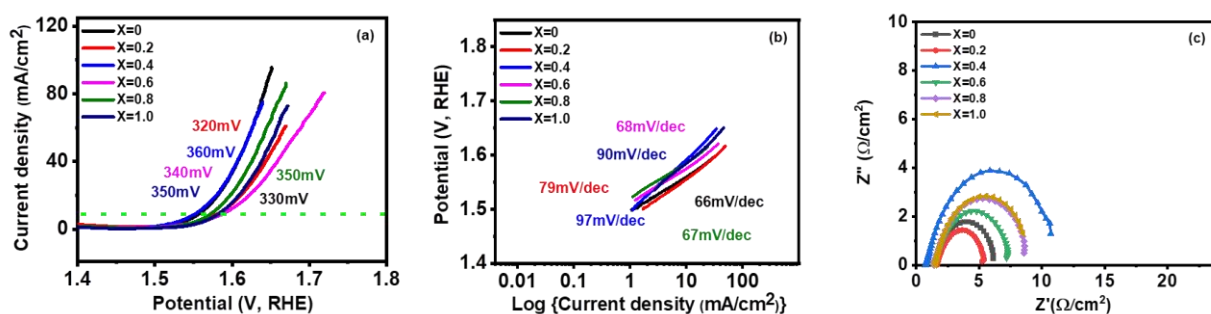


Fig. 2.17. (a) OER polarization curves, (b) Tafel slopes for various samples (c) Electrochemical impedance spectroscopic spectra of all the samples at various potentials (vs. SCE) at 0.5 V

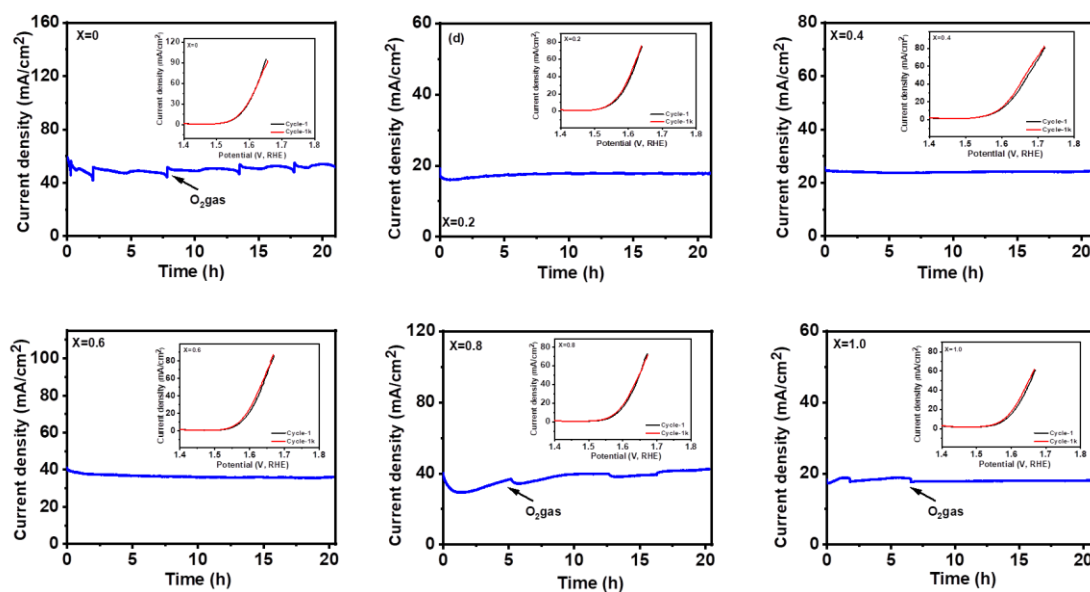


Fig. 2.18. Chronoamperometry characteristics of the various samples in 1 M KOH (inset) OER polarization curves at various cycles for the various samples.

Table 2.4. Comparison of OER performance of the synthesized $\text{Ni}_{0.8}\text{Co}_{0.2}\text{Fe}_2\text{O}_4$ with other reported Ni/Co-based electrocatalysts in alkaline electrolyte.

Catalyst	Synthetic method	η_{10} (mV) in 1 M KOH	Tafel slope (1) (mV/dec)	Reference
$\text{NiS/Bi}_2\text{WO}_6$	Hydrothermal	527	238	85
$\text{Ni}_x\text{Co}_{3-x}\text{O}_4/\text{NF}$	Hydrothermal	320	38	86
$\text{Ni}_x\text{Co}_{3-x}\text{O}_4$	Hydrothermal	337	75	87
nonowires				
Co/Fe-MOFs	Solvothermal	410	101	88
$\text{MnO}_2/\text{NiCo}_2\text{O}_4/\text{NF}$	Hydrothermal	340	139	89
$\text{NiCo}_2\text{O}_4/\text{NF}$	Solvothermal	465	137	90
NiCoP/C nanoboxes	MOF	330	96	91
Mn-Co oxyphosphide	Thermal oxidation and phosphidation	370	66	92
CuCo_2S_4	Colloidal	395	115	93
Mn-Co oxide	Thermal oxidation	420	60	92
NiCo_2O_4	Hydrothermal	346	94	94
$\text{CoNi}_{0.2}\text{Fe}_{0.05}\text{-Z-H-P}$	MOF and phosphidation	329	48.2	95
CoS	Electrodeposition	372	86.6	96
CoMnP nanoparticles	Solvothermal	330	61	97
CoP-PBSCF	<i>In-situ</i> exsolution	340	81.5	98
$\text{Co}_2\text{Mo}_3\text{O}_8@\text{NC}$	<i>In situ</i> pyrolysis	331	87.5	99
NiCo_2O_4	Hydrothermal	500	119	89
$\text{Ni}_{0.8}\text{Co}_{0.2}\text{Fe}_2\text{O}_4$	Solventless	320	79	This study

2.6 Conclusion

Summarily, the advantages of eco-friendliness, simplicity and scalability of the solventless thermolysis method have been exploited to synthesize nanoscale $\text{Ni}_{1-x}\text{Co}_x\text{Fe}_2\text{O}_4$ ($0 \leq x \leq 1$) solid solutions. The p-XRD analysis confirmed the formation of a series of single-phase cubic spinel ferrites with space group $Fd3m$. It was observed that the nanospinel $\text{Ni}_{0.4}\text{Co}_{0.6}\text{Fe}_2\text{O}_4$ electrode demonstrated a longer charge-discharge time, signifying superior charge storage capacity. It exhibited a specific capacitance of 237 F/g at a current density of 1 A/g, which was higher compared to other samples. For efficient HER electrocatalysis, the $\text{Ni}_{0.6}\text{Co}_{0.4}\text{Fe}_2\text{O}_4$ electrode showed low overpotential (168 mV) and Tafel slope (120 mV/dec) as well as high stability, which are crucial elements for HER. Similarly, $\text{Ni}_{0.8}\text{Co}_{0.2}\text{Fe}_2\text{O}_4$ exhibited a lower overpotential of 320 mV with a low Tafel slope of 79 mV/dec, indicating enhanced OER activity. The results in this study affirmed that the synergism between nickel and cobalt in the crystal lattice of spinel nickel ferrite has a tremendous influence on the electrochemical performance of the resultant $\text{Ni}_{1-x}\text{Co}_x\text{Fe}_2\text{O}_4$ solid solution for energy conversion and storage.

References

1. Yang, W.; Wang, Z.; Zhang, W.; Guo, S. *Trends in Chemistry* **2019**, 1, (2), 259-271.
2. Chu, S.; Majumdar, A. *Nature* **2012**, 488, (7411), 294-303.
3. Li, X.; Hao, X.; Abudula, A.; Guan, G. *Journal of Materials Chemistry A* **2016**, 4, (31), 11973-12000.
4. Reier, T.; Oezaslan, M.; Strasser, P. *ACS Catalysis* **2012**, 2, (8), 1765-1772.
5. Dalai, N.; Mohanty, B.; Mitra, A.; Jena, B. *ChemistrySelect* **2019**, 4, (27), 7791-7796.
6. Liu, S.; Ni, D.; Li, H.-F.; Hui, K. N.; Ouyang, C.-Y.; Jun, S. C. *Journal of Materials Chemistry A* **2018**, 6, (23), 10674-10685.
7. Maksoud, M. A.; Fahim, R. A.; Shalan, A. E.; Abd Elkodous, M.; Olojede, S.; Osman, A. I.; Farrell, C.; Ala'a, H.; Awed, A.; Ashour, A. *Environmental Chemistry Letters* **2020**, 1-65.
8. Yuan, C.; Wu, H. B.; Xie, Y.; Lou, X. W. *Angewandte Chemie International Edition* **2014**, 53, (6), 1488-1504.
9. Teh, P. F.; Sharma, Y.; Pramana, S. S.; Srinivasan, M. *Journal of Materials Chemistry* **2011**, 21, (38), 14999-15008.
10. Sutka, A.; Millers, M.; Vanags, M.; Joost, U.; Maiorov, M.; Kisand, V.; Pärna, R.; Juhneva, I. *Research on Chemical Intermediates* **2015**, 41, (12), 9439-9449.
11. Sutka, A.; Mezinskis, G.; Lusis, A.; Jakovlevs, D. *Sensors and Actuators B: Chemical* **2012**, 171, 204-209.
12. Rodrigues, A. R. O.; Gomes, I. T.; Almeida, B. G.; Araújo, J. P.; Castanheira, E. M.; Coutinho, P. J. *Physical Chemistry Chemical Physics* **2015**, 17, (27), 18011-18021.
13. Rani, R.; Kumar, G.; Batoo, K. M.; Singh, M. *American Journal of Nanomaterials* **2013**, 1, (1), 9-12.
14. Caltun, O.; Rao, G.; Rao, K.; Rao, B. P.; Kim, C.; Kim, C.-O.; Dumitru, I.; Lupu, N.; Chiriac, H. *Sensor Letters* **2007**, 5, (1), 45-47.
15. Shobana, M.; Kim, K.; Kim, J.-H. *Physica E: Low-dimensional Systems and Nanostructures* **2019**, 108, 100-104.
16. Bhujun, B.; Tan, M. T.; Shanmugam, A. S. *Results in Physics* **2017**, 7, 345-353.
17. Zhao, Q.; Yan, Z.; Chen, C.; Chen, J. *Chemical Reviews* **2017**, 117, (15), 10121-10211.
18. Toh, R. J.; Eng, A. Y. S.; Sofer, Z.; Sedmidubsky, D.; Pumera, M. *ChemElectroChem* **2015**, 2, (7), 982-987.

19. Zhang, C.; Bhoyate, S.; Zhao, C.; Kahol, P. K.; Kostoglou, N.; Mitterer, C.; Hinder, S. J.; Baker, M. A.; Constantinides, G.; Polychronopoulou, K. *Catalysts* **2019**, 9, (2), 176.
20. Gao, X.; Wang, W.; Bi, J.; Chen, Y.; Hao, X.; Sun, X.; Zhang, J. *Electrochimica Acta* **2019**, 296, 181-189.
21. Fan, H.; Bahmani, F.; Kaneti, Y. V.; Guo, Y.; Alothman, A. A.; Wu, X.; Yamauchi, Y.; Li, W.; Zhang, J. *Chemistry—A European Journal* **2020**.
22. Lai, F.; Zhang, X.; Wu, Q.; Zhang, J.; Li, Q.; Huang, Y.; Liao, Z.; Wang, H. *ACS Sustainable Chemistry & Engineering* **2018**, 6, (1), 570-578.
23. Martínez-Lázaro, A.; Rico-Zavala, A.; Espinosa-Lagunes, F.; Torres-González, J.; Álvarez-Contreras, L.; Gurrola, M.; Arriaga, L.; Ledesma-García, J.; Ortiz-Ortega, E. *Journal of Power Sources* **2019**, 412, 505-513.
24. Ou, G.; Wu, F.; Huang, K.; Hussain, N.; Zu, D.; Wei, H.; Ge, B.; Yao, H.; Liu, L.; Li, H. *ACS Applied Materials & Interfaces* **2019**, 11, (4), 3978-3983.
25. Guo, C.; Liu, X.; Gao, L.; Ma, X.; Zhao, M.; Zhou, J.; Kuang, X.; Deng, W.; Sun, X.; Wei, Q. *Journal of Materials Chemistry A* **2019**, 7, (38), 21704-21710.
26. Regulacio, M. D.; Han, M.-Y. *Accounts of Chemical Research* **2010**, 43, (5), 621-630.
27. Liu, B.; Bando, Y.; Liu, L.; Zhao, J.; Masanori, M.; Jiang, X.; Golberg, D. *Nano Letters* **2013**, 13, (1), 85-90.
28. Lestari, M.; Lusi, M. *Chemical Communications* **2019**, 55, (16), 2297-2300.
29. Lusi, M. *Crystal Growth & Design* **2018**, 18, (6), 3704-3712.
30. Valenzuela, R. *Physics Research International* **2012**, 2012.
31. Khan, M. D.; Awan, S. U.; Zequine, C.; Zhang, C.; Gupta, R. K.; Revaprasadu, N. *ACS Applied Energy Materials* **2020**, 3, (2), 1448-1460.
32. Singh, R.; Singh, J.; Lal, B.; Thomas, M.; Bera, S. *Electrochimica Acta* **2006**, 51, (25), 5515-5523.
33. Singh, R.; Singh, J.; Lal, B.; Singh, A. *International Journal of Hydrogen Energy* **2007**, 32, (1), 11-16.
34. Liu, B.; Li, J.; Yang, W.; Zhang, X.; Jiang, X.; Bando, Y. *Small* **2017**, 13, (45), 1701998.
35. Lewis, E.; Haigh, S.; O'Brien, P. *Journal of Materials Chemistry A* **2014**, 2, (3), 570-580.
36. Shombe, G. B.; Khan, M. D.; Zequine, C.; Zhao, C.; Gupta, R. K.; Revaprasadu, N. *Scientific Reports* **2020**, 10, (1), 1-14.
37. Sodhi, R. K.; Paul, S. *Catalysis Surveys from Asia* **2018**, 22, (1), 31-62.

38. Ungár, T. *Scripta Materialia* **2004**, 51, (8), 777-781.
39. George, M.; John, A. M.; Nair, S. S.; Joy, P.; Anantharaman, M. *Journal of Magnetism and Magnetic Materials* **2006**, 302, (1), 190-195.
40. Ati, A. A.; Othaman, Z.; Samavati, A. *Journal of Molecular Structure* **2013**, 1052, 177-182.
41. Mukherjee, R.; Sahu, T.; Sen, S.; Sahu, P. *Materials Chemistry and Physics* **2011**, 128, (3), 365-370.
42. Zaki, H.; Al-Heniti, S.; Elmosalami, T. *Journal of Alloys and Compounds* **2015**, 633, 104-114.
43. Denton, A. R.; Ashcroft, N. W. *Physical Review A* **1991**, 43, (6), 3161.
44. Iqbal, M. J.; Farooq, S. *Materials Science and Engineering: B* **2007**, 136, (2-3), 140-147.
45. Jalaiah, K.; Babu, K. V. *Journal of Magnetism and Magnetic Materials* **2017**, 423, 275-280.
46. Zare, S.; Ati, A. A.; Dabagh, S.; Rosnan, R.; Othaman, Z. *Journal of Molecular Structure* **2015**, 1089, 25-31.
47. Tirpude, S.; Sarkar, N.; Sawadh, P.; Rewatkar, K. *Journal of the Gujarat Research Society* **2019**, 21, (1), 13-15.
48. Joshi, S.; Kamble, V. B.; Kumar, M.; Umarji, A. M.; Srivastava, G. *Journal of Alloys and Compounds* **2016**, 654, 460-466.
49. Singh, C.; Goyal, A.; Singhal, S. *Nanoscale* **2014**, 6, (14), 7959-7970.
50. Harish, K.; Naik, H. B.; Viswanath, R. *Catalysis Science & Technology* **2012**, 2, (5), 1033-1039.
51. Kim, K. J.; Park, Y. R. *Applied Physics Letters* **2002**, 81, (8), 1420-1422.
52. Lassoued, A.; Lassoued, M. S.; Karolak, F.; García-Granda, S.; Dkhil, B.; Ammar, S.; Gadri, A. *Journal of Materials Science: Materials in Electronics* **2017**, 28, (24), 18480-18488.
53. Guragain, D.; Zequine, C.; Bhattarai, R.; Choi, J.; Gupta, R.; Shen, X.; Mishra, S. *MRS Advances*, 1-8.
54. Bhoyate, S.; Ranaweera, C. K.; Zhang, C.; Morey, T.; Hyatt, M.; Kahol, P. K.; Ghimire, M.; Mishra, S. R.; Gupta, R. K. *Global Challenges* **2017**, 1, (8), 1700063.
55. Nazim, S.; Shahid, M.; Warsi, M. F.; Agboola, P. O.; Khan, M. A.; Shakir, I. *Ceramics International* **2018**, 44, (8), 9616-9622.

56. Sharifi, S.; Yazdani, A.; Rahimi, K. *Materials Science in Semiconductor Processing* **2020**, 108, 104902.
57. Reddy, R. N.; Reddy, R. G. *Journal of Power Sources* **2006**, 156, (2), 700-704.
58. Rani, B. J.; Ravi, G.; Yuvakkumar, R.; Ganesh, V.; Ravichandran, S.; Thambidurai, M.; Rajalakshmi, A.; Sakunthala, A. *Applied Physics A* **2018**, 124, (7), 511.
59. Dinesh, M.; Haldorai, Y.; Kumar, R. T. R. *Ceramics International* **2020**.
60. Vignesh, V.; Subramani, K.; Sathish, M.; Navamathavan, R. *Colloids and Surfaces A: Physicochemical and Engineering Aspects* **2018**, 538, 668-677.
61. Maitra, S.; Mitra, R.; Nath, T. *Current Applied Physics* **2021**, 27, 73-88.
62. Tipsawat, P.; Wongpratrat, U.; Phumying, S.; Chanlek, N.; Chokprasombat, K.; Maensiri, S. *Applied Surface Science* **2018**, 446, 287-292.
63. Wu, Y. Q.; Chen, X. Y.; Ji, P. T.; Zhou, Q. Q. *Electrochimica Acta* **2011**, 56, (22), 7517-7522.
64. Cai, W.; Lai, T.; Dai, W.; Ye, J. *Journal of Power Sources* **2014**, 255, 170-178.
65. Ghadimi, L. S.; Arsalani, N.; Ahadzadeh, I.; Hajalilou, A.; Abouzari-Lotf, E. *Applied Surface Science* **2019**, 494, 440-451.
66. Bhagwan, J.; Sahoo, A.; Yadav, K.; Sharma, Y. *Journal of Alloys and Compounds* **2017**, 703, 86-95.
67. Wongpratrat, U.; Tipsawat, P.; Khajonrit, J.; Swatsitang, E.; Maensiri, S. *Journal of Alloys and Compounds* **2020**, 831, 154718.
68. Maitra, S.; Mitra, R.; Nath, T. *Journal of Alloys and Compounds* **2021**, 858, 157679.
69. Adamson, W.; Bo, X.; Li, Y.; Suryanto, B. H.; Chen, X.; Zhao, C. *Catalysis Today* **2020**, 351, 44-49.
70. Elakkiya, R.; Ramkumar, R.; Maduraiveeran, G. *Materials Research Bulletin* **2019**, 116, 98-105.
71. Zhao, Q.; Yang, J.; Liu, M.; Wang, R.; Zhang, G.; Wang, H.; Tang, H.; Liu, C.; Mei, Z.; Chen, H. *ACS Catalysis* **2018**, 8, (6), 5621-5629.
72. Thoufeeq, S.; Rastogi, P. K.; Thomas, S.; Shravani, A.; Narayanan, T. N.; Anantharaman, M. *ChemistrySelect* **2020**, 5, (4), 1385-1395.
73. Dai, Z.; Geng, H.; Wang, J.; Luo, Y.; Li, B.; Zong, Y.; Yang, J.; Guo, Y.; Zheng, Y.; Wang, X. *ACS Nano* **2017**, 11, (11), 11031-11040.
74. Ding, Y.; Zhao, J.; Zhang, W.; Zhang, J.; Chen, X.; Yang, F.; Zhang, X. *ACS Applied Energy Materials* **2018**, 2, (2), 1026-1032.

75. Zhao, G.; Wang, X.; Wang, S.; Rui, K.; Chen, Y.; Yu, H.; Ma, J.; Dou, S. X.; Sun, W. *Chemistry–An Asian Journal* **2019**, 14, (2), 301-306.
76. Man, H.-W.; Tsang, C.-S.; Li, M. M.-J.; Mo, J.; Huang, B.; Lee, L. Y. S.; Leung, Y.-c.; Wong, K.-Y.; Tsang, S. C. E. *Applied Catalysis B: Environmental* **2019**, 242, 186-193.
77. Zhang, H.; Nengzi, L.-c.; Li, B.; Cheng, Q.; Gou, J.; Cheng, X. *Renewable Energy* **2020**, 155, 717-724.
78. Döner, A. *international journal of hydrogen energy* **2018**, 43, (51), 22797-22806.
79. Sivanantham, A.; Ganesan, P.; Shanmugam, S. *Advanced Functional Materials* **2016**, 26, (26), 4661-4672.
80. Zhao, G.; Li, P.; Rui, K.; Chen, Y.; Dou, S. X.; Sun, W. *Chemistry–A European Journal* **2018**, 24, (43), 11158-11165.
81. Jin, W.; Chen, J.; Wu, H.; Zang, N.; Li, Q.; Cai, W.; Wu, Z. *Catalysis Science & Technology* **2020**, 10, (16), 5559-5565.
82. Shi, H.; Zhao, G. *The Journal of Physical Chemistry C* **2014**, 118, (45), 25939-25946.
83. Chen, S.; Qiao, S.-Z. *Acs Nano* **2013**, 7, (11), 10190-10196.
84. Shen, M.; Ruan, C.; Chen, Y.; Jiang, C.; Ai, K.; Lu, L. *ACS Applied Materials & Interfaces* **2015**, 7, (2), 1207-1218.
85. Li, J.; Xu, X.; Zhang, B.; Hou, W.; Lv, S.; Shi, Y. *Applied Surface Science* **2020**, 526, 146718.
86. Bao, J.; Liu, W.; Xie, J.; Xu, L.; Guan, M.; Lei, F.; Zhao, Y.; Huang, Y.; Xia, J.; Li, H. *Chemistry–An Asian Journal* **2019**, 14, (3), 480-485.
87. Yan, X.; Li, K.; Lyu, L.; Song, F.; He, J.; Niu, D.; Liu, L.; Hu, X.; Chen, X. *ACS Applied Materials & Interfaces* **2016**, 8, (5), 3208-3214.
88. Iqbal, B.; Saleem, M.; Arshad, S. N.; Rashid, J.; Hussain, N.; Zaheer, M. *Chemistry–A European Journal* **2019**, 25, (44), 10490-10498.
89. Yan, K.-L.; Shang, X.; Gao, W.-K.; Dong, B.; Li, X.; Chi, J.-Q.; Liu, Y.-R.; Chai, Y.-M.; Liu, C.-G. *Journal of Alloys and Compounds* **2017**, 719, 314-321.
90. Yin, X.; Sun, G.; Wang, L.; Bai, L.; Su, L.; Wang, Y.; Du, Q.; Shao, G. *International Journal of Hydrogen Energy* **2017**, 42, (40), 25267-25276.
91. He, P.; Yu, X. Y.; Lou, X. W. *Angewandte Chemie International Edition* **2017**, 56, (14), 3897-3900.
92. Guan, B. Y.; Yu, L.; Lou, X. W. *Angewandte Chemie International Edition* **2017**, 56, (9), 2386-2389.

93. Wiltrout, A. M.; Read, C. G.; Spencer, E. M.; Schaak, R. E. *Inorganic Chemistry* **2016**, 55, (1), 221-226.
94. Jeghan, S. M. N.; Lee, G. *Nanotechnology* **2020**, 31, (29), 295405.
95. Wang, M.; Dong, C. L.; Huang, Y. C.; Li, Y.; Shen, S. *Small* **2018**, 14, (35), 1801756.
96. Xie, H.; Geng, Q.; Liu, X.; Mao, J. *Frontiers of Chemical Science and Engineering* **2021**, 1-8.
97. Li, D.; Baydoun, H.; Verani, C. N.; Brock, S. L. *Journal of the American Chemical Society* **2016**, 138, (12), 4006-4009.
98. Zhang, Y.-Q.; Tao, H.-B.; Chen, Z.; Li, M.; Sun, Y.-F.; Hua, B.; Luo, J.-L. *Journal of Materials Chemistry A* **2019**, 7, (46), 26607-26617.
99. Ouyang, T.; Wang, X. T.; Mai, X. Q.; Chen, A. N.; Tang, Z. Y.; Liu, Z. Q. *Angewandte Chemie International Edition* **2020**, 59, (29), 11948-11957.

CHAPTER 3

**Composition-tuneable synthesis of $\text{Co}_{1-x}\text{Zn}_x\text{Fe}_2\text{O}_4$ ($0 \leq x \leq 1$)
solid solutions by melt pyrolysis for electrochemical energy
conversion and storage**

3.1 Introduction

Spinel-type oxides represented by the nominal composition AB_2O_4 (where A, B = metals) have generated interest owing to their diverse properties which render them suitable for numerous applications.¹ These materials are endowed with a blend of useful physical properties along with low production cost, and high structural and chemical stability.² The stable spinel structure is known to facilitate the movement of electrons between the mixed oxidation states available for cations in oxygen sites, improving their electronic conductivity.³ Crystallographic studies show that spinel oxides can assume normal or inverse crystal structure depending on how the cations are distributed in the tetrahedral and octahedral sites. In the normal spinel system, divalent oxygen ion (O^{2-}) forms a face-centred cubic structure with divalent cations (A^{+2}) in the tetrahedral positions whereas trivalent cations (B^{+3}) populate octahedral sites. However, in the inverse spinel system, the tetrahedral sites are only taken by (B^{+3}) while the octahedral vacancies are equally occupied by both trivalent (B^{+3}) and divalent cations (A^{+2}).¹ This elegant distribution of cations along with the crystal field effect contributes to the spinels' vast array of properties and applications.

Spinel nanoferrites constitute a prominent class of spinel oxides with distinct properties and applications. Since their future applications are intimately connected to environmental and energy issues, recent studies have predominantly focused on their efficacy as environmentally benign materials for energy applications.⁴⁻⁶ In particular, $CoFe_2O_4$ and $ZnFe_2O_4$ are amongst the widely explored ferrites, and have demonstrated promising potential in supercapacitors, dye sensitized solar cells, batteries, and catalysis.^{1, 7} Spinel cobalt ferrite ($CoFe_2O_4$) exists in an inverse structure wherein all the Co^{2+} ions populate the octahedral site whilst Fe^{3+} ions are equally located between octahedral and tetrahedral sites.⁸ The diamagnetic normal spinel $ZnFe_2O_4$ have Zn^{2+} ions preferentially occupying tetrahedral sites because of their sp^3 bonding affinity with O^{2-} ions, allowing Fe^{3+} ions to populate the octahedral positions.⁹ Recent studies have revealed that amongst other factors, the chemical properties and hence the electrochemical performance of spinels can be influenced by rational changes in the identity and composition of the constituents.^{10, 11} The properties can be systematically tuned via partial substitution or by changing the chemical identity and composition of one of the divalent metal ions while the basic crystal structure remains intact. This adjustment produces spinels with enhanced electrochemical activities, which can further narrow the polarization, speed up and extend the life of batteries, fuel cells, and water splitting devices.¹ For example, Zhao *et al.* examined the influence of the Ni content on the

electrochemical activity of $\text{Ni}_x\text{Co}_{1-x}\text{Fe}_2\text{O}_4$ ($0 \leq x \leq 0.75$) nanoparticles prepared by employing the hydrothermal method.¹¹ The Ni-doped CoFe_2O_4 showed improved electrocatalytic activity at different doping levels in comparison with pristine CoFe_2O_4 . The catalytic activity of $\text{Ni}_{0.75}\text{Co}_{0.25}\text{Fe}_2\text{O}_4$ for OER was found to be higher, recording a maximum current density of 36.0 mA/cm^2 at 1.0 V. Singh *et al.* synthesized chromium substituted MnFe_2O_4 catalyst and examined the influence of Cr substitution towards oxygen evolution in the alkaline medium.¹² Their investigation demonstrated that Cr substitution in the range of 0.1 to 1.0 mol significantly enhanced the OER activity. Another investigation carried out by Singh *et al.* demonstrated that inclusion of both Fe by Cr in the pure CuFe_2O_4 system led to an improvement of the geometrical and electrochemical properties of the material in favour of OER.¹³ On the basis of these studies, it is evident that the inclusion of foreign atoms in spinel ferrites along with composition tuning augments their electrochemical performance. It enhances the performance by boosting the electronic conductivity of the material, exposing the available catalytic active sites and/or reduce the activation energy barrier for proficient energy storage and generation.¹

Spinel ferrites have historically been prepared via high temperature solid-state reactions which involve prolonged mechanical mixing of the corresponding metal hydroxides, oxides, nitrates or carbonates.¹⁴ Although this method is capable of producing large-scale bulk ceramic powders, it is unsuitable for producing pure nanoferrites because its reliance on high temperatures and prolonged heating schedules may lead to the coarsening of grains. Also, volatilization/melting of the constituent components may occur during the high temperature processing of some of the multicomponent oxides which may in turn pose serious effects to the materials' properties.¹⁵ Low and/or intermediate-temperature synthetic routes such as co-precipitation, hydrothermal, sol-gel and solvothermal techniques have recently been developed and used to prepare unprecedented materials with interesting properties.¹ Nonetheless, these methods have disadvantages of low purity, low yield and time-consuming and/or complicated procedures.¹⁶

Besides the synthesis protocol, the choice of proper precursor materials is another matter of paramount significance. The most explored synthetic routes involve thermolysis of mixed precursors such as metal carbonyls, acetylacetonates, chlorides, acetates, nitrates, carbonates, etc., in high boiling point solvents and/or surfactants.^{15, 17-20} However, the use of a large quantity of templates, shape-controlling agents, and surfactants is not an environmentally benign choice.²¹ Although there are reports on the synthesis of spinel ferrites using metal acetylacetonate complexes, the synthesis has thus far been limited to solution-

based protocols.^{18, 22} To this end, a synthetic route that allows the preparation of spinel ferrites using metal acetylacetonates in a solvent/surfactant-free environment is a promising strategy towards achieving superior properties with high efficiency and controllability.

To develop efficient mixed spinel ferrite electrocatalysts with the above concerns in mind, we describe herein a unique solid state pyrolysis strategy for the rational synthesis of nanoscale $\text{Co}_{1-x}\text{Zn}_x\text{Fe}_2\text{O}_4$ ($0 \leq x \leq 1$) solid solution from molecular organometallic precursors. This approach is based on the thermal decomposition of the mixture of metal acetylacetonates in air atmosphere and subsequent crystallization into spinels at mild temperature. In comparison to other precursors, metal acetylacetonates are less costly and have low moisture sensitivity, making them less susceptible to hydrolysis, which is a common limitation of metal halides and alkoxides.²³ The solvent-free approach offers advantages of fabricating multi-component materials with desired stoichiometry eliminating contamination.

3.2 Experimental

3.2.1 Chemicals

Cobalt (II) acetylacetonates (98%, Merck-Schuchardt), zinc (II) acetylacetonates (98%, Merck-Schuchardt), and iron (III) acetylacetonate (97%, Sigma-Aldrich). All precursor materials were used as received.

3.2.2 Synthesis of $\text{Co}_{1-x}\text{Zn}_x\text{Fe}_2\text{O}_4$ ($0 \leq x \leq 1$) solid solutions

The spinel $\text{Co}_{1-x}\text{Zn}_x\text{Fe}_2\text{O}_4$ ($0 \leq x \leq 1$) solid solutions of different stoichiometric compositions were prepared by melt pyrolysis of metal acetylacetonates. For the typical synthesis of ternary CoFe_2O_4 nanoparticles, 0.10 g (0.28 mmol) of cobalt acetylacetonate and 0.198 g (0.56 mmol) of iron acetylacetonate were mixed and the solid mixture was grounded using pestle and mortar for ≈ 20 minutes to obtain a homogeneous mixture. The precursor mixture was then placed into a ceramic boat, which was placed in a reactor tube. The reactor tube was then introduced inside the carbolite tube furnace in such a way that the ceramic boat must be placed almost in the middle of the heating zone, followed by thermal treatment at 450 °C, at a heating rate of 20 °C per minute for 1 h. After 1 h of annealing, the heating was switched off, and the furnace was left to cool naturally to ambient temperature. The reactor tube was taken out of the furnace upon cooling, and the product was collected for analysis without any post-treatment. Likewise, the synthesis of ZnFe_2O_4 nanoparticles was achieved by employing similar procedures except that zinc acetylacetonate was used instead of cobalt

acetylacetonate and the amount of zinc and iron complexes were maintained in the same mole ratio of 1:2.

For the synthesis of quaternary $\text{Co}_{1-x}\text{Zn}_x\text{Fe}_2\text{O}_4$ ($x = 0.2, 0.4, 0.6, 0.8$) solid solutions, a known quantity of cobalt acetylacetonate was partially substituted by appropriate amounts of zinc acetylacetonate by adjusting the mole ratios of Zn and Co in the intervals of 0.2, 0.4, 0.6, and 0.8, while keeping the amount of iron acetylacetonate unchanged in the reaction mixture. The reaction procedures for the entire series of solid solutions were kept similar to those employed to synthesize the ternary cobalt and zinc ferrites.

3.3 Instrumentation

Powder X-ray diffraction (p-XRD) analysis was carried out by employing a Bruker AXS D8 Advance X-ray diffractometer. The instrument uses nickel-filtered $\text{Cu K}\alpha$ radiation ($\lambda=1.5418\text{\AA}$) at 40 kV, 40 mA. The scan was performed at 2θ values in the range of 10 to 80° .

3.3.1 Scanning electron microscopy (SEM) and Energy dispersive X-ray (EDX) analyses

SEM imaging was carried out on a ZEISS-Auriga Cobra SEM Field Emission Scanning Electron Microscope (FE SEM) while EDX elemental analysis was performed on a JEOL JSM-7500F Field Emission Scanning Electron Microscope (FE-SEM) Equipped with Energy Dispersive X-ray spectroscopy (EDX).

3.3.2 Transmission electron microscopy (TEM) and High resolution TEM (HRTEM) analyses

TEM imaging was performed on a JEOL 1400 TEM at accelerating voltages of 120 kV while HRTEM images were captured on a JEOL 2100 HRTEM at accelerating voltage of 200 kV.

3.3.3 UV-visible spectroscopy

The optical absorbance measurements were conducted in the UV-Vis spectral range on a Varian Cary 50 UV/Vis spectrophotometer.

3.4 Electrochemical characterization

Electrochemical measurements were investigated by a Versastat 4-500 electrochemical workstation (Princeton Applied Research, Oak Ridge, TN, USA). The cell setup for supercapacitor was made up of a three electrode system consisting of platinum (Pt) wire, a

saturated Hg/HgO electrode, and the $\text{Co}_{1-x}\text{Zn}_x\text{Fe}_2\text{O}_4$ electrodes for counter, reference, and working electrode, correspondingly. For electrocatalytic water-splitting studies, only the reference electrode was changed to a saturated calomel electrode (SCE) in the same three electrode configuration. To make the working electrode, Ni foam was used as a substrate. The working electrode was prepared by mixing 80 wt. % of the $\text{Co}_{1-x}\text{Zn}_x\text{Fe}_2\text{O}_4$ ($0 \leq x \leq 1$), 10 wt. % of polyvinylidene difluoride (PVDF) binder, and 10 wt. % of acetylene black with N-methyl pyrrolidinone (NMP) solvent. The paste was then dried at 60°C for 24 h. In order to evaluate the electrochemical performance of the $\text{Co}_{1-x}\text{Zn}_x\text{Fe}_2\text{O}_4$ ($0 \leq x \leq 1$) @ Ni electrodes, cyclic voltammetry (CV), and galvanostatic charge-discharge (GCD) measurements were used for supercapacitor test with 3 M KOH solution. For the water splitting measurements, linear sweep voltammetry (LSV) measurements were utilized at the scan rate of 2 mV/s, and the potential (V, SCE) was converted into a reversible hydrogen electrode (RHE) with iR-correction. Furthermore, electrochemical impedance spectroscopy (EIS) and chronoamperometry (CA) measurements were performed at 0.5, 0.55 V (V, SCE), respectively. All water-splitting tests were studied in 1 M KOH solution.

3.5 Results and discussion

3.5.1 Structural analysis of $\text{Co}_{1-x}\text{Zn}_x\text{Fe}_2\text{O}_4$ ($0 \leq x \leq 1$) solid solutions

Powder X-ray diffraction (p-XRD) measurements were performed to investigate the structural properties of $\text{Co}_{1-x}\text{Zn}_x\text{Fe}_2\text{O}_4$ ($0 \leq x \leq 1$) nanoparticles. Close investigation of the p-XRD patterns presented in Fig. 3.1(a) reveal that all the reflections can be indexed respectively as the (220), (311), (400), (422), (511), and (440) planes, matching perfectly with a cubic spinel structure.²⁴ The diffraction patterns of the pristine ferrite systems prepared with zinc composition $x = 0$ and $x = 1$ are consistent with the pure cubic phases of CoFe_2O_4 (ICDD # 00-001-1121) and ZnFe_2O_4 (ICDD # 01-073-1963), respectively. Meanwhile, the diffraction peaks of the solid solutions with composition $x = 0.2, 0.4, 0.6$ and 0.8 lie between those of the two pristine ferrite systems. The absence of impurity peaks and/or peak splitting rules out phase separation or separated nucleation of CoFe_2O_4 and ZnFe_2O_4 , confirming the formation of monophasic $\text{Co}_{1-x}\text{Zn}_x\text{Fe}_2\text{O}_4$ solid solutions with good distribution of Co^{2+} and Zn^{2+} in the $\text{Co}_{1-x}\text{Zn}_x\text{Fe}_2\text{O}_4$ matrix.

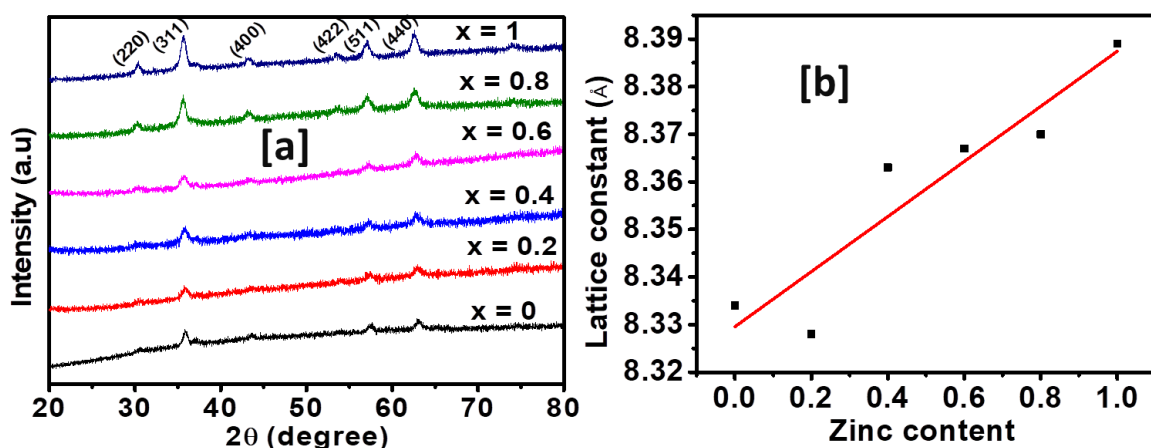


Fig.3.1. (a) Powder-XRD patterns of $\text{Co}_{1-x}\text{Zn}_x\text{Fe}_2\text{O}_4$ ($0 \leq x \leq 1$) nanoparticles, (b) Variation of lattice constants as a function of zinc composition.

The values of lattice parameters are provided in Table 3.1. The values obtained for ZnFe_2O_4 (8.389 Å) and CoFe_2O_4 (8.334 Å) nanoferrites are consistent with the literature values.^{8, 25} A sequential increase in the lattice parameter was noted with respect to the amount of zinc in the CoFe_2O_4 nanoparticles. This could be due to the difference in the sizes of Zn^{2+} and Co^{2+} ions, and the general preferences of these cations for specific coordination. Considering the different sizes of Co^{2+} (0.72 Å), Zn^{2+} (0.74 Å) and Fe^{3+} (0.59 Å), and the fact that tetrahedral vacancies are smaller compared to octahedral sites, a higher population of the smaller sites by larger metal ions causes an expansion of the structure, and consequently, the lattice constants increase. Therefore, the increasing concentration of Zn^{2+} ions led to the increase of lattice constants due to the enlargement of unit cell following the replacement of smaller Co^{2+} (0.72 Å) ions with slightly larger Zn^{2+} (0.74 Å) ions.²⁶ In some cases, taking into account the inverse spinel structure of CoFe_2O_4 with equal population of Fe^{3+} ions in both octahedral and tetrahedral sites, increasing Zn^{2+} content may substitute Fe^{3+} ions in tetrahedral sites due to its preference of the tetrahedral position.²⁷ As clearly displayed in Fig. 3.1(b), upon the formation of the solid solutions within the miscibility range, a linear relationship between the lattice parameters and amount of substituent is observed. This is in agreement with the behaviour of homogeneous alloys obeying Vegard's law.²⁸ Estimation of the average crystallite size was performed by employing the Debye-Scherrer equation.²⁹ The computed average crystallite size of $\text{Co}_{1-x}\text{Zn}_x\text{Fe}_2\text{O}_4$ ($0 \leq x \leq 1$) solid solutions was found in the range of 4.95 - 10.96 nm. It can be observed from Table 3.1 that the increase in the amount of Zn^{2+} ions from $x = 0$ to $x = 0.4$ resulted in the decrease of size from 9.67 to 4.95 nm. This is because introducing Zn^{2+} ions in the crystal structure of pristine CoFe_2O_4 obstructs the crystal growth, which is based on the entropy stabilization, forming disorder in the spinel structure.³⁰ It is

known that the introduction of zinc in the system causes liberation of more heat, decreasing the molecular concentration at the crystal surface and thereby obstructing the crystal growth.^{31, 32} As the concentration of zinc increased from 0.6 to 1, the crystallite size was observed to increase from 9.760 to 10.960 nm.

Table 3.1. Lattice parameter (a), crystallite size (d), unit cell volume (V), band gap (E_g) and EDX composition of $\text{Co}_{1-x}\text{Zn}_x\text{Fe}_2\text{O}_4$ solid solutions at different zinc contents (x).

(x)	Target ferrite composition	Stoichiometry obtained from EDX	a (Å)	d (nm)	V (Å ³)	E(eV)
0	CoFe_2O_4	$\text{Co}_{1.0}\text{Fe}_{2.06}\text{O}_{3.94}$	8.334	9.677	578.843	1.77
0.2	$\text{Co}_{0.8}\text{Zn}_{0.2}\text{Fe}_2\text{O}_4$	$\text{Co}_{0.74}\text{Zn}_{0.19}\text{Fe}_{1.96}\text{O}_{4.10}$	8.338	6.011	579.676	1.74
0.4	$\text{Co}_{0.6}\text{Zn}_{0.4}\text{Fe}_2\text{O}_4$	$\text{Co}_{0.54}\text{Zn}_{0.39}\text{Fe}_{2.02}\text{O}_{4.06}$	8.363	4.952	584.906	1.69
0.6	$\text{Co}_{0.4}\text{Zn}_{0.6}\text{Fe}_2\text{O}_4$	$\text{Co}_{0.37}\text{Zn}_{0.55}\text{Fe}_{2.11}\text{O}_{3.97}$	8.367	9.760	585.746	1.66
0.8	$\text{Co}_{0.2}\text{Zn}_{0.8}\text{Fe}_2\text{O}_4$	$\text{Co}_{0.19}\text{Zn}_{0.70}\text{Fe}_{2.15}\text{O}_{3.96}$	8.370	10.64	586.376	1.88
1	ZnFe_2O_4	$\text{Zn}_{0.93}\text{Fe}_{2.04}\text{O}_{4.04}$	8.389	10.96	590.378	1.89

3.5.2 EDX analysis

The elemental composition, homogeneity and stoichiometry of the synthesized solid solutions of $\text{Co}_{1-x}\text{Zn}_x\text{Fe}_2\text{O}_4$ ($0 \leq x \leq 1$) was studied using energy-dispersive X-ray spectroscopy (EDX). The EDX spectra for the series of spinel ferrite samples are presented in Fig. 3.2. Only the peaks conforming to Zn, Fe, and O are seen in ZnFe_2O_4 ($x = 1$) while the EDX spectrum of CoFe_2O_4 ($x = 0$) shows the presence of Co, Fe, and O only. On the other hand, the EDX spectra of solid solutions with composition $0.2 \leq x \leq 0.8$ show the presence of Co, Zn, Fe and O only. No evidence of impurities in all samples indicating the purity of $\text{Co}_{1-x}\text{Zn}_x\text{Fe}_2\text{O}_4$, which agree well with p-XRD results. The theoretical percentage atomic composition of Zn, Fe, Co and O computed from the starting compositions are in close agreement with the observed atomic percentages obtained from EDX with slight deviations (Table 3.2). The possibility of material defects and vacancies may account for the observed deviation. As expected, the experimental data observed from EDX shows slight decrease in the amount of cobalt with subsequent increase in zinc content in the $\text{Co}_{1-x}\text{Zn}_x\text{Fe}_2\text{O}_4$ samples. A graph of the atomic percentage composition of Zn and Co observed from EDX, as a function of mole fraction of $[\text{Zn}]/[\text{Zn} + \text{Co}]$ in precursor feed confirms a continuous decrease

in the amount of cobalt with a continuous increase in zinc content (Fig. 3.3). The amount of iron and oxygen also vary slightly during zinc substitution. The homogeneity of the samples was determined from the EDX spectrum over a selected zone. Figs.3.4 and 3.5 shows EDX elemental mapping of Co, Zn, Fe and O for $\text{Co}_{1-x}\text{Zn}_x\text{Fe}_2\text{O}_4$ samples with mole fraction of zinc over the entire range. It can be seen from these figures that the Co, Zn, Fe and O elements are evenly dispersed over the selected zone of the samples investigated.

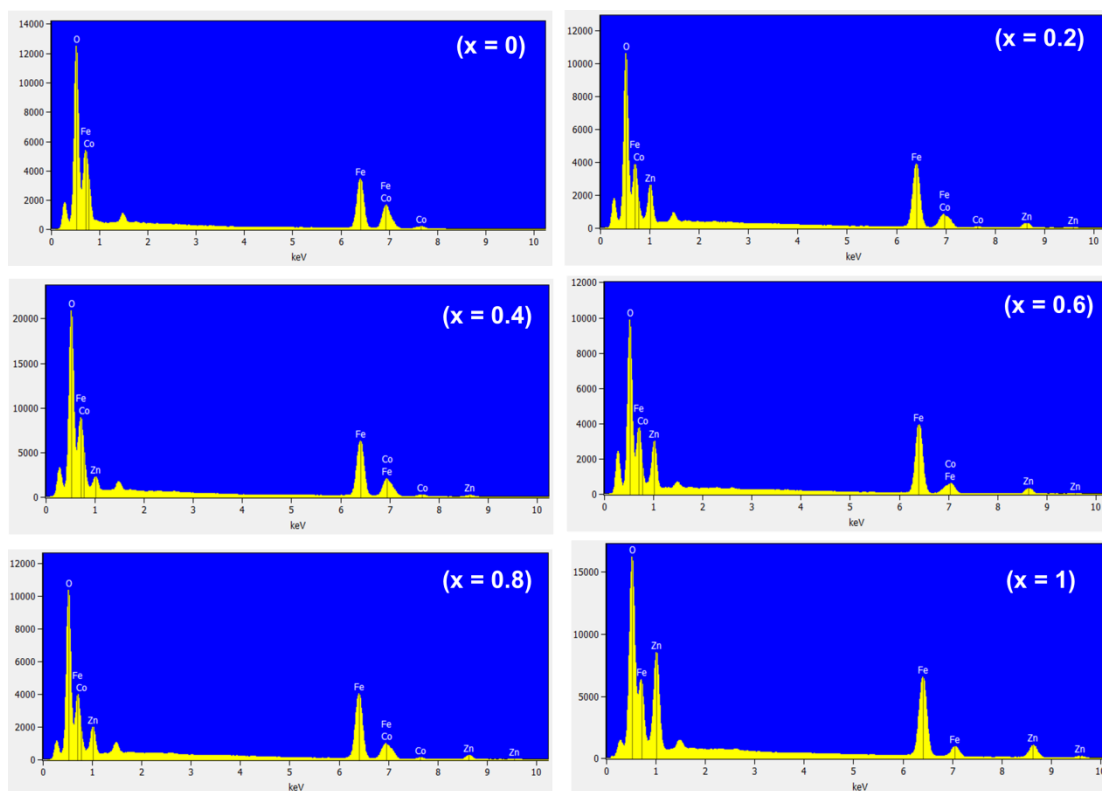


Fig.3.2. EDX spectra of $\text{Co}_{1-x}\text{Zn}_x\text{Fe}_2\text{O}_4$ ($0 \leq x \leq 1$) nanoparticles.

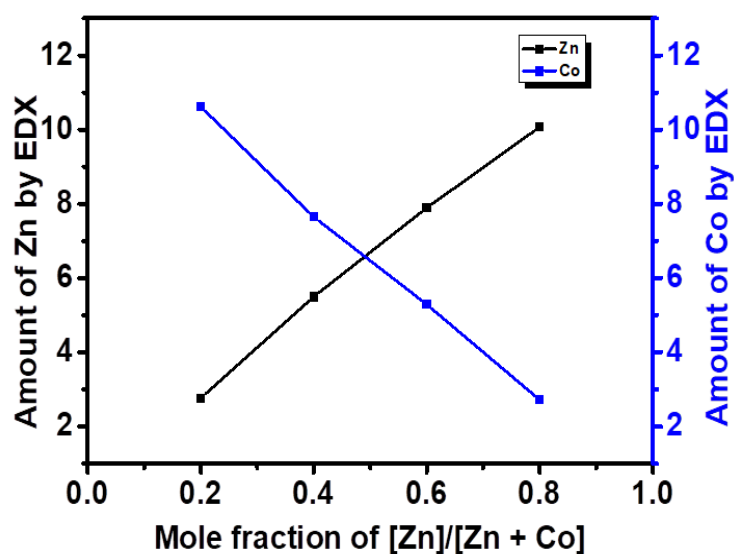


Fig.3.3. Change in the amount of zinc and cobalt as a function of mole fraction of [Zn]/[Zn+Co] in precursor feed.

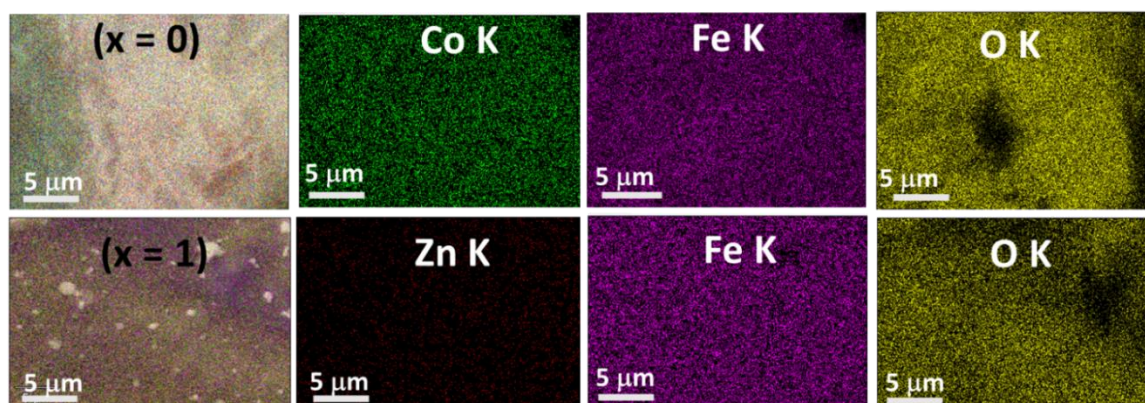


Fig.3.4. EDX elemental mapping of CoFe_2O_4 ($x = 0$) and ZnFe_2O_4 . ($x = 1$) nanoparticles.

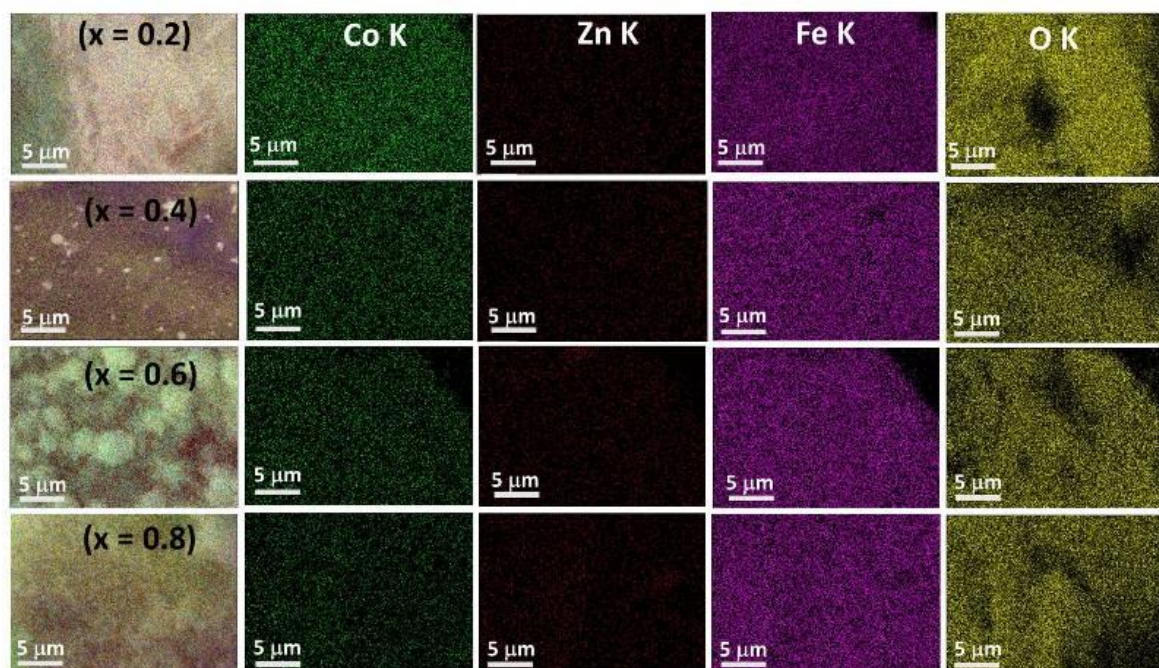


Fig.3.5. EDX elemental mapping of $\text{Co}_{1-x}\text{Zn}_x\text{Fe}_2\text{O}_4$ ($0.2 \leq x \leq 0.8$) solid solutions.

Table 3.2. Theoretical and actual elemental composition of $\text{Co}_{1-x}\text{Zn}_x\text{Fe}_2\text{O}_4$ ($0 \leq x \leq 1$) solid solutions.

(x)	Theoretical atomic %					Atomic % from EDX				
	Co	Zn	Fe	O	Total	Co	Zn	Fe	O	Total
0	14.29	-	28.57	57.14	100	14.35	-	29.40	56.25	100

0.2	11.43	2.86	28.57	57.14	100	10.62	2.76	28.03	58.59	100
0.4	8.57	5.71	28.57	57.14	100	7.65	5.50	28.87	57.98	100
0.6	5.71	8.57	28.57	57.14	100	5.29	7.89	30.10	56.72	100
0.8	2.86	11.43	28.57	57.14	100	2.72	10.07	30.68	56.53	100
1	-	14.29	28.57	57.14	100	-	13.30	29.15	57.67	100

3.5.3 SEM, TEM and HRTEM analyses

The scanning electron micrographs of $\text{Co}_{1-x}\text{Zn}_x\text{Fe}_2\text{O}_4$ ($0 \leq x \leq 1$) solid solutions shown in Fig. 3.6 indicate the formation of agglomerated nanoparticles. This aggregation is possibly due to the permanent magnetic moment of the prepared spinel ferrite which makes the particles permanently magnetized and clusters with other particles.³³ Additionally, the observed agglomeration could also be ascribed to the absence of a capping agent during solid-state thermolysis of the precursors. Similar findings have been documented in the literature.³⁴

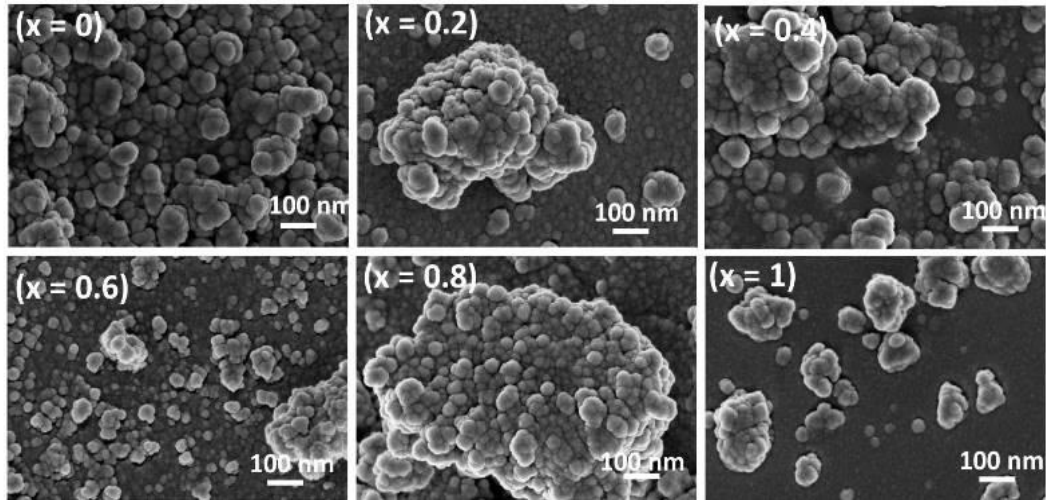


Fig.3.6. SEM images of $\text{Co}_{1-x}\text{Zn}_x\text{Fe}_2\text{O}_4$ ($0 \leq x \leq 1$) samples prepared by solventless method.

Through TEM analysis, further studies were performed to explore the size and morphology of the as-prepared solid solutions. The TEM images of $\text{Co}_{1-x}\text{Zn}_x\text{Fe}_2\text{O}_4$ ($0 \leq x \leq 1$) solid solution nanoparticles are provided in Fig. 3.7. The typical TEM micrographs revealed agglomeration of the particles for all compositions but somehow separated from each other as opposed to SEM images. Close examination of particle morphology revealed a mixture of cubic, rectangular cubic and polyhedral-shaped nanoparticles, some with truncated edges. The average grain sizes of the as-prepared ferrites estimated from the TEM

micrographs were obtained in the range of 12.54-20.98 nm. These values agree with the crystallite sizes quantified from the XRD data. However, the average size estimated from the TEM micrographs was observed to be larger than those obtained from the XRD data using the Scherrer formula. This is probably due to the agglomeration of fine crystallites, indicating that every single particle is formed by a number of agglomerated grains or crystallites.^{35, 36}

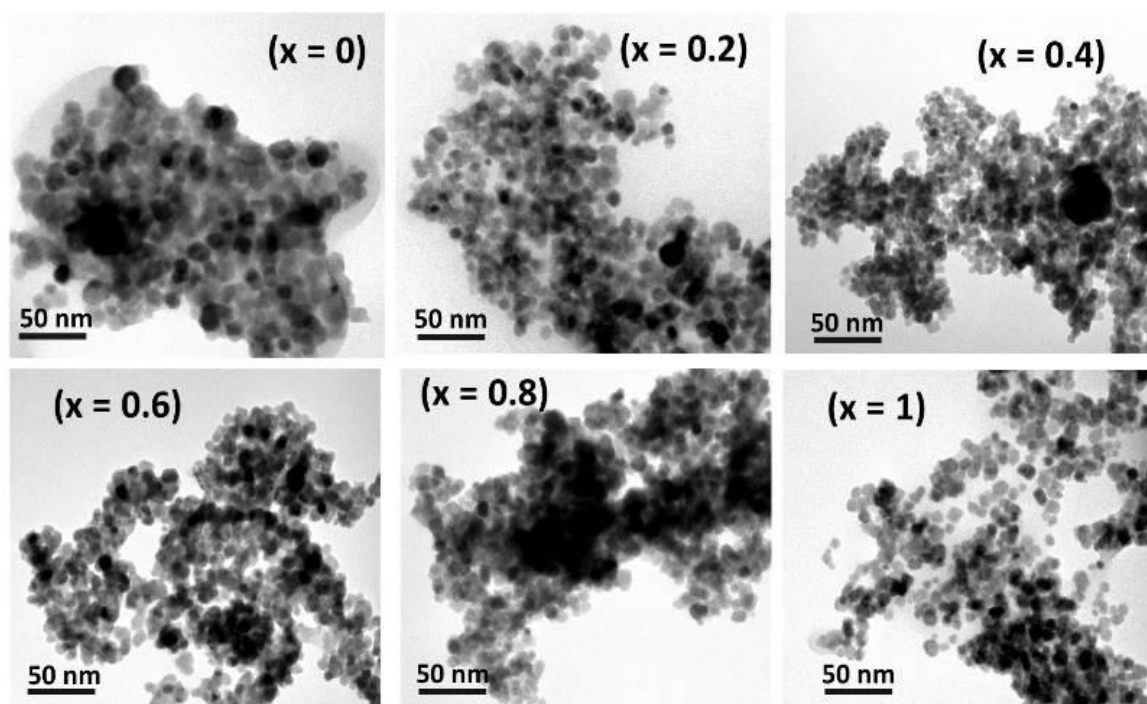


Fig.3.7. The typical TEM images of $\text{Co}_{1-x}\text{Zn}_x\text{Fe}_2\text{O}_4$ ($0 \leq x \leq 1$) nanospinels.

The typical HRTEM micrographs of $\text{Co}_{1-x}\text{Zn}_x\text{Fe}_2\text{O}_4$ ($0 \leq x \leq 1$) nanospinels are presented in Fig. 3.8. From the HRTEM micrograph of every single nanoparticle, the parallel lattice fringes as well as particle boundaries existing between the crystals show the oriented cluster of nanodimension crystallites. The observed prominent lattice fringes of $d = 0.26$ and 0.25 nm obtained in all samples are in line with the separation between the (311) lattice planes.³⁷ Other lattice spacing observed in all samples are 0.21 nm and 0.30 nm which relate to the (400) and (220) lattice planes, respectively.^{38, 39} The observed inter-planar spacing and their corresponding lattice planes are in agreement with those of pristine ZnFe_2O_4 and CoFe_2O_4 nanospinels.²⁵ These results are in line with those obtained from p-XRD analysis.

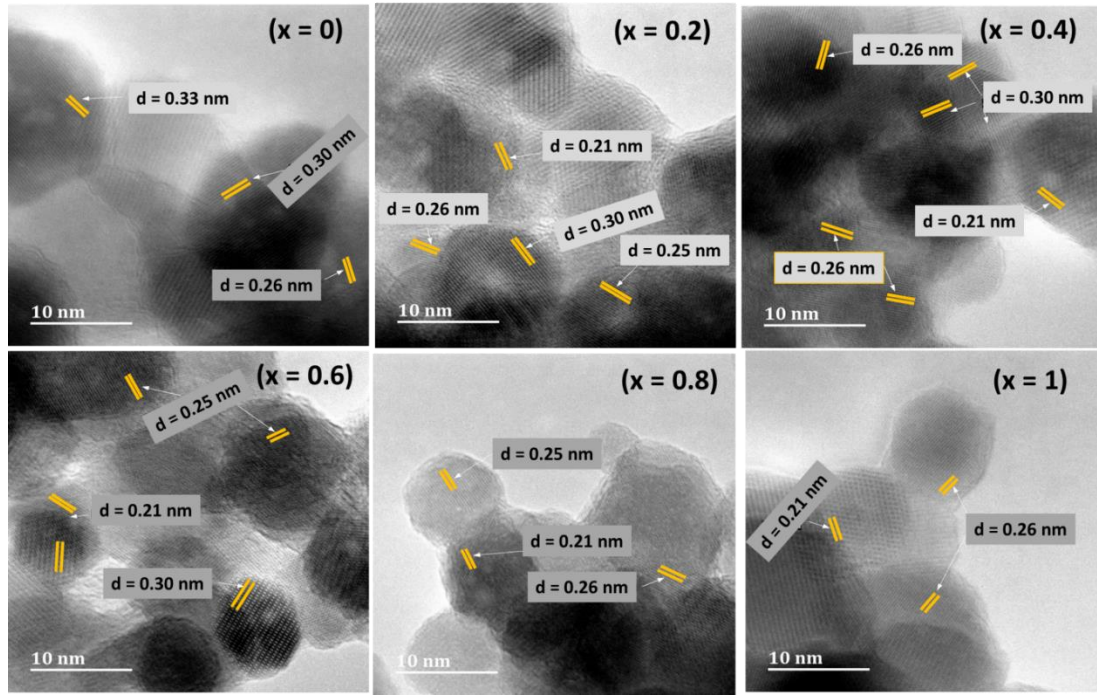


Fig.3.8. The typical HRTEM images of $\text{Co}_{1-x}\text{Zn}_x\text{Fe}_2\text{O}_4$ ($0 \leq x \leq 1$) nanospinels.

3.5.4 UV-vis analysis

The optical properties of the synthesized nanostructured $\text{Co}_{1-x}\text{Zn}_x\text{Fe}_2\text{O}_4$ ($0 \leq x \leq 1$) solid solutions were studied by UV-visible absorption spectroscopy. The ultraviolet-visible spectrum occurs due to the electronic transition, where an electron takes energy of a photon and makes transition from valence to conduction band.⁴⁰ Generally, the absorbance of the material hinges on several parameters including band gap, lattice strain, oxygen deficiency, impurity centres, surface roughness, and particle size.⁴¹ The optical absorption spectra of $\text{Co}_{1-x}\text{Zn}_x\text{Fe}_2\text{O}_4$ nanoparticles displayed in Fig. 3.9(a) shows that the adsorption edge shifts to the region of lower wavelength with the rise of zinc content. This shift gives an indication of changes in the materials' optical band gap. Cobalt ferrite is a material with semiconductor characteristics possessing a direct bandgap. The optical bandgaps of the series of $\text{Co}_{1-x}\text{Zn}_x\text{Fe}_2\text{O}_4$ ($0 \leq x \leq 1$) were computed by employing the following formula.⁴²

$$\alpha = A \frac{(h\nu - E_g)^{\frac{1}{2}}}{h\nu} \quad (1)$$

Where; $h\nu$, A , E_g , and α represent photon energy, constant, bandgap, and coefficient of absorption, respectively. The energy gap is determined from the intercept of the plot of $(\alpha h\nu)^2$ vs $h\nu$ (energy) displayed in Fig. 3.9(b) by extrapolating the linear portion of the curve. The estimated values of the band gaps for $\text{Co}_{1-x}\text{Zn}_x\text{Fe}_2\text{O}_4$ solid solutions as presented in Table 1

are 1.77, 1.74, 1.69, 1.66, 1.88, and 1.89 eV for $x = 0, 0.2, 0.4, 0.6, 0.8,$ and $1,$ correspondingly. The value of direct optical band gap for parent CoFe_2O_4 ($x = 0$) nanoparticles obtained in this study is smaller than that of the bulk material, which is about 1.95 eV.⁴³ This observation could be due to the increase of internal lattice strain and structural changes that occur due to changes in composition and cation distribution in the crystal lattice.^{45, 46} It can be observed that the optical band gap decreased from 1.77 to 1.66 eV with increasing zinc content from $x = 0$ to $x = 0.6$ in the CoFe_2O_4 matrices. This narrowing of energy gap with zinc substitution can be described by the creation of sub-bands and their combination with the conduction band to form a continuous band.⁴⁴ It may also be contributed by the underlying mechanism of zinc substitution, which is likely to induce the electron energy states into the band gap of CoFe_2O_4 , leading to the formation of new lowest unoccupied energy levels.⁴⁵ It was also noted that for Zn^{2+} content from $x = 0$ to 0.4 , the energy band decreased with the decreasing particle size. This is contrary to the typical quantum confinement behaviour and could be because of the sp-d exchange interaction occurring between the localized d-electrons and band electrons of Zn^{2+} and CoFe_2O_4 , respectively.⁴¹ With $x = 0.6$, the decrease in band gap with the increasing particle size is ascribed to the quantum confinement effect occurring in materials at the nano scale. Increasing the zinc content to $x = 0.8$ resulted in an increase in the optical band gap of the solid solution to about 1.88 eV. This is probably as a result of changes in the relative distribution of Co^{2+} at tetrahedral and octahedral sites of the spinel ferrite system. The inverse nature of the spinel CoFe_2O_4 allows equal distribution of Co^{2+} ions in both octahedral and tetrahedral sites. Thus, the incorporation of high Zn^{2+} content which preferably occupies the tetrahedral site changes the population of Co^{2+} ions at the site which in turn augments the energy gap.⁴⁶ The optical energy band gap of pure zinc ferrite nanoparticles ($x = 1$) obtained in this study was 1.89 eV. The values of band gaps for the synthesized nanoparticles lie in the semiconductor band gap range. In general, the observed tuning of the band gap for CoFe_2O_4 nanoparticles via zinc inclusion and regulating its content in continuum is vital in the design and fabrication of semiconductor devices.⁴⁷

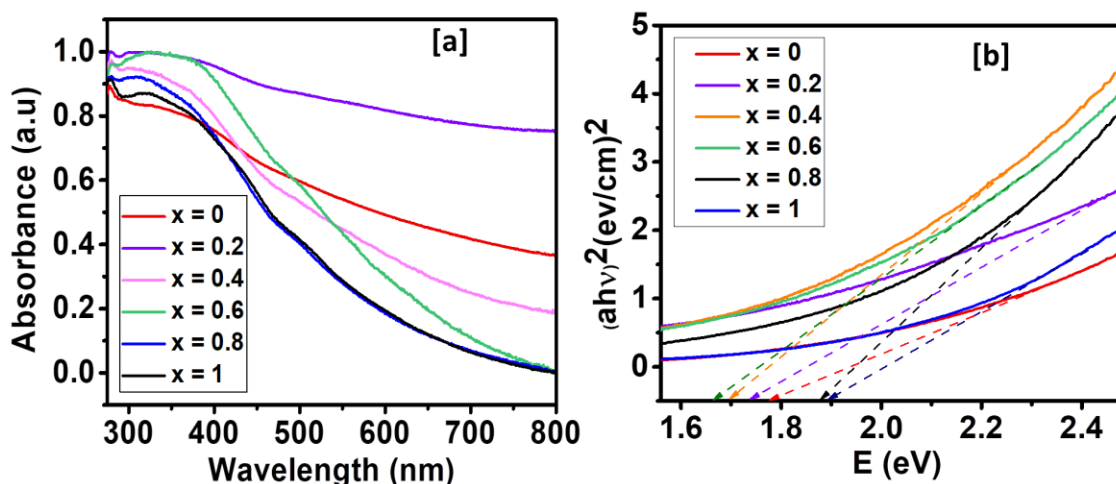


Fig.3.9 (a). UV-Vis absorption spectra, (b) Tauc plot of $(\alpha h\nu)^2$ versus photon energy, for $\text{Co}_{1-x}\text{Zn}_x\text{Fe}_2\text{O}_4$ ($0 \leq x \leq 1$) solid solutions.

3.6 Electrochemical evaluation of $\text{Co}_{1-x}\text{Zn}_x\text{Fe}_2\text{O}_4$ ($0 \leq x \leq 1$) nanoparticles

3.6.1 Supercapacitance

The evaluation of the supercapacitive performance of the $\text{Co}_{1-x}\text{Zn}_x\text{Fe}_2\text{O}_4$ ($0 \leq x \leq 1$) electrodes was performed by cyclic voltammetry (CV) and galvanostatic charge-discharge (GCD) measurements. All measurements were conducted in 3M KOH electrolyte within a potential range of 0 – 0.6 V (V, Hg/HgO). Figs. 3.10(a-f) show the CV behavior of the $\text{Co}_{1-x}\text{Zn}_x\text{Fe}_2\text{O}_4$ ($0 \leq x \leq 1$) electrodes carried out at different scan rate ranging from 2- 300 mV/s. Both the pristine electrodes ($x = 0$ and 1) and the solid solutions ($0.2 \leq x \leq 0.8$) exhibit similar shape of the CV curves at low and high scan rates, suggesting high reversibility and rate capability of the materials.⁴⁸ The typical shape of CV curves for all samples investigated is quite different from the rectangular shaped curves of the electric double-layer capacitance (EDLC). Similarly, each anode and cathode peak of the CV curves of all electrode materials examined demonstrates oxidation and reduction processes, respectively, signifying the pseudocapacitive nature of the electrodes. The pseudocapacitive behavior of nanospinel $\text{Co}_{1-x}\text{Zn}_x\text{Fe}_2\text{O}_4$ ($0 \leq x \leq 1$) electrodes is ascribed to the intercalation and deintercalation processes occurring between Fe^{3+} and electrolytic K^+ ion onto the electrode surface.⁴⁹ Moreover, the obvious redox peaks can be ascribed to the surface Faradaic processes, suggesting that the capacitance mainly originates from the surface electrochemical reactions. However, owing to the dissimilar redox potentials of Zn and Co, the position of redox peaks of $\text{Co}_{1-x}\text{Zn}_x\text{Fe}_2\text{O}_4$ ($0 \leq x \leq 1$) materials vary differently with the amount of Zn in the solid solutions. The area under the CV curve is directly related to the specific capacitance; thus, it determines the

energy storage performance of the material.⁴⁹ It can be noted from the CV curves that, the increasing scan rate from 2 to 300 mV/s leads to an increase in the area under the CV curve which gives redox peaks at maximum current density.⁵⁰ Moreover, the solid solutions with composition $0.2 \leq x \leq 0.8$ shows large area under the CV curve compared to the parent CoFe_2O_4 . In particular, sample $x = 0.6$ (i.e. $\text{Co}_{0.4}\text{Zn}_{0.6}\text{Fe}_2\text{O}_4$) displays the largest enclosed CV area than all other electrode materials, indicating that it has the highest specific capacitance.

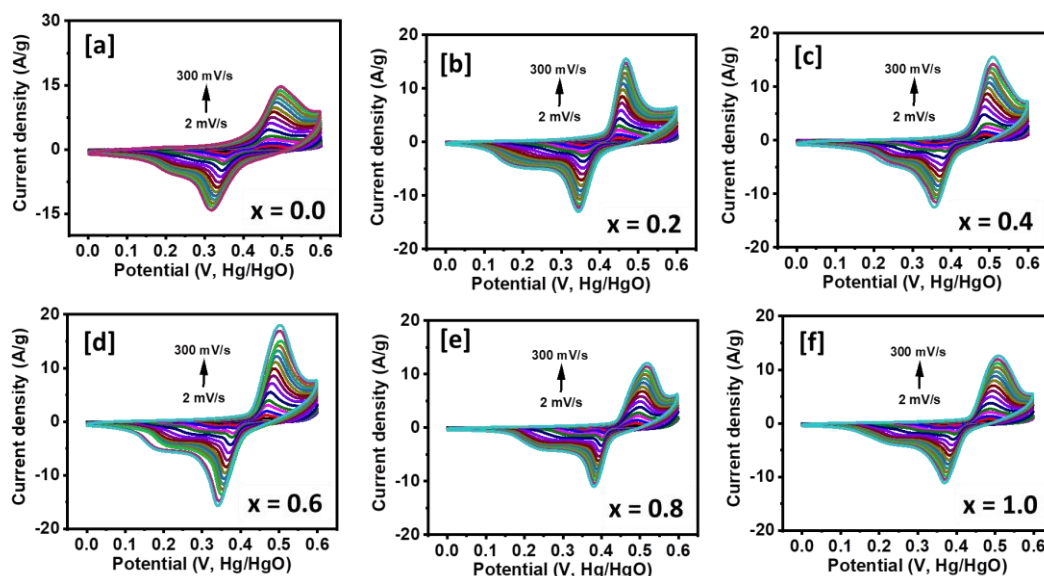


Fig.3.10. Cyclic voltammograms of $\text{Co}_{1-x}\text{Zn}_x\text{Fe}_2\text{O}_4$ ($0 \leq x \leq 1$) electrodes.

To further confirm the supercapacitive properties of the $\text{Co}_{1-x}\text{Zn}_x\text{Fe}_2\text{O}_4$ electrodes, GCD studies were also conducted at various current densities spanning from 1 - 20 A/g. Figs. 3.11(a-f) display the GCD curves for the $\text{Co}_{1-x}\text{Zn}_x\text{Fe}_2\text{O}_4$ electrodes with Zn compositions from $x = 0$ to $x = 1$. Unlike EDLC types of supercapacitor with linear graphs, pseudocapacitive characteristics of the as-prepared $\text{Co}_{1-x}\text{Zn}_x\text{Fe}_2\text{O}_4$ electrode materials were noted from the nonlinearity and plateau regions of the GCD curves. These features demonstrate the presence of Faradaic redox processes and they agree well with redox peaks in the CV curves.⁵¹ Also, higher discharge time was achieved after inclusion of Zn ($x = 0.6$) in the pristine cobalt ferrite, which indicates higher specific capacitance of the material compared to other electrode compositions. Variation of specific capacitance with current density is displayed in Fig. 3.12. The computed specific capacitance shows a decreasing trend along with the increase in current density, which is due to the low diffusion of electrolytic cation (K^+) and the somewhat unsatisfactory faradaic redox reaction at elevated current densities.⁵²

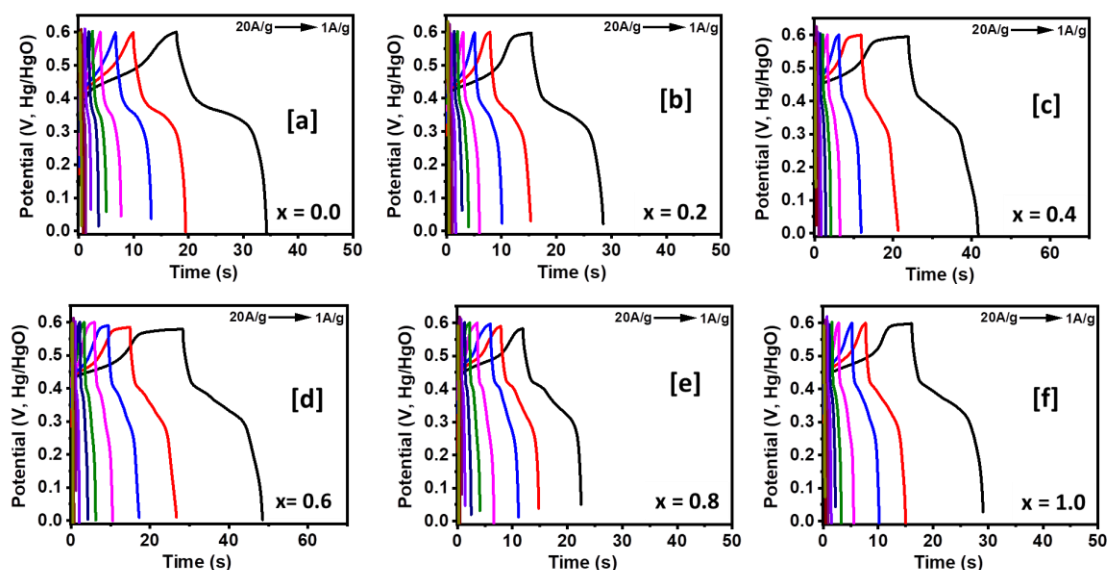


Fig.3.11. GCD of $\text{Co}_{1-x}\text{Zn}_x\text{Fe}_2\text{O}_4$ ($0 \leq x \leq 1$) electrodes.

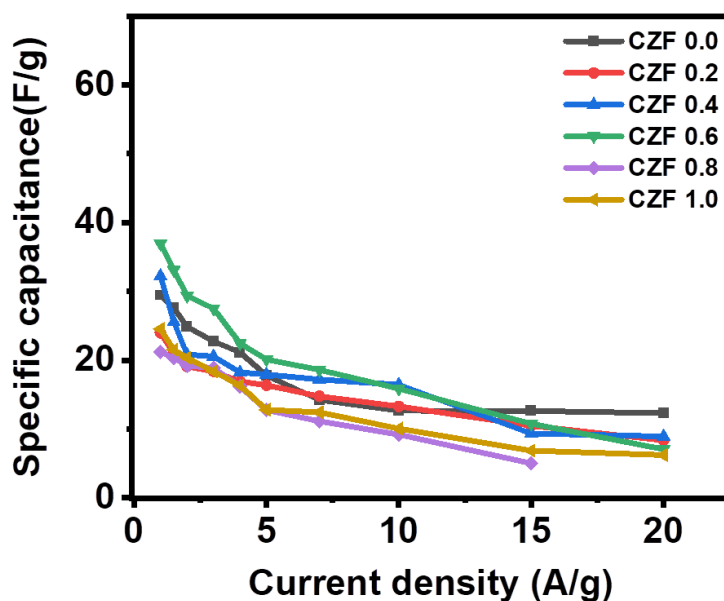


Fig.3.12. Variation of specific capacitance with current density for $\text{Co}_{1-x}\text{Zn}_x\text{Fe}_2\text{O}_4$ ($0 \leq x \leq 1$) electrodes.

3.6.2 Electrocatalytic water splitting

Fig. 3.13 (a) displays the OER polarization curves of the quaternary $\text{Co}_{1-x}\text{Zn}_x\text{Fe}_2\text{O}_4$ ($0 \leq x \leq 1$) electrodes in 1 M KOH electrolyte. The curves were obtained by LSV measurements at a scan rate of 2 mV/s. The parent CoFe_2O_4 ($x = 0$) electrode needed 404 mV of the overpotential to deliver the current density of 10 mA/cm². Interestingly, the introduction of

Zn in the crystal structure of cobalt ferrite lowered the value of the overpotential from 404 mV at $x = 0$ to 317, 378, 330, 347 mV for the solid solutions with composition $x = 0.2, 0.4, 0.6,$ and $0.8,$ respectively. Similarly, at the same current density, the ternary ZnFe_2O_4 ($x = 1$) required an overpotential of 343 mV which is relatively small compared to 404 mV of the pristine CoFe_2O_4 ($x = 0$). Impressively, the $\text{Co}_{1-x}\text{Zn}_x\text{Fe}_2\text{O}_4$ ($x = 0.2$) catalyst electrode displayed the best OER activity with an overpotential of 317 mV to afford an anodic current density of 10 mA/cm^2 , which is significantly lower than 400 mV of the pristine CoFe_2O_4 . The value of overpotential recorded for the $\text{Co}_{1-x}\text{Zn}_x\text{Fe}_2\text{O}_4$ ($x = 0.2$) solid solution in this study is comparable to most previously published catalyst electrodes for OER in alkaline electrolytes. For example, nanoscale $\text{Zn}_x\text{Co}_{3-x}\text{O}_4$ synthesized by Liu *et al.* recorded an overpotential of 320 mV at a current density of 10 mA/cm^2 during OER electrocatalysis, which is comparable to 317 mV of $\text{Co}_{0.8}\text{Zn}_{0.2}\text{Fe}_2\text{O}_4$ ⁵³. In another study, Gong *et al.* employed hydrothermal method to grow ZnCo_2O_4 nanostructure arrays on nickel foam, requiring an overpotential of 340 mV to deliver a current density of 10 mA/cm^2 in 1 M KOH, which is higher compared to 317 mV of $\text{Co}_{0.8}\text{Zn}_{0.2}\text{Fe}_2\text{O}_4$ nanoparticles.⁵⁴ The catalytic activity observed for $\text{Co}_{0.8}\text{Zn}_{0.2}\text{Fe}_2\text{O}_4$ (317 mV) is also superior to that of Co-Zn/PNC (348 mV) electrocatalyst synthesized using colloidal route.⁵⁵ The Tafel plot displayed in Fig. 3.13(b) was derived from the OER LSV curve for $\text{Co}_{1-x}\text{Zn}_x\text{Fe}_2\text{O}_4$ ($0 \leq x \leq 1$) catalyst electrodes, and the values of Tafel slopes were found in the range of 43 - 79 mV/dec. Remarkably, with the introduction of Zn in the crystal lattice of CoFe_2O_4 , the Tafel slope of the resulting $\text{Co}_{1-x}\text{Zn}_x\text{Fe}_2\text{O}_4$ solid solutions dropped from 79 mV/dec of CoFe_2O_4 ($x = 0$) to 56, 69, 56, and 43 mV/dec for $x = 0.2, 0.4, 0.6$ and $0.8,$ respectively. The observed reduction in overpotential and Tafel slope demonstrates fast surface reaction kinetics and hence improved activity of the quaternary solid solution nanocatalysts when compared to the pristine CoFe_2O_4 . This could be ascribed to the band alignment across the ferrosipinel systems thereby boosting the transport of electrons and encouraging the adsorption-desorption kinetics of oxygenated species on the $\text{Co}_{1-x}\text{Zn}_x\text{Fe}_2\text{O}_4$ electrode under optimized conditions.^{56, 57} A more detailed comparison of OER performance observed in this study with previous reports is presented in Table 3.3.

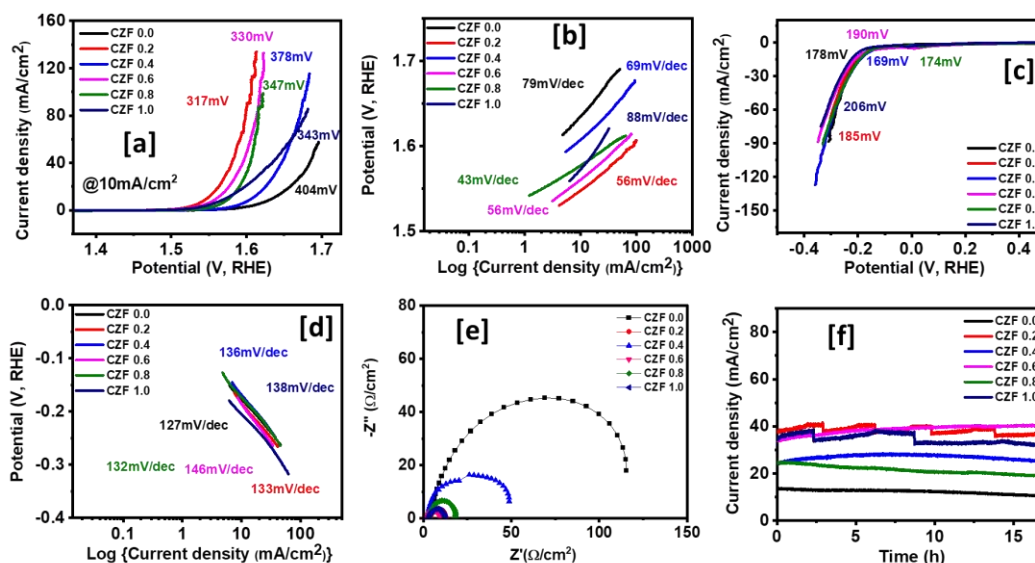


Fig.3.13: (a) OER polarization curves, (b) OER Tafel slopes, (c) HER polarization curves, (d) HER Tafel slopes, (e) Nyquist plots at 0.5 V, and (f) CA measurement at 0.55 V, for $\text{Co}_{1-x}\text{Zn}_x\text{Fe}_2\text{O}_4$ ($0 \leq x \leq 1$) electrodes.

Similar to OER studies, the HER activity of the prepared ferrites was also investigated by LSV measurements using 1 M KOH electrolyte at a scan rate of 2 mV/s. The HER polarization curves of all $\text{Co}_{1-x}\text{Zn}_x\text{Fe}_2\text{O}_4$ ($0 \leq x \leq 1$) electrodes and their corresponding Tafel slopes are shown in Fig. 3.13(c-d), respectively. For all electrode composition from $x = 0$ to $x = 1$, the overpotentials in the range of 169 - 206 mV are required to deliver the current density of 10 mA/cm^2 , along with the Tafel slope in the range of 127–146 mV/dec. As it can be seen in this work, the $\text{Co}_{0.6}\text{Zn}_{0.4}\text{Fe}_2\text{O}_4$ catalyst electrode could afford a cathodic current density of 10 mA/cm^2 at the lowest overpotential of 169 mV along with Tafel slope of 136 mV/dec compared to the other studied samples. These values signify the excellent catalytic abilities of $\text{Co}_{0.6}\text{Zn}_{0.4}\text{Fe}_2\text{O}_4$ solid solutions that could render superior electron and mass transfer processes compared to other electrode configurations. The HER performance was also much higher as compared to the commonly reported HER catalysts. For example, Ilanchezhian *et al.* have previously synthesized $\text{In}_2\text{O}_3/\text{ZnO}/\text{Co}_3\text{O}_4$ ternary oxide nanostructure, which required an overpotential of 510 mV to reach a cathodic current density of 10 mA/cm^2 in alkaline solution.⁵⁸ According to Digraaskar *et al.*, Co-doped CuZnSnS_4 prepared by sonochemical method exhibited overpotentials of 200 and 298 mV at 2 and 10 mA/cm^2 , respectively.⁵⁹ A comprehensive comparison of the HER activity obtained in this work with other electrocatalysts is provided in Table 3.4. Fig.3.13(e) shows the Nyquist plot

for all electrodes at 0.5 V (V, SCE). The resistances to charge transfer calculated from the diameter loop are 111, 8.5, 46.3, 7.3, 14.5, 9.8 Ω for $x = 0, 0.2, 0.4, 0.8$ and 1.0 , respectively. The charge transfer resistance of the parent CoFe_2O_4 (111 Ω) is relatively large compared to those exhibited by the zinc substituted ferros spinels with varying zinc content from $x = 0.2$ to $x = 1$. It is obvious that the addition of Zn lowered charge resistance thereby improving the transfer of charge at the electrode-electrolyte interface, which in turn boosted the HER activity of electrocatalysts.^{60, 61} Unlike the CoFe_2O_4 , the improved catalytic activity demonstrated by $\text{Co}_{1-x}\text{Zn}_x\text{Fe}_2\text{O}_4$ ($0.2 \leq x \leq 0.8$) solid solution electrodes could further be ascribed to the elegant combination of Co, Zn and Fe elements and their improved physicochemical properties, which improves the active sites and enhances the catalyst's conductivity.⁶² For the electrocatalytic stability analysis of all samples towards water splitting process, CA measurements were conducted at 0.55 V for 17 h and the results are shown in Fig. 3.13(f). The electrodes were found to be stable around the same current densities for about 17 h. In Figs. 3.13(a-f), the notations CZF 0.0, CZF 0.2, CZF 0.4, CZF 0.6, CZF 0.8 and CZF 1.0 represent $x = 0, x = 0.2, x = 0.4, x = 0.6, x = 0.8$, and $x = 1.0$, respectively. Further evaluation of electrode stability was also conducted by establishing a comparison between the first polarization curve and the CV curve after 1k cycles for both HER and OER (Figs. 3.14 & 3.15). All electrodes demonstrated negligible deviation between the first and the 1k cycle, suggesting high durability of the prepared catalysts for electrolysis of water. However, the observed slight fluctuation of the graph might be due to the gas generated during the CA experiment.

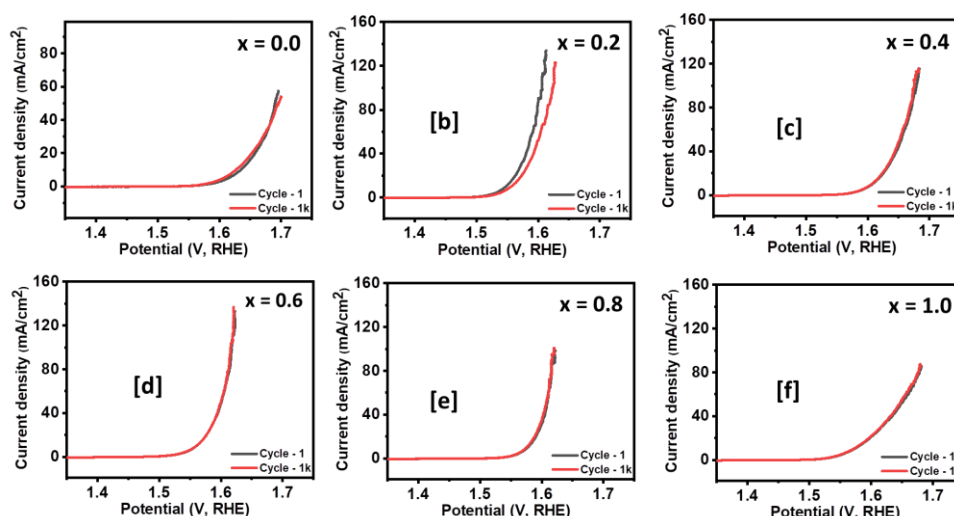


Fig.3.14. Comparison of OER polarization curve between LSV 1 curve and LSV 1k curve for $\text{Co}_{1-x}\text{Zn}_x\text{Fe}_2\text{O}_4$ ($0 \leq x \leq 1$) electrodes.

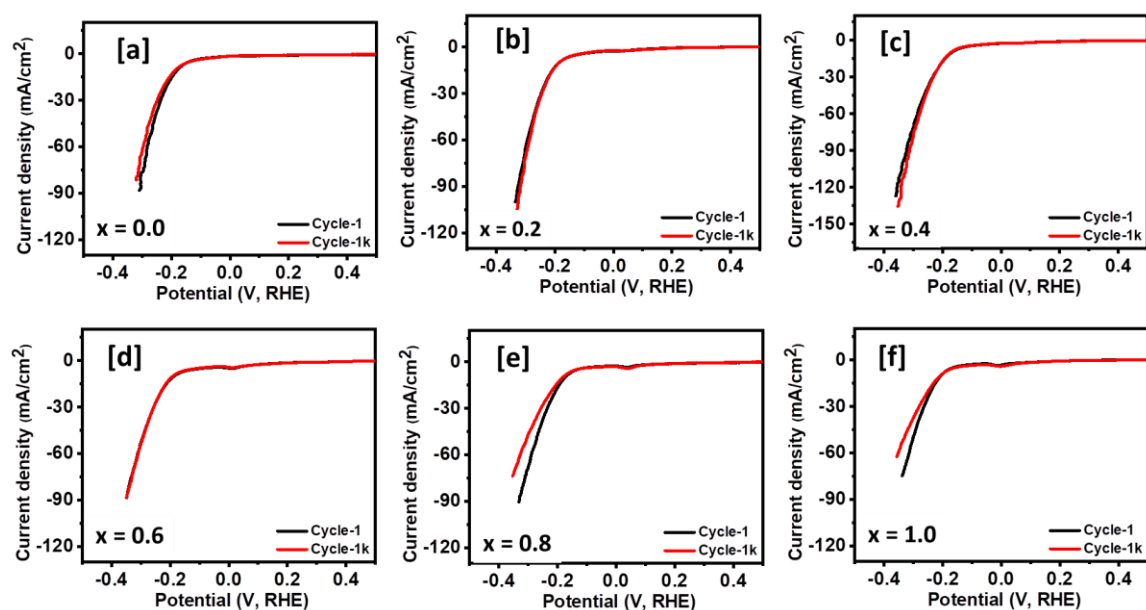


Fig.3.15. Comparison of HER polarization curve between LSV 1 curve and LSV 1k curve for $\text{Co}_{1-x}\text{Zn}_x\text{Fe}_2\text{O}_4$ ($0 \leq x \leq 1$) electrodes.

Table 3.3. Comparison of OER activities of $\text{Co}_{0.8}\text{Zn}_{0.2}\text{Fe}_2\text{O}_4$ with previously reported electrocatalyst electrodes in alkaline solution.

Catalyst material	Synthetic route	η_{OER} (mV)	Tafel slope	Reference
		at 10 mA/cm^2	(mV/dec)	
$\text{MoS}_2@\text{NiFe}_2\text{O}_4$	Hydrothermal	290	69.2	63
CoFe_2O_4	Hydrothermal	430	44	64
$\text{NiCo}_2\text{O}_4/\text{Ti}$	Solvothermal	353	61	65
$\text{Fe}_3\text{O}_4\text{-FeSe}/\text{CoSe}_2$	Hydrothermal	279	68.78	66
$\text{ZnCo}_2\text{S}_4/\text{Ni}$	Solvothermal	278	64.3	67
$\text{Zn}_x\text{Co}_{3-x}\text{O}_4$	Hydrothermal	320	51	53
$\text{Co}_3\text{V}_2\text{O}_8$	Hydrothermal	359	65	68
$\text{Ni}_{0.98}\text{Co}_{0.02}\text{Fe}_2\text{O}_4$	Hydrothermal	227	35	69
ZnCo_2O_4	Solvothermal	389	59.54	70
ZnO/Ni foam	Hydrothermal	340	-	71
$\text{Co}_3\text{Fe}_7\text{O}_x$	Hydrothermal	328	31.4	72

FeO@CuCo ₂ S ₄	Hydrothermal	240	51	⁷³
CuCo ₂ S ₄	Hydrothermal	368	119	⁷⁴
Co_{0.8}Zn_{0.2}Fe₂O₄	Solventless	317	56	This work

Table 3.4. Comparison of HER activities of Co_{0.6}Zn_{0.4}Fe₂O₄ with previously reported electrocatalyst electrodes in alkaline solution.

Catalyst material	Synthetic route	η_{HER} (mV) at 10 mA/cm ²	Tafel slope (mV/dec)	Reference
NiCo/Sm ₂ O ₃	Electrodeposition	276	162	⁷⁵
FeSe ₂ /CoFe ₂ O ₄	Hydrothermal	231	88.76	⁷⁶
NiFe ₂ O ₄	Solvothermal	300	125	⁷⁷
NiCo ₂ Se ₄ /NiCoS ₄	Solvothermal	180	107.4	⁷⁸
Ni-doped Co ₃ O ₄	Hydrothermal	120	62	⁷⁹
LaCo _{0.94} Pt _{0.06} O _{3-δ}	Sol-gel	294	148	⁸⁰
Co-	Hydrothermal	226	138	⁸¹
CoO/ZnFe ₂ O ₄ @CNWs				
CoMn ₂ O ₄ /NiOOH/Ni	Solvothermal	132	61.51	⁸²
CuCo ₂ O ₄	Hydrothermal	115	153	⁸³
NiFe ₂ O ₄ /CoNi-S	Hydrothermal & electrodeposition	149	90	⁸⁴
Co ₃ O ₄ -NiO	Co-precipitation	378	90	⁸⁵
2D ZnCo ₂ O ₄	Template method	335	43	⁸⁶
Nd _x Co _{1-x} FeO ₃	Solvothermal	239	68	⁸⁷
Co_{0.6}Zn_{0.4}Fe₂O₄	Solventless	169	136	This work

It is interesting to note that after introducing Zn in the spinel cobalt ferrite system, the performance of the Co_{1-x}Zn_xFe₂O₄ ($0 \leq x \leq 1$) electrodes for supercapacitor and water splitting was generally improved. Theoretical and experimental studies show that the introduction of Zn in a particular material lowers the charge resistance thereby improving electrolytic conductivity.^{55, 88} As pointed out in the previous sections, the inclusion of Zn resulted in the increase of the lattice parameter and cell volume, facilitating electrolyte diffusion and access to more OH.⁸⁸ However, it was also observed that the band gap decreased with increasing the ratio of Zn, and then started to increase after $x = 0.6$, suggesting the decrease of the

performance of the electrode after $x = 0.6$. Therefore, the electrochemical performance of the as-prepared solid solutions is attributed to the consideration of the changes in the lattice parameter, cell volume, crystallite size, and the band gap of the synthesized materials.

3.7 Conclusion

In summary, single-phase $\text{Co}_{1-x}\text{Zn}_x\text{Fe}_2\text{O}_4$ ($0 \leq x \leq 1$) solid solutions with varying amounts of Co and Zn have been successfully prepared by a simple solventless thermolysis route. The findings obtained from p-XRD and EDX analyses confirm the successful incorporation of zinc into the crystal structure of cobalt ferrite. Enhancement of the electrochemical performance was evident as the solid solutions provided more electrochemical active sites and diffusion channels for electrochemical reactions. Higher discharge time displayed by $\text{Co}_{0.4}\text{Zn}_{0.6}\text{Fe}_2\text{O}_4$ is indicative of higher specific capacitance of the material compared to the pristine CoFe_2O_4 . For OER, the $\text{Co}_{0.8}\text{Zn}_{0.2}\text{Fe}_2\text{O}_4$ solid solution exhibits higher activity with low overpotential of 317 mV along with a small Tafel slope of 56 mV/dec. As for HER in alkaline electrolyte, $\text{Co}_{0.6}\text{Zn}_{0.4}\text{Fe}_2\text{O}_4$ has displayed decent performance with a low overpotential of 169 mV and Tafel slope of 136 mV/dec compared to other electrode compositions. The notable OER and HER activity of the solid solutions can be attributed to their comparatively small crystallite size (i.e. 6.01 nm for $\text{Co}_{0.8}\text{Zn}_{0.2}\text{Fe}_2\text{O}_4$ and 4.95 nm for $\text{Co}_{0.6}\text{Zn}_{0.4}\text{Fe}_2\text{O}_4$), and the synergistic effect of Co, Zn and Fe, resulting to considerably improved electron transfer, compared to pristine CoFe_2O_4 . Interestingly, these electrodes were found to be stable with negligible deviation in current density for about 17 h of electrochemical tests.

References

1. Zhao, Q.; Yan, Z.; Chen, C.; Chen, J. *Chemical Reviews* **2017**, 117, (15), 10121-10211.
2. Sharifianjazi, F.; Moradi, M.; Parvin, N.; Nemati, A.; Rad, A. J.; Sheysi, N.; Abouchenari, A.; Mohammadi, A.; Karbasi, S.; Ahmadi, Z. *Ceramics International* **2020**.
3. Sharifi, S.; Yazdani, A.; Rahimi, K. *Materials Science in Semiconductor Processing* **2020**, 108, 104902.
4. Malaie, K.; Ganjali, M. R. *Journal of Energy Storage* **2020**, 102097.
5. Yuan, C.; Wu, H. B.; Xie, Y.; Lou, X. W. *Angewandte Chemie International Edition* **2014**, 53, (6), 1488-1504.
6. Álvarez-Serrano, I.; Arillo, M. A.; López, M. L.; Veiga, M. L.; Pico, C., Tunable ferrites as environmentally friendly materials for energy-efficient processes. Wiley Online Library: 2011.
7. Gao, H.; Liu, S.; Li, Y.; Conte, E.; Cao, Y. *Energies* **2017**, 10, (11), 1787.
8. Jnaneshwara, D.; Avadhani, D.; Prasad, B. D.; Nagabhushana, B.; Nagabhushana, H.; Sharma, S.; Prashantha, S.; Shivakumara, C. *Journal of Alloys and Compounds* **2014**, 587, 50-58.
9. Gabal, M.; Al-Juaid, A.; Al-Rashed, S.; Hussein, M.; Al-Marzouki, F. *Journal of Magnetism and Magnetic Materials* **2017**, 426, 670-679.
10. Wongpratrat, U.; Tipsawat, P.; Khajonrit, J.; Swatsitang, E.; Maensiri, S. *Journal of Alloys and Compounds* **2020**, 831, 154718.
11. Zhao, X.; Fu, Y.; Wang, J.; Xu, Y.; Tian, J.-H.; Yang, R. *Electrochimica Acta* **2016**, 201, 172-178.
12. Singh, R.; Singh, J.; Cong, H. N.; Chartier, P. *International Journal of Hydrogen Energy* **2006**, 31, (10), 1372-1378.
13. Singh, R.; Singh, J.; Lal, B.; Singh, A. *International Journal of Hydrogen Energy* **2007**, 32, (1), 11-16.
14. Li, C.; Han, X.; Cheng, F.; Hu, Y.; Chen, C.; Chen, J. *Nature Communications* **2015**, 6, (1), 1-8.
15. Hazra, S.; Ghosh, N. *Journal of Nanoscience and Nanotechnology* **2014**, 14, (2), 1983-2000.
16. Cao, Y.; Qin, H.; Niu, X.; Jia, D. *Ceramics International* **2016**, 42, (9), 10697-10703.
17. Tatarchuk, T.; Bououdina, M.; Vijaya, J. J.; Kennedy, L. J. In *Spinel ferrite nanoparticles: synthesis, crystal structure, properties, and perspective applications*,

- International Conference on Nanotechnology and Nanomaterials, 2016; Springer: pp 305-325.
18. Pérez-Mirabet, L.; Solano, E.; Martínez-Julián, F.; Guzmán, R.; Arbiol, J.; Puig, T.; Obradors, X.; Pomar, A.; Yáñez, R.; Ros, J. *Materials Research Bulletin* **2013**, 48, (3), 966-972.
 19. Naidek, K. P.; Bianconi, F.; Da Rocha, T. C. R.; Zanchet, D.; Bonacin, J. A.; Novak, M. A.; Vaz, M. d. G. F.; Winnischofer, H. *Journal of Colloid and Interface Science* **2011**, 358, (1), 39-46.
 20. Angermann, A.; Hartmann, E.; Töpfer, J. *Journal of Magnetism and Magnetic Materials* **2010**, 322, (21), 3455-3459.
 21. Li, M.; Xiong, Y.; Liu, X.; Bo, X.; Zhang, Y.; Han, C.; Guo, L. *Nanoscale* **2015**, 7, (19), 8920-8930.
 22. Song, Q.; Zhang, Z. J. *Journal of the American Chemical Society* **2012**, 134, (24), 10182-10190.
 23. Willis, A. L.; Chen, Z.; He, J.; Zhu, Y.; Turro, N. J.; O'Brien, S. *Journal of Nanomaterials* **2007**, 2007.
 24. Raut, A.; Barkule, R.; Shengule, D.; Jadhav, K. *Journal of Magnetism and Magnetic Materials* **2014**, 358, 87-92.
 25. Singh, C.; Jauhar, S.; Kumar, V.; Singh, J.; Singhal, S. *Materials Chemistry and Physics* **2015**, 156, 188-197.
 26. Schmidt, M.; Andersen, H. L.; Granados-Miralles, C.; Saura-Múzquiz, M.; Stingaciu, M.; Christensen, M. *Dalton Transactions* **2016**, 45, (15), 6439-6448.
 27. Smit, J.; Wijn, H. *Eindhoven, The Netherlands* **1959**, 278.
 28. West, A. R., *Basic Solid State Chemistry*. John Wiley & Sons Incorporated: 1999.
 29. Holzwarth, U.; Gibson, N. *Nature Nanotechnology* **2011**, 6, (9), 534-534.
 30. Sharifi, I.; Shokrollahi, H. *Journal of Magnetism and Magnetic Materials* **2012**, 324, (15), 2397-2403.
 31. Upadhyay, C.; Verma, H.; Anand, S. *Journal of Applied Physics* **2004**, 95, (10), 5746-5751.
 32. Gul, I.; Ahmed, W.; Maqsood, A. *Journal of Magnetism and Magnetic Materials* **2008**, 320, (3-4), 270-275.
 33. Tatarchuk, T.; Bououdina, M.; Macyk, W.; Shyichuk, O.; Paliychuk, N.; Yaremiy, I.; Al-Najar, B.; Pacia, M. *Nanoscale Research Letters* **2017**, 12, (1), 141.

34. Borhan, A. I.; Hulea, V.; Iordan, A. R.; Palamaru, M. N. *Polyhedron* **2014**, 70, 110-118.
35. Tatarchuk, T.; Bououdina, M.; Paliychuk, N.; Yaremiy, I.; Moklyak, V. *Journal of Alloys and Compounds* **2017**, 694, 777-791.
36. Pradeep, A.; Priyadharsini, P.; Chandrasekaran, G. *Journal of Alloys and Compounds* **2011**, 509, (9), 3917-3923.
37. Nikam, D. S.; Jadhav, S. V.; Khot, V. M.; Bohara, R.; Hong, C. K.; Mali, S. S.; Pawar, S. *RSC Advances* **2015**, 5, (3), 2338-2345.
38. Yaseneva, P.; Bowker, M.; Hutchings, G. *Physical Chemistry Chemical Physics* **2011**, 13, (41), 18609-18614.
39. Praveena, K.; Sadhana, K. *International Journal of Scientific and Research Publications* **2015**, 5, (4), 1-21.
40. Zaki, H.; Al-Heniti, S.; Elmosalami, T. *Journal of Alloys and Compounds* **2015**, 633, 104-114.
41. Ahmed, A. S.; Singla, M.; Tabassum, S.; Naqvi, A. H.; Azam, A. *Journal of Luminescence* **2011**, 131, (1), 1-6.
42. Tauc, J., *Amorphous an Liquid Semiconductors*. Springer Science & Business Media: 2012.
43. Himcinschi, C.; Vrejoiu, I.; Salvan, G.; Fronk, M.; Talkenberger, A.; Zahn, D. R.; Rafaja, D.; Kortus, J. *Journal of Applied Physics* **2013**, 113, (8), 084101.
44. Bai, H.; Liu, Z.; Sun, D. D. *International Journal of Hydrogen Energy* **2012**, 37, (19), 13998-14008.
45. Sundararajan, M.; Kennedy, L. J.; Vijaya, J. J.; Aruldoss, U. *Spectrochimica Acta Part A: Molecular and Biomolecular Spectroscopy* **2015**, 140, 421-430.
46. Sharma, D.; Khare, N. *AIP Advances* **2016**, 6, (8), 085005.
47. Supriya, S.; Kumar, S.; Kar, M. In *Band gap engineering of zinc substituted cobalt ferrite for optoelectronic applications*, 2017 IEEE 12th Nanotechnology Materials and Devices Conference (NMDC), 2017; IEEE: pp 33-34.
48. Pang, M.; Jiang, S.; Zhao, J.; Zhang, S.; Liu, R.; Qu, W.; Pan, Q.; Xing, B.; Gu, L.; Wang, H. *New Journal of Chemistry* **2018**, 42, (23), 19153-19163.
49. Rani, B. J.; Ravi, G.; Yuvakkumar, R.; Ganesh, V.; Ravichandran, S.; Thambidurai, M.; Rajalakshmi, A.; Sakunthala, A. *Applied Physics A* **2018**, 124, (7), 1-12.
50. Vadiyar, M.; Bhise, S.; Patil, S.; Patil, S.; Pawar, D.; Ghule, A.; Patil, P.; Kolekar, S. *RSC Advances* **2015**, 5, (57), 45935-45942.

51. Guragain, D.; Zequine, C.; Bhattarai, R.; Choi, J.; Gupta, R.; Shen, X.; Mishra, S. *MRS Advances* **2020**, 5, (48), 2487-2494.
52. Chen, S.; Xue, M.; Li, Y.; Pan, Y.; Zhu, L.; Zhang, D.; Fang, Q.; Qiu, S. *Inorganic Chemistry Frontiers* **2015**, 2, (2), 177-183.
53. Liu, X.; Chang, Z.; Luo, L.; Xu, T.; Lei, X.; Liu, J.; Sun, X. *Chemistry of Materials* **2014**, 26, (5), 1889-1895.
54. Gong, Y.; Pan, H.; Xu, Z.; Yang, Z.; Lin, Y.; Zhang, M. *International Journal of Hydrogen Energy* **2018**, 43, (31), 14360-14368.
55. Peng, W.; Zheng, G.; Wang, Y.; Cao, S.; Ji, Z.; Huan, Y.; Zou, M.; Yan, X. *International Journal of Hydrogen Energy* **2019**, 44, (36), 19782-19791.
56. Jothi, V. R.; Bose, R.; Rajan, H.; Jung, C.; Yi, S. C. *Advanced Energy Materials* **2018**, 8, (34), 1802615.
57. Liang, H.; Gandi, A. N.; Xia, C.; Hedhili, M. N.; Anjum, D. H.; Schwingenschlögl, U.; Alshareef, H. N. *ACS Energy Letters* **2017**, 2, (5), 1035-1042.
58. Ilanchezhian, P.; Kumar, G. M.; Siva, C.; Madhankumar, A.; Jeon, H.; Kang, T.; Kim, D. *International Journal of Hydrogen Energy* **2019**, 44, (41), 23081-23090.
59. Digraaskar, R. V.; Sapner, V. S.; Narwade, S. S.; Mali, S. M.; Ghule, A. V.; Sathe, B. R. *RSC Advances* **2018**, 8, (36), 20341-20346.
60. Wang, P.; Liu, X.; Yan, Y.; Cao, J.; Feng, J.; Qi, J. *Catalysis Science & Technology* **2020**, 10, (5), 1395-1400.
61. Rani, B. J.; Ravi, G.; Yuvakkumar, R.; Ravichandran, S.; Ameen, F.; Al-Sabri, A. *Journal of Sol-Gel Science and Technology* **2019**, 89, (2), 500-510.
62. Hao, Y.; Xu, Y.; Liu, J.; Sun, X. *Journal of Materials Chemistry A* **2017**, 5, (11), 5594-5600.
63. Karpuraranjith, M.; Chen, Y.; Wang, B.; Ramkumar, J.; Yang, D.; Srinivas, K.; Wang, W.; Zhang, W.; Manigandan, R. *Journal of Colloid and Interface Science* **2021**, 592, 385-396.
64. Rana, S.; Yadav, K. K.; Guchhait, S. K.; Nishanthi, S.; Mehta, S.; Jha, M. *Journal of Materials Science* **2021**, 56, (14), 8383-8395.
65. Bao, W.; Xiao, L.; Zhang, J.; Jiang, P.; Zou, X.; Yang, C.; Hao, X.; Ai, T. *International Journal of Hydrogen Energy* **2021**, 46, (17), 10259-10267.
66. Zhang, L.-C.; Wang, M.-Q.; Chen, H.; Liu, H.; Wang, Y.; Zhang, L.-Z.; Hou, G.-R.; Bao, S.-J. *Materials Research Bulletin* **2020**, 122, 110680.

67. Song, G.; Wang, Z.; Sun, J.; Sun, J.; Yuan, D.; Zhang, L. *Electrochemistry Communications* **2019**, 105, 106487.
68. Xing, M.; Kong, L.-B.; Liu, M.-C.; Liu, L.-Y.; Kang, L.; Luo, Y.-C. *Journal of Materials Chemistry A* **2014**, 2, (43), 18435-18443.
69. Zhang, Z.; Yan, X.; Liu, J.; Liu, B.; Gu, Z.-G. *Sustainable Energy & Fuels* **2021**, 5, (10), 2668-2677.
70. Zhang, J.; Zhang, D.; Yang, Y.; Ma, J.; Cui, S.; Li, Y.; Yuan, B. *RSC Advances* **2016**, 6, (95), 92699-92704.
71. Kashif, M.; Fiaz, M.; Athar, M. *Inorganic and Nano-Metal Chemistry* **2020**, 1-7.
72. Lin, X.; Li, X.; Li, F.; Fang, Y.; Tian, M.; An, X.; Fu, Y.; Jin, J.; Ma, J. *Journal of Materials Chemistry A* **2016**, 4, (17), 6505-6512.
73. Ahmed, A. T. A.; Pawar, S. M.; Inamdar, A. I.; Im, H.; Kim, H. *International Journal of Energy Research* **2020**, 44, (3), 1798-1811.
74. Sethulakshmi, N.; Nellaiappan, S.; Pentiyala, P.; Sharma, M.; Irusta, S.; Deshpande, P. A.; Sharma, S. *Electrochimica Acta* **2021**, 370, 137701.
75. Liu, H.; Zeng, S.; He, P.; Dong, F.; He, M.; Zhang, Y.; Wang, S.; Li, C.; Liu, M.; Jia, L. *Electrochimica Acta* **2019**, 299, 405-414.
76. Zhang, H.; Nengzi, L.-c.; Li, B.; Cheng, Q.; Gou, J.; Cheng, X. *Renewable Energy* **2020**, 155, 717-724.
77. Dalai, N.; Mohanty, B.; Mitra, A.; Jena, B. *ChemistrySelect* **2019**, 4, (27), 7791-7796.
78. Wang, K.; Lin, Z.; Tang, Y.; Tang, Z.; Tao, C.-L.; Qin, D.-D.; Tian, Y. *Electrochimica Acta* **2021**, 368, 137584.
79. Li, L.; Xu, Q.; Zhang, Y.; Li, J.; Fang, J.; Dai, Y.; Cheng, X.; You, Y.; Li, X. *Journal of Alloys and Compounds* **2020**, 823, 153750.
80. Wang, C.; Zeng, L.; Guo, W.; Gong, C.; Yang, J. *RSC advances* **2019**, 9, (61), 35646-35654.
81. Liu, W.; Zhou, Y.; Bao, J.; Wang, J.; Zhang, Y.; Sheng, X.; Xue, Y.; Guo, C.; Chen, X. *Journal of colloid and interface science* **2020**, 561, 620-628.
82. Lee, J.; Son, N.; Park, N.-K.; Ryu, H.-J.; Baek, J.-I.; Sohn, Y.; Do, J. Y.; Kang, M. *Electrochimica Acta* **2021**, 379, 138168.
83. Aqueel Ahmed, A. T.; Pawar, S. M.; Inamdar, A. I.; Kim, H.; Im, H. *Advanced Materials Interfaces* **2020**, 7, (2), 1901515.
84. Shi, Y.; Feng, X.; Guan, H.; Zhang, J.; Hu, Z. *International Journal of Hydrogen Energy* **2021**, 46, (12), 8557-8566.

85. Kumar, G. M.; Ilanchezhiyan, P.; Siva, C.; Madhankumar, A.; Kang, T.; Kim, D. *International Journal of Hydrogen Energy* **2020**, 45, (1), 391-400.
86. Gu, J.; Zhang, C.; Du, Z.; Yang, S. *Small* **2019**, 15, (45), 1904587.
87. Ilanchezhiyan, P.; Siva, C.; Cho, H.; Tamilselvan, S.; Seal, S.; Kang, T.; Kim, D. *Journal of Materials Research and Technology* **2021**, 11, 2246-2254.
88. Chen, Y.; Ni, D.; Yang, X.; Liu, C.; Yin, J.; Cai, K. *Electrochimica Acta* **2018**, 278, 114-123.

CHAPTER 4

Direct solid-state synthesis of nanometric $\text{Ni}_{1-x}\text{Mg}_x\text{Fe}_2\text{O}_4$ ($0 \leq x \leq 1$) solid solutions as eco-friendly electrode materials for water splitting and supercapacitance

4.1 Introduction

Recently, the significance and scope of solid-state chemistry has grown drastically, responding to the demand of novel eco-friendly materials for advanced applications.¹⁻³ In particular, the invention of multifunctional materials with unique properties is vital in realizing a clean and enduring energy economy driven by both renewables and energy efficiency. Nowadays, the context of research is focused on the preparation and characterization of new materials for potential applications in energy transformation, optimization, storage as well as device fabrication.⁴⁻⁶ Amongst the many compounds, mixed metal oxides are currently being investigated as potential electroactive materials for energy-efficient processes.⁷⁻¹⁰ Benefiting from their remarkable electrochemical properties, mixed spinel ferrites are of particular interest in the current search for economical and eco-compatible materials for energy storage and/or conversion technologies.^{11, 12}

Spinel NiFe_2O_4 and MgFe_2O_4 are amongst the auspicious ferrites with applications in batteries, supercapacitors, and oxygen and/or hydrogen evolution reactions.¹³⁻¹⁷ Both NiFe_2O_4 and MgFe_2O_4 are considered eco-friendly, abundant, non-toxic, and economically feasible materials.^{18, 19} Their cubic structure and multifarious cations enable the formation of materials with diverse properties.^{20, 21} To date, it has been demonstrated that unlike the bulk, nanostructured NiFe_2O and MgFe_2O_4 display excellent electric, dielectric and electrochemical behaviour.^{13, 22, 23} For example, Majumder and co-workers employed an auto-combustion supported sol-gel route to prepare nanometric MgFe_2O_4 , and the resulting electrode material demonstrated a high specific capacitance of 428.9 F/g at 0.0625 A/g.²⁴ Samuel *et al.*²⁵ successfully synthesized NiFe_2O nanosheets which displayed a specific capacitance of 560 F/g at 1 A/g. Recently, Simon *et al.* synthesized mesoporous NiFe_2O_4 electrocatalysts by a soft-template method.²⁶ During OER electrocatalysis, it required an overpotential of 410 mV to deliver a current density of 10 mA/cm² in alkaline solution. Another study demonstrated the potential of MgFe_2O_4 nanoparticles synthesized by the sol-gel method for HER and OER. The OER electrocatalysis required an overpotential of 1090 mV whereas the HER electrocatalysis needed an overpotential 402 mV.²⁷ However, the electrochemical performance of these oxides still needs improvement.

Alloying of pristine semiconductor nanoparticles with foreign elements has received considerable attention recently owing to its ability to engineer the materials' properties via tunable compositions,²⁸ and consequently change the materials' electrochemical properties.²⁹ Interestingly, both NiFe_2O and MgFe_2O_4 possess the same cubic symmetry with a space

group of $Fd3m$, and since the crystal size of Ni^{2+} (0.69 Å) is comparable to that of Mg^{2+} (0.72 Å), a substitutional solid solution can be obtained by varying the stoichiometric amounts of Ni and Mg during the preparation process. Studies have demonstrated that the formation of solid solution yields materials with enhanced properties and performance compared to the parent material. For instance, Yang *et al.*³⁰ reported enhanced specific capacitance of 3762 F/g at 5 A/g for $(\text{Ni}_x\text{Co}_{1-x})_9\text{Se}_8$ ($0 < x < 1$) after introduction of Ni^{2+} , surpassing other nickel-cobalt sulfide and selenide based pseudocapacitors. By Mn^{2+} substitution in NiCo_2O_4 , Chang and co-workers obtained $\text{NiMn}_x\text{Co}_{2-x}\text{O}_{4-y}$ ($0 \leq x \leq 1$) supercapacitors which exhibited a much better electrochemical capacitance compared to the pristine oxides.³¹ Very recently, a series of $\text{Ni}_{1-x}\text{Co}_x\text{Fe}_2\text{O}_4$ ($x = 0.01, 0.02, 0.05$, and 0.1) were fabricated via hydrothermal process and the optimized solid solution exhibited a small overpotential of 227 mV at 10 mA/cm² in 1 M KOH for OER.³²

Preparation of such materials by eco-friendly routes that allow control of composition is crucial in ascertaining variations of their physico-chemical properties with respect to chemical composition. Technically, spinel nanoferrites are known to display tunable magnetic and conductive properties when the cation composition and preparative conditions are decently monitored.³³ Meanwhile, it has been well established that MgFe_2O_4 is very responsive to thermal treatment owing to high Mg^{2+} diffusibility in contrast to NiFe_2O_4 which does not display temperature dependent cation arrangement because of strong preference of Ni^{2+} in the octahedral voids. However, a solid solution between the two spinels is predicted to display changes in cation distribution, and hence properties depending on the atomistic composition and reaction temperature.³³ Because of the strong preference of Ni^{2+} ions to occupy the octahedral site, there exists a competition between Mg^{2+} and Fe^{3+} ions to populate the tetrahedral sites. Also, the magnetic Ni^{2+} ions in the spinel system are being replaced by the non-magnetic Mg^{2+} ions. It is therefore expected that substitution of Ni^{2+} by Mg^{2+} causes distortion of the lattice and variation in the unit cell,³⁴ leading to the formation of more electrochemical active sites on the surface of the material and realization of higher electrical conductivity. Furthermore, benefiting from the synergistic effect between Ni^{2+} and Mg^{2+} , the mixed nanoferrite of $\text{Ni}_{1-x}\text{Mg}_x\text{Fe}_2\text{O}_4$ with rational chemical composition is anticipated to demonstrate excellent electrochemical performances. While numerous studies report the use of pristine NiFe_2O_4 and MgFe_2O_4 nanoparticles for energy applications, limited reports exist on the electrochemical activity of $\text{Ni}_{1-x}\text{Mg}_x\text{Fe}_2\text{O}_4$ nanoalloys towards HER and/OER and supercapacitance. Therefore, it would be interesting to gain insights into the physicochemical

and electrochemical behaviour of $\text{Ni}_{1-x}\text{Mg}_x\text{Fe}_2\text{O}_4$ ($0 \leq x \leq 1$) in light of the above considerations.

In this study, a convenient and economic solvent-free approach was employed to fabricate nanometric $\text{Ni}_{1-x}\text{Mg}_x\text{Fe}_2\text{O}_4$ ($0 \leq x \leq 1$) solid solutions via pyrolysis of metal acetylacetonates. Interestingly, the typical synthesis proceeds without the use of solvents or organic reagents and has delivered unprecedented control over the materials composition and property. This straightforward and green synthesis procedure has afforded the formation of monophasic nanoferrite solid solutions that crystallize in a cubic spinel structure.

4.2 Experimental

4.2.1 Chemicals

Nickel (II) acetylacetonate (98%, Merck-Schuchardt), magnesium (II) acetylacetonate (98%, Merck-Schuchardt), and iron (III) acetylacetonate (97%, Sigma-Aldrich). These metal complexes were used as received.

4.2.2 Synthesis of $\text{Ni}_{1-x}\text{Mg}_x\text{Fe}_2\text{O}_4$ ($0 \leq x \leq 1$) solid solutions

The $\text{Ni}_{1-x}\text{Mg}_x\text{Fe}_2\text{O}_4$ ($0 \leq x \leq 1$) solid solutions of different stoichiometric compositions were prepared by solventless thermolysis of metal acetylacetonates. For the typical synthesis of ternary NiFe_2O_4 nanoparticles, 0.10 g (0.39 mmol) of nickel acetylacetonate and 0.27 g (0.78 mmol) of iron acetylacetonate were mixed and the solid mixture was grounded using pestle and mortar for ≈ 20 minutes to obtain a homogeneous mixture. The precursor mixture was then placed into a ceramic boat, which was placed in a reactor tube. The reactor tube was then introduced inside the carbolite tube furnace in such a way that the ceramic boat must be placed almost in the middle of the heating zone, followed by thermal treatment at 450 °C, at a heating rate of 20 °C per minute for 1 h. After 1 h of annealing, the heating was switched off, and the furnace was left to cool naturally to ambient temperature. The reactor tube was taken out of the furnace upon cooling, and the product was collected for analysis without any post-treatment. Likewise, the synthesis of MgFe_2O_4 nanoparticles was achieved by employing similar procedures except that magnesium acetylacetonate was used instead of nickel acetylacetonate and the amount of cobalt and iron complexes were maintained in the same mole ratio of 1:2.

For the synthesis of quaternary $\text{Ni}_{1-x}\text{Mg}_x\text{Fe}_2\text{O}_4$ ($x = 0.2, 0.4, 0.6, 0.8$) solid solutions, a known quantity of nickel acetylacetonate was partially substituted by appropriate amounts of magnesium acetylacetonate by adjusting the mole ratios of Mg and Ni in the intervals of 0.2,

0.4, 0.6, and 0.8, while keeping the amount of iron acetylacetonate unchanged in the reaction mixture. The reaction procedures for the entire series of solid solutions were kept similar to those employed to synthesize the ternary nickel and magnesium ferrites.

4.3 Characterization techniques

4.3.1 Powder X-ray diffraction (p-XRD) analysis

Structural analysis of the $\text{Ni}_{1-x}\text{Mg}_x\text{Fe}_2\text{O}_4$ nanoparticles was ascertained by powder X-ray diffraction (p-XRD) analysis employing a Bruker AXS D8 Advance X-ray diffractometer. The instrument uses nickel-filtered $\text{Cu K}\alpha$ radiation ($\lambda=1.5418\text{\AA}$) at 40 kV, 40 mA. The measurements were recorded at 2θ values ranging from 10 to 80° .

4.3.2 Scanning electron microscopy (SEM) and Energy dispersive X-ray (EDX) analyses

SEM imaging was carried out on a ZEISS-Auriga Cobra SEM Field Emission Scanning Electron Microscope (FE SEM) while EDX elemental analysis was performed on a JEOL JSM-7500F Field Emission Scanning Electron Microscope (FE-SEM) Equipped with Energy Dispersive X-ray spectroscopy (EDX).

4.3.3 Transmission electron microscopy (TEM), High resolution TEM (HRTEM) and Selected area electron diffraction (SAED) analyses

The SAED, TEM and HRTEM analyses were performed on a JEOL 2100 HRTEM at accelerating voltages of 200 kV.

4.3.4 UV-visible spectroscopy

The optical absorbance measurements were conducted in the UV-Vis spectral range on a Varian Cary 50 UV/Vis spectrophotometer.

4.4 Electrochemical characterization

Electrochemical property of the $\text{Ni}_{1-x}\text{Mg}_x\text{Fe}_2\text{O}_4$ ($0 \leq x \leq 1$) materials was studied in a three-electrode system using a Versastat 4-500 electrochemical workstation (Princeton Applied Research, Oak Ridge, TN, USA). For the preparation of the working electrode, the electrode paste was synthesized using $\text{Ni}_{1-x}\text{Mg}_x\text{Fe}_2\text{O}_4$ material (80 %), PVDF (10 %), carbon black (10 %) with N-methyl pyrrolidinone (NMP) solvent as active materials, binder, and conducting agent, respectively. The paste was dipped into the clean Ni foam, and it was dried for 48 hr. Pt wire was used as counter electrode, as well as SCE, Hg/HgO reference electrode

was utilized for electrocatalytic and supercapacitive studies, respectively. To examine the performance of electrocatalyst for overall water splitting, linear sweep voltammetry (LSV) was carried out at a scan rate of 2 mV/s. Also, electrochemical impedance spectroscopy (EIS) was performed at the potential of 0.6 V (V, SCE) in the frequency range of 0.05 Hz to 10 kHz at an applied AC amplitude of 10 mV. For the stability of electrocatalysts, chronoamperometry techniques were utilized at the potential of 0.57 V (V, SCE). All measurements for electrocatalysts were conducted using 1 M KOH electrolyte. In the case of supercapacitive behavior, cyclic voltammetry (CV) and galvanostatic charge–discharge (GCD) measurement were performed at various scan rates and current densities using 3 M KOH electrolyte.

4.5 Results and discussion

4.5.1 Structural analysis of $\text{Ni}_{1-x}\text{Co}_x\text{Fe}_2\text{O}_4$ ($0 \leq x \leq 1$) solid solutions

Structural characterization of the prepared $\text{Ni}_{1-x}\text{Mg}_x\text{Fe}_2\text{O}_4$ ($0 \leq x \leq 1$) nanoferrites was performed by powder X-ray diffraction and the typical p-XRD pattern of all samples are displayed in Fig. 4.1(a). The diffraction peaks found in the pure ternary systems prepared at $x = 0$ and $x = 1$ are exclusively indexed with the spinel crystal system having the space group $Fd\bar{3}m$. These two pristine ferrites are consistent with the cubic phases of pure trevorite, NiFe_2O_4 (ICDD #. 01-086-2267) and magnesioferrite, MgFe_2O_4 (ICDD #. 01-089-3084) for $x = 0$ and $x = 1$, respectively. The p-XRD data for the nanoferrites with $x = 0.2$ to $x = 0.8$ indicate the formation of solid solution phases regardless of the composition of the Ni^{2+} and Mg^{2+} in the spinel matrix. Notably, their diffraction peaks lie between those of the two pristine ternary ferrite systems, and these solid solution nanoparticles maintain the same crystallinity of cubic system throughout the composition regulation.

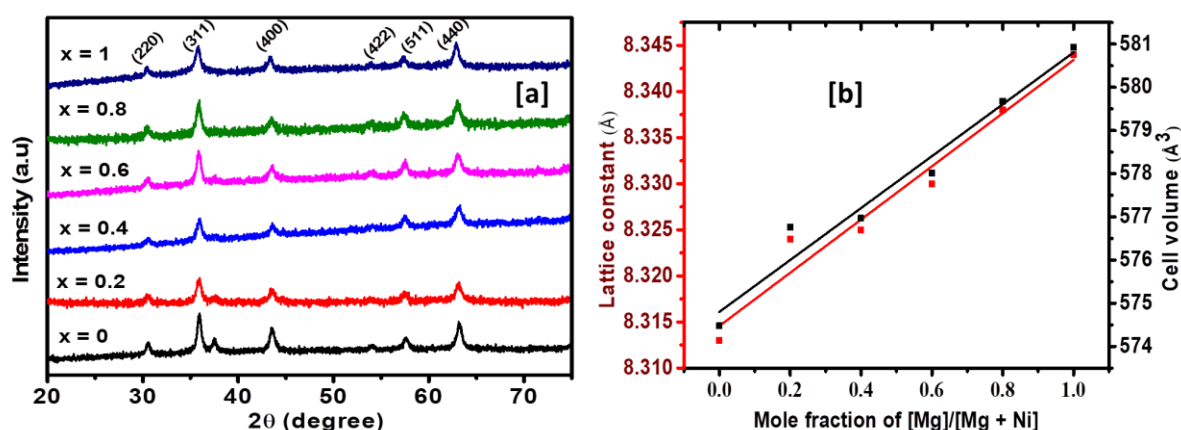


Fig. 4.1. (a) Powder-XRD patterns (b) Variation of lattice constant (left y-axis) and cell volume (right y-axis) with Mg^{2+} content for $\text{Ni}_{1-x}\text{Mg}_x\text{Fe}_2\text{O}_4$ ($0 \leq x \leq 1$) solid solutions.

The lattice constants ($a = b = c$) of all $\text{Ni}_{1-x}\text{Mg}_x\text{Fe}_2\text{O}_4$ ($0 \leq x \leq 1$) nanospinels were obtained from the XRD data by employing the formula $1/d^2 = (h^2 + k^2 + l^2)/a^2$ and the results are shown in Table 4.1. The lattice constants of NiFe_2O_4 were found to be 8.313 Å, conforming to those reported in the standard data (8.337 Å, ICDD #: 01-086-2267). After incorporation of magnesium, a slight increase in the values of the lattice parameters is observed, which is also ascribed to the slightly larger size of Mg^{2+} (0.72 Å) relative to the replaced Ni^{2+} (0.69 Å).³⁵ The lattice parameters computed for pure MgFe_2O_4 (8.344 Å) are also comparable with the values reported in standard data (8.369 Å, ICDD #: 01-089-3084). The values of lattice parameters were then plotted as a function of Mg^{2+} content (x) as shown in Fig. 4.1(b). It is obvious that the lattice constant increases in a linear fashion with Mg^{2+} inclusion from 8.313 Å for NiFe_2O_4 to 8.344 Å for MgFe_2O_4 . This linear relationship between the lattice parameters and Mg^{2+} content is in agreement with Vegard's law.³⁶ The values of the lattice constants obtained in this study are consistent with previously reported values for magnesium substituted nickel ferrite nanoparticles prepared via a co-precipitation route.³⁷ Likewise, the data in Table 4.1 and Fig.4.1(b) demonstrate that the cell volume increases monotonically with increasing magnesium content. All these findings confirm successful inclusion of Mg^{2+} into the crystal structure of NiFe_2O_4 . The Debye-Scherrer formula,³⁸ $L = 0.89\lambda/\beta\cos\theta$ was employed to compute the average crystallite size of $\text{Ni}_{1-x}\text{Mg}_x\text{Fe}_2\text{O}_4$ samples and the values obtained are provided in Table 4.1. In the formula, L = average crystallite size, λ = X-ray wavelength, β = full width at half maximum, and θ = Bragg's angle of the (311) plane. The average crystallite sizes of $\text{Ni}_{1-x}\text{Mg}_x\text{Fe}_2\text{O}_4$ nanoparticles vary between 19.42 and 10.50 nm. The average crystallite size obtained for the parent nickel ferrite was larger compared to those exhibited by magnesium substituted samples.

Table 4.1. Lattice parameter (a), crystallite size (d), unit cell volume (V), and EDX composition of nanospinel $\text{Ni}_{1-x}\text{Mg}_x\text{Fe}_2\text{O}_4$ solid solutions at various magnesium contents (x).

(x)	Target ferrite composition	Stoichiometry obtained from EDX	a (Å)	d (nm)	V (Å ³)
0	NiFe ₂ O ₄	Ni _{1.01} Fe _{1.81} O _{4.17}	8.313	19.42	574.478

0.2	Ni _{0.8} Mg _{0.2} Fe ₂ O ₄	Ni _{0.74} Mg _{0.23} Fe _{1.97} O _{4.07}	8.324	17.07	576.761
0.4	Ni _{0.6} Mg _{0.4} Fe ₂ O ₄	Ni _{0.43} Mg _{0.40} Fe _{2.03} O _{4.14}	8.325	10.50	576.969
0.6	Ni _{0.4} Mg _{0.6} Fe ₂ O ₄	Ni _{0.41} Mg _{0.58} Fe _{1.90} O _{4.11}	8.330	13.30	578.010
0.8	Ni _{0.2} Mg _{0.8} Fe ₂ O ₄	Ni _{0.13} Mg _{0.75} Fe _{1.88} O _{4.25}	8.338	14.43	579.676
1	MgFe ₂ O ₄	Mg _{0.99} Fe _{1.83} O _{4.18}	8.344	11.78	580.929

4.5.2 Elemental composition

The formation of a solid solution phase of the alloyed nanospinels was further checked by examining the composition and elemental distributions of Co, Mg, Fe, and O using energy-dispersive X-ray analysis (Fig. 4.2). The EDX results indicate the presence of Ni, Fe and O for $x = 0$, and Mg, Fe and O for $x = 1$. For the solid solution nanocrystals with compositions $x = 0.2$ to 0.8 , the presence of Ni, Mg, Fe, and O was confirmed. A summary of the atomistic composition of each of the components in the alloyed nanoferrites is provided in Tables 4.1 and 4.2. The stoichiometry of the elements obtained are consistent with that of expected values within the substitution limits, suggesting that there is no side reaction or significant loss of the starting materials. In Fig. 4.3, the relationship between the amount of Ni²⁺ and Mg²⁺ detected from EDX with respect to the mole fraction of [Mg]/[Mg+Ni] in precursor feed indicates a decrease of nickel content with a linear increase in magnesium content. In addition, the EDX mapping of the as-prepared Ni_{1-x}Mg_xFe₂O₄ ($0 \leq x \leq 1$) nanoparticles given in Figs. 4.4 and 4.5, indicate that the distribution of the respective elements in the structure are nearly uniform, ruling out the possibility of dealloying or phase separation. This also confirms the formation of the solid solution of the two components i.e. NiFe₂O₄ and MgFe₂O₄ in the single-crystalline alloyed nanospinel.

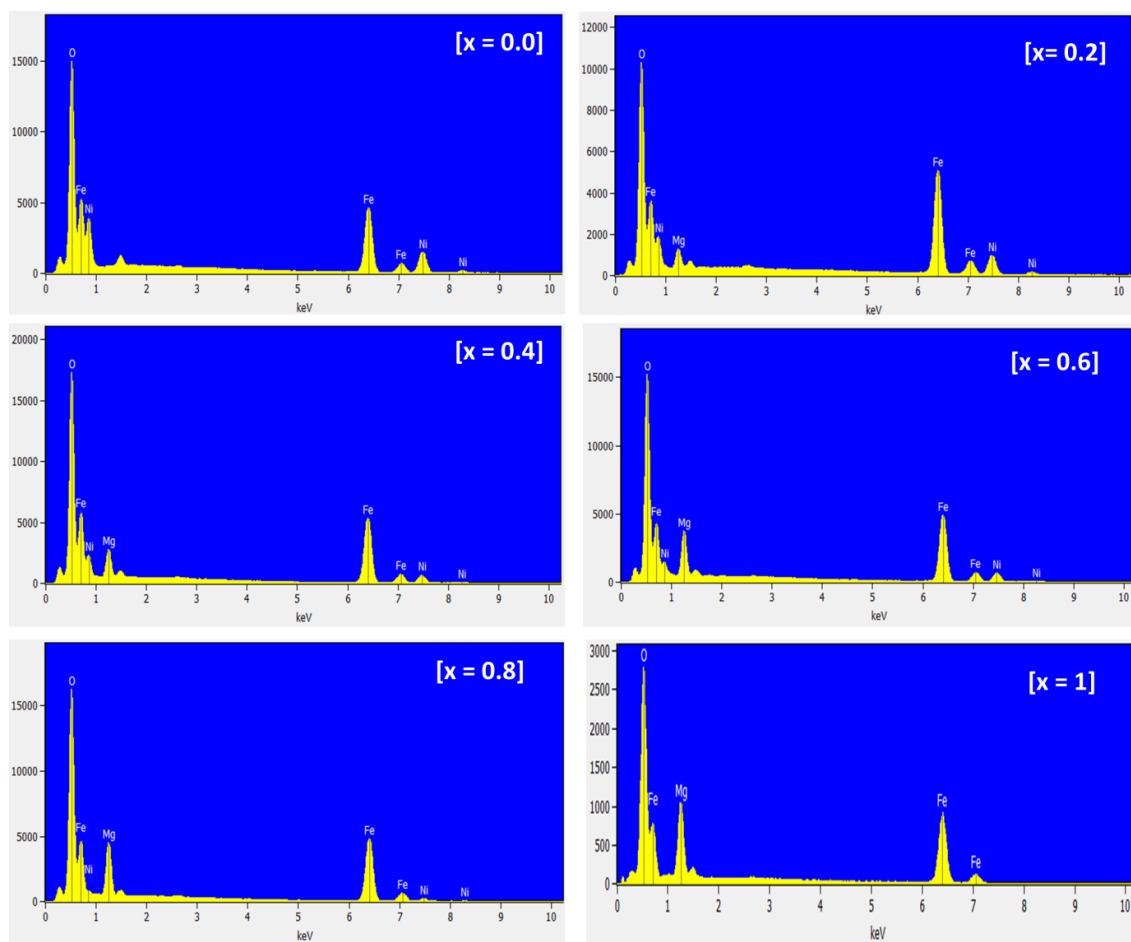


Fig. 4.2. EDX pattern of $\text{Ni}_{1-x}\text{Mg}_x\text{Fe}_2\text{O}_4$ ($0 \leq x \leq 1$) solid solution nanoparticles.

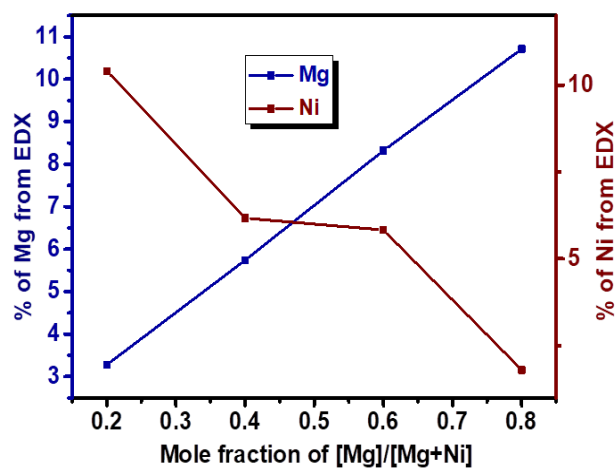


Fig. 4.3. Change in the amount of Mg and Ni as a function of mole fraction of $[\text{Mg}]/[\text{Mg}+\text{Ni}]$ in precursor feed.

Table 4.2. Summary of the theoretical and experimental atomic % for $\text{Ni}_{1-x}\text{Mg}_x\text{Fe}_2\text{O}_4$ solid solutions obtained from EDX analysis.

(x)	Theoretical atomic %					Atomic % from EDX				
	Ni	Mg	Fe	O	Total	Ni	Mg	Fe	O	Total
0	14.29	-	28.57	57.14	100	14.55	-	25.89	59.56	100
0.2	11.43	2.86	28.57	57.14	100	10.40	3.28	28.17	58.15	100
0.4	8.57	5.71	28.57	57.14	100	6.17	5.74	29	59.10	100
0.6	5.71	8.57	28.57	57.14	100	5.83	8.32	27.15	58.70	100
0.8	2.86	11.43	28.57	57.14	100	1.80	10.71	26.84	60.66	100
1	-	14.29	28.57	57.14	100	-	14.09	26.14	59.77	100

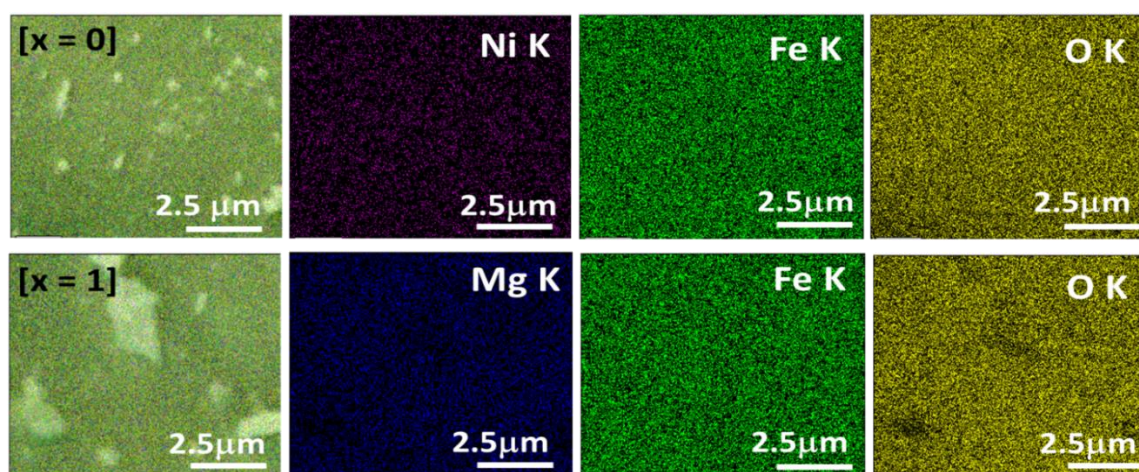


Fig. 4.4. EDX elemental mapping of $\text{Ni}_{1-x}\text{Mg}_x\text{Fe}_2\text{O}_4$ ($x = 0$ and 1) nanoparticles.

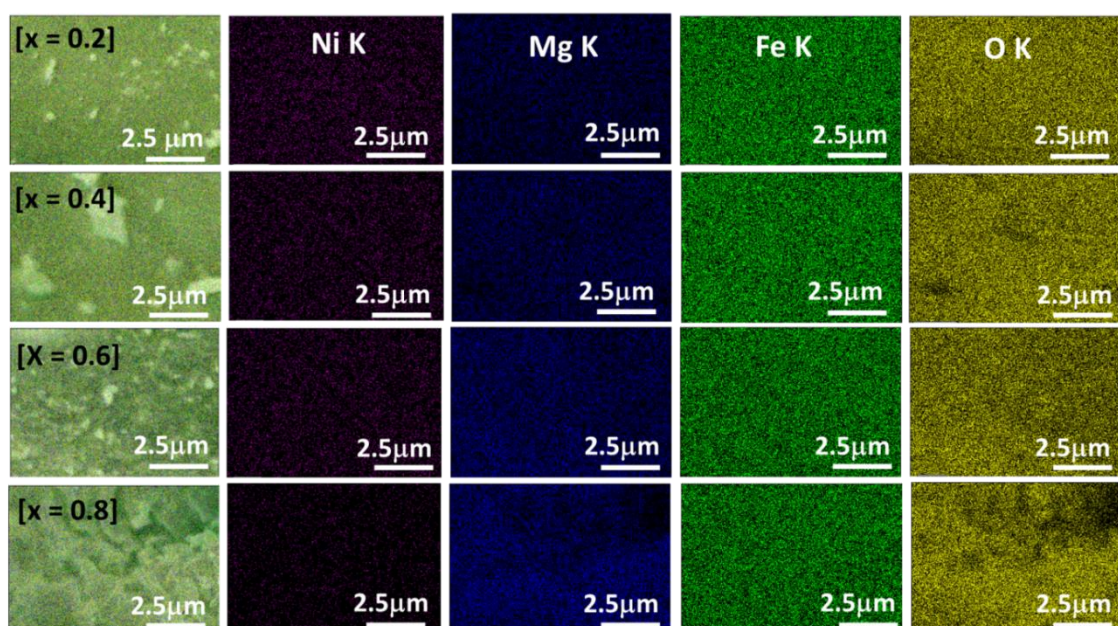


Fig. 4.5. EDX elemental mapping of $\text{Ni}_{1-x}\text{Mg}_x\text{Fe}_2\text{O}_4$ ($0.2 \leq x \leq 0.8$) nanoparticles.

4.5.3 Microstructure and morphological studies

The morphology of nanoparticulate $\text{Ni}_{1-x}\text{Mg}_x\text{Fe}_2\text{O}_4$ ($0 \leq x \leq 1$) solid solutions was examined by using SEM and TEM analyses. Fig. 4.6 shows SEM micrographs of $\text{Ni}_{1-x}\text{Mg}_x\text{Fe}_2\text{O}_4$ nanostructures with different compositions varying from $x = 0$ to $x = 1$. It can be seen that for all compositions, the images show agglomerated nanoparticles, making it difficult to ascertain the exact shape and size of the particles. To have clear information about the particle morphology, size and microstructure of $\text{Ni}_{1-x}\text{Mg}_x\text{Fe}_2\text{O}_4$ samples, both TEM and HRTEM analyses were carried out. The TEM images displayed in Fig. 4.7 shows a mixture of cubic, rectangular cubic and pseudooctahedral shaped $\text{Ni}_{1-x}\text{Mg}_x\text{Fe}_2\text{O}_4$ ($0 \leq x \leq 1$) solid solutions. Some of these nanoparticles have truncated edges. The nanoparticles are of different sizes in the range of 12.79 – 31.62 nm. Additionally, from HRTEM images in Fig. 4.8, the lattice fringes with several interplaner spacing of $d = 4.81, 2.94, 2.51, 2.40$, and 2.08 \AA were observed, corresponding to the (111), (220), (311), (222), and (400) planes of cubic spinel $\text{Ni}_{1-x}\text{Mg}_x\text{Fe}_2\text{O}_4$ nanoparticles. These results are consistent with the characteristic d-spacing and miller indices observed from XRD data. Moreover, information regarding the crystalline nature of the nanoparticles was evaluated by using SAED analysis. The SAED patterns displayed in Fig. 4.9 reveal several circular rings, which indicates the polycrystalline nature of $\text{Ni}_{1-x}\text{Mg}_x\text{Fe}_2\text{O}_4$ samples. Evidently, the SAED patterns are composed of several diffraction rings showing the presence of (111) and (311) crystallographic planes, based on their d-spacings, the positions of which match well with standard spinel $\text{Ni}_{1-x}\text{Mg}_x\text{Fe}_2\text{O}_4$ ($0 \leq x \leq 1$) nanoparticles. The absence of any additional diffraction spots and rings of secondary phases corresponding to the magnesium, nickel and iron oxides, confirms the solventless fabrication of phase-pure ferrite nanospinels, and the SAED results agree well with XRD and EDX analyses.

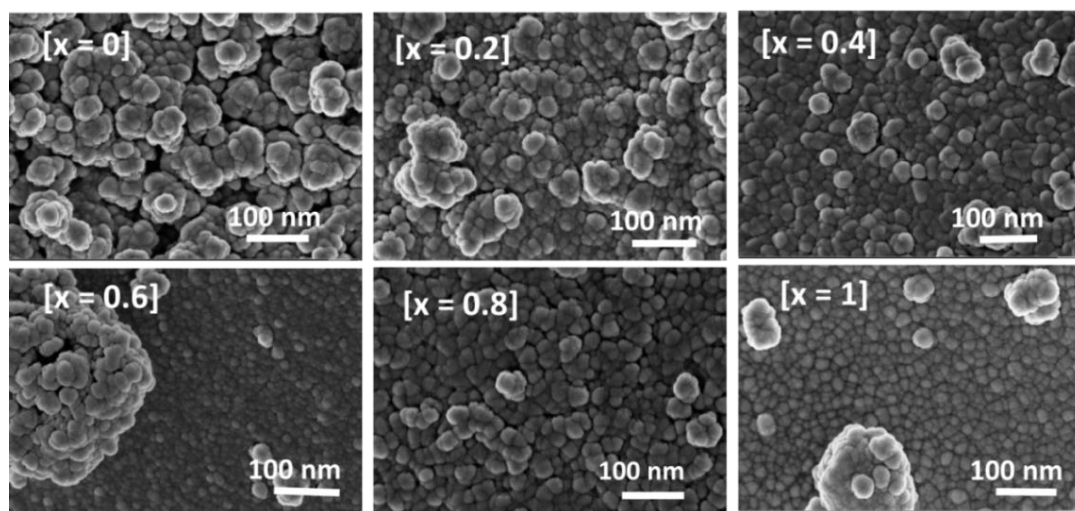


Fig. 4.6. SEM images of $\text{Ni}_{1-x}\text{Mg}_x\text{Fe}_2\text{O}_4$ ($0 \leq x \leq 1$) samples prepared by solid state pyrolysis of metal acetylacetonates precursors with different mole fractions of magnesium.

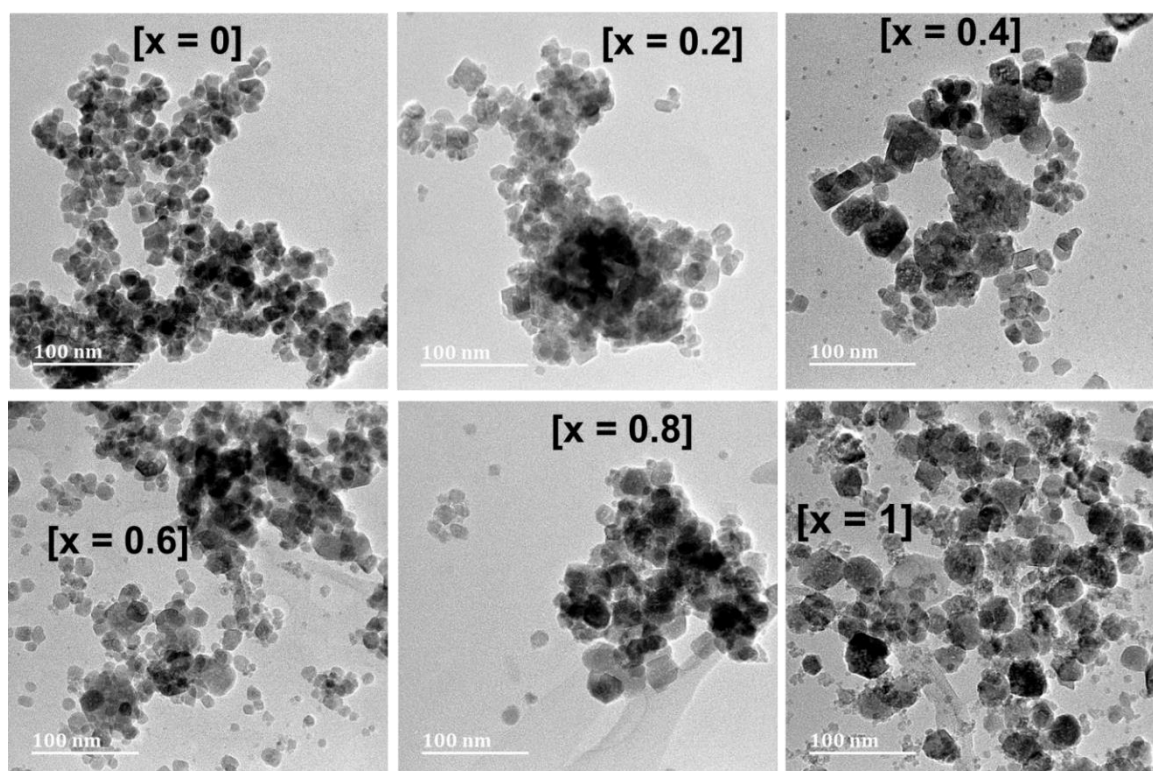


Fig. 4.7. TEM images of $\text{Ni}_{1-x}\text{Mg}_x\text{Fe}_2\text{O}_4$ ($0 \leq x \leq 1$) nanoparticles.

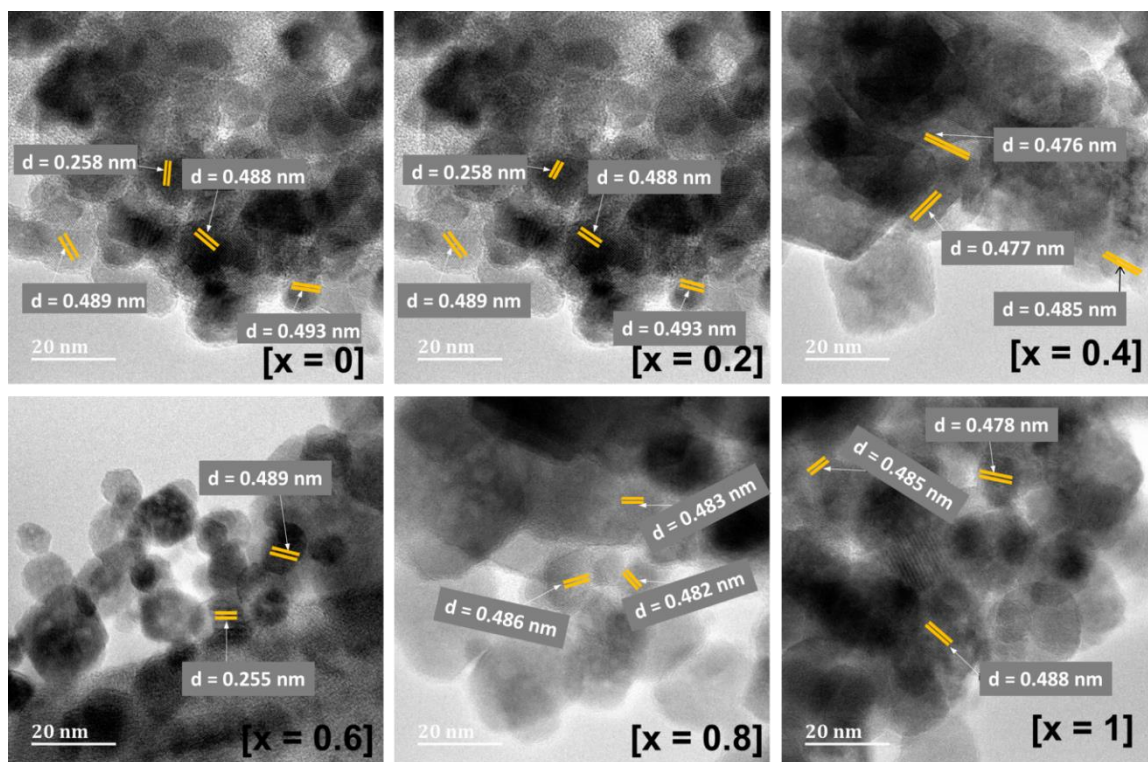


Fig. 4.8. HRTEM images of $\text{Ni}_{1-x}\text{Mg}_x\text{Fe}_2\text{O}_4$ ($0 \leq x \leq 1$) nanoparticles.

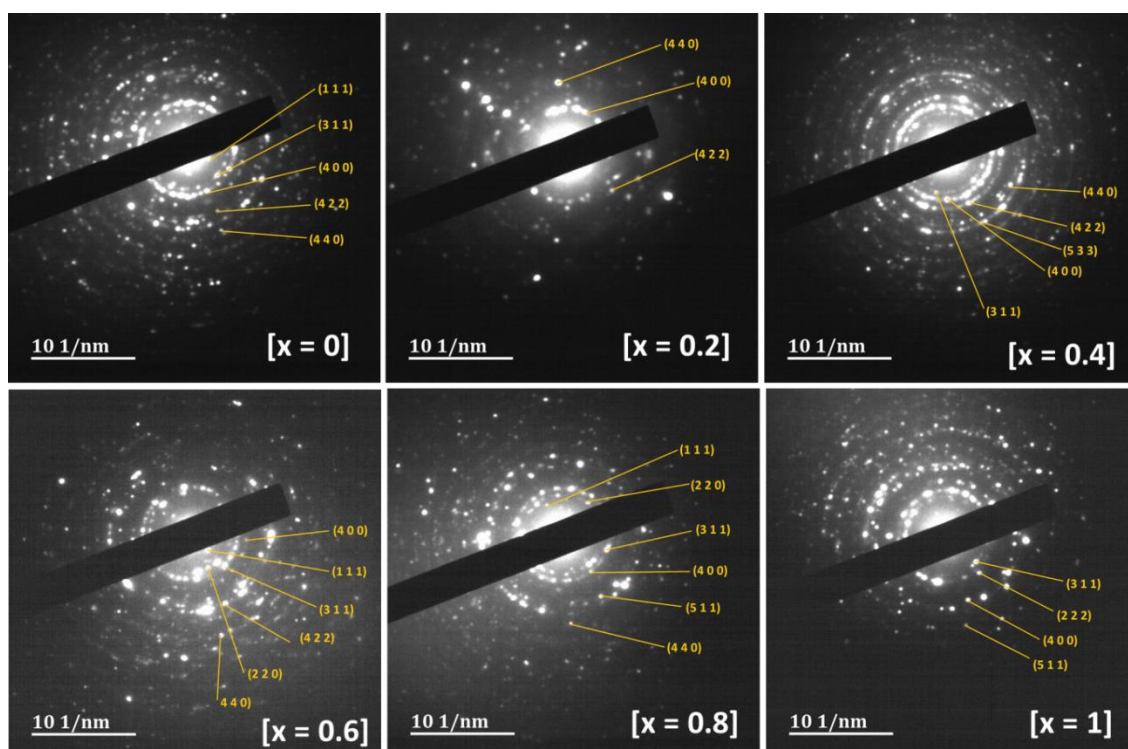


Fig. 4.9. SAED images of $\text{Ni}_{1-x}\text{Mg}_x\text{Fe}_2\text{O}_4$ ($0 \leq x \leq 1$) nanoparticles

4.5.4 UV-Vis analysis

The optical properties of the synthesized $\text{Ni}_{1-x}\text{Mg}_x\text{Fe}_2\text{O}_4$ ($0 \leq x \leq 1$) solid solutions were investigated by analysing the measured UV-Visible absorbance at room temperature for all compositions. The absorption spectra in Fig. 4.10 clearly indicate the absorption of the $\text{Ni}_{1-x}\text{Mg}_x\text{Fe}_2\text{O}_4$ nanoparticles in the visible range. The spectra demonstrate that the largest nanoparticles ($x = 0$) absorb in longer wavelength while the smallest nanoparticles ($x = 0.4$) absorb at shorter wavelength. The values of the optical band gap was computed according to the prominent Tauc's equation,³⁹ represented in the form of $\alpha h\nu = \beta(h\nu - E_g^{opt})^m$. In this equation, α = absorption coefficient, ν = frequency of the incident light, h = planks constant, β = edge width parameter and E_g^{opt} = optical band gap. The graph of $(\alpha h\nu)^{1/m}$ versus the photon energy, $h\nu$ for different m values revealed that the synthesized $\text{Ni}_{1-x}\text{Mg}_x\text{Fe}_2\text{O}_4$ nanospinels are direct band gap materials exhibiting the allowed transition $m = 1/2$ which is consistent with previous results reported for spinel ferrites.⁴⁰⁻⁴² The typical Tauc plots of $(\alpha h\nu)^2$ versus the photon energy ($h\nu$) for $\text{Ni}_{1-x}\text{Mg}_x\text{Fe}_2\text{O}_4$ solid solutions with Mg^{2+} concentration in the whole composition range of x are shown in Fig. 4.11. The optical band gap (E_g^{opt}) was obtained by extrapolating the mostly divergent linear part of the Tauc plot into the energy axis (x -axis) to $(\alpha h\nu)^2 = 0$, and the values are presented in Table 4.3. It was noted that the optical band gap increases from 1.609 to 1.922 eV upon incorporation of Mg^{2+} ions from $x = 0$ to 0.4 in spinel NiFe_2O_4 nanoparticles. This increase in band gap is compatible with the decrease of crystallite size from 19.42-10.50 nm in the same composition range of $x = 0$ to $x = 0.4$. The observed shift in band gap values of the spinel $\text{Ni}_{1-x}\text{Mg}_x\text{Fe}_2\text{O}_4$ with decreasing crystallite size is the result of quantum confinement effects emanating from the small size of the nanoparticles.⁴³ Moving from $x = 0.6$ to 0.8, the decrease in band gap from 1.870 to 1.856 was noted and is ascribed to the increase in crystallite size from 13.30 to 14.43 nm. With reference to the optical band gap of bulk NiFe_2O_4 which is 2.0 eV, a red shift is obvious for all composition, which could be due to the increase of internal lattice strain.⁴⁴ Generally, the observed change in the magnitude of the optical band gap with respect to Mg^{2+} content is a reflection of structural changes that occur due to changes in composition and cation distribution in the crystal lattice.^{45, 46}

Table 4.3. The optical band gaps for $\text{Ni}_{1-x}\text{Mg}_x\text{Fe}_2\text{O}_4$ ($0 \leq x \leq 1$) nanoparticles.

Zinc content (x)	0	0.2	0.4	0.6	0.8	1
E (eV)	1.609	1.916	1.922	1.870	1.856	1.803

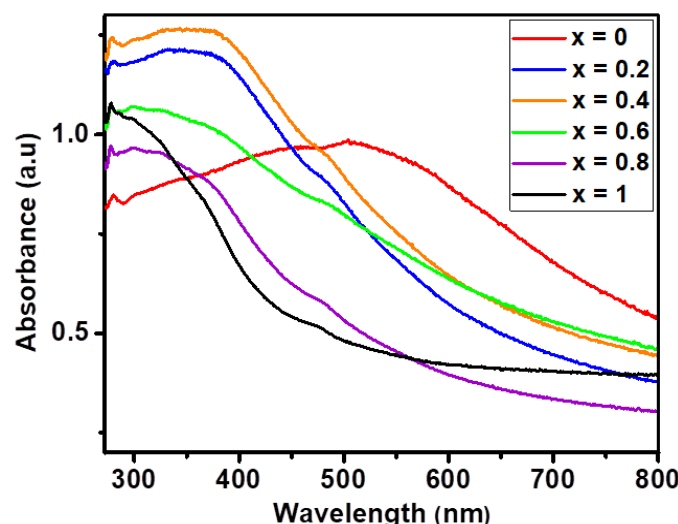


Fig. 4.10. UV-Vis absorption spectra of $\text{Ni}_{1-x}\text{Mg}_x\text{Fe}_2\text{O}_4$ ($0 \leq x \leq 1$) solid solutions.

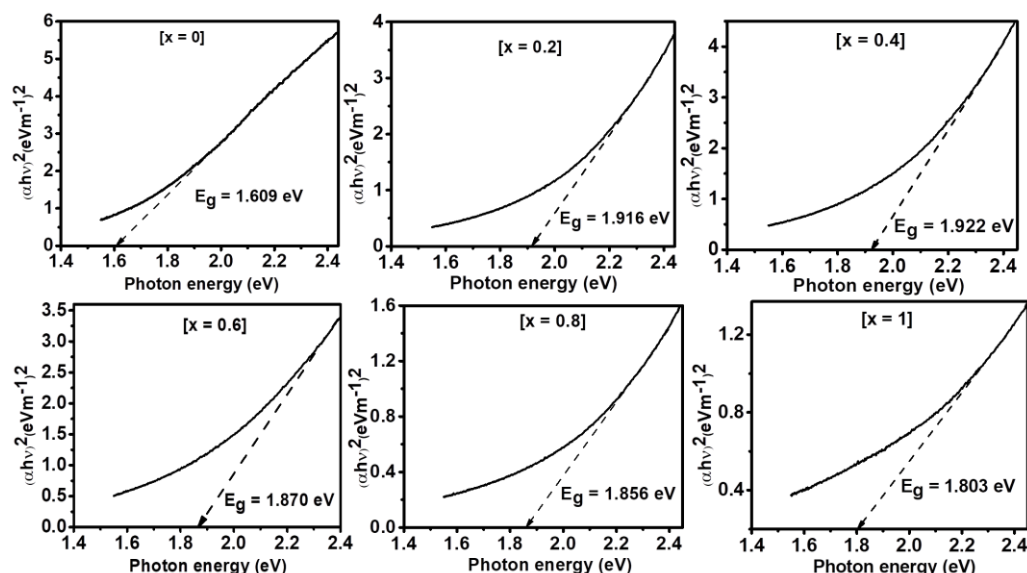


Fig. 4.11. Tauc plots of $(\alpha h\nu)^2$ versus energy for $\text{Ni}_{1-x}\text{Mg}_x\text{Fe}_2\text{O}_4$ ($0 \leq x \leq 1$) solid solutions.

4.5.5 Electrocatalytic water splitting studies of $\text{Ni}_{1-x}\text{Mg}_x\text{Fe}_2\text{O}_4$ solid solutions

The HER activities of $\text{Ni}_{1-x}\text{Mg}_x\text{Fe}_2\text{O}_4$ ($0 \leq x \leq 1$) catalysts were investigated under alkaline conditions (1 M KOH) in a usual three-electrode arrangement. Fig. 4.12(a) displays the LSV polarization curves of $\text{Ni}_{1-x}\text{Mg}_x\text{Fe}_2\text{O}_4$ with varying mole ratios of Ni and Mg at a scan rate of 5 mV/s. Pure NiFe_2O_4 displays low catalytic performance with an overpotential of 159 mV which was needed to produce a current density of 10 mA/cm^2 . Upon Mg incorporation, the electrocatalytic activity was enormously improved as manifested by the reduction of overpotential from 159 mV of bare NiFe_2O_4 to $\text{Ni}_{0.8}\text{Mg}_{0.2}\text{Fe}_2\text{O}_4$ (135 mV), $\text{Ni}_{0.6}\text{Mg}_{0.4}\text{Fe}_2\text{O}_4$ (130 mV), $\text{Ni}_{0.4}\text{Mg}_{0.6}\text{Fe}_2\text{O}_4$ (121 mV), $\text{Ni}_{0.2}\text{Mg}_{0.8}\text{Fe}_2\text{O}_4$ (134 mV), and

MgFe₂O₄ (153 mV). Remarkably, at the current density of 10 mA/cm², the Ni_{1-x}Mg_xFe₂O₄ (x = 0.6) electrode exhibited the best electrocatalytic activity for HER with an overpotential of 121 mV which is smaller compared to its counterparts. This reduction in overpotentials demonstrate that incorporation of proper content of Mg in the crystal lattice of NiFe₂O₄ can effectively improve its catalytic activity for HER. These results further demonstrated that the value of overpotential of Ni_{0.4}Mg_{0.6}Fe₂O₄ at the geometric current density of 10 mA/cm² is superior to many binary and ternary metal oxide catalysts such as NiFe₂O₄ (290 mV),⁴⁷ Ni/Co₃O₄ (145 mV),⁴⁸ Fe₂O₃/NCs (350 mV),⁴⁹ δ-MnO₂ (196 mV),⁵⁰ and MgFe₂O₄ (402 mV).²⁷ It is noteworthy that the Ni_{0.4}Mg_{0.6}Fe₂O₄ also shows great superiority to other previously reported HER electrocatalysts summarized in Table 4.4. In Fig. 4.12(b), the Tafel slopes of all electrodes were measured from the LSV measurements. Remarkably, the Tafel slope of Ni_{0.4}Mg_{0.6}Fe₂O₄ was found to be 125 mV/dec, which is lower than that of NiFe₂O₄ (136 mV/dec), Ni_{0.8}Mg_{0.2}Fe₂O₄ (146 mV/dec), Ni_{0.6}Mg_{0.4}Fe₂O₄ (130 mV/dec), Ni_{0.8}Mg_{0.2}Fe₂O₄ (184 mV/dec), and MgFe₂O₄ (143 mV/dec). The reduction of Tafel slope from 136 mV/dec (NiFe₂O₄) to 125 mV/dec (Ni_{0.4}Mg_{0.6}Fe₂O₄) may be ascribed to probable modification effect of the surface electronic state due to incorporation of Mg element, which in turn enhances the inherent conductivity of Ni_{0.4}Mg_{0.6}Fe₂O₄.⁵¹ These changes indicate that among other factors, the electrochemical kinetics depend on the ratio of Mg dopants. Generally, the lower Tafel slope of the electrode indicates better process kinetics, even when significant H₂ generation is needed at elevated voltage or current densities.

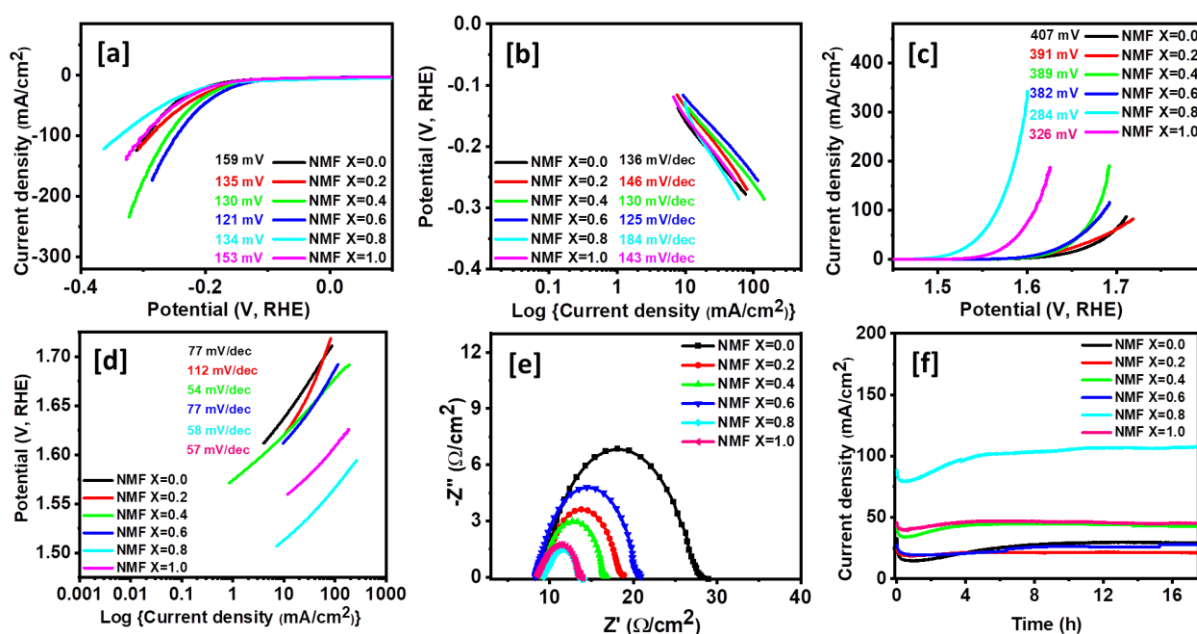


Fig. 4.12. (a) HER polarization curves, (b) HER Tafel slopes, (c) OER polarization curves, (d) OER Tafel slopes, (e) Nyquist plots at 0.5 V, and (f) CA measurement at 0.55 V, for $\text{Ni}_{1-x}\text{Mg}_x\text{Fe}_2\text{O}_4$ ($0 \leq x \leq 1$) electrodes.

The OER activities of a series of $\text{Ni}_{1-x}\text{Mg}_x\text{Fe}_2\text{O}_4$ ($0 \leq x \leq 1$) catalysts in 1 M KOH solution were also investigated. The polarization curves of $\text{Ni}_{1-x}\text{Mg}_x\text{Fe}_2\text{O}_4$ catalysts with different mole ratios of Ni to Mg show significant decrease in the overpotential upon Mg incorporation in NiFe_2O_4 (Fig. 4.12(c)). While the pristine NiFe_2O_4 needed an overpotential of 407 mV to deliver a current density of 10 mA/cm^2 , the solid solutions exhibited lower overpotentials of 391, 389, 382, and 284 mV for $x = 0.2, 0.4, 0.6$ and 0.8 , respectively. Also the pristine MgFe_2O_4 displayed a lower overpotential of 326 mV compared to NiFe_2O_4 . Among the studied series of $\text{Ni}_{1-x}\text{Mg}_x\text{Fe}_2\text{O}_4$ ($0 \leq x \leq 1$) catalysts, $\text{Ni}_{0.2}\text{Mg}_{0.8}\text{Fe}_2\text{O}_4$ demonstrated the best OER performance with lower overpotential of 284 mV, within the window of potential examined. The electrocatalytic activity demonstrated by $\text{Ni}_{0.2}\text{Mg}_{0.8}\text{Fe}_2\text{O}_4$ surpasses many other previously reported metal oxide-based catalysts. For example, MnFe_2O_4 was reportedly synthesized by Li *et al.* and showed an overpotential of 470 mV at a current density of 10 mA/cm^2 under alkaline media.⁵² In a similar study, CoFe_2O_4 exhibited 370 mV under similar electrolytic conditions. Hirai *et al.* reported that Mn_3O_4 needed an overpotential of 600 mV to produce a current density of 10 mA/cm^2 in 1 M KOH solution. They further reported the synthesis of $\text{Mn}_{2.4}\text{Co}_{0.6}\text{O}_4$ which exhibited a high overpotential of 510 mV.⁵³ Also, Co_3O_4 nanocubes fabricated by Chen *et al.* were reported to display an overpotential of 580 mV (at 10 mA/cm^2) in alkaline electrolyte.⁵⁴ Table 4.4 shows the comparison of the values of overpotentials $\text{Ni}_{0.2}\text{Mg}_{0.8}\text{Fe}_2\text{O}_4$ with other non-precious metal catalysts. The values of Tafel slope indicated in Fig.4.12(d) were obtained in the range of 54 - 112 mV/dec. The low overpotential and small Tafel slope make $\text{Ni}_{0.2}\text{Mg}_{0.8}\text{Fe}_2\text{O}_4$ a more promising OER catalyst.

The electrical conductivity of $\text{Ni}_{1-x}\text{Mg}_x\text{Fe}_2\text{O}_4$ ($0 \leq x \leq 1$) nanocatalysts was elucidated by the electrochemical impedance spectroscopy. The Nyquist plot displayed in Fig. 4.12(e) shows that the pristine NiFe_2O_4 nanoparticles possess the large semicircle, demonstrating poor electron transfer capability, compared to $\text{Ni}_{1-x}\text{Mg}_x\text{Fe}_2\text{O}_4$ ($0.2 \leq x \leq 0.8$) solid solutions. The lowest charge resistance values displayed by the solid solutions imply intimate contact between current collector and $\text{Ni}_{1-x}\text{Mg}_x\text{Fe}_2\text{O}_4$ and is an indication of more swift charge transfer kinetics. The results confirm further that the incorporation of Mg in spinel NiFe_2O_4 lattices contributed to the improvement of electrical conductivity via reduction of the charge transfer resistance, and consequently boosting the electrocatalytic properties of $\text{Ni}_{1-x}\text{Mg}_x\text{Fe}_2\text{O}_4$.

$x\text{Mg}_x\text{Fe}_2\text{O}_4$ electrodes. Of all electrode configurations investigated, $\text{Ni}_{0.2}\text{Mg}_{0.8}\text{Fe}_2\text{O}_4$ shows the smallest semicircle, indicating superior conductivity, and hence high electrocatalytic activity towards water splitting.

Evaluation of the catalyst's electrochemical stability is important for practical water splitting applications. To explore the electrochemical stability of $\text{Ni}_{1-x}\text{Mg}_x\text{Fe}_2\text{O}_4$ ($0 \leq x \leq 1$) electrocatalysts, chronoamperometry measurements were performed at 0.55 V. Remarkably, no significant changes in the current density were observed during 17 h tests, signifying an excellent electrochemical stability of all $\text{Ni}_{1-x}\text{Mg}_x\text{Fe}_2\text{O}_4$ systems in alkaline electrolyte (Fig. 4.12(f)). The stability of $\text{Ni}_{1-x}\text{Mg}_x\text{Fe}_2\text{O}_4$ ($0 \leq x \leq 1$) electrocatalysts was further examined by continuous LSV scans in 1 M KOH. The results indicate the absence of significant change in the polarization curve after 1000 cycles, signifying superior stability of the nanocatalysts for both OER and HER in alkaline solution (Figs. 4.13 and 4.14).

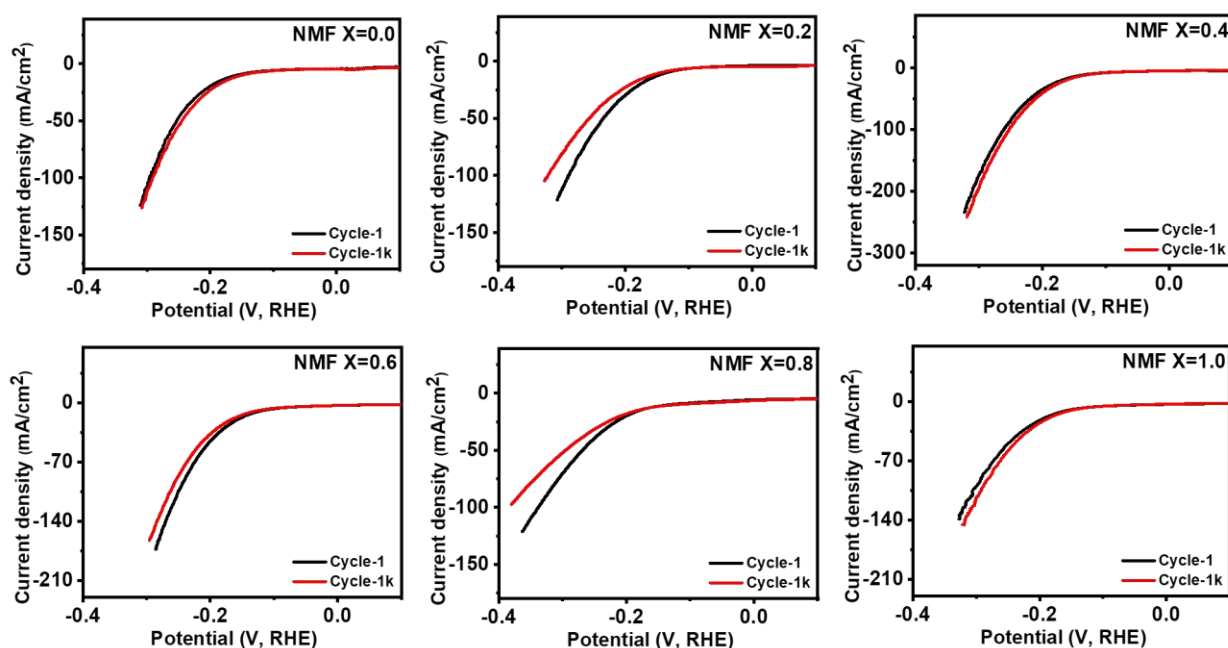


Fig. 4.13. Comparison of HER polarization curve between LSV 1 curve and LSV 1k curve for $\text{Ni}_{1-x}\text{Mg}_x\text{Fe}_2\text{O}_4$ ($0 \leq x \leq 1$) electrodes.

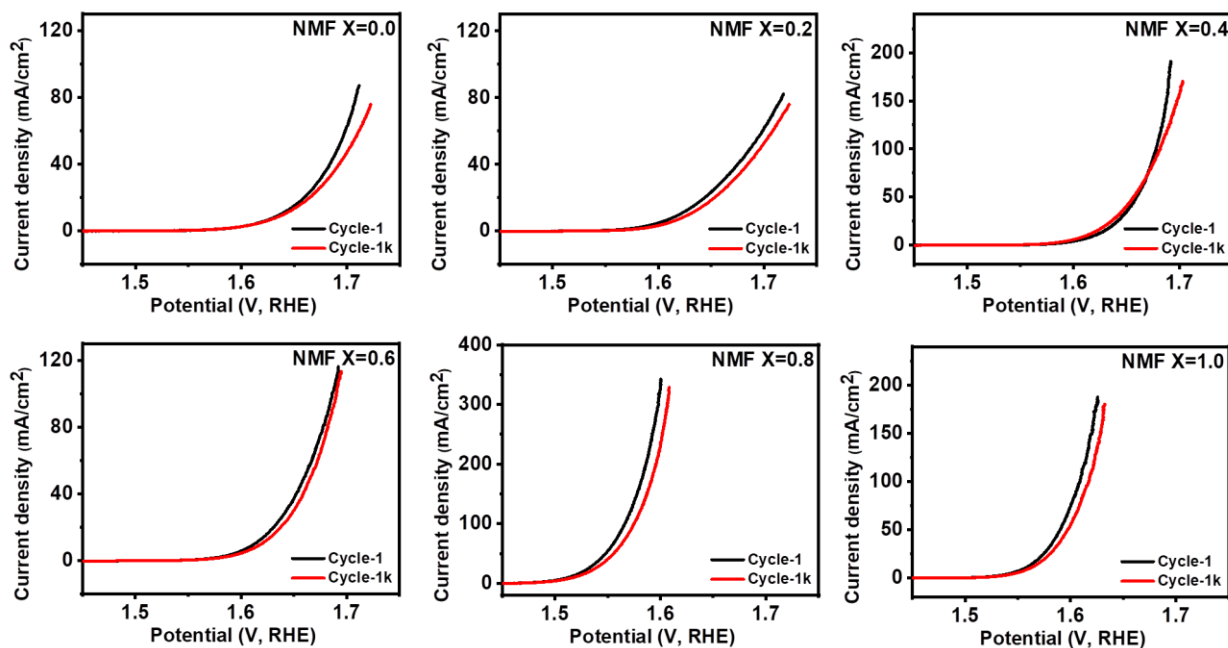


Fig. 4.14. Comparison of OER polarization curve between LSV 1 curve and LSV 1k curve for $\text{Ni}_{1-x}\text{Mg}_x\text{Fe}_2\text{O}_4$ ($0 \leq x \leq 1$) ($0 \leq x \leq 1$) electrodes.

Table 4.4. Comparison of HER performance of $\text{Ni}_{0.4}\text{Mg}_{0.6}\text{Fe}_2\text{O}_4$ with previously reported electrocatalysts in alkaline electrolyte.

Catalyst	Preparation method		η_{10} (mV) in 1 M KOH	Tafel slope (mV/dec)	Reference
MgFe_2O_4	Sol-gel		402	241	27
N-doped $\text{Ni}_3\text{S}_2/\text{VS}_2$	Hydrothermal		151	107.5	55
Ni-MoSe_2	Hydrothermal		206	81	56
$\text{CuO@Cu}_2\text{O}$	Solid state reaction		135	135	57
MoSe_2	Solvothermal		310	93	58
Ni_3S_2	Chemical	vapor deposition	116	96	59
NiS	Chemical	vapor deposition	124	154	59
MoP/MoNiP@C	Calcination	and phosphorization	134	66	60
$\text{S}_2\text{-NiCoP}_x/\text{NF}$	Hydrothermal, phosphorization	and	144	66	61

	sulfuration			
CuFe ₂ O ₄	Ball milling	241(6 M KOH)	114	62
FeSe ₂ /CoFe ₂ O ₄	Hydrothermal	231	88.76	63
NiS/Ni ₃ S ₄	Hydrothermal	221	-	64
Fe-doped α-NiS	Solventless	146	113	65
CoSe ₂ /MoSe ₂	Solvothermal	218	76	66
Cu-doped NiS	Solventless	154	114	65
Co-doped NiS	Solventless	156	98	65
Fe ₂ O ₃		376	173	67
Ni-NiO		516	207	67
Ni-Ni Fe ₂ O ₄	Hydrothermal followed by thermal decomposition	217	96	67
NiFe ₂ O ₄	Hydrothermal	187	122.7	68
Exfoliated NiFe ₂ O ₄	Hydrothermal	274	85.8	68
NiFe ₂ O ₄ @N/rGO - 800 °C	Pyrolytic method	157	94.7	69
NiFe ₂ O ₄ @rGO - 800 °C	Pyrolytic method	186	129.9	69
Ni_{0.4}Mg_{0.6}Fe₂O₄	Solventless	121	125	This work

Table 4.5. Comparison of OER performance of Ni_{0.2}Mg_{0.8}Fe₂O₄ with previously reported electrocatalysts in alkaline electrolyte.

Catalyst	Preparation method	η_{10} (mV) in 1 M KOH	Tafel slope (mV/decade)	Reference
MgFe ₂ O ₄	Sol-gel	1090	317	27
LiCoO ₂		520	48	70
CoCr ₂ O ₄	Calcination	422	63.3	71
Ni ₅₉ Cu ₁₉ P ₉	Electrodeposition	307	42.5	72
FeC/MnO ₂	Wet-chemical	254	39.81	73
MnO ₂	Wet-chemical	364	60.84	73
CuO@Cu ₂ O	Solid state reaction	315	63	57
CeO ₂ /NiFeCo	Precipitation	260	-	74
Co ₃ S ₄	Solvothermal	310	84.7	75
Ni ₅ P ₄	Hot injection	350 (50 mA/cm ²)	-	76

NiCoS	Solvothermal sulfidation	320	58.8	77
	and calcination			
CrMnFeCoNi) S_x	Pulse thermal decomposition	295 (100 mA/cm ²)	66	78
FeCo ₂ S ₄ NTA/CC	Template-free	317 (100 mA/cm ²)	36	79
V-doped NiS ₂	Hydrothermal	290	90	80
Fe ₂ O ₃	Hydrothermal followed by decomposition	304	84	67
Ni-NiO	Hydrothermal followed by decomposition	397	104	67
S-NiO	Electrodeposition and calcination	306	148	81
S-NiFe ₂ O ₄	Thiourea-assisted electrodeposition and calcination	343	124.5	81
NiFe ₂ O ₄	Hydrothermal followed by decomposition	342	44	82
NiO	Hydrothermal followed by decomposition	364	58	82
NiO-Ni	Hydrothermal–	296	42.8	83
Fe ₂ O ₄ /rGO	calcination method			
MgFe ₂ O ₄	Sol-gel	1090	317	27
NiO/NiFe ₂ O ₄	Hydrothermal followed by decomposition	302	42	82
Ni_{0.2}Mg_{0.8}Fe₂O₄	Solventless	284	58	This work

4.5.6 Supercapacitance

The charge storage capacity of Ni_{1-x}Mg_xFe₂O₄ (0 ≤ x ≤ 1) electrodes was investigated using CV and GCD studies. Fig. 15 (a-f) displays the CV plots of the Ni_{1-x}Mg_xFe₂O₄ (0 ≤ x ≤ 1) electrodes measured at various scan rates spanning from 2 to 300 mV/s. The CV curves for all samples display a similar shape. The Ni_{1-x}Mg_xFe₂O₄ (0 ≤ x ≤ 1) materials show a pair of apparent redox peaks that signify the supercapacitor characteristics of the electrode, which is a result of Faradaic reversible redox processes of Mg²⁺ ↔ Mg³⁺, Ni²⁺ ↔ Ni³⁺ and Fe²⁺ ↔ Fe³⁺ transitions with the aid of OH⁻ ions. Also, the peak currents slowly improve as a function of scan rates. It is obvious that the oxidation and reduction peaks still can be noticed at higher scan rate up to 300 mV/s, which suggests admirable kinetic reversibility and rate performance. Moreover, a slight shift is observed in the position of the redox peaks towards more positive and negative potentials as a function of scan rate, which is attributable to the polarization of Ni_{1-x}Mg_xFe₂O₄ (0 ≤ x ≤ 1) electrodes.⁸⁴⁻⁸⁶

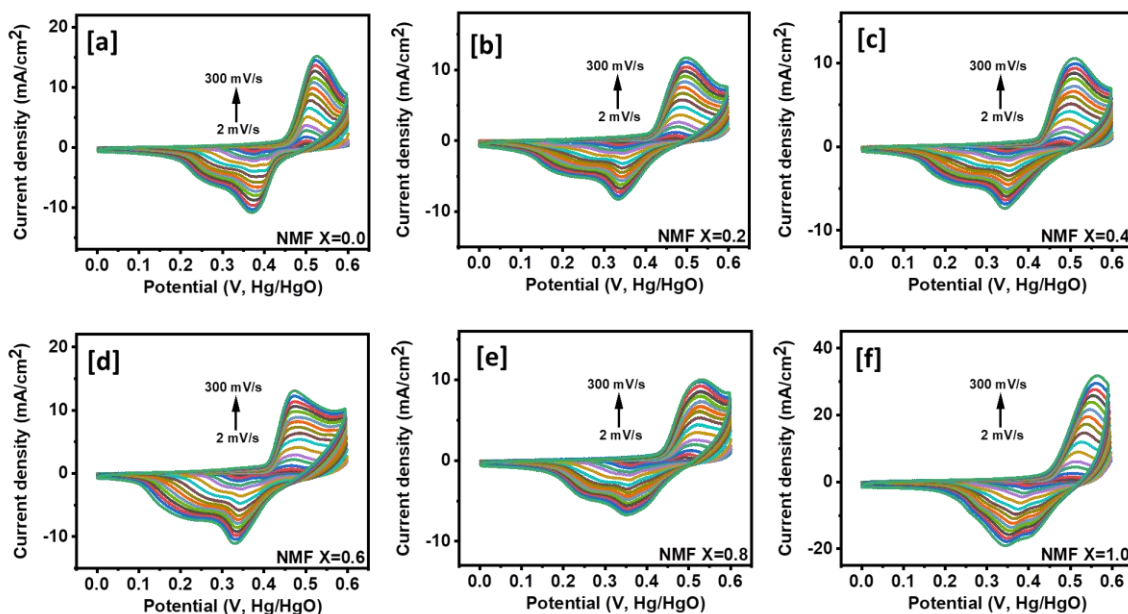


Fig. 4.15. Cyclic voltammograms of $\text{Ni}_{1-x}\text{Mg}_x\text{Fe}_2\text{O}_4$ ($0 \leq x \leq 1$) electrodes.

The GCD curves of $\text{Ni}_{1-x}\text{Mg}_x\text{Fe}_2\text{O}_4$ ($0 \leq x \leq 1$) samples measured at various current densities in the range of 1 to 20 A/g are displayed in Fig.4.16 (a-f). Noticeably, the non-linearity in the GCD plots further confirms the pseudocapacitance nature of $\text{Ni}_{1-x}\text{Mg}_x\text{Fe}_2\text{O}_4$ ($0 \leq x \leq 1$), which conform to the results from CV curves. The charge-discharge curves at all current densities manifest remarkable electrochemical reversibility. The $\text{Ni}_{1-x}\text{Mg}_x\text{Fe}_2\text{O}_4$ electrode with $x = 1$ exhibits the longer discharge time than other compositions, corresponding to higher specific capacitance. The specific capacitances computed from the discharge curves were plotted in Fig. 4.17. Apparently, the specific capacitance of the $\text{Ni}_{1-x}\text{Mg}_x\text{Fe}_2\text{O}_4$ electrode with $x = 1$ is 46 F/g at 1 A/g, which is significantly greater than those of $x = 0$ (19 F/g), $x = 0.2$ (23 F/g), $x = 0.4$ (20 F/g), $x = 0.6$ (23 F/g), and $x = 0.8$ (21 F/g). The value of specific capacitance obtained for MgFe_2O_4 (46 F/g) in this study is higher than the value MgFe_2O_4 nanospheres (43 F/g) reported by Maitra *et al.* recently.²⁷ It also surpasses the specific capacitance (33 F/g) of the previously reported MWNT- α - Fe_2O_3 /MWNT hybrid supercapacitor synthesized by employing hydrothermal and spray deposition methods.⁸⁷ Moreover, compared to other electrodes, the $\text{Ni}_{1-x}\text{Mg}_x\text{Fe}_2\text{O}_4$ ($x = 1$) still maintains high specific capacitance of 23 F/g at 20 A/g, which is around 50 % of the magnitude of specific capacitance at 1 A/g, demonstrating the superior rate capability. However, the specific capacitance exhibited by electrodes described in this study is relatively low compared to some previously reported Mg/Ni metal oxide-based supercapacitor electrode materials. For

example, through a sol-gel technique, Uke *et al.* prepared Zn doped MgFe_2O_4 nanocrystals which displayed specific capacitance of 484.6 F/g.⁸⁸ Nanomeric MgFe_2O_4 prepared by auto-combustion supported sol-gel technique was found to exhibit specific capacitance of 428.9 F/g at the current density 0.0625 A/g.²⁴ Gao *et al.* prepared NiFe_2O_4 nanoparticles exhibiting specific capacitance of 240.9 F/g at the current density of 1 A/g.¹⁶ The relationship between specific capacitance and current density shows that the specific capacitance of all electrodes decreased with the increase in current density, which is due to the reduction of degree of polarization.⁸⁹

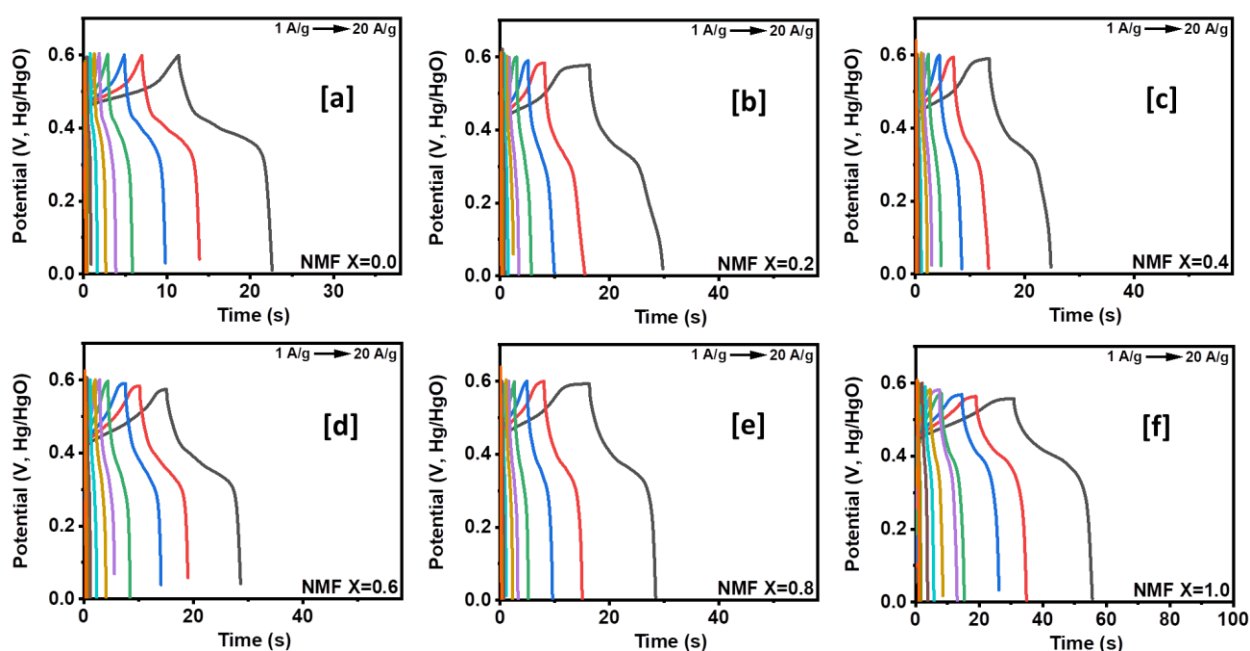


Fig. 4.16. GCD of $\text{Ni}_{1-x}\text{Mg}_x\text{Fe}_2\text{O}_4$ ($0 \leq x \leq 1$) electrodes.

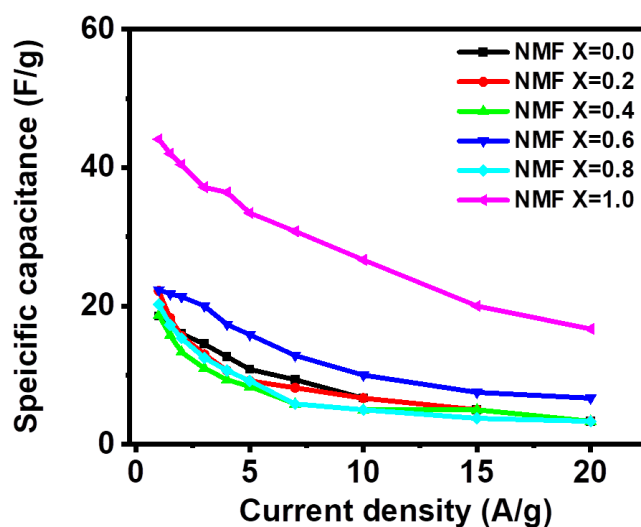


Fig. 4.17. Specific capacitance versus current density for $\text{Ni}_{1-x}\text{Mg}_x\text{Fe}_2\text{O}_4$ ($0 \leq x \leq 1$) electrodes.

4.5.7 Conclusion

In conclusion, this chapter reports a composition programmed fabrication of homogeneous $\text{Ni}_{1-x}\text{Mg}_x\text{Fe}_2\text{O}_4$ ($0 \leq x \leq 1$) solid solutions by solventless pyrolysis method. By regulating the molar composition of Mg and Ni in the preparation process, the physicochemical and the electrochemical performance of the material were modified. The as-synthesized $\text{Ni}_{1-x}\text{Mg}_x\text{Fe}_2\text{O}_4$ ($x = 0.6$) nanoparticles exhibited the best electrocatalytic activity for HER with an overpotential of only 121 mV which is much smaller compared to its analogues, at current density of 10 mA/cm^2 and the electrode exhibits good stability during long-term electrolysis. Meanwhile, $\text{Ni}_{0.2}\text{Mg}_{0.8}\text{Fe}_2\text{O}_4$ showed the best OER activity, requiring an overpotential of 284 mV to deliver the same current density within the window of potential examined. The outstanding electrocatalytic performance of these solid solutions are largely ascribed to the inherent conductivity, nanoparticulate nature and synergism of Mg, Ni and Fe in the spinel structure. The results described in this chapter paves the way for the design of mixed spinel oxides with high electrocatalytic activity for application in sustainable energy systems.

References

1. Álvarez-Serrano, I.; Arillo, M. A.; López, M. L.; Veiga, M. L.; Pico, C. *Advanced Materials* **2011**, 23, (44), 5237-5242.
2. Xu, C.; Chen, Q.; Ding, R.; Huang, S.; Zhang, Y.; Fan, G. *Chinese Journal of Catalysis* **2021**, 42, (2), 251-258.
3. Abakumov, A. M.; Fedotov, S. S.; Antipov, E. V.; Tarascon, J.-M. *Nature Communications* **2020**, 11, (1), 1-14.
4. Li, X.; Yang, X.; Xue, H.; Pang, H.; Xu, Q. *EnergyChem* **2020**, 2, (2), 100027.
5. Yang, Y. *Nanoscale* **2020**, 12, (6), 3560-3573.
6. Singh, B.; Sharma, V.; Gaikwad, R. P.; Fornasiero, P.; Zbořil, R.; Gawande, M. B. *Small* **2021**, 2006473.
7. Chikoidze, E.; Sartel, C.; Madaci, I.; Mohamed, H.; Vilar, C.; Ballesteros, B.; Belarre, F.; Del Corro, E.; Vales-Castro, P.; Sauthier, G. *Crystal Growth & Design* **2020**, 20, (4), 2535-2546.
8. Elanthamilan, E.; Rajkumar, S.; Merlin, J. P.; Jona, D. S.; Monisha, K.; Meena, B. C. *Electrochimica Acta* **2020**, 359, 136953.
9. Gonçalves, J. M.; Silva, M. N.; Naik, K. K.; Martins, P. R.; Rocha, D. P.; Nossol, E.; Munoz, R. A.; Angnes, L.; Rout, C. S. *Journal of Materials Chemistry A* **2021**.
10. Zhang, Y.; Zhang, W.; Yu, C.; Liu, Z.; Yu, X.; Meng, F. *Ceramics International* **2021**, 47, (7), 10063-10071.
11. Ismael, M. *Solar Energy Materials and Solar Cells* **2021**, 219, 110786.
12. Tan, J.; Xu, S.; Zhang, H.; Cao, H.; Zheng, G. *Electrochimica Acta* **2021**, 138199.
13. Maitra, S.; Mitra, R.; Nath, T. *Current Applied Physics* **2021**.
14. Lim, D.; Kong, H.; Kim, N.; Lim, C.; Ahn, W. S.; Baeck, S. H. *ChemNanoMat* **2019**, 5, (10), 1296-1302.
15. Islam, M.; Ali, G.; Jeong, M.-G.; Choi, W.; Chung, K. Y.; Jung, H.-G. *ACS Applied Materials & Interfaces* **2017**, 9, (17), 14833-14843.
16. Gao, X.; Wang, W.; Bi, J.; Chen, Y.; Hao, X.; Sun, X.; Zhang, J. *Electrochimica Acta* **2019**, 296, 181-189.
17. Liu, J.; Wang, R.; Zhong, X.; Yan, K.; Li, Y.; Xu, Z. *Int. J. Electrochem. Sci* **2019**, 14, (2), 1725-1732.
18. Permien, S.; Indris, S.; Scheuermann, M.; Schürmann, U.; Mereacre, V.; Powell, A. K.; Kienle, L.; Bensch, W. *Journal of Materials Chemistry A* **2015**, 3, (4), 1549-1561.
19. Zhang, Z.; Yan, X.; Liu, J.; Liu, B.; Gu, Z.-G. *Sustainable Energy & Fuels* **2021**.

20. Sharifi, S.; Yazdani, A.; Rahimi, K. *Materials Science in Semiconductor Processing* **2020**, 108, 104902.
21. Zong, W.; Rao, D.; Guo, H.; Ouyang, Y.; Miao, Y.-E.; Wang, W.; Wang, J.; Lai, F.; Liu, T. *Nanoscale* **2020**, 12, (20), 10977-10986.
22. Bashir, A.; Matinise, N.; Sackey, J.; Kaviyarasu, K.; Madiba, I.; Kodseti, L.; Ezema, F.; Maaza, M. *Physica E: Low-dimensional Systems and Nanostructures* **2020**, 119, 114002.
23. Narsimulu, D.; Rao, B. N.; Venkateswarlu, M.; Srinadhu, E.; Satyanarayana, N. *Ceramics International* **2016**, 42, (15), 16789-16797.
24. Majumder, S.; Kumar, S.; Banerjee, S. In *Nanometric MgFe₂O₄: Synthesis, characterization and its application towards supercapacitor and electrochemical uric acid sensor*, AIP Conference Proceedings, 2017; AIP Publishing LLC: p 050161.
25. Samuel, E.; Aldalbahi, A.; El-Newehy, M.; El-Hamshary, H.; Yoon, S. S. *Journal of Alloys and Compounds* **2021**, 852, 156929.
26. Simon, C.; Timm, J.; Tetzlaff, D.; Jungmann, J.; Apfel, U. P.; Marschall, R. *ChemElectroChem* **2021**, 8, (1), 227-239.
27. Maitra, S.; Mitra, R.; Nath, T. *Current Applied Physics* **2021**, 27, 73-88.
28. Yang, W.; Wang, Z.; Zhang, W.; Guo, S. *Trends in Chemistry* **2019**, 1, (2), 259-271.
29. Chen, W.; Yuan, P.; Guo, S.; Gao, S.; Wang, J.; Li, M.; Liu, F.; Wang, J.; Cheng, J. *Journal of Electroanalytical Chemistry* **2019**, 836, 134-142.
30. Yang, P.; Wu, Z.; Jiang, Y.; Pan, Z.; Tian, W.; Jiang, L.; Hu, L. *Advanced Energy Materials* **2018**, 8, (26), 1801392.
31. Chang, S.-K.; Lee, K.-T.; Zainal, Z.; Tan, K.-B.; Yusof, N. A.; Yusoff, W. M. D. W.; Lee, J.-F.; Wu, N.-L. *Electrochimica Acta* **2012**, 67, 67-72.
32. Zhang, Z.; Yan, X.; Liu, J.; Liu, B.; Gu, Z.-G. *Sustainable Energy & Fuels* **2021**, 5, (10), 2668-2677.
33. Seshan, K.; Shashimohan, A.; Chakrabarty, D.; Biswas, A. *Physica Status Solidi (a)* **1981**, 68, (1), 97-101.
34. El-Fadl, A. A.; Hassan, A. M.; Kassem, M. A. *Physica Scripta* **2020**, 95, (5), 055813.
35. Shannon, R. D. *Acta crystallographica section A: crystal physics, diffraction, theoretical and general crystallography* **1976**, 32, (5), 751-767.
36. Jacob, K.; Raj, S.; Rannesh, L. *International Journal of Materials Research* **2007**, 98, (9), 776-779.

37. Naeem, M.; Shah, N. A.; Gul, I. H.; Maqsood, A. *Journal of Alloys and Compounds* **2009**, 487, (1-2), 739-743.
38. Cullity, B. D., *Elements of X-ray Diffraction*. Addison-Wesley Publishing: 1956.
39. Kannan, Y.; Saravanan, R.; Srinivasan, N.; Ismail, I. *Journal of Magnetism and Magnetic Materials* **2017**, 423, 217-225.
40. Shobana, M.; Kim, K.; Kim, J.-H. *Physica E: Low-dimensional Systems and Nanostructures* **2019**, 108, 100-104.
41. Srivastava, M.; Ojha, A. K.; Chaubey, S.; Materny, A. *Journal of Alloys and Compounds* **2009**, 481, (1-2), 515-519.
42. Manikandan, A.; Vijaya, J. J.; Sundararajan, M.; Meganathan, C.; Kennedy, L. J.; Bououdina, M. *Superlattices and Microstructures* **2013**, 64, 118-131.
43. Casbeer, E.; Sharma, V. K.; Li, X.-Z. *Separation and Purification Technology* **2012**, 87, 1-14.
44. Singh, S.; Khare, N. *Applied Physics A* **2018**, 124, (2), 107.
45. Tehrani, F. S.; Daadmehr, V.; Rezakhani, A.; Akbarnejad, R. H.; Gholipour, S. *Journal of Superconductivity and Novel Magnetism* **2012**, 25, (7), 2443-2455.
46. El-Fadl, A. A.; Hassan, A. M.; Kassem, M. A. *Physica Scripta* **2020**.
47. Dalai, N.; Mohanty, B.; Mitra, A.; Jena, B. *ChemistrySelect* **2019**, 4, (27), 7791-7796.
48. Riaz, M. S.; Zhao, S.; Dong, C.; Iqbal, M. J.; Zhao, Y.; Huang, F. *Energy Technology* **2020**, 8, (5), 1901310.
49. Jiang, J.; Zhu, L.; Sun, Y.; Chen, Y.; Chen, H.; Han, S.; Lin, H. *Journal of Power Sources* **2019**, 426, 74-83.
50. Zhao, Y.; Chang, C.; Teng, F.; Zhao, Y.; Chen, G.; Shi, R.; Waterhouse, G. I.; Huang, W.; Zhang, T. *Advanced Energy Materials* **2017**, 7, (18), 1700005.
51. Liu, P.; Zhu, J.; Zhang, J.; Xi, P.; Tao, K.; Gao, D.; Xue, D. *ACS Energy Letters* **2017**, 2, (4), 745-752.
52. Li, M.; Xiong, Y.; Liu, X.; Bo, X.; Zhang, Y.; Han, C.; Guo, L. *Nanoscale* **2015**, 7, (19), 8920-8930.
53. Hirai, S.; Yagi, S.; Seno, A.; Fujioka, M.; Ohno, T.; Matsuda, T. *RSC Advances* **2016**, 6, (3), 2019-2023.
54. Chen, Z.; Kronawitter, C. X.; Koel, B. E. *Physical Chemistry Chemical Physics* **2015**, 17, (43), 29387-29393.
55. Zhong, X.; Tang, J.; Wang, J.; Shao, M.; Chai, J.; Wang, S.; Yang, M.; Yang, Y.; Wang, N.; Wang, S. *Electrochimica Acta* **2018**, 269, 55-61.

56. Zhao, G.; Wang, X.; Wang, S.; Rui, K.; Chen, Y.; Yu, H.; Ma, J.; Dou, S. X.; Sun, W. *Chemistry—An Asian Journal* **2019**, 14, (2), 301-306.
57. Xing-Xing, M.; Li, C.; ZHANG, Z.; Ji-Lin, T. *Chinese Journal of Analytical Chemistry* **2020**, 48, (1), e20001-e20012.
58. Meiron, O. E.; Kuraganti, V.; Hod, I.; Bar-Ziv, R.; Bar-Sadan, M. *Nanoscale* **2017**, 9, (37), 13998-14005.
59. Kajbafvala, M.; Moradlou, O.; Moshfegh, A. Z. *Vacuum* **2021**, 188, 110209.
60. Li, J.; Zheng, H.; Xu, C.; Su, Z.; Li, X.; Sun, J. *Inorganic Chemistry* **2021**, 60, (3), 1624-1630.
61. Sun, Q.; Tong, Y.; Chen, P.; Chen, L.; Xi, F.; Liu, J.; Dong, X. *Journal of Colloid and Interface Science* **2021**, 589, 127-134.
62. Tan, J.; Xu, S.; Zhang, H.; Cao, H.; Zheng, G. *Electrochimica Acta* **2021**, 381, 138199.
63. Zhang, H.; Nengzi, L.-c.; Li, B.; Cheng, Q.; Gou, J.; Cheng, X. *Renewable Energy* **2020**, 155, 717-724.
64. Qin, Z.; Chen, Y.; Huang, Z.; Su, J.; Diao, Z.; Guo, L. *The Journal of Physical Chemistry C* **2016**, 120, (27), 14581-14589.
65. Shombe, G. B.; Khan, M. D.; Alenad, A. M.; Choi, J.; Ingsel, T.; Gupta, R. K.; Revaprasadu, N. *Sustainable Energy & Fuels* **2020**, 4, (10), 5132-5143.
66. Zhao, G.; Li, P.; Rui, K.; Chen, Y.; Dou, S. X.; Sun, W. *Chemistry—A European Journal* **2018**, 24, (43), 11158-11165.
67. Zhang, J.; Jiang, Y.; Wang, Y.; Yu, C.; Cui, J.; Wu, J.; Shu, X.; Qin, Y.; Sun, J.; Yan, J. *Electrochimica Acta* **2019**, 321, 134652.
68. Munonde, T. S.; Zheng, H.; Matseke, M. S.; Nomngongo, P. N.; Wang, Y.; Tsiakaras, P. *Renewable Energy* **2020**, 154, 704-714.
69. Cao, L.; Li, Z.; Su, K.; Zhang, M.; Cheng, B. *Journal of Energy Chemistry* **2021**, 54, 595-603.
70. Lu, Z.; Wang, H.; Kong, D.; Yan, K.; Hsu, P.-C.; Zheng, G.; Yao, H.; Liang, Z.; Sun, X.; Cui, Y. *Nature Communications* **2014**, 5, (1), 1-7.
71. Al-Mamun, M.; Su, X.; Zhang, H.; Yin, H.; Liu, P.; Yang, H.; Wang, D.; Tang, Z.; Wang, Y.; Zhao, H. *Small* **2016**, 12, (21), 2866-2871.
72. Kim, B. K.; Kim, S.-K.; Cho, S. K.; Kim, J. J. *Applied Catalysis B: Environmental* **2018**, 237, 409-415.
73. Ye, M.; Hu, F.; Yu, D.; Han, S.; Li, L.; Peng, S. *Ceramics International* **2021**, 47, (13), 18424-18432.

74. Wang, Y.; Gao, F.-m. *Nanotechnology* **2021**.
75. Zhu, M.; Zhang, Z.; Zhang, H.; Zhang, H.; Zhang, X.; Zhang, L.; Wang, S. *Journal of Colloid and Interface Science* **2018**, 509, 522-528.
76. Ayom, G. E.; Khan, M. D.; Ingsel, T.; Lin, W.; Gupta, R. K.; Zamisa, S. J.; van Zyl, W. E.; Revaprasadu, N. *Chemistry–A European Journal* **2020**, 26, (12), 2693-2704.
77. Yu, Z.; Bai, Y.; Zhang, S.; Liu, Y.; Zhang, N.; Sun, K. *International Journal of Hydrogen Energy* **2018**, 43, (18), 8815-8823.
78. Cui, M.; Yang, C.; Li, B.; Dong, Q.; Wu, M.; Hwang, S.; Xie, H.; Wang, X.; Wang, G.; Hu, L. *Advanced Energy Materials* **2021**, 11, (3), 2002887.
79. Hu, X.; Wang, R.; Sun, P.; Xiang, Z.; Wang, X. *ACS Sustainable Chemistry & Engineering* **2019**, 7, (24), 19426-19433.
80. Liu, H.; He, Q.; Jiang, H.; Lin, Y.; Zhang, Y.; Habib, M.; Chen, S.; Song, L. *ACS Nano* **2017**, 11, (11), 11574-11583.
81. Liu, J.; Zhu, D.; Ling, T.; Vasileff, A.; Qiao, S.-Z. *Nano Energy* **2017**, 40, 264-273.
82. Liu, G.; Gao, X.; Wang, K.; He, D.; Li, J. *International Journal of Hydrogen Energy* **2016**, 41, (40), 17976-17986.
83. Zhang, G.; Li, Y.; Zhou, Y.; Yang, F. *ChemElectroChem* **2016**, 3, (11), 1927-1936.
84. Wang, Y.; Liu, Y.; Wang, H.; Liu, W.; Li, Y.; Zhang, J.; Hou, H.; Yang, J. *ACS Applied Energy Materials* **2019**, 2, (3), 2063-2071.
85. Li, Q.; Lu, C.; Chen, C.; Xie, L.; Liu, Y.; Li, Y.; Kong, Q.; Wang, H. *Energy Storage Materials* **2017**, 8, 59-67.
86. Mohamed, S. G.; Hussain, I.; Shim, J.-J. *Nanoscale* **2018**, 10, (14), 6620-6628.
87. Zhao, X.; Johnston, C.; Grant, P. S. *Journal of Materials Chemistry* **2009**, 19, (46), 8755-8760.
88. Uke, S. J.; Mardikar, S. P.; Bambole, D. R.; Kumar, Y.; Chaudhari, G. N. *Materials Science for Energy Technologies* **2020**, 3, 446-455.
89. Ndambakuwa, W.; Ndambakuwa, Y.; Choi, J.; Fernando, G.; Neupane, D.; Mishra, S. R.; Perez, F.; Gupta, R. K. *Surface and Coatings Technology* **2021**, 410, 126933.

CHAPTER 5

Electrochemical investigation of uncapped $\text{Ni}_{1-x}\text{Zn}_x\text{Fe}_2\text{O}_4$ ($0 \leq x \leq 1$) solid solutions prepared by a solventless thermolytic approach

5.1 Introduction

Electrochemical energy conversion and storage technologies play vital roles in our daily life, responding to the growing society's demand for affordable, portable, and renewable power supply. They stand out as the most viable option for enabling and accelerating the transition to a low-carbon economy, providing a cleaner and more sustainable planet.¹ With the existing over-reliance on non-renewable energy systems, and the increasing use of smart electronics, desirable factors such as operability, high performance, durability, consistent energy supply and eco-friendliness are required.² For this purpose, great expectations are held for energy storage systems such as supercapacitors, metal-ion batteries and metal-air batteries, and energy conversion systems constituting a sequence of electrochemical processes taking place in fuel cells or electrolyzers.³⁻⁵ Normally, electrochemical energy systems constitute a series of complex physical interactions and chemical processes occurring at the surface and within electrodes/electrolytes. The transport behaviors and kinetics of diverse carriers such as ions, electrons, molecules and holes are closely related to the type of electroactive materials employed for electrodes/electrocatalysts. The nature of the electroactive material, amongst others influences the electrochemical activity, device performance and cost.⁶ Improving the electrochemical performance of the two technologies has been the focus of research in recent years attracting intensive attention from academia and industry.

The advent of nanotechnology gave electrochemical energy systems a new lease of life, providing advantages with regards to power, materials sustainability, capacity and cost that are still far from being fully realised.⁷ Additionally, the innovation of new nanomaterials and in-depth knowledge of their quantitative and qualitative structure-composition-property-performance relationships have played a crucial role in advancing the energy systems.⁸ In recent years, amongst inorganic solids, nanoscale transition metal oxides have demonstrated promising potential for supercapacitors and electrocatalytic water splitting.⁹ In particular, ferros spinels such as MgFe_2O_4 ,¹⁰ NiFe_2O_4 ,¹¹ MnFe_2O_4 ,¹² CoFe_2O_4 ,¹³ etc., have demonstrated superior electrochemical behaviour than the corresponding single metal oxides due to their structural and compositional versatility, making them a better choice over other options. Furthermore, they exhibit interesting properties including admirable redox reversibility and conductivity which contribute to improved electrochemical behaviour.¹⁴ The synergistic contributions of each transition metal ion in the mixed ferrite structure leads to the substantial

improvement of conductivity,¹⁵ along with abundant reaction sites emanating from multiple elements, contributing to superior electrochemical activities.⁹

Spinel zinc ferrite (ZnFe_2O_4) and nickel ferrite (NiFe_2O_4) are among the ferros spinels which are currently investigated for energy related applications. Due to their cost-effectiveness, decent electron transport properties, easy accessibility, recent studies have mainly focused on their suitability as electroactive materials for lithium ion batteries, supercapacitors and electrocatalytic water splitting.¹⁶⁻²⁰ For example, a recent investigation by Simon *et al.* revealed high electrocatalytic activity of mesoporous NiFe_2O_4 for oxygen evolution reaction under alkaline condition.²¹ The as-prepared NiFe_2O_4 obtained via a soft-templating method delivered a current density of 10 mA/cm^2 at an overpotential of 410 mV with a relatively small Tafel slope of 50 mV/dec. Sun *et al.* synthesized a stable ZnFe_2O_4 electrocatalyst with better hydrogen evolution activity manifested by an overpotential of 170 mV.²² Zhang *et al.* reported yolk-shell ordered ZnFe_2O_4 nanoparticles prepared by using a simple solvothermal approach. The nanocatalyst exhibited an overpotential of 280 mV at a current density of 10 mA/cm^2 and the Tafel slope of 70 mV/dec, demonstrating excellent electrocatalytic oxygen evolution capability.²³ Joshi *et al.* employed a single step electrodeposition method to fabricate bimetallic ZnFe_2O_4 nanosheets as a supercapacitor electrode which yielded a specific capacitance of 1093 F/g at a current rate of 1 A/g.²⁴ Dalai *et al.* prepared a ternary NiFe_2O_4 electrocatalyst which exhibited higher activity for OER, with an overpotential of 290 mV and lower Tafel slope of 42 mV/dec.²⁵

There is still potential to further upgrade the electrochemical performance of ZnFe_2O_4 and NiFe_2O_4 materials. As a result, some approaches are developed to achieve this goal. One strategy involves the formation of composites comprising metal oxides and highly conductive materials, such as carbon nanotubes, graphene, etc.²⁶⁻²⁸ Another approach is to modify or change their composition while the materials' phase and structure remain intact.^{20, 29, 30} Interestingly, both ZnFe_2O_4 and NiFe_2O_4 possess the same cubic structure and space group of $Fd3m$ as per their standard XRD patterns. Meanwhile, the ionic size of Zn^{2+} (0.82 Å) is very close to that of Ni^{2+} (0.78 Å), demonstrating the likelihood of obtaining a series of substitutional solid solutions with diverse compositions and stoichiometries via substitution of Ni with Zn during the synthesis process. In this case, it is anticipated that a solid solution between ZnFe_2O_4 and NiFe_2O_4 within the whole composition range, is possible and the phase and crystal structure remain unchanged due to similar crystallographic structure of the two parent spinels.

Therefore, in this chapter, a simple solvent free thermolysis method was employed to fabricate $\text{Ni}_{1-x}\text{Zn}_x\text{Fe}_2\text{O}_4$ ($0 \leq x \leq 1$) solid solutions from metal acetylacetonate precursors. The solventless thermolysis (melt) method is rapid, versatile, and binder-free, and it has not yet been used to produce monophasic $\text{Ni}_{1-x}\text{Zn}_x\text{Fe}_2\text{O}_4$ solid solutions from metal acetylacetonate precursors. During the synthesis process, the concentration of Ni^{2+} and Zn^{2+} was varied in continuum with the aim of identifying the optimal amount that would yield the highest specific capacitance, HER and OER activities.

5.2 Experimental

5.2.1 Chemicals

Nickel (II) acetylacetonates (98%, Merck-Schuchardt), zinc (II) acetylacetonates (98%, Merck-Schuchardt), and iron (III) acetylacetonate (97%, Sigma-Aldrich). The precursors employed in this study were used as received.

5.2.2 Synthesis of $\text{Ni}_{1-x}\text{Zn}_x\text{Fe}_2\text{O}_4$ ($x = 0, 0.2, 0.4, 0.6, 0.8, 1$) solid solutions

Nanostructured $\text{Ni}_{1-x}\text{Zn}_x\text{Fe}_2\text{O}_4$ ($0 \leq x \leq 1$) solid solutions of different stoichiometric compositions were prepared by solvent-free thermolysis of metal acetylacetonates. For the typical synthesis of ternary NiFe_2O_4 nanoparticles, 0.10 g (0.39 mmol) of nickel acetylacetonate and 0.27 g (0.78 mmol) of iron acetylacetonate were mixed and the solid mixture was ground using pestle and mortar for ≈ 20 minutes to obtain a homogeneous mixture. The precursor mixture was then placed into a ceramic boat, which was placed in a reactor tube. The reactor tube was then introduced inside the carbolite tube furnace in such a way that the ceramic boat must be placed almost in the middle of the heating zone, followed by thermal treatment at 450 °C, at a heating rate of 20 °C per minute for 1 h. After 1 h of annealing, the heating was switched off, and the furnace was left to cool naturally to ambient temperature. The reactor tube was taken out of the furnace upon cooling, and the product was collected for analysis without any post-treatment. Likewise, the synthesis of ZnFe_2O_4 nanoparticles was achieved by employing similar procedures except that zinc acetylacetonate was used instead of nickel acetylacetonate and the amount of zinc and iron complexes were maintained in the same mole ratio of 1:2.

For the synthesis of quaternary $\text{Ni}_{1-x}\text{Zn}_x\text{Fe}_2\text{O}_4$ ($x = 0.2, 0.4, 0.6, 0.8$) solid solutions, a known quantity of nickel acetylacetonate was partially substituted by appropriate amounts of zinc acetylacetonate by adjusting the mole ratios of Zn and Ni in the intervals of 0.2, 0.4, 0.6,

and 0.8, while keeping the amount of iron acetylacetonate unchanged in the reaction mixture. The reaction procedures for the entire series of solid solutions were kept similar to those employed to synthesize the ternary nickel and zinc ferrites.

5.3 Characterization of $\text{Ni}_{1-x}\text{Zn}_x\text{Fe}_2\text{O}_4$ ($0 \leq x \leq 1$) solid solutions

5.3.1 Powder X-ray diffraction (p-XRD) analysis

Structural analysis of the $\text{Ni}_{1-x}\text{Zn}_x\text{Fe}_2\text{O}_4$ nanoparticles was ascertained by powder X-ray diffraction (p-XRD) analysis employing a Bruker AXS D8 Advance X-ray diffractometer. The instrument uses nickel-filtered Cu K α radiation ($\lambda=1.5418\text{\AA}$) at 40 kV, 40 mA. The measurements were recorded at 2θ values ranging from 10 to 80°.

5.3.2 Scanning electron microscopy (SEM) and Energy dispersive X-ray (EDX) analyses

SEM imaging was carried out on a ZEISS-Auriga Cobra SEM Field Emission Scanning Electron Microscope (FE SEM) while EDX elemental analysis was performed on a JEOL JSM-7500F Field Emission Scanning Electron Microscope (FE-SEM) Equipped with Energy Dispersive X-ray spectroscopy (EDX).

5.3.3 Transmission electron microscopy (TEM), High resolution TEM (HRTEM) and Selected area electron diffraction (SAED) analyses

The SAED, TEM and HRTEM analyses were performed on a JEOL 2100 HRTEM at accelerating voltages of 200 kV.

5.3.4 UV-visible spectroscopy

The optical absorbance measurements were conducted in the UV-Vis spectral range on a Varian Cary 50 UV/Vis spectrophotometer.

5.4 Electrochemical evaluation of $\text{Ni}_{1-x}\text{Zn}_x\text{Fe}_2\text{O}_4$ ($0 \leq x \leq 1$) solid solutions

Electrochemical measurements were investigated by a Versastat 4-500 electrochemical workstation (Princeton Applied Research, Oak Ridge, TN, USA). The cell setup for supercapacitor was made up of a three electrode system consisting of platinum (Pt) wire, a saturated Hg/HgO electrode, and the as-synthesized $\text{Ni}_{1-x}\text{Zn}_x\text{Fe}_2\text{O}_4$ ($0 \leq x \leq 1$) electrodes for counter, reference, and working electrode, correspondingly. For electrocatalytic water-splitting studies, only the reference electrode was changed to a saturated calomel electrode (SCE) in the same three electrode configuration. To make the working electrode, Ni foam

was used as a substrate. The working electrode was prepared by mixing 80 wt. % of the $\text{Ni}_{1-x}\text{Zn}_x\text{Fe}_2\text{O}_4$ ($0 \leq x \leq 1$), 10 wt. % of polyvinylidene difluoride (PVDF) binder, and 10 wt. % of acetylene black with N-methyl pyrrolidinone (NMP) solvent. The paste was then dried at 60°C for 24 h. In order to evaluate the electrochemical performance of the $\text{Ni}_{1-x}\text{Zn}_x\text{Fe}_2\text{O}_4$ ($0 \leq x \leq 1$) @ Ni electrodes, cyclic voltammetry (CV), and galvanostatic charge-discharge (GCD) measurements were used for supercapacitor test with 3 M KOH solution. For the water splitting measurements, linear sweep voltammetry (LSV) measurements were utilized at the scan rate of 2 mV/s, and the potential (V, SCE) was converted into a reversible hydrogen electrode (RHE) with iR-correction. Furthermore, electrochemical impedance spectroscopy (EIS) and chronoamperometry (CA) measurements were performed at 0.5, 0.55 V (V, SCE), respectively. All water-splitting tests were studied in 1 M KOH solution.

5.5 Results and discussion

5.5.1 Powder X-ray diffraction (p-XRD) study

The p-XRD analysis was performed to confirm the phase purity, crystal structure and determine the structural parameters of a series of $\text{Ni}_{1-x}\text{Zn}_x\text{Fe}_2\text{O}_4$ ($0 \leq x \leq 1$) solid solutions with $x = 0, 0.2, 0.4, 0.6, 0.8$ and 1. The p-XRD patterns shown in Fig. 5.1 (a) demonstrate that the position of all the detected characteristic peaks for pure samples $x = 0$ and $x = 1$ can be indexed well with the standard pattern of the trevorite phase of pure NiFe_2O_4 (ICDD #. 00-044-1485) and ZnFe_2O_4 (ICDD #. 01-073-1963), respectively. It can be seen that the incorporation of zinc did not affect the crystal symmetry of nickel ferrite since the p-XRD patterns of the as-prepared $\text{Ni}_{1-x}\text{Zn}_x\text{Fe}_2\text{O}_4$ solid solutions with $x = 0.2$ to $x = 0.8$ still match well with the standard XRD profile of NiFe_2O_4 . In the limit of instrument sensitivity, no evidence of extra peaks corresponding to impurity were observed except those ascribed to the parent spinel ferrite systems. This suggests that Zn^{2+} was successfully incorporated and perfectly distributed into the lattice site of NiFe_2O_4 , signalling the formation of a single-phase system of $\text{Ni}_{1-x}\text{Zn}_x\text{Fe}_2\text{O}_4$ ($0 \leq x \leq 1$) solid solution with a cubic spinel structure.³¹

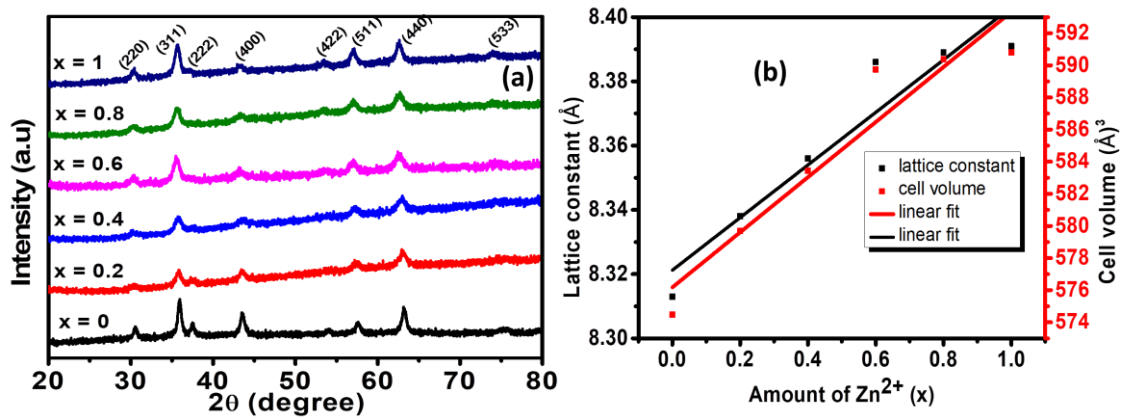


Fig.5.1.(a) p-XRD patterns of $\text{Ni}_{1-x}\text{Zn}_x\text{Fe}_2\text{O}_4$ ($0 \leq x \leq 1$) nanoparticles. **(b)** Variation of lattice constant (left y-axis) and cell volume (right y-axis) as a function of Zn^{2+} concentration.

The variation of different structural parameters such as cell volume, lattice constant and crystallite size with respect to the amount of Zn^{2+} ions were computed and tabulated in Table 5.1. A slight increase in cell volume and lattice parameter was noted for the prepared nanospinel solid solutions, due to the slight difference in ionic size between Zn^{2+} (0.82 Å) and Ni^{2+} (0.78 Å) ions. It should be noted that both Zn^{2+} (0.82 Å) and Ni^{2+} (0.78 Å) possess larger ionic size compared to the size of interstices in tetrahedral (0.58 Å) and octahedral (0.73 Å) sites in the spinel cubic system. This difference in sizes in turn causes expansion of lattice when these ions are substituted into the interstices.³² Nonetheless, the lattice expansion is expected to be more when Ni^{2+} ions are substituted by bigger Zn^{2+} ions. Therefore, it is obvious that samples with higher Zn^{2+} content have larger lattice constants and hence higher cell volume.³³ Generally, the results indicate a linear increase in cell volume from 574.478 to 590.801 Å³, and lattice parameters from 8.313 to 8.391 Å when the composition of zinc was varied from $x = 0$ to $x = 1$, respectively. The observed linear increase of structural parameters with zinc substitution presented in Fig. 5.1(b) is consistent with Vegard's law.³⁴

Table 5.1: Lattice parameter (a), unit cell volume (V), crystallite size (d), and EDX composition of $\text{Ni}_{1-x}\text{Zn}_x\text{Fe}_2\text{O}_4$ ($0 \leq x \leq 1$) solid solutions.

Zn^{2+} content	Target ferrite composition	Stoichiometry obtained from EDX	$a = b = c$ (Å)	d (nm)	V (Å ³)
0	NiFe_2O_4	$\text{Ni}_{0.95}\text{Fe}_{1.93}\text{O}_{4.13}$	8.313	19.420	574.478

0.2	Ni _{0.8} Zn _{0.2} Fe ₂ O ₄	Ni _{0.89} Zn _{0.23} Fe _{1.96} O _{3.92}	8.338	13.740	579.676
0.4	Ni _{0.6} Zn _{0.4} Fe ₂ O ₄	Ni _{0.64} Zn _{0.36} Fe _{1.97} O _{4.03}	8.356	9.907	583.438
0.6	Ni _{0.4} Zn _{0.6} Fe ₂ O ₄	Ni _{0.39} Zn _{0.62} Fe _{2.09} O _{3.85}	8.386	7.998	589.745
0.8	Ni _{0.2} Zn _{0.8} Fe ₂ O ₄	Ni _{0.26} Zn _{0.71} Fe _{2.14} O _{3.89}	8.389	9.845	590.379
1.0	ZnFe ₂ O ₄	Zn _{0.88} Fe _{1.82} O _{4.29}	8.391	10.960	590.801

The average crystallite sizes of Ni_{1-x}Zn_xFe₂O₄ ($0 \leq x \leq 1$) nanoparticles were calculated from XRD data according to the Scherrer formula.³⁵ The formula allows the estimation of the crystallite size from the Braggs angle, the full width at half maximum of the peak and wavelength of X-ray source. The crystallite size of pure NiFe₂O₄ obtained in this study was 19.420 nm. The decrease in the average crystallite size with the increasing amount of Zn²⁺ ions suggests that the addition of Zn²⁺ has obstructed the crystallite growth of the material. This may be attributed to the strong chemical affinity of specific cations such as Zn²⁺ to the tetrahedral position,³⁶ and the metastable cation distribution in nano regime of the ferrosipinel particles.³⁷ It is also well known that the formation of ZnFe₂O₄ is more exothermic than the formation of NiFe₂O₄. Therefore, more heat is expected to be evolved upon the introduction of Zn²⁺ in the NiFe₂O₄ system, lowering the molecular concentration at the crystal surface and consequently hampering the grain growth.³⁸ Furthermore, the decrease in crystallite size can be explained in relation to the electronic structure of Ni²⁺ (3d⁸) and Zn²⁺ (3d¹⁰) ions. Unlike Zn²⁺, Ni²⁺ has more tendencies to interact with ligands and O²⁻ anions by virtue of its incomplete electronic structure. The absence of unpaired d electrons in Zn²⁺ causes minimal covalent interaction and propensity toward extension between Zn²⁺ and its ligands. Thus, incorporating zinc into nickel ferrite hinders the growth of particle, and hence reducing the crystallite size. Again, the smaller crystallite sizes of the zinc substituted nickel ferrites are ascribed to small bond energy between zinc and oxygen (Zn²⁺-O²⁻) in comparison to that existing between nickel and oxygen (Ni²⁺-O²⁻).³⁹ The reduction in crystallite size of spinel nanoferrites provides intriguing changes in the distribution of ions in the spinel structure, giving rise to modification of overall properties. Similar results of reduced average crystallite size on addition of Zn²⁺ ions in the spinel ferrite lattice systems have been reported previously.^{38, 40}

5.5.2 Compositional studies

The elemental analysis of the solid solutions synthesized from the metal acetylacetonate complexes are shown by the EDX spectra in Fig.5.2. For $\text{Ni}_{1-x}\text{Zn}_x\text{Fe}_2\text{O}_4$ solid solutions with compositions $x = 0.2$ to $x = 0.8$, the spectra show the presence of nickel, zinc, iron and oxygen as the only constituents in the samples. The spectra patterns of the parent nickel ferrite ($x = 0$) show the presence of nickel, iron and oxygen only, whereas zinc, iron and oxygen are present in pure zinc ferrite ($x = 1$) nanoparticles. Table 5.2 indicates that the atomistic composition of all samples matches with the relative amounts of the starting materials used. Also, the observed percentage elemental compositions are in good agreement with theoretical values. The slight deviation of the experimental values as compared to theoretical values can be caused by minor experimental errors or slight difference in the reactivity of the precursors. Elemental mapping of $\text{Ni}_{1-x}\text{Zn}_x\text{Fe}_2\text{O}_4$ ($0 \leq x \leq 1$) nanoparticles showed uniform dispersion of the respective elements in the samples (Figs.5.3 and 5.4).

Table 5.2. Summary of $\text{Ni}_{1-x}\text{Zn}_x\text{Fe}_2\text{O}_4$ ($0 \leq x \leq 1$) compositions obtained from EDX analysis.

(x)	Theoretical atomic %					Atomic % from EDX analysis				
	Ni	Zn	Fe	O	Total	Ni	Zn	Fe	O	Total
0	14.29	-	28.57	57.14	100	13.55	-	27.52	58.93	100
0.2	11.43	2.86	28.57	57.14	100	12.69	3.24	28.06	56.00	100
0.4	8.57	5.71	28.57	57.14	100	9.13	5.21	28.09	57.57	100
0.6	5.71	8.57	28.57	57.14	100	5.68	8.90	29.84	55.00	100
0.8	2.86	11.43	28.57	57.14	100	3.71	10.19	30.52	55.58	100
1.0	-	14.29	28.57	57.14	100	-	12.62	26.04	61.34	100

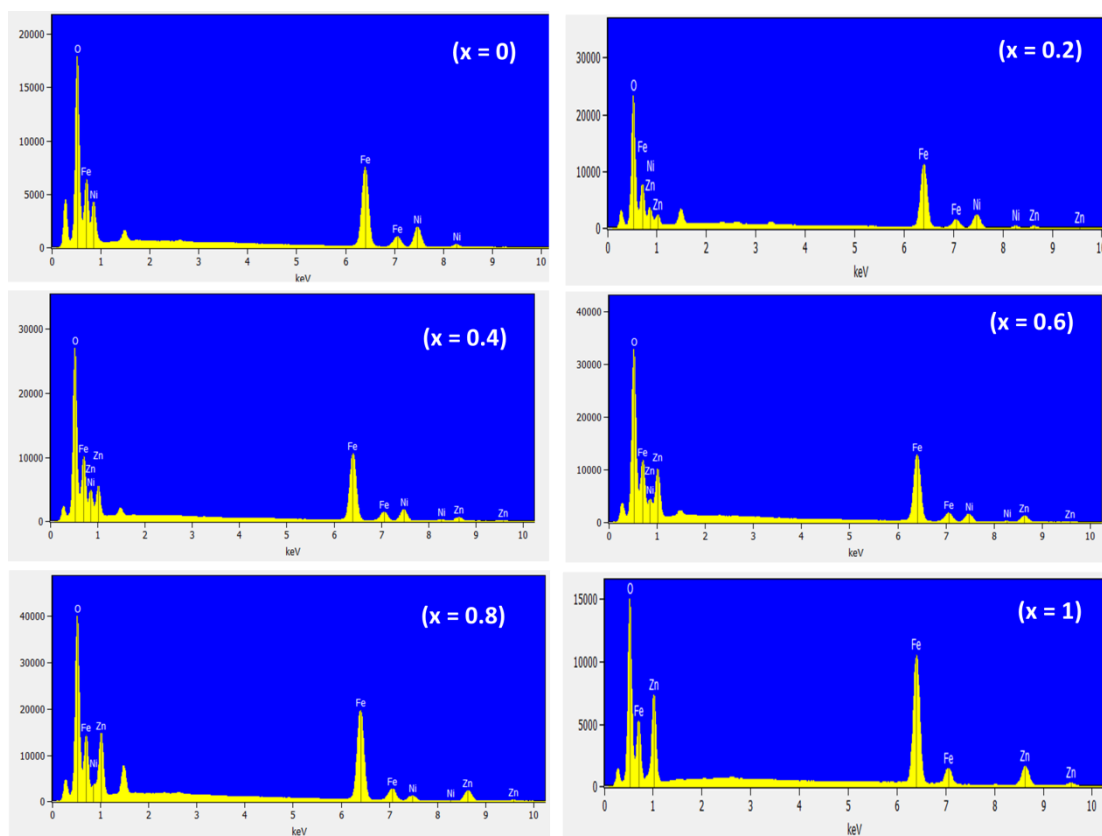


Fig.5.2. EDX pattern of $\text{Ni}_{1-x}\text{Zn}_x\text{Fe}_2\text{O}_4$ ($0 \leq x \leq 1$) solid solution nanoparticles.

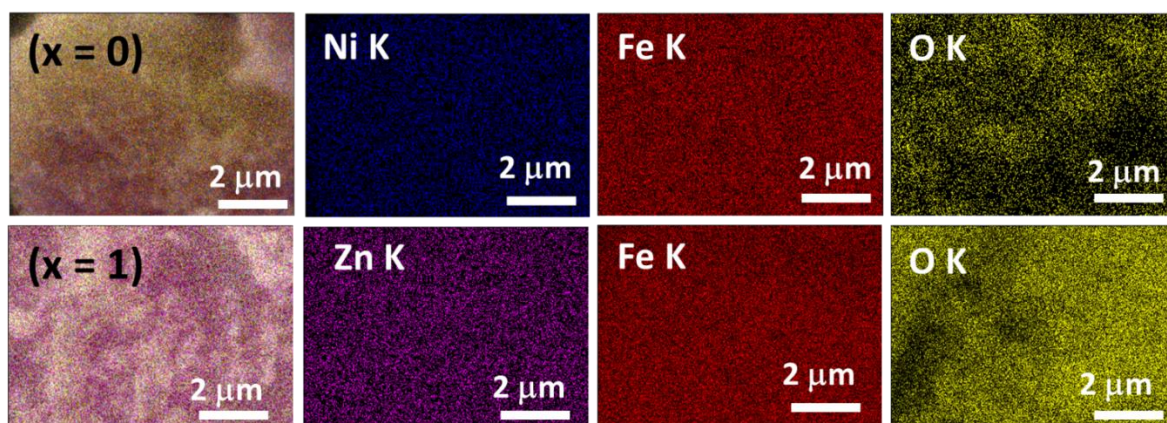


Fig.5.3. EDX elemental mapping of $\text{Ni}_{1-x}\text{Zn}_x\text{Fe}_2\text{O}_4$ ($x = 0$ and 1) showing uniform distribution of elements.

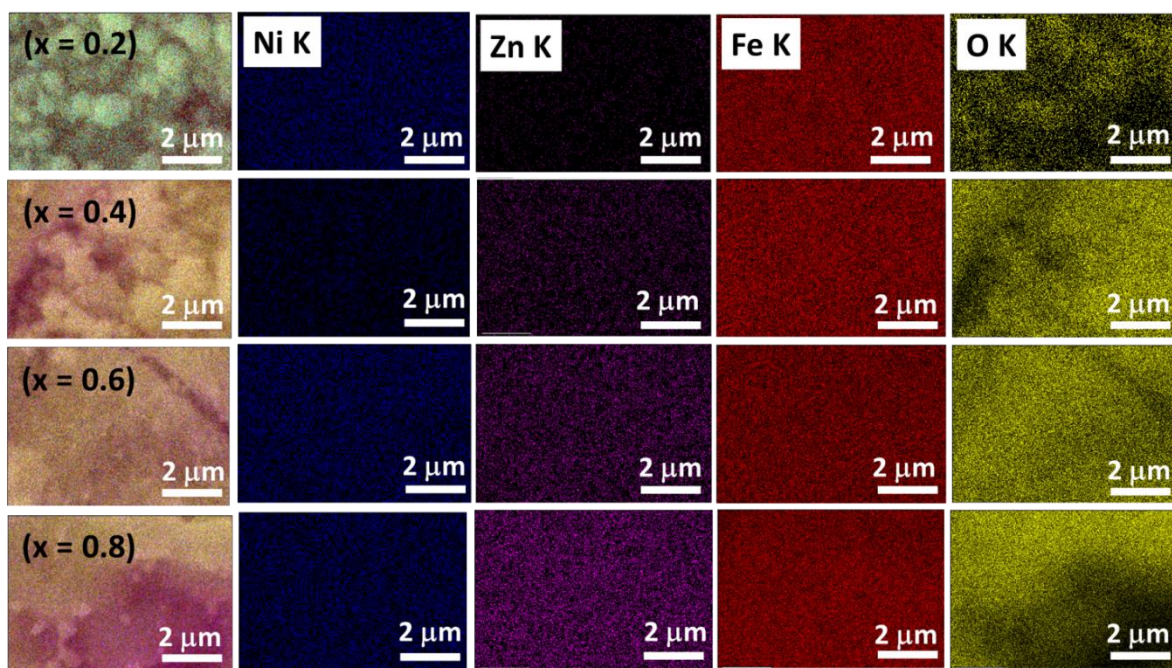


Fig.5.4. EDX elemental mapping of $\text{Ni}_{1-x}\text{Zn}_x\text{Fe}_2\text{O}_4$ ($0.2 \leq x \leq 0.8$) solid solutions showing uniform distribution of elements.

5.5.3 Analysis of microstructure and morphology

The SEM images of the synthesized ferrite solid solutions are shown in Fig.5.5. The images show agglomerated particles in all the prepared compositions. TEM observation was further utilized to study $\text{Ni}_{1-x}\text{Zn}_x\text{Fe}_2\text{O}_4$ ($0 \leq x \leq 1$) nanoparticles in terms of morphology and microstructure. As displayed in Fig. 5.6, a series of crystalline nanocubes, rectangular nanocubes and nanooctahedrons of nickel-zinc ferrites were observed. The size of these nanostructures were estimated to be in the range of 11.56 - 25.61 nm. Typical high-resolution TEM (HRTEM) images of $\text{Ni}_{1-x}\text{Zn}_x\text{Fe}_2\text{O}_4$ samples are shown in Fig. 5.7, from which the lattice fringes with d-spacing of 0.258, 0.294, and 0.482 nm were obtained and are consistent with that of (311), (220), and (111) planes of spinel NiFe_2O_4 and ZnFe_2O_4 . From the HRTEM images, it is further confirmed that the nanoparticles are polycrystalline. Moreover, the selected-area electron diffraction (SAED) patterns of all samples confirmed the polycrystalline nature of nanoparticles due to obvious spoty rings, which can be well indexed to (311), (400), (440), (422) and (511) planes of spinel ferrites (Fig. 5.8).

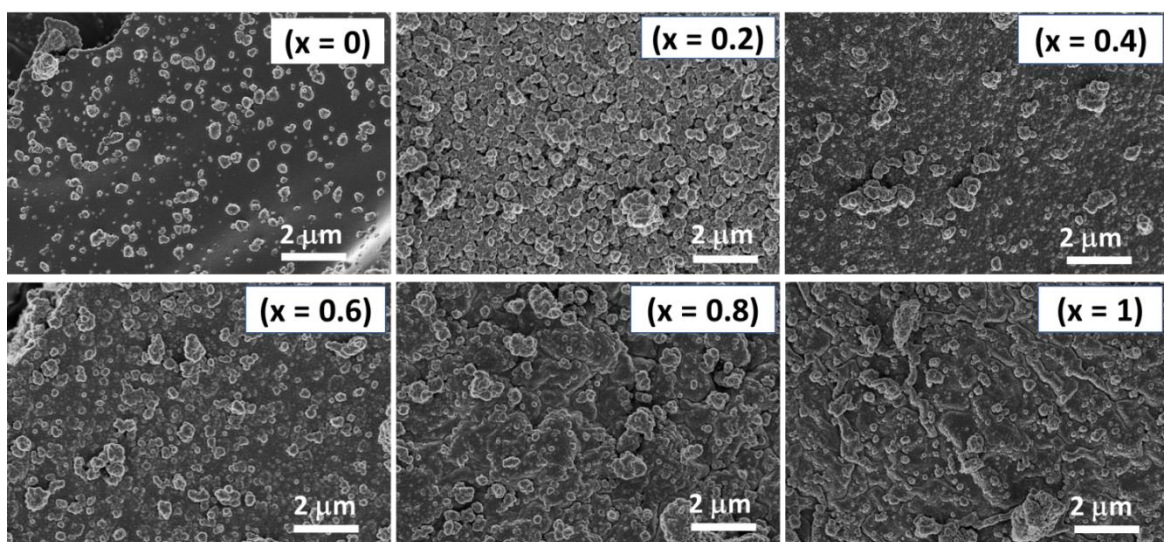


Fig.5.5. SEM images of $\text{Ni}_{1-x}\text{Zn}_x\text{Fe}_2\text{O}_4$ ($0 \leq x \leq 1$) samples.

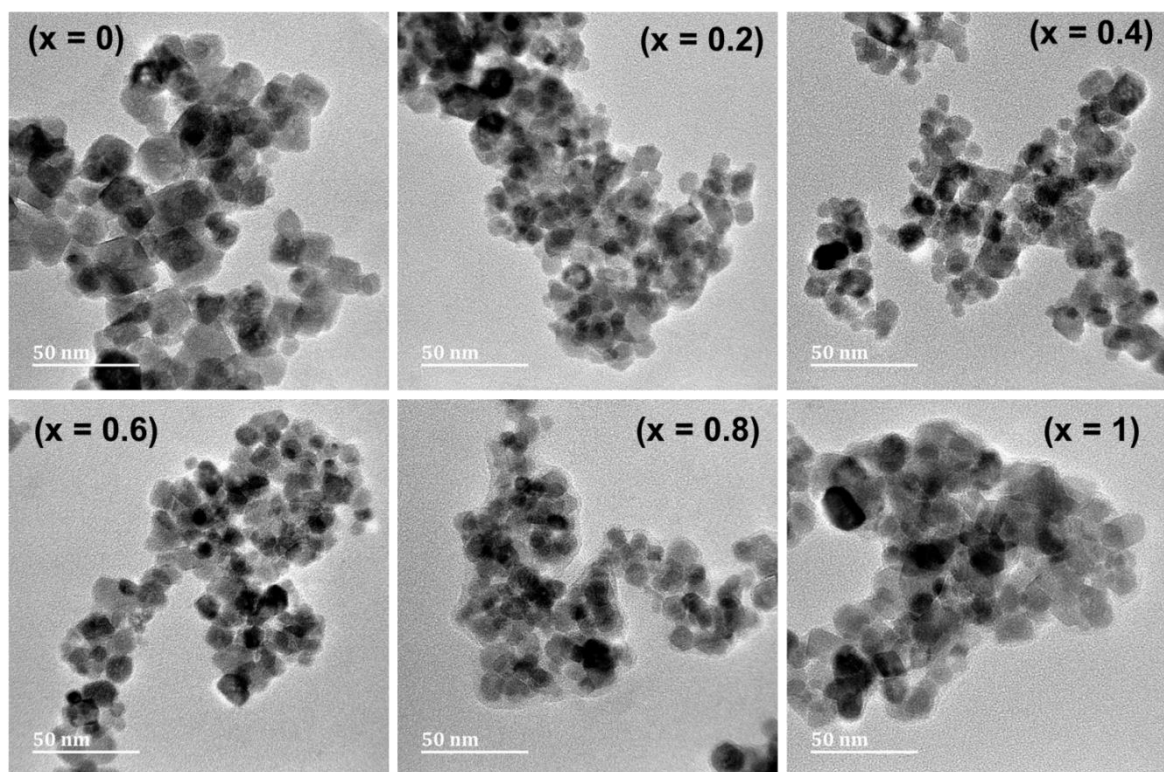


Fig.5.6. TEM images of $\text{Ni}_{1-x}\text{Zn}_x\text{Fe}_2\text{O}_4$ ($0 \leq x \leq 1$) nanoparticles.

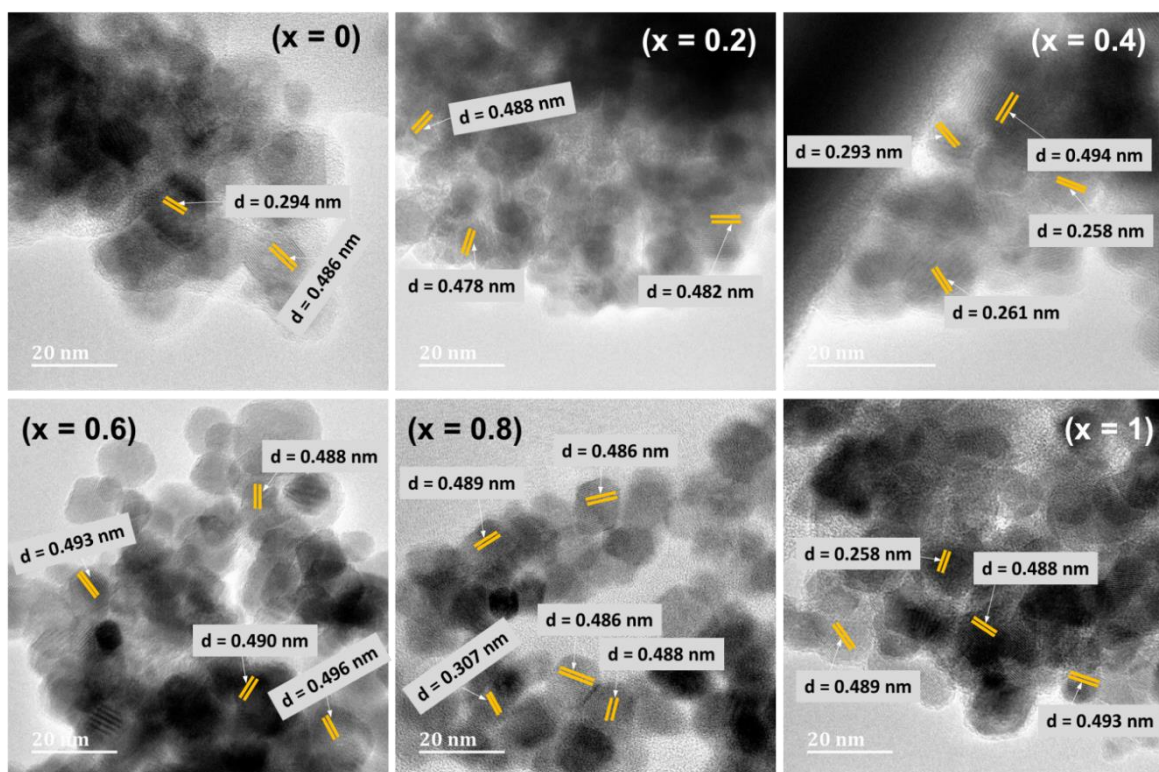


Fig.5.7. HRTEM images of $\text{Ni}_{1-x}\text{Zn}_x\text{Fe}_2\text{O}_4$ ($0 \leq x \leq 1$) nanoparticles.

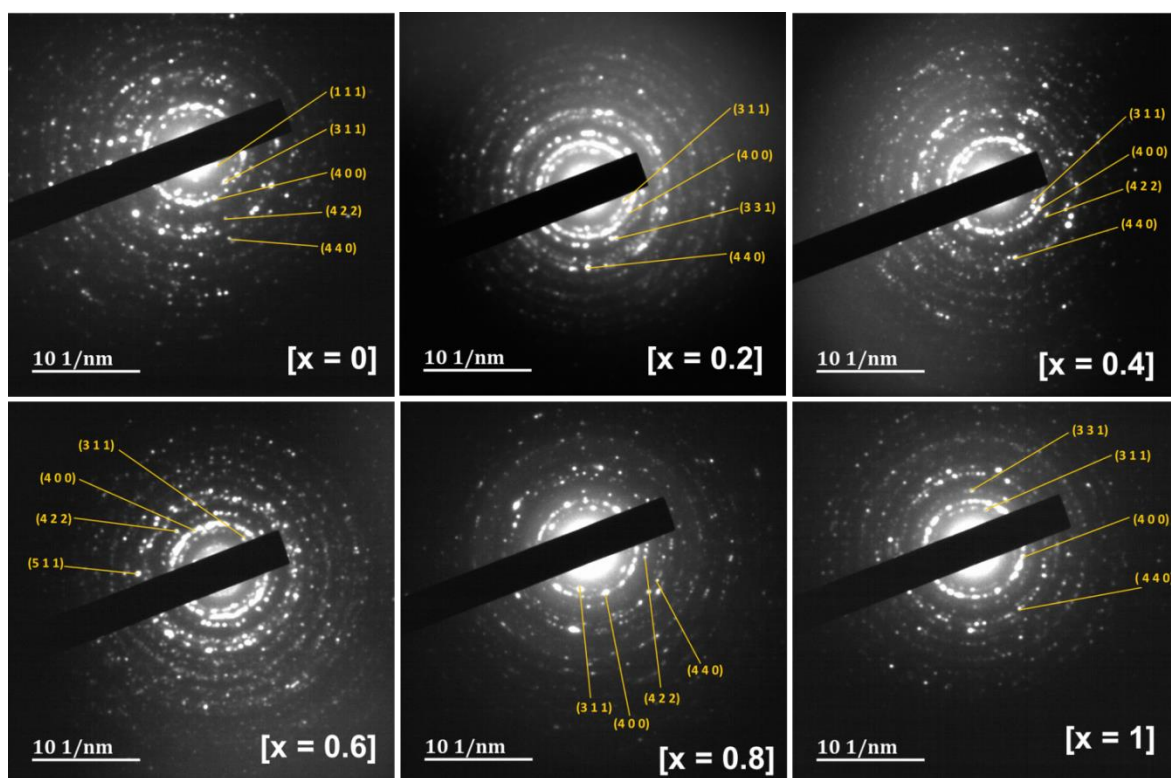


Fig.5.8. SAED images of $\text{Ni}_{1-x}\text{Zn}_x\text{Fe}_2\text{O}_4$ ($0 \leq x \leq 1$) nanoparticles.

5.5.4 Analysis of optical properties

The optical properties of the pristine spinel ferrite systems and the corresponding solid solutions were determined by UV-Vis spectroscopy and the results are displayed in Fig.5.9. Broad absorption was observed within the wavelength range of 300 - 800 nm of the UV-visible absorption spectra of the as-prepared $\text{Ni}_{1-x}\text{Zn}_x\text{Fe}_2\text{O}_4$ ($0 \leq x \leq 1$) systems. The estimated energy band gap for pristine NiFe_2O_4 ($x = 0$) computed via the Tauc plot method was found to be 1.605 eV. This band gap value is roughly comparable to the experimental values reported in the literature.^{41, 42} The optical band gap of pure nanospinel NiFe_2O_4 obtained in this study was significantly red shifted from the bulk value which is around 2.1 eV. With reference to the band gap of pure NiFe_2O_4 nanoparticles, it is noted from Fig.5.10 and Table 5.3 that, the introduction of zinc causes a gradual blue shift in the optical absorption edge for the zinc substituted samples. This is attributed to size miniaturization and change in unit cell volume.⁴³ The change in lattice constants and crystallite size may cause the formation of some of the defects and localized states, thereby inducing changes in the band gap.⁴⁴ In general, the band gap of semiconductor solid solutions is expected to behave linearly with respect to the values of lattice constants. Thus, if the variation in the lattice constants of the solid solutions is in compliance with Vegard's law, then a linear relationship between composition of the solid solutions and band gap can be obtained. Noticeably, the compositional dependence of the direct optical band gap of the synthesized spinel ferrite solid solutions presented in Fig.5.11 shows a linear shift from NiFe_2O_4 ($x = 0$) to ZnFe_2O_4 ($x = 1$). Our results are in close agreement to that reported by Mir *et al.* for Ni substituted NdFeO_3 nanocrystals.⁴³

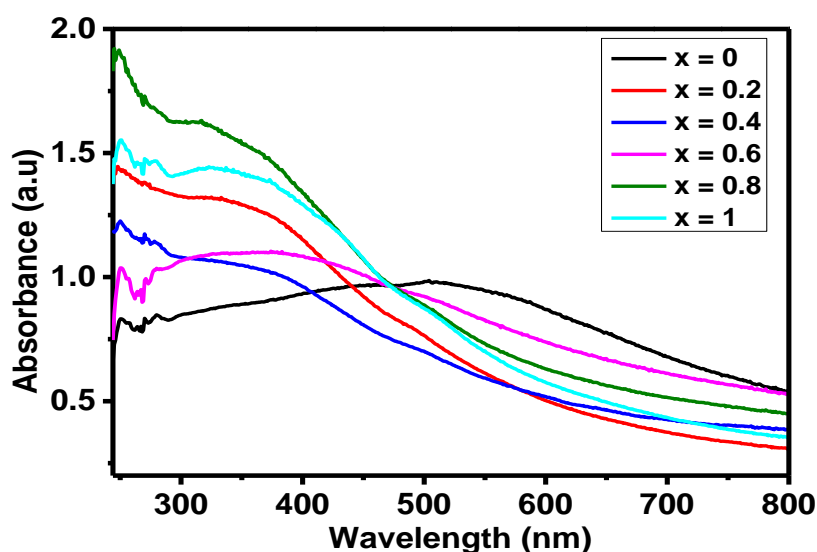


Fig.5.9. UV-Vis of $\text{Ni}_{1-x}\text{Zn}_x\text{Fe}_2\text{O}_4$ ($0 \leq x \leq 1$) nanoparticles at different zinc contents.

Table 5.3. The optical band gaps for $\text{Ni}_{1-x}\text{Zn}_x\text{Fe}_2\text{O}_4$ ($0 \leq x \leq 1$) nanoparticles.

Zinc content (x)	0	0.2	0.4	0.6	0.8	1
E_g (eV)	1.605	1.940	1.879	1.887	1.943	1.976

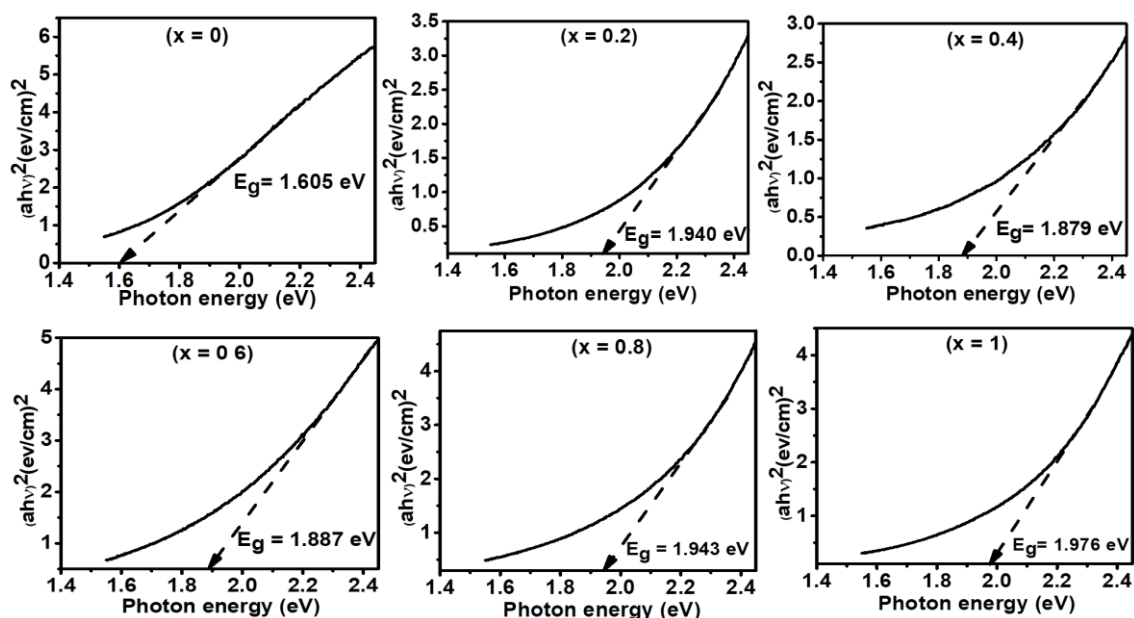


Fig. 5.10. Tauc plot of $\text{Ni}_{1-x}\text{Zn}_x\text{Fe}_2\text{O}_4$ ($0 \leq x \leq 1$) nanoparticles at different zinc content.

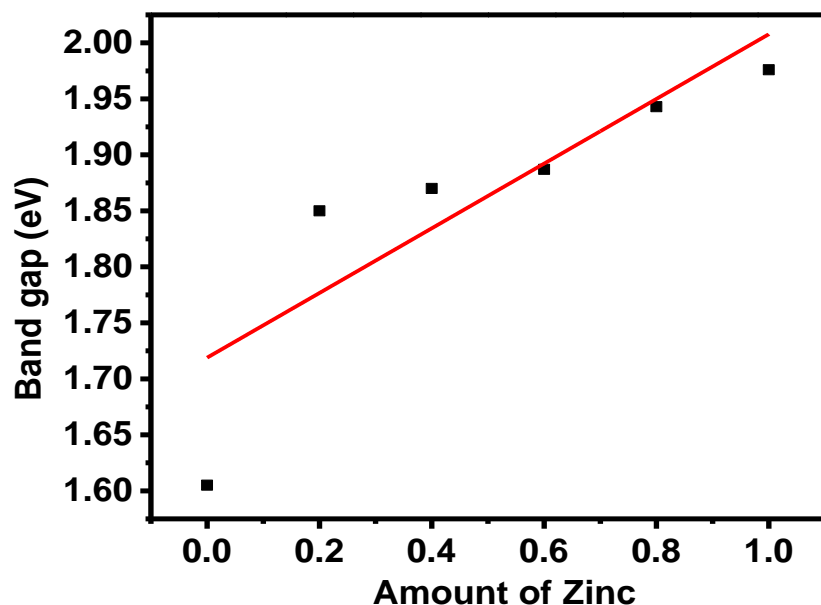


Fig.5.11. Variation of band gap of $\text{Ni}_{1-x}\text{Zn}_x\text{Fe}_2\text{O}_4$ ($0 \leq x \leq 1$) as a function of Zn^{2+} ions concentration.

5.5.5 Evaluation of the potential of $\text{Ni}_{1-x}\text{Zn}_x\text{Fe}_2\text{O}_4$ nanospinels for energy applications

5.5.5.1 Electrochemical water splitting

In order to explore the composition-tunable electrochemical performance of $\text{Ni}_{1-x}\text{Zn}_x\text{Fe}_2\text{O}_4$ ($0 \leq x \leq 1$) nanoparticles towards water splitting, HER and OER activities were examined in alkaline electrolyte. Fig 5.12 (a) shows HER LSV plots of the $\text{Ni}_{1-x}\text{Zn}_x\text{Fe}_2\text{O}_4$ systems performed in 1 M KOH solution. Remarkable catalytic performance was exhibited by $\text{Ni}_{1-x}\text{Zn}_x\text{Fe}_2\text{O}_4$ ($x = 0.8$) which recorded a small overpotential of 87 mV at a current density of 10 mA/cm^2 . This potential is significantly lower compared to that of pure NiFe_2O_4 (213 mV) at the same current density, and convincingly confirms the advantage of metallic Zn doping in NiFe_2O_4 toward HER. The superior HER activity of $\text{Ni}_{1-x}\text{Zn}_x\text{Fe}_2\text{O}_4$ ($x = 0.8$) is related to optimum doping level which could tune Gibbs free energies of hydrogen adsorption.⁴⁵ Similarly, other nanocatalysts displayed high catalytic performance than the pristine NiFe_2O_4 ($x = 0$), registering small overpotentials of 137 mV ($x = 0.2$), 98 mV ($x = 0.4$), 153 mV ($x = 0.6$), and 164 mV ($x = 1$). The corresponding Tafel slopes presented in Fig 5.12(b) obtained for a series of $\text{Ni}_{1-x}\text{Zn}_x\text{Fe}_2\text{O}_4$ ($0 \leq x \leq 1$) nanocatalysts were found in the range of 118-152 mV/dec. The HER catalytic performance demonstrated by $\text{Ni}_{1-x}\text{Zn}_x\text{Fe}_2\text{O}_4$ ($x = 0.8$) nanocatalyst is significantly superior and competitive with many of the previously reported electrocatalysts. For example, the ZnFeNiS/NC electrode synthesized by Jing et al. achieved overpotential of 162.57 mV at 10 mA/cm^2 , which is comparably larger than that of $\text{Ni}_{1-x}\text{Zn}_x\text{Fe}_2\text{O}_4$ ($x = 0.8$) prepared in this study.⁴⁶ The HER catalytic activity observed for nanoscale $\text{Ni}_{1-x}\text{Zn}_x\text{Fe}_2\text{O}_4$ ($x = 0.8$) is also superior to that of Zn-Co-PNNs/3D-NF catalyst (138 mV) prepared by chemical vapour deposition.⁴⁷ Furthermore, the OER performance displayed by $\text{Ni}_{1-x}\text{Zn}_x\text{Fe}_2\text{O}_4$ ($x = 0.8$) is comparable to that of $\text{Fe}_{0.09}\text{Co}_{0.13}\text{-NiSe}_2/\text{CFC}$ (92 mV) synthesized via hydrothermal- method followed by selenization.⁴⁸ Further comparison of HER performance between $\text{Ni}_{1-x}\text{Zn}_x\text{Fe}_2\text{O}_4$ ($x = 0.8$) and other electrocatalysts is shown in Table 5.3.

The catalytic activity of $\text{Ni}_{1-x}\text{Zn}_x\text{Fe}_2\text{O}_4$ ($0 \leq x \leq 1$) nanoparticles towards OER was also examined. The LSV results in Fig 5.12 (c) indicate that $\text{Ni}_{1-x}\text{Zn}_x\text{Fe}_2\text{O}_4$ ($x = 1$) possesses higher OER catalytic performance than $\text{Ni}_{1-x}\text{Zn}_x\text{Fe}_2\text{O}_4$ ($x = 0$) and even superior activity compared to all series of solid solutions investigated. The $\text{Ni}_{1-x}\text{Zn}_x\text{Fe}_2\text{O}_4$ ($x = 1$) nanocatalyst required lower overpotential of 330 mV compared to 349 mV of bare NiFe_2O_4 to deliver the current density of 10 mA/cm^2 . Other catalysts exhibited overpotentials of 389 mV ($x = 0.2$), 416 mV ($x = 0.4$), 387 mV ($x = 0.6$), and 399 mV ($x = 0.8$). The value of overpotential (330

mV) obtained for $\text{Ni}_{1-x}\text{Zn}_x\text{Fe}_2\text{O}_4$ ($x = 1$) in this work shows superior OER performance compared to other previously reported OER catalysts (Table 5.4). Furthermore, to elucidate the reaction kinetics of $\text{Ni}_{1-x}\text{Zn}_x\text{Fe}_2\text{O}_4$ ($0 \leq x \leq 1$) nanocatalysts, a comparison of the Tafel slopes of all electrocatalysts was further established as shown in Fig 5.12 (d). Evidently, after linear fitting of Tafel plots, $\text{Ni}_{1-x}\text{Zn}_x\text{Fe}_2\text{O}_4$ ($x = 1$) catalyst exhibited a Tafel slope of 45 mV/dec, which is observably smaller compared to 52 mV/dec ($x = 0$), 56 mV/dec ($x = 0.2$), 66 mV/dec ($x = 0.4$), and 56 mV/dec ($x = 0.8$). These findings disclose the faster reaction kinetics and good OER performance of the optimized $\text{Ni}_{1-x}\text{Zn}_x\text{Fe}_2\text{O}_4$ ($x = 1$) catalyst.

To get insight into the inherent conductivity of $\text{Ni}_{1-x}\text{Zn}_x\text{Fe}_2\text{O}_4$ ($0 \leq x \leq 1$) nanocatalysts, electrochemical impedance spectroscopy studies were performed. Fig 5.12 (e) presents the Nyquist plot comprising semicircles of different sizes. The diameter of the particular semicircle signifies the resistance to charge transfer produced from the mass transfer process. Apparently, $\text{Ni}_{1-x}\text{Zn}_x\text{Fe}_2\text{O}_4$ ($x = 1$) exhibits the smallest charge transfer resistance, demonstrating a more swift charge transfer during electrochemical water splitting process.

Long-term durability and stability of the $\text{Ni}_{1-x}\text{Zn}_x\text{Fe}_2\text{O}_4$ ($0 \leq x \leq 1$) nanocatalysts for electrochemical water splitting were further examined due to their significant role in practical applications. The long-term durability tests were carried out by chronoamperometry measurements. The CA plot in Fig 5.12(f) shows that all catalysts preserved the electrochemical catalytic activity which is demonstrated by negligible change in current density even after 23 h at a constant voltage of 0.55 V, confirming the good stability of the catalysts. In addition, the catalysts stability was tested by linear sweep voltammetry, and the HER and OER polarization curves in Figs. 5.13 and 5.14, respectively show comparable results between the 1st cycle and the 1,000th cycle. However, a little fluctuation was observed in some graphs which is related to evolution of gas during water splitting. Generally, compared to many other catalysts, the cubic spinel structure of the ferrites described in this work is beneficial for their stability under prolonged electrocatalysis in alkaline solution.

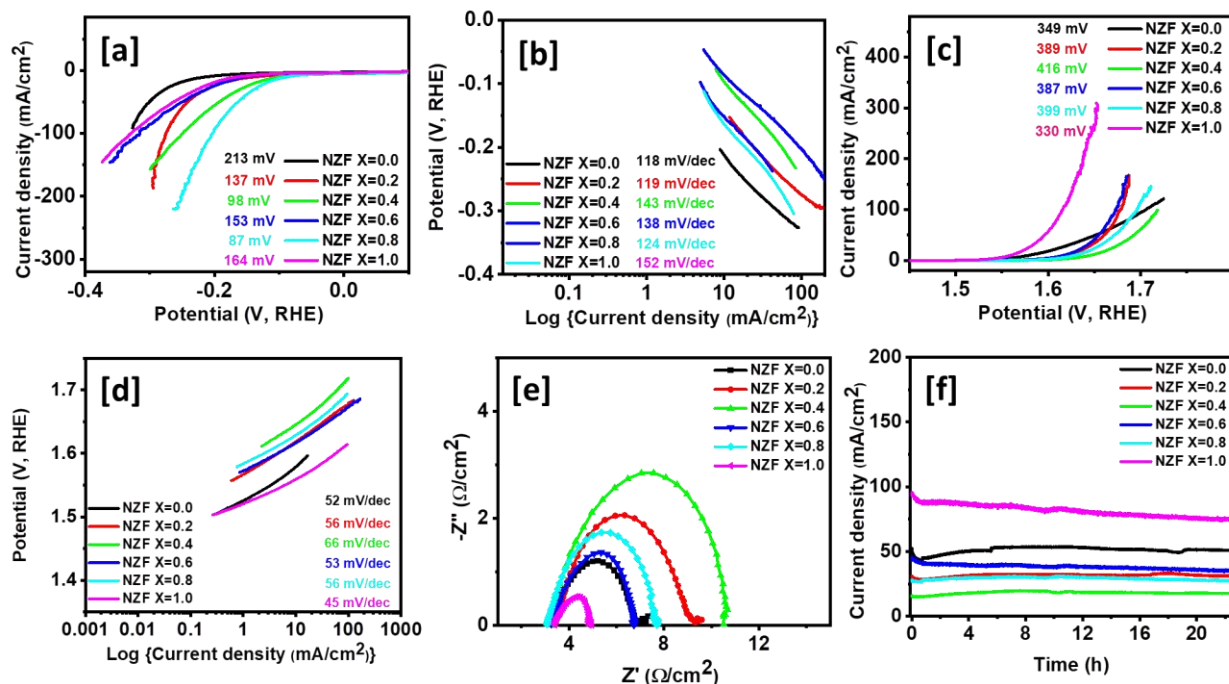


Fig. 5.12. (a) HER polarization curves, (b) HER Tafel slopes, (c) OER polarization curves, (d) OER Tafel slopes, (e) Nyquist plots at 0.5 V, and (f) CA measurement at 0.55 V, for $\text{Ni}_{1-x}\text{Zn}_x\text{Fe}_2\text{O}_4$ ($0 \leq x \leq 1$) electrodes.

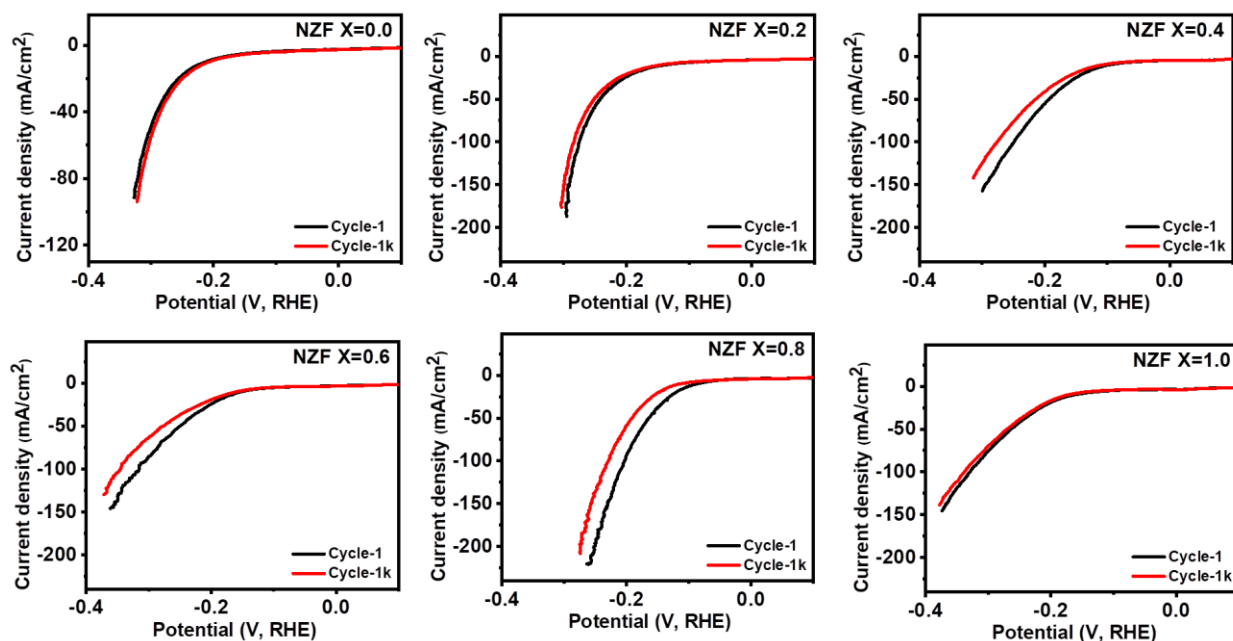


Fig. 5.13. Comparison of HER polarization curve between LSV 1 curve and LSV 1k curve for $\text{Ni}_{1-x}\text{Zn}_x\text{Fe}_2\text{O}_4$ ($0 \leq x \leq 1$) electrodes.

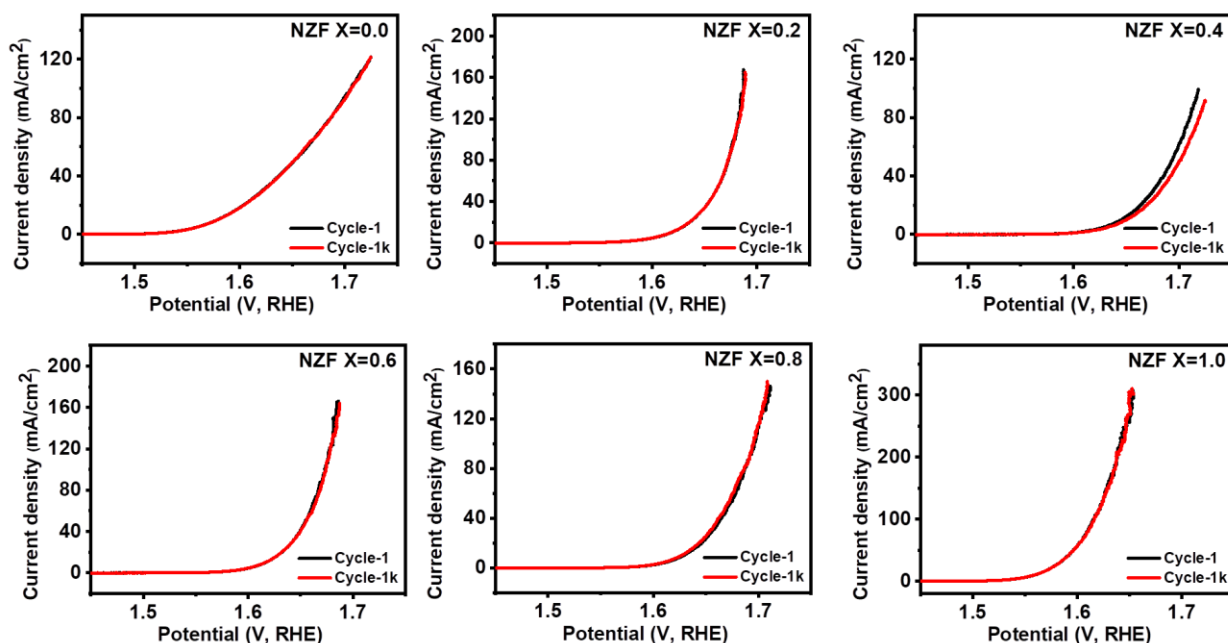


Fig. 5.14. Comparison of OER polarization curve between LSV 1 curve and LSV 1k curve for $\text{Ni}_{1-x}\text{Zn}_x\text{Fe}_2\text{O}_4$ ($0 \leq x \leq 1$) electrodes.

Table 5.3. Comparison of HER performance of $\text{Ni}_{0.2}\text{Zn}_{0.8}\text{Fe}_2\text{O}_4$ with previously reported electrocatalysts in alkaline electrolyte.

Catalyst	1. Preparation method	η_{10} (mV) in 1 M KOH	b (mV/dec)	Reference
ZnFeNiS/NC	Pyrolysis, absorption, and sulfurization	162.57	65.48	46
Zn-Co-P	Hydrothermal and phosphidization	138	81.9	47
$\text{Ni}_{0.7}\text{Fe}_{0.3}\text{S}_2$	Hydrothermal and sulfuration	155	109	49
$\text{MoS}_2\text{-ZnO}$	Chemical exfoliated combined microwave assisted method	239	62	50
(0.5 M H_2SO_4)				
$\text{Ni/Co}_3\text{O}_4$	Hydrothermal, etching and reduction	145	109	51
$\text{Co}_{0.75}\text{Fe}_{0.25}\text{P}$	Nanocasting method	209	55.5	52
$\text{NiFe@Zn}_3\text{V}_3\text{O}_8$	Hydrothermal and calcination	476	85.4	53
$\text{NiFe@V}_2\text{O}_3$	Hydrothermal and calcination	255	51	53
$\text{Ni}_2\text{P/Fe}_2\text{P}$	Hydrothermal and	121	67	54

	phosphidization			
Fe _{0.09} Co _{0.13} -NiSe ₂ /CFC	Hydrothermal-selenization	92	63	48
S-NiFe ₂ O ₄ /NF	Electrodeposition and calcination	138	81	55
NiCo ₂ O ₄	Solvothermal and annealing	110	50	56
NiFe LDH@NiCoP	Hydrothermal-phosphorization-hydrothermal method	120	89	57
Ni_{0.2}Zn_{0.8}Fe₂O₄	Solventless	87	124	This work

Table 5.4. Comparison of OER performance of ZnFe₂O₄ with previously reported electrocatalysts in alkaline electrolyte.

Catalyst	Preparation method	η_{10} (mV) in 1M KOH	b (mV/dec)	Reference
ZnFe ₂ O ₄ @ZnFe ₂ S ₄	Hydrothermal	320	73	58
ZnFe ₂ O ₄	Hydrothermal	379	99	58
Ni ₃ S ₂	Atomic layer deposition	400	51	59
Mn ₂ O ₃ /PdO/ZnO	Biomimetic	422	93	60
Zn-Co-S nanosheets	Hydrothermal, annealing & sulfidization	390	136	61
ZnO/Mn ₃ O ₄	Biomimetic and modified co-precipitation	420	96	62
NiFe ₂ O ₄ /CC	Solvothermal	340	53.3	63
CoFe ₂ O ₄ /CC	Solvothermal	392	64	63
Fe ₃ O ₄ /CC	Solvothermal	432	122.5	63
FeOOH/CC	Solvothermal	483	142.5	63
ZnFe₂O₄	Solventless	330	45	This work

5.5.5.2 Supercapacitance application

The CV and GCD experiments were performed to explore the supercapacitive behaviour of Ni_{1-x}Zn_xFe₂O₄ (0 ≤ x ≤ 1) nanoparticles in a three electrode setup in 3 M KOH

aqueous electrolyte. The CV curves of all electrode composition within the voltage range of 0-0.5 V at a scanning rate of 2-300 mV/s are presented in Fig. 5.15. All electrode materials examined show a pair of approximately symmetrical oxidation and reduction peaks, inferring that favorable reversible redox processes were obvious.⁶⁴ The response current density of the redox peaks is observed to increase as a function of scan rates (2-300 mV/s), which can be explained by the rapid redox processes taking place at the interface between $\text{Ni}_{1-x}\text{Zn}_x\text{Fe}_2\text{O}_4$ electrodes and the electrolyte.⁶⁵ The CV curves of $\text{Ni}_{1-x}\text{Zn}_x\text{Fe}_2\text{O}_4$ ($x = 0.8$) at different scan rates show higher peak current density of the redox reaction compared to other electrodes, demonstrating the enhanced energy storage ability and ion diffusion.⁶⁶ Moreover, the locations of the cathodic and anodic peaks shift toward the negative and positive potentials, correspondingly, due to polarization effect.⁶⁷ Nevertheless, the shapes of the CV curves of all $\text{Ni}_{1-x}\text{Zn}_x\text{Fe}_2\text{O}_4$ electrodes are well retained, signifying the ideal pseudocapacitance characteristics and good rate capability.⁶⁸

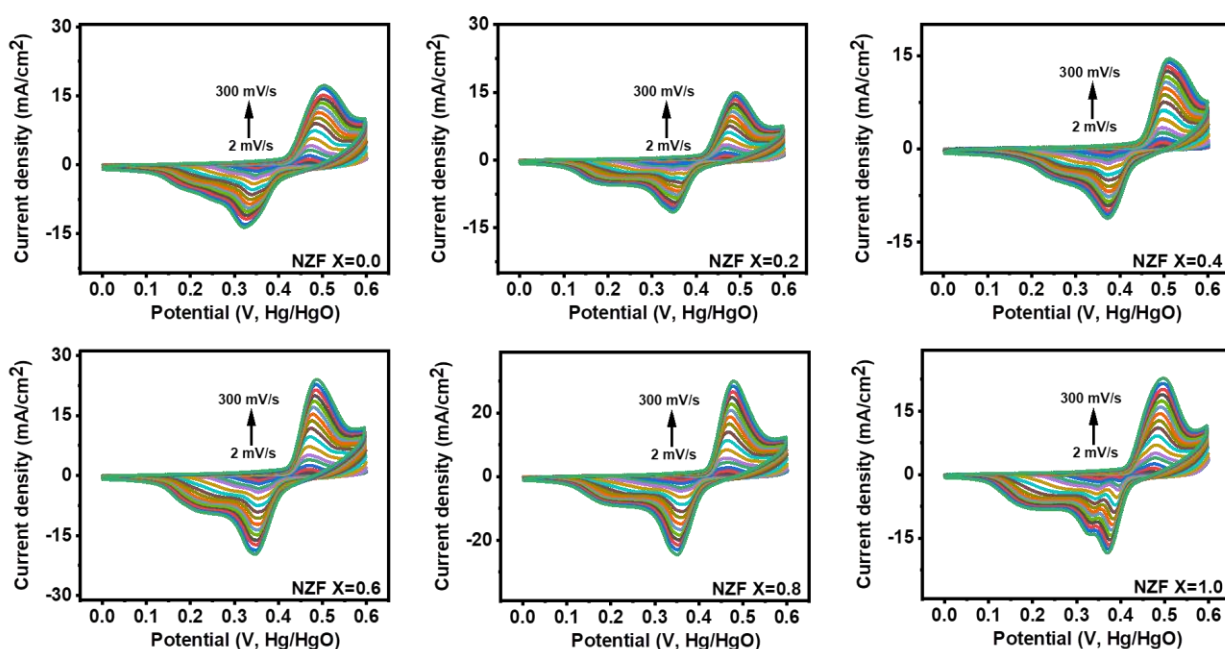


Fig. 5.15. CV curves of $\text{Ni}_{1-x}\text{Zn}_x\text{Fe}_2\text{O}_4$ ($0 \leq x \leq 1$) electrodes at different scanning rates.

Fig. 5.16. displays the GCD curves of $\text{Ni}_{1-x}\text{Zn}_x\text{Fe}_2\text{O}_4$ ($0 \leq x \leq 1$) electrodes performed at various current densities ranging from 1 to 20 A/g. The nonlinear and symmetrical GCD curves with apparent charge-discharge plateaus further confirm the behavior of redox reaction exhibited by the as-prepared nanoparticles. It is expected that, the electrode exhibiting longer discharge time demonstrates higher specific capacitance. Apparently, the discharge time of $\text{Ni}_{1-x}\text{Zn}_x\text{Fe}_2\text{O}_4$ ($x = 0.8$) was much longer compared to other electrodes, representing a higher specific capacitance.

This may be ascribed to synergistic effect brought by multicomponent elements of Ni, Zn and Fe in the spinel system. On the other hand, the variation of specific capacitance with respect to current density for $\text{Ni}_{1-x}\text{Zn}_x\text{Fe}_2\text{O}_4$ ($0 \leq x \leq 1$) electrodes is indicated in Fig.5.17. At the current density of 1 A/g, specific capacitance of 54 F/g was obtained for $\text{Ni}_{1-x}\text{Zn}_x\text{Fe}_2\text{O}_4$ ($x = 0.8$), which is higher compared to those of $x = 0$ (28 F/g), $x = 0.2$ (24 F/g), $x = 0.4$ (21 F/g), $x = 0.6$ (38 F/g), and $x = 1$ (40 F/g).

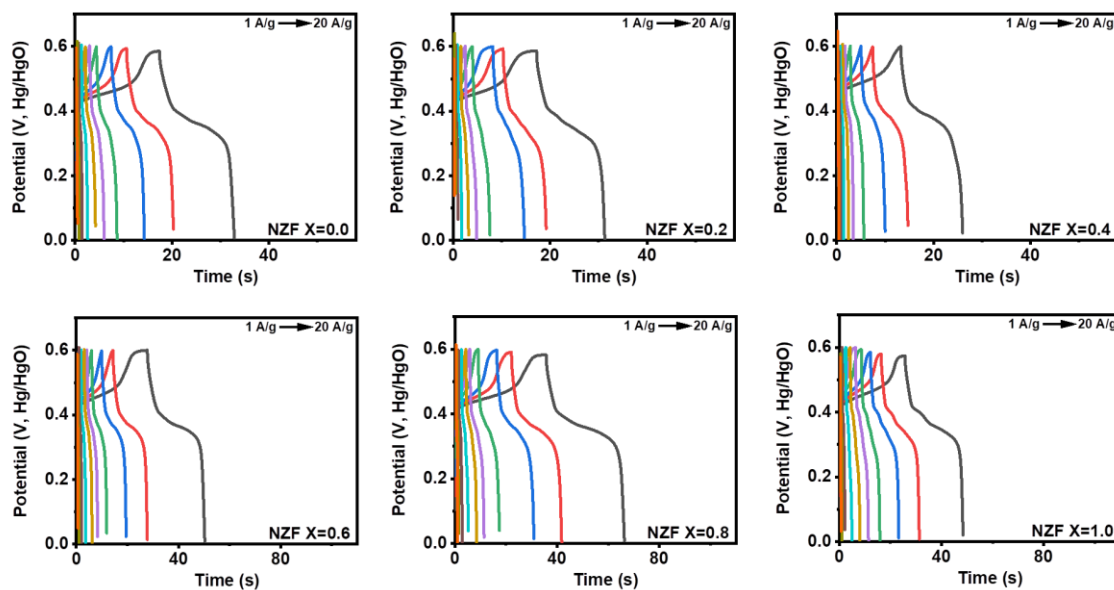


Fig. 5.16. GCD curves $\text{Ni}_{1-x}\text{Zn}_x\text{Fe}_2\text{O}_4$ ($0 \leq x \leq 1$) ($0 \leq x \leq 1$) electrodes at a current densities.

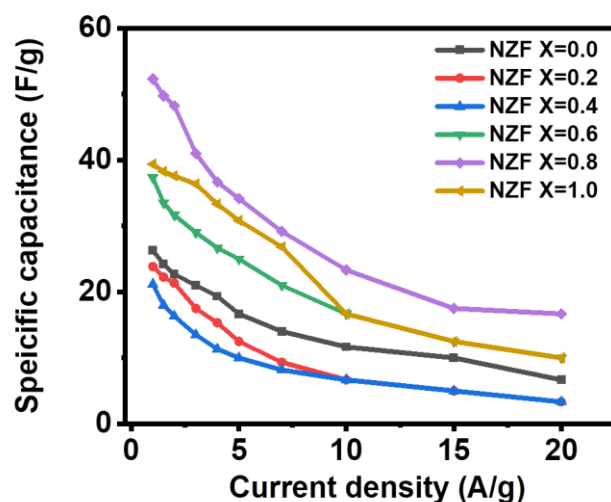


Fig. 5.17. Specific capacity of $\text{Ni}_{1-x}\text{Zn}_x\text{Fe}_2\text{O}_4$ ($0 \leq x \leq 1$) electrodes at different current densities.

5.6 Conclusion

In summary, a series of $\text{Ni}_{1-x}\text{Zn}_x\text{Fe}_2\text{O}_4$ ($0 \leq x \leq 1$) solid solutions with varying amounts of zinc and nickel have been efficaciously fabricated via a solventless pyrolysis method. The p-XRD and EDX analyses confirmed the formation of homogeneous phase-pure $\text{Ni}_{1-x}\text{Zn}_x\text{Fe}_2\text{O}_4$ ($0 \leq x \leq 1$) nanoparticles. In comparison, the incorporation of zinc in the crystal lattices of nickel ferrite endows a larger benefit on HER and OER than on supercapacitance. Specifically, the $\text{Ni}_{1-x}\text{Zn}_x\text{Fe}_2\text{O}_4$ ($x = 0.8$) nanocatalyst displays excellent HER performance with superior activity which is manifested by a small overpotential of 87 mV, whereas $\text{Ni}_{1-x}\text{Zn}_x\text{Fe}_2\text{O}_4$ ($x = 1$) catalyst exhibit superior OER performance with a small overpotential of 330 mV. Additionally, all catalysts were found to be stable after prolonged polarization tests. The excellent catalytic performance may be ascribed to composition versatility and structural stability, both synergistically promoting the electron transfer and modulating the electronic structure. The results of this study have provided a practical approach to fine-tune physicochemical and electrochemical properties of ternary metal oxides, and provided guidance for rational design of multicomponent solid solutions based on composition engineering.

References

1. Xu, R.; Du, L.; Adekoya, D.; Zhang, G.; Zhang, S.; Sun, S.; Lei, Y. *Advanced Energy Materials* **2021**, 11, (15), 2001537.
2. Zhou, M.; Xu, Y.; Lei, Y. *Nano Today* **2018**, 20, 33-57.
3. Cano, Z. P.; Banham, D.; Ye, S.; Hintennach, A.; Lu, J.; Fowler, M.; Chen, Z. *Nature Energy* **2018**, 3, (4), 279-289.
4. Herranz, J.; Durst, J.; Fabbri, E.; Patru, A.; Cheng, X.; Permyakova, A. A.; Schmidt, T. *J. Nano Energy* **2016**, 29, 4-28.
5. Eftekhari, A.; Fang, B. *International Journal of Hydrogen Energy* **2017**, 42, (40), 25143-25165.
6. Manthiram, A.; Murugan, A. V.; Sarkar, A.; Muraliganth, T. *Energy & Environmental Science* **2008**, 1, (6), 621-638.
7. Abdalla, A. M.; Elnaghi, B. E.; Hossain, S.; Dawood, M.; Abdelrehim, O.; Azad, A. K. *Advanced Energy Conversion Materials* **2020**, 30-54.
8. Manthiram, A. *Nature Communications* **2020**, 11, (1), 1-9.
9. Yuan, C.; Wu, H. B.; Xie, Y.; Lou, X. W. *Angewandte Chemie International Edition* **2014**, 53, (6), 1488-1504.
10. Maitra, S.; Mitra, R.; Nath, T. *Current Applied Physics* **2021**.
11. Liu, G.; Wang, K.; Gao, X.; He, D.; Li, J. *Electrochimica Acta* **2016**, 211, 871-878.
12. Guo, P.; Li, Z.; Liu, S.; Xue, J.; Wu, G.; Li, H.; Zhao, X. *Journal of Materials Science* **2017**, 52, (9), 5359-5365.
13. Zhang, C.; Bhoyate, S.; Zhao, C.; Kahol, P. K.; Kostoglou, N.; Mitterer, C.; Hinder, S. J.; Baker, M. A.; Constantinides, G.; Polychronopoulou, K. *Catalysts* **2019**, 9, (2), 176.
14. Maksoud, M. A.; Fahim, R. A.; Shalan, A. E.; Abd Elkodous, M.; Olojede, S.; Osman, A. I.; Farrell, C.; Ala'a, H.; Awed, A.; Ashour, A. *Environmental Chemistry Letters* **2020**, 1-65.
15. Bhujun, B.; Tan, M. T.; Shanmugam, A. S. *Results in Physics* **2017**, 7, 345-353.
16. Wang, Z.; Zhang, X.; Liu, X.; Zhang, W.; Zhang, Y.; Li, Y.; Qin, C.; Zhao, W.; Bakenov, Z. *Chemical Engineering Journal* **2020**, 388, 124207.
17. Bandgar, S. B.; Vadiyar, M. M.; Jambhale, C. L.; Kim, J.-H.; Kolekar, S. S. *Journal of Alloys and Compounds* **2021**, 853, 157129.
18. Ren, P.; Wang, Z.; Liu, B.; Lu, Y.; Jin, Z.; Zhang, L.; Li, L.; Li, X.; Wang, C. *Journal of Alloys and Compounds* **2020**, 812, 152014.

19. Doiphode, V.; Vairale, P.; Sharma, V.; Waghmare, A.; Punde, A.; Shinde, P.; Shah, S.; Pandharkar, S.; Hase, Y.; Aher, R. *Journal of Solid State Electrochemistry* **2021**, 1-12.
20. Zhang, Z.; Yan, X.; Liu, J.; Liu, B.; Gu, Z.-G. *Sustainable Energy & Fuels* **2021**.
21. Simon, C.; Timm, J.; Tetzlaff, D.; Jungmann, J.; Apfel, U.-P.; Marschall, R. *ChemElectroChem* **2021**, 8, (1), 227-239.
22. Sun, M.; Chen, Y.; Tian, G.; Wu, A.; Yan, H.; Fu, H. *Electrochimica Acta* **2016**, 190, 186-192.
23. Li, L.; Zhang, Y.; Li, J.; Huo, W.; Li, B.; Bai, J.; Cheng, Y.; Tang, H.; Li, X. *Inorganic Chemistry Frontiers* **2019**, 6, (2), 511-520.
24. Joshi, B.; Samuel, E.; Park, C.; Kim, Y.; Lee, H.-S.; Yoon, S. S. *Applied Surface Science* **2021**, 149951.
25. Dalai, N.; Mohanty, B.; Mitra, A.; Jena, B. *ChemistrySelect* **2019**, 4, (27), 7791-7796.
26. Askari, M. B.; Salarizadeh, P. *International Journal of Hydrogen Energy* **2020**, 45, (51), 27482-27491.
27. Yu, X.; Chen, G.; Wang, Y.; Liu, J.; Pei, K.; Zhao, Y.; You, W.; Wang, L.; Zhang, J.; Xing, L. *Nano Research* **2020**, 13, (2), 437-446.
28. Yang, S.; Han, Z.; Sun, J.; Yang, X.; Li, C.; Wang, R.; Cao, B. *Electrochemistry Communications* **2018**, 92, 19-23.
29. Sathiyamurthy, K.; Sivagurunathan, P. *International Journal Of Advanced Science and Research* **2017**, 2 (6), 33-41.
30. Wongpratrat, U.; Tipsawat, P.; Khajonrit, J.; Swatsitang, E.; Maensiri, S. *Journal of Alloys and Compounds* **2020**, 831, 154718.
31. Brabers, V. *Handbook of Magnetic Materials* **1995**, 8, 189-324.
32. Rath, C.; Anand, S.; Das, R.; Sahu, K.; Kulkarni, S.; Date, S.; Mishra, N. *Journal of Applied Physics* **2002**, 91, (4), 2211-2215.
33. Smit, J.; Wijn, H. *Eindhoven, The Netherlands* **1959**, 278.
34. Patange, S. M.; Shirsath, S. E.; Jadhav, S. S.; Jadhav, K. M. *Physica Status Solidi (a)* **2012**, 209, (2), 347-352.
35. Monshi, A.; Foroughi, M. R.; Monshi, M. R. *World Journal of Nano Science and Engineering* **2012**, 2, (3), 154-160.
36. Barkatt, A., *Magnetic Ceramics By Raul Valenzuela* (National University of Mexico). Cambridge University Press: Cambridge, UK 1994. xix+ 312 pp. \$79.95. ISBN 0-521-36485-X. ACS Publications: 1996.

37. Rath, C.; Sahu, K.; Anand, S.; Date, S.; Mishra, N.; Das, R. *Journal of Magnetism and Magnetic Materials* **1999**, 202, (1), 77-84.
38. Upadhyay, C.; Verma, H.; Anand, S. *Journal of Applied Physics* **2004**, 95, (10), 5746-5751.
39. Sharifi, I.; Shokrollahi, H. *J. Magn. Magn. Mater.* **2012**, 2012, 324.
40. Kurmude, D.; Barkule, R.; Raut, A.; Shengule, D.; Jadhav, K. *Journal of Superconductivity and Novel Magnetism* **2014**, 27, (2), 547-553.
41. Domínguez-Arvizu, J.; Jiménez-Miramontes, J.; Salinas-Gutiérrez, J.; Meléndez-Zaragoza, M.; López-Ortiz, A.; Collins-Martínez, V. *International Journal of Hydrogen Energy* **2017**, 42, (51), 30242-30248.
42. Rekhila, G.; Bessekhoud, Y.; Trari, M. *International Journal of Hydrogen Energy* **2013**, 38, (15), 6335-6343.
43. Mir, S. A.; Ikram, M.; Asokan, K. *Optik* **2014**, 125, (23), 6903-6908.
44. Nawle, A. C.; Humbe, A. V.; Babrekar, M.; Deshmukh, S.; Jadhav, K. *Journal of Alloys and Compounds* **2017**, 695, 1573-1582.
45. Liu, H.; He, Q.; Jiang, H.; Lin, Y.; Zhang, Y.; Habib, M.; Chen, S.; Song, L. *ACS Nano* **2017**, 11, (11), 11574-11583.
46. Jing, Y.; Yang, Y.; Yin, H.; Yang, J.; Yang, Y.; Yan, M.; Zhang, Q.; Luo, D.; Zeng, Q.; Li, B. *Journal of Electroanalytical Chemistry* **2020**, 879, 114804.
47. Nguyen, C.; Pham, T.; Vu, T.; Mai, V.; Vu-Huynh, K. *Journal of Electroanalytical Chemistry* **2020**, 858, 113803.
48. Sun, Y.; Xu, K.; Wei, Z.; Li, H.; Zhang, T.; Li, X.; Cai, W.; Ma, J.; Fan, H. J.; Li, Y. *Advanced Materials* **2018**, 30, (35), 1802121.
49. Yu, J.; Cheng, G.; Luo, W. *Journal of Materials Chemistry A* **2017**, 5, (30), 15838-15844.
50. Sumesh, C. *International Journal of Hydrogen Energy* **2020**, 45, (1), 619-628.
51. Riaz, M. S.; Zhao, S.; Dong, C.; Iqbal, M. J.; Zhao, Y.; Huang, F. *Energy Technology* **2020**, 8, (5), 1901310.
52. Huang, Y.; Li, M.; Yang, W.; Yu, Y.; Hao, S. *Science China Materials* **2020**, 63, (2), 240-248.
53. Xu, H.; Liu, L.; Gao, J.; Du, P.; Fang, G.; Qiu, H.-J. *ACS Applied Materials & Interfaces* **2019**, 11, (42), 38746-38753.
54. Ge, Y.; Dong, P.; Craig, S. R.; Ajayan, P. M.; Ye, M.; Shen, J. *Advanced Energy Materials* **2018**, 8, (21), 1800484.

55. Liu, J.; Zhu, D.; Ling, T.; Vasileff, A.; Qiao, S.-Z. *Nano Energy* **2017**, 40, 264-273.
56. Gao, X.; Zhang, H.; Li, Q.; Yu, X.; Hong, Z.; Zhang, X.; Liang, C.; Lin, Z. *Angewandte Chemie International Edition* **2016**, 55, (21), 6290-6294.
57. Zhang, H.; Li, X.; Hähnel, A.; Naumann, V.; Lin, C.; Azimi, S.; Schweizer, S. L.; Maijenburg, A. W.; Wehrspohn, R. B. *Advanced Functional Materials* **2018**, 28, (14), 1706847.
58. Valenzuela, M.; Bosch, P.; Jiménez-Becerrill, J.; Quiroz, O.; Páez, A. *Journal of Photochemistry and Photobiology A: Chemistry* **2002**, 148, (1-3), 177-182.
59. Ho, T. A.; Bae, C.; Nam, H.; Kim, E.; Lee, S. Y.; Park, J. H.; Shin, H. *ACS Applied Materials & Interfaces* **2018**, 10, (15), 12807-12815.
60. Zahra, T.; Ahmad, K. S. *International Journal of Energy Research* **2021**.
61. Wu, X.; Han, X.; Ma, X.; Zhang, W.; Deng, Y.; Zhong, C.; Hu, W. *ACS Applied Materials & Interfaces* **2017**, 9, (14), 12574-12583.
62. Zahra, T.; Ahmad, K. S.; Thomas, A. G.; Zequine, C.; Malik, M. A.; Gupta, R. K. *RSC Advances* **2020**, 10, (17), 9854-9867.
63. Yuan, F.; Cheng, X.; Wang, M.; Ni, Y. *Electrochimica Acta* **2019**, 324, 134883.
64. Wu, C.; Cai, J.; Zhang, Q.; Zhou, X.; Zhu, Y.; Shen, P. K.; Zhang, K. *ACS Applied Materials & Interfaces* **2015**, 7, (48), 26512-26521.
65. Yang, Y.; Zhou, Y.; Hu, Z.; Wang, W.; Zhang, X.; Qiang, L.; Wang, Q. *Journal of Alloys and Compounds* **2019**, 772, 683-692.
66. Wu, X.; Xu, Y.; Hu, Y.; Wu, G.; Cheng, H.; Yu, Q.; Zhang, K.; Chen, W.; Chen, S. *Nature Communications* **2018**, 9, (1), 1-11.
67. Liang, M.; Zhao, M.; Wang, H.; Shen, J.; Song, X. *Journal of Materials Chemistry A* **2018**, 6, (6), 2482-2493.
68. He, W.; Wang, C.; Li, H.; Deng, X.; Xu, X.; Zhai, T. *Advanced Energy Materials* **2017**, 7, (21), 1700983.

CHAPTER 6

Facile solventless synthesis and physicochemical properties of nanostructured $\text{Co}_{1-x}\text{Mg}_x\text{Fe}_2\text{O}_4$ ($0 \leq x \leq 1$) solid solutions

6.1 Introduction

Nano-engineered semiconductors are the foundation of myriad technologies including communications, electronics, sensing, and optoelectronics.¹ Since the majority of their properties and applications are closely related to the band gap energy, recent work has focussed on the preparation of nanoscale semiconductor materials with tunable band gaps.^{2, 3} Band gap engineering in semiconductors can be realized via different approaches including the formation of heterostructures or core/shells,^{4, 5} superlattices,⁶ size tuning, strain,⁷ and composition modulation by alloying or doping.⁸ Such modification of band structure have led to profoundly distinct properties that are surprisingly different from those of the bulk counterparts and have resulted into numerous applications. However, it remains challenging to tailor the band gap of semiconductors through size tuning, especially for multicomponent semiconductor nanomaterials. This is so because the tuning of the band gap by manipulation of particle size could lead to instability of the very small nanoparticles in some practical applications. Another challenge is the disappearance of the quantum confinement effect in thin films and polycrystalline materials.^{9, 10} Moreover, it is equally challenging to obtain monodispersity in core-shells and other heterostructured systems due to the multistep synthesis protocols involved. Their synthesis requires growth of the shell with proper thickness which in turn increases the overall size of the nanocrystals.^{11, 12}

Unlike the case of size and shape manipulation, composition engineering offers another opportunity to tailor the materials' properties. This can be achieved through the formation of a solid solution, doping or alloying of foreign elements/compound into the host lattices. This process changes the arrangement of cations between the available tetrahedral and octahedral voids in the crystallographic unit cell structures.^{13, 14} Consequently, substantial changes in lattice parameters, energy band gap, electrical transport, and luminescence properties of the host material are realized.¹⁵⁻¹⁷ The formation of solid solutions allows the dopant to randomly inhabit the position of the anions or cations in the host material. This permits more control and flexibility on tailoring of the overall properties of the nanocrystals, and the alloyed nanostructures may not only acquire the properties of their pristine materials but also display new distinct properties.² To date, a great deal of solid solutions with tunable composition have been reportedly prepared,¹⁸⁻²¹ and they have demonstrated fascinating properties that are not found in the simpler parent systems.

MgFe₂O₄ and CoFe₂O₄ are ternary metal oxides which have attracted a huge research interest. They both exhibit a cubic spinel structure in which the cations are distributed between the tetrahedral and octahedral positions. These spinel ferrite systems have

demonstrated excellent performance in various technologically relevant applications including catalysis,^{22, 23} biomedical,^{24, 25} energy storage,²⁶⁻²⁸ gas sensing,^{29, 30} and energy generation,³¹⁻³³ applications. Their outstanding performance is considered to be a result of their structural and chemical versatility. To further improve their physicochemical properties for a wide range of applications, the focus of current research is to prepare composition-tunable multicomponent solid solutions. Interestingly, the two spinel ferrites are isovalent, exhibit the same cubic structure, and the corresponding divalent cations have comparable ionic size (Co^{2+} , 0.88 Å, Mg^{2+} 0.86 Å). This structural and chemical similarity infers that a solid solution is viable across the entire composition range between the two ternary systems. For example, using modified sol-gel combustion method, nonmagnetic Mg was partially substituted in CoFe_2O_4 to yield $\text{Co}_{1-x}\text{Mg}_x\text{Fe}_2\text{O}_4$ ($0 \leq x \leq 0.75$) nanoparticles exhibiting structural, electrical and magnetic properties distinct from the host ferrite material.³⁴ In another study Wongpratrat *et al.* employed hydrothermal route to afford $\text{Co}_{1-x}\text{Mg}_x\text{Fe}_2\text{O}_4$ ($0 \leq x \leq 1$) exhibiting composition dependent particle size and magnetic properties.³⁵ Another set of cubic $\text{Co}_{1-x}\text{Mg}_x\text{Fe}_2\text{O}_4$ nanoparticles was reportedly prepared via coprecipitation method.³⁶

With the advent of nanoscience and nanotechnology, it has been established that the overall chemical and physical properties of nanostructured semiconductors depend hugely on the synthesis method.³⁷ Consequently, there has been great developments of reliable and reproducible methods for producing solid solution nanostructures over the past years, with wet-chemical synthesis dominating the field.^{38, 39} While the synthesis of nanomaterials via wet-chemical routes is achieved in the presence of capping ligands, studies have indicated that these ligands may, in certain cases, act as impurities on the nanoparticles' surface, block the active sites and weaken its ultimate application.⁴⁰ Additionally, the method suffers from poor yield and proceeds with the use of expensive solvents. The synthesis of nanomaterials in the absence of capping agents and a solvent-free environment is therefore crucial for their enhanced property and overall performance in numerous applications. As a step towards green chemistry protocols, the preparation of nanomaterials via solvent-free thermolysis of organometallic precursors has recently been proven as economical, simple, eco-friendly and highly efficient.^{41, 42} Unlike most solution-based approaches, the method is self-capping, with better control over the size and shape of the resultant particles. The approach thus offers the opportunity of producing nanomaterials without the use of passivating ligands. In this chapter, phase pure $\text{Co}_{1-x}\text{Mg}_x\text{Fe}_2\text{O}_4$ ($0 \leq x \leq 1$) solid solution nanoparticles were synthesized via the solventless, surfactant free pyrolysis of metal acetylacetonate precursors. The solid solution was generated by varying the stoichiometric composition of Co and Mg in the

mixture. Investigations were also performed to ascertain the influence of substituent composition on the physicochemical properties of the resulting solid solution nanocrystals.

6.2 Experimental

6.2.1 Chemicals

Cobalt (II) acetylacetonates (98%, Merck-Schuchardt), magnesium (II) acetylacetonates (98%, Merck-Schuchardt), and iron (III) acetylacetonate (97%, Sigma-Aldrich). All metal complexes were used as received without further purification.

6.2.2 Solventless synthesis of $\text{Co}_{1-x}\text{Mg}_x\text{Fe}_2\text{O}_4$ ($0 \leq x \leq 1$) solid solutions

The synthesis of spinel $\text{Co}_{1-x}\text{Mg}_x\text{Fe}_2\text{O}_4$ nanoparticles of different stoichiometric amount was performed via solventless thermolysis of metal acetylacetonates. For the preparation of pristine CoFe_2O_4 nanoparticles, 0.10 g (0.28 mmol) of cobalt acetylacetonate and 0.198 g (0.56 mmol) of iron acetylacetonate were mixed and ground using pestle and mortar for ≈ 20 minutes to obtain a uniform mixture. The precursor mixture was then placed into a ceramic boat, which was placed in a reactor tube. The reactor tube was then introduced inside the carbolite tube furnace in such a way that the ceramic boat must be placed almost in the middle of the heating zone, followed by thermal treatment at 450 °C, at a heating rate of 20 °C per minute for 1 h. After 1 h of annealing, the heating was switched off, and the furnace was left to cool naturally to ambient temperature. The reactor tube was removed from the furnace upon cooling, and the product was collected for analysis without any post-treatment. Similarly, MgFe_2O_4 nanoparticles was synthesized by employing similar procedures except that magnesium acetylacetonate was used instead of cobalt acetylacetonate and the amount of magnesium and iron complexes were maintained in the same ratio of 1:2.

For the synthesis of quaternary $\text{Co}_{1-x}\text{Mg}_x\text{Fe}_2\text{O}_4$ ($x = 0.2, 0.4, 0.6, 0.8$) solid solutions, a known quantity of cobalt acetylacetonate was partially substituted by appropriate amounts of magnesium acetylacetonate by adjusting the mole ratios of Mg and Co in the intervals of 0.2, 0.4, 0.6, and 0.8, while keeping the amount of iron acetylacetonate unchanged in the reaction mixture. The reaction procedures for the entire series of solid solutions were kept similar to those employed to synthesize the ternary cobalt and magnesium ferrites.

6.3 Instrumentation

6.3.1 Powder X-ray diffraction (p-XRD) analysis

The phase of the synthesized spinel $\text{Co}_{1-x}\text{Mg}_x\text{Fe}_2\text{O}_4$ ($0 \leq x \leq 1$) solid solutions was elucidated by powder X-ray diffraction (p-XRD) analysis employing a Bruker AXS D8 Advance X-ray diffractometer. Measurements were carried out in the values of 2θ ranging from 10 to 80° and the data obtained were used to compute the structural parameters such as cell volume, lattice constants and crystallite size.

6.3.2 Scanning electron microscopy (SEM) and Energy dispersive X-ray (EDX) analyses

Characterization of surface characteristics and elemental composition of the nanoparticles was performed by a Zeiss Ultra Plus FEG Scanning Electron Microscope (SEM) equipped with an Oxford detector EDX at 20 kV using Aztec software for elemental analysis. The EDX analysis was performed on nanoparticles on carbon tape.

6.3.3 Transmission electron microscopy (TEM) and High resolution TEM (HRTEM) analyses

The TEM and HRTEM imaging techniques were collectively used to determine the morphological features of the as-prepared $\text{Co}_{1-x}\text{Mg}_x\text{Fe}_2\text{O}_4$ ($0 \leq x \leq 1$) solid solutions. Imaging was performed on a JEOL 1400 TEM and JEOL 2100 HRTEM, at accelerating voltages of 120 kV and 200 kV, respectively.

6.3.4 UV-visible spectroscopy

Measurement of optical absorbance was performed in the UV-Vis spectral range on a Varian Cary 50 UV/Vis spectrophotometer.

6.4 Results and discussion

6.4.1 Phase and structure analysis

The powder X-ray diffraction pattern of the as-prepared $\text{Co}_{1-x}\text{Mg}_x\text{Fe}_2\text{O}_4$ solid solutions with different Mg content (x) ranging from 0 to 1 are shown in Fig. 6.1(a). The XRD patterns of the pristine samples with $x = 0$ showed the presence of CoFe_2O_4 phase (ICDD #. 00-022-1086) while that with $x = 1$ indicated the formation of MgFe_2O_4 phase (ICDD #.01-089-3084). Both samples were observed to exhibit a cubic spinel ferrite structure. The diffraction

patterns of the solid solutions with different magnesium contents $x = 0.2$ to 0.8 retained cubic spinel structures, which were similar to the parent spinel CoFe_2O_4 . No impurity elements were detected in all compositions. Fig 6.1 (b) shows that the lattice constants of the spinel $\text{Co}_{1-x}\text{Mg}_x\text{Fe}_2\text{O}_4$ solid solution nanoparticles varied monotonically with Mg doping due to the comparable atomic sizes of Co and Mg. The observed monotonic increase of the lattice parameters as a function of Mg content is in agreement with Vegard's law. The consequent increase in the lattice parameters causes the expansion of the unit cell, leading to an increase in cell volume (Fig 6.1 (b)). The average crystallite size of all samples was estimated from the p-XRD diffraction data by using Scherrer's formula and was found in the range of 9.68 to 14.19 nm. It can be observed that, replacement of Co^{2+} by different amounts of Mg^{2+} results to an increase in crystallite size.

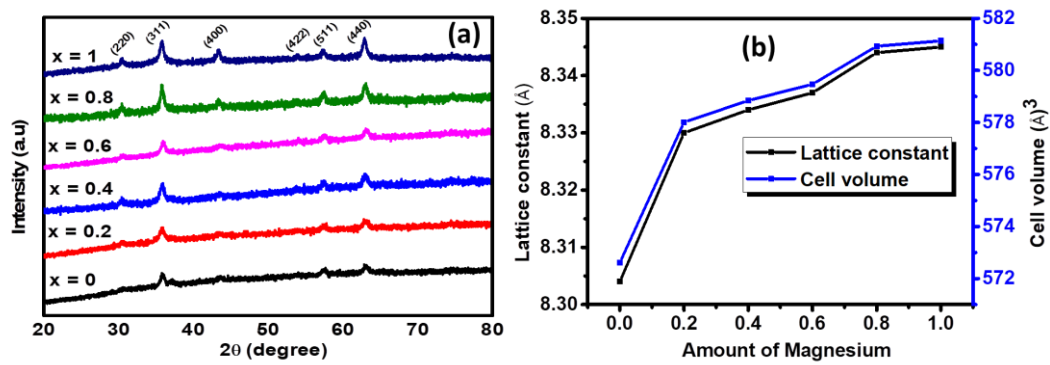


Fig. 6.1. (a) p-XRD diffractograms of $\text{Co}_{1-x}\text{Mg}_x\text{Fe}_2\text{O}_4$ ($0 \leq x \leq 1$), (b) variation of lattice constant (left y-axis) and cell volume (right y-axis) of as a function of magnesium content.

6.4.2 EDX analysis

The chemical composition of the as-prepared solid solutions was ascertained by energy-dispersive X-ray spectroscopy (EDX). The experimental stoichiometric values (Table 6.1), and the obtained weight percentage (Table 6.2) of Mg, Co, Fe, and O are in agreement with the initial amount used in the respective precursors. These EDX results give an indication of successful inclusion of Mg into cobalt ferrite lattice and the absence of phase segregation at the grain boundary.⁴³ This also signifies complete solid solubility of Mg in CoFe_2O_4 lattice to form single-phase $\text{Co}_{1-x}\text{Mg}_x\text{Fe}_2\text{O}_4$ ($0 \leq x \leq 1$) solid solutions. The corresponding EDX spectra represented by Fig.6.2 exhibited signals of Co, Fe and O for $x = 0$, and Mg, Fe and O for $x = 1$. Likewise, the solid solutions with composition in the range of $0.2 \leq x \leq 0.8$ show signals of Co, Mg, Fe and O, confirming the purity of the as-prepared nanoparticles. The compositional homogeneity was investigated by elemental mapping and Fig.6.3 shows that the elements

were uniformly distributed in the spinel $\text{Co}_{1-x}\text{Mg}_x\text{Fe}_2\text{O}_4$ nanoparticles over the entire composition range.

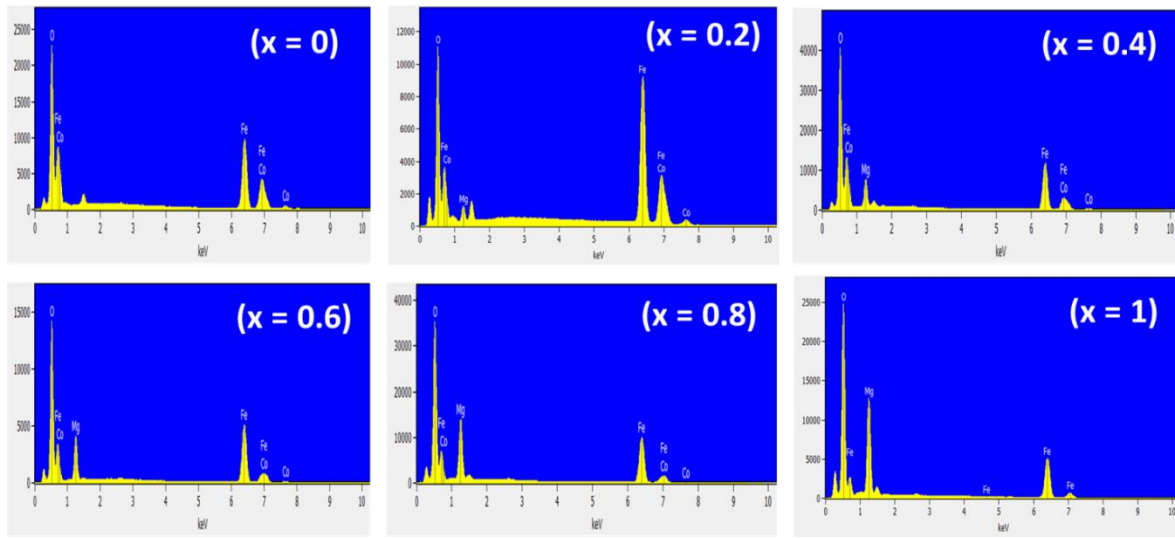


Fig.6.2. EDX spectrum for the prepared $\text{Co}_{1-x}\text{Mg}_x\text{Fe}_2\text{O}_4$ ($0 \leq x \leq 1$) nanoparticles.

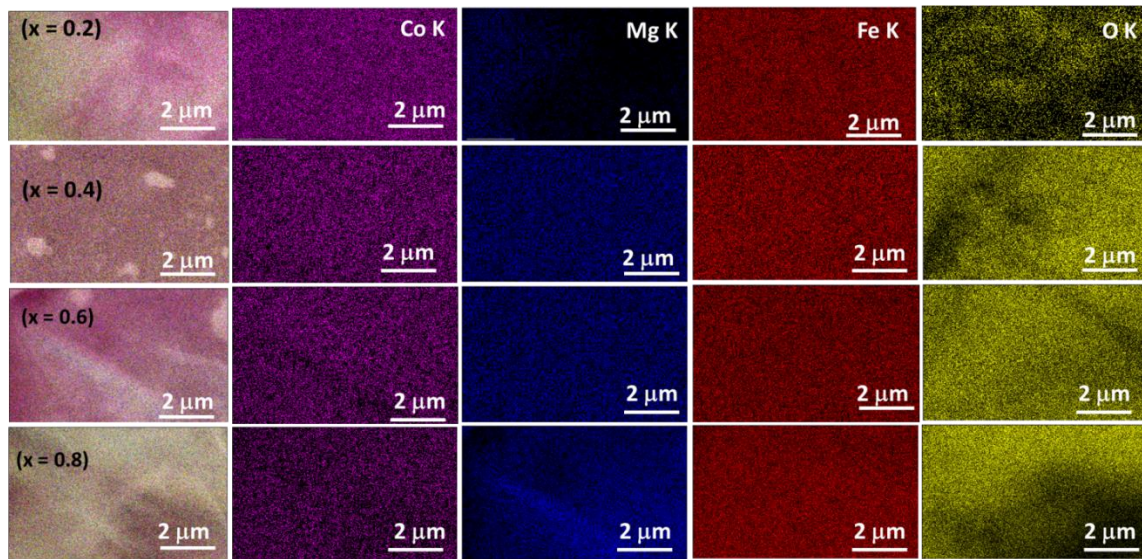


Fig. 6.3. EDX elemental mapping of $\text{Co}_{1-x}\text{Mg}_x\text{Fe}_2\text{O}_4$ ($0 \leq x \leq 1$) solid solutions showing a uniform distribution of elements.

Table 6.1. Lattice parameter (a), crystallite size (d), unit cell volume (V), and EDX composition of $\text{Co}_{1-x}\text{Mg}_x\text{Fe}_2\text{O}_4$ ($0 \leq x \leq 1$) solid solutions.

(x)	Target ferrite composition	Stoichiometry obtained	a (Å)	d (nm)	V (Å ³)
0	CoFe ₂ O ₄	Co _{1.04} Fe _{1.98} O _{3.98}	8.304	9.68	572.614

0.2	$\text{Co}_{0.8}\text{Mg}_{0.2}\text{Fe}_2\text{O}_4$	$\text{Co}_{0.77}\text{Mg}_{0.22}\text{Fe}_{2.03}\text{O}_{3.99}$	8.330	9.83	578.010
0.4	$\text{Co}_{0.6}\text{Mg}_{0.4}\text{Fe}_2\text{O}_4$	$\text{Co}_{0.55}\text{Mg}_{0.39}\text{Fe}_{1.97}\text{O}_{4.09}$	8.334	10.52	578.843
0.6	$\text{Co}_{0.4}\text{Mg}_{0.6}\text{Fe}_2\text{O}_4$	$\text{Co}_{0.32}\text{Mg}_{0.65}\text{Fe}_{1.92}\text{O}_{4.10}$	8.337	11.70	579.468
0.8	$\text{Co}_{0.2}\text{Mg}_{0.8}\text{Fe}_2\text{O}_4$	$\text{Co}_{0.23}\text{Mg}_{0.72}\text{Fe}_{1.95}\text{O}_{4.10}$	8.344	14.19	580.929
1	MgFe_2O_4	$\text{Mg}_{1.03}\text{Fe}_{1.94}\text{O}_{4.03}$	8.345	11.78	581.138

Table 6.2. Expected and experimental atomic percentage for $\text{Co}_{1-x}\text{Mg}_x\text{Fe}_2\text{O}_4$ ($0 \leq x \leq 1$) solid solutions.

[Co ²⁺], (x)	Theoretical atomic % (expected)					Atomic % from EDX (actual/experimental)				
	Co	Mg	Fe	O	Total	Co	Mg	Fe	O	Total
0	14.29	-	28.57	57.14	100	14.88	-	28.31	56.81	100
0.2	11.43	2.86	28.57	57.14	100	10.93	3.14	28.94	56.99	100
0.4	8.57	5.71	28.57	57.14	100	7.79	5.55	28.10	58.55	100
0.6	5.71	8.57	28.57	57.14	100	4.55	9.26	27.48	58.71	100
0.8	2.86	11.43	28.57	57.14	100	3.23	10.28	27.90	58.59	100
1	-	14.29	28.57	57.14	100	-	14.68	27.72	57.60	100

6.4.3 SEM, TEM, HRTEM and SAED analyses

SEM micrographs of $\text{Co}_{1-x}\text{Mg}_x\text{Fe}_2\text{O}_4$ solid solutions with different magnesium contents are displayed in Fig. 6.4. These images show agglomerated nanoparticles regardless of the amount of magnesium present in each sample. Due to the extent of particle agglomerations, the particle size and morphology could not be deduced from SEM images. Instead, TEM analysis was employed to provide insight into the shape and size of the nanoparticles. The TEM images indicated in Fig. 6.5 show the presence of cubic nanoparticles with the size in the range of 13.87-19.29 nm. The nanoparticles maintained the same morphology irrespective of the amount of magnesium being incorporated in the CoFe_2O_4 system. As shown in Fig. 6.6, lattice fringes with the spacing of 0.255, 297 and 0.485 nm were observed in the HRTEM images, and they could be attributed to the (311), (220) and (111) crystal planes, respectively. Fig. 6.7 shows the presentative SAED pattern of $\text{Co}_{1-x}\text{Mg}_x\text{Fe}_2\text{O}_4$ ($x = 0, 0.8$ and 1) which confirms the well crystalline nature of the spinel nanoferrites. The spotty ring patterns observed in the images conform well to the crystallites of the spinel ferrite structure. The

Miller indices identified from the SAED images by relating to their d-spacing match well with those obtained from the XRD measurements.

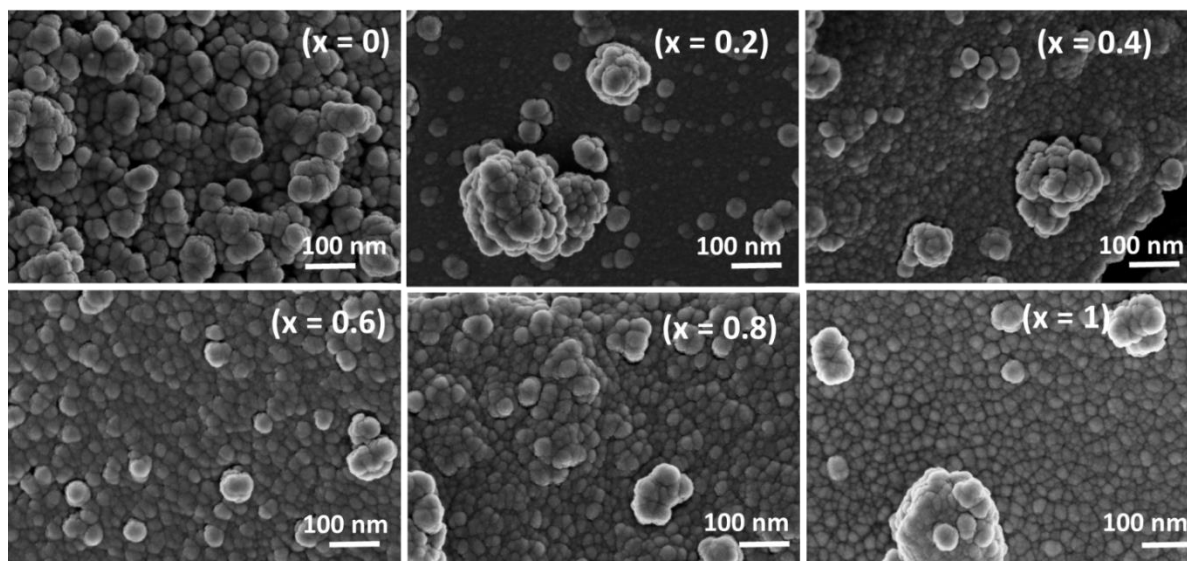


Fig. 6.4. SEM images of $\text{Co}_{1-x}\text{Mg}_x\text{Fe}_2\text{O}_4$ ($0 \leq x \leq 1$) solid solutions.

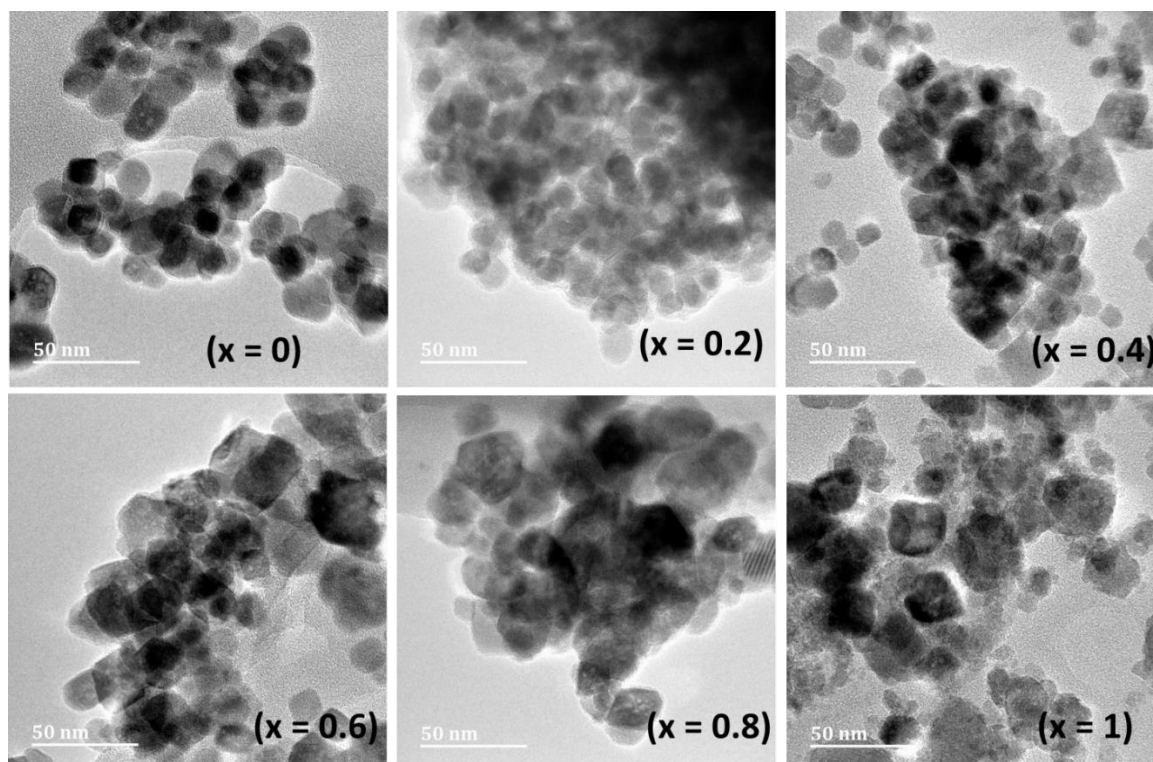


Fig. 6.5. TEM images of $\text{Co}_{1-x}\text{Mg}_x\text{Fe}_2\text{O}_4$ ($0 \leq x \leq 1$) solid solutions.

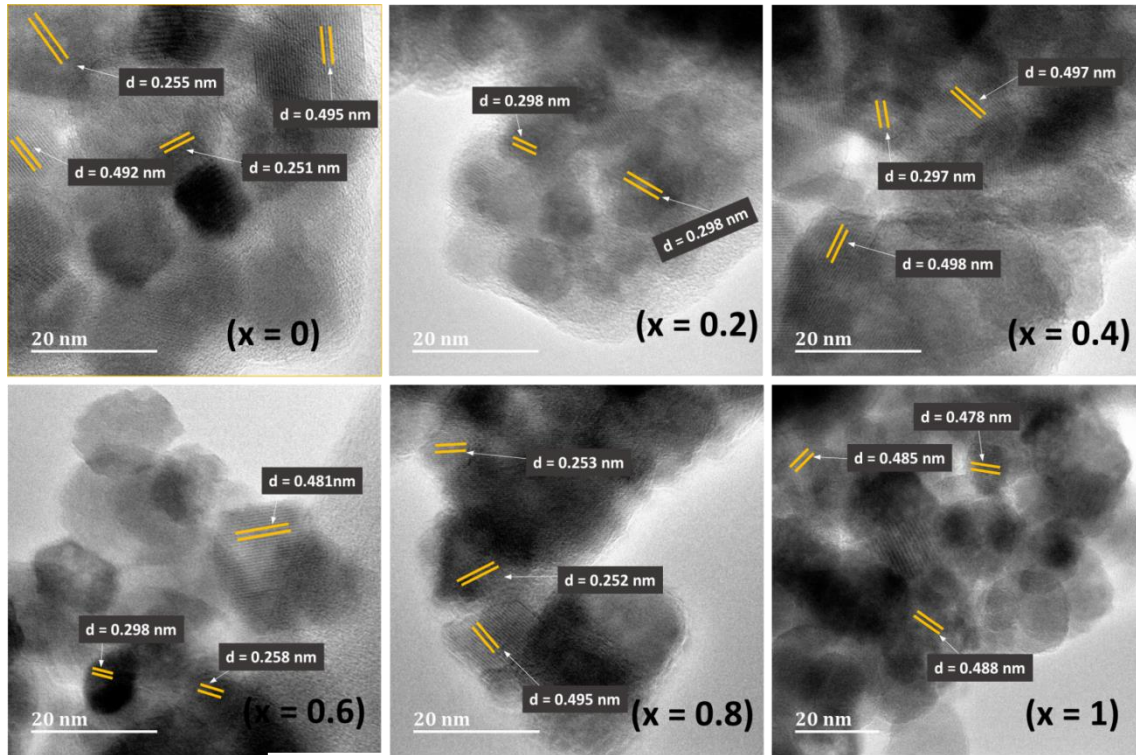


Fig. 6.6. HRTEM images of $\text{Co}_{1-x}\text{Mg}_x\text{Fe}_2\text{O}_4$ ($0 \leq x \leq 1$) solid solutions.

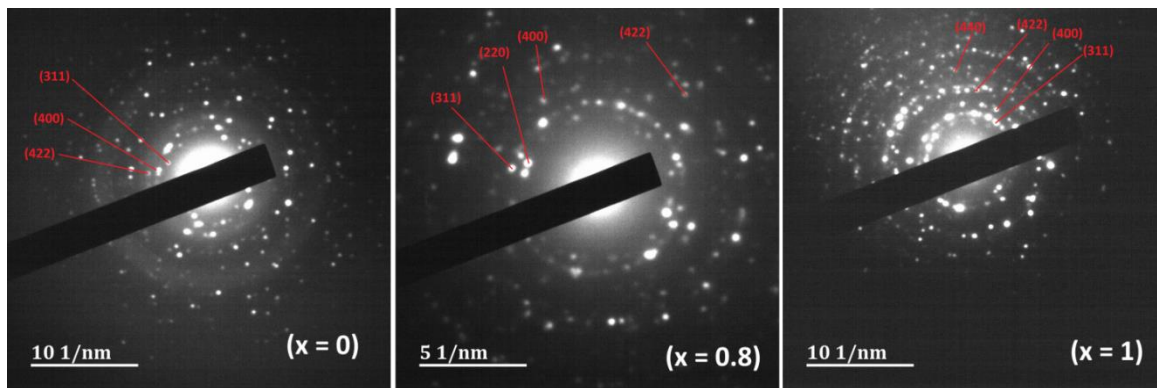


Fig. 6.7. Representative SAED images of $\text{Co}_{1-x}\text{Mg}_x\text{Fe}_2\text{O}_4$ ($x = 0, 0.8$ and 1) nanoparticles.

6.4.4 Optical absorbance and band gap tuning

It is well established that the formation of solid solutions results to modifications of the band gap, crystal structure, lattice parameters, and local electronic structure of the material,⁴⁴ all of which can influence its application in diverse fields. In this regard, an attempt was made to examine the optical absorption properties and the band gap tuning of the synthesized spinel nanoferrites. In this study, the UV-Vis absorption spectra were measured by using UV-Vis spectrophotometry to ascertain the optical absorption and band-gap energy of the $\text{Co}_{1-x}\text{Mg}_x\text{Fe}_2\text{O}_4$ ($0 \leq x \leq 1$) solid solutions. Fig. 6.8 shows the observed absorbance spectra of all

samples with respect to the wavelength (200 - 800 nm). The samples displayed a broader absorption from the UV to the visible light region as the Mg content was increased. Initially, there was a gradual decrease in absorbance which is observed to get saturated at higher wavelengths with lower absorbance.

With the aid of UV-Vis absorbance spectral data, Tauc plots of $(\alpha h\nu)^2$ versus $(h\nu)$ were plotted to estimate the optical band-gap energy (E_g) values of all ferrite samples. The optical band-gaps were estimated from the tangent drawn at x-axis of the Tauc plots as indicated in Fig. 6.9, and the values are summarized in Table 6.3. The values of E_g were found to be in the range of 1.741 - 1.943 eV. It is clearly seen from Table 1 that, the band gap of pristine CoFe_2O_4 ($x = 0$) was obtained to be around 1.873 eV, which is lower than its bulk value ~ 1.92 eV.⁴⁵ With addition of Mg^{2+} to the crystal matrix of cobalt ferrite from $x = 0.2$ to 0.6, the band gap increased from 1.741 to 1.943 eV. It was then observed to drop to 1.906 eV for $x = 0.8$ and finally to 1.757 eV after complete substitution of Co^{2+} by Mg^{2+} ($x = 1$). Considering the band gap value of pristine cobalt ferrite, there is a blue shift for all compositions except for $x = 0.2$ and 1, which are red shifted. The results and findings are of profound significance for the design of novel optoelectronic devices.

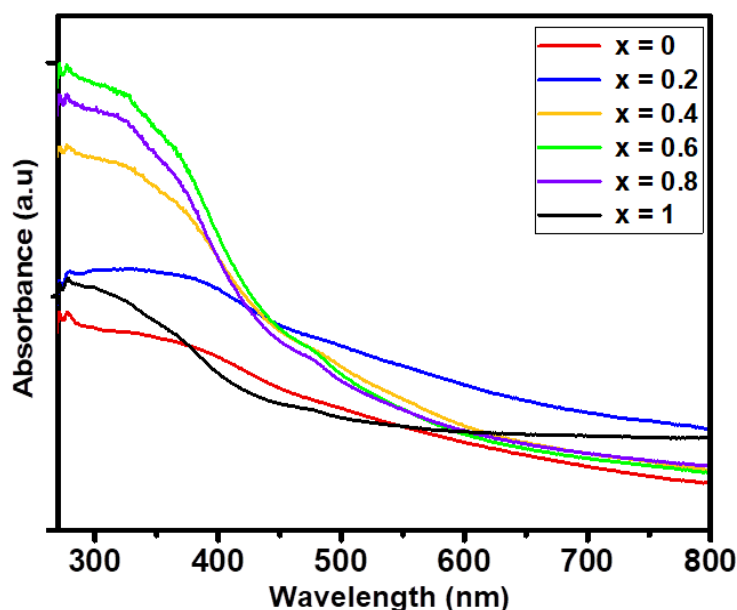


Fig. 6.8. UV-Vis absorption spectrum of $\text{Co}_{1-x}\text{Mg}_x\text{Fe}_2\text{O}_4$ ($0 \leq x \leq 1$) solid solutions.

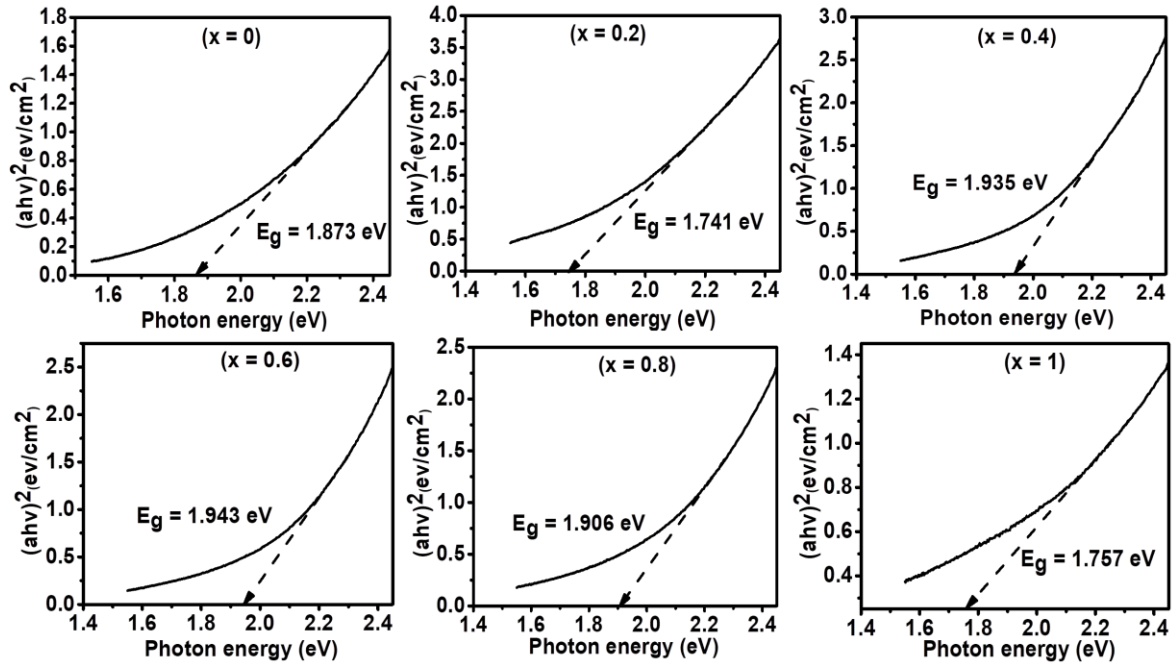


Fig. 6.9. Tauc plots of $(\alpha h\nu)^2$ versus energy for $\text{Co}_{1-x}\text{Mg}_x\text{Fe}_2\text{O}_4$ ($0 \leq x \leq 1$) solid solution.

Table 6.3. The optical band gaps for $\text{Co}_{1-x}\text{Mg}_x\text{Fe}_2\text{O}_4$ ($0 \leq x \leq 1$) nanoparticles obtained at different magnesium content.

Mg content (x)	0	0.2	0.4	0.6	0.8	1
E_g (eV)	1.873	1.741	1.935	1.943	1.906	1.757

6.5 Conclusion

The work described in this chapter provides evidence that fabricating solid solution with continuously composition-tunable properties is one of the most effective strategies to develop semiconductor devices with high performance. Solid solutions of spinel $\text{Co}_{1-x}\text{Mg}_x\text{Fe}_2\text{O}_4$ ($0 \leq x \leq 1$) were successfully prepared by a solventless method at 450 °C for 1hr using metal acetylacetonates precursors. Structural analysis showed that all samples exhibited a cubic spinel ferrite structure with space group $Fd3m$. All samples showed the same cubic morphology irrespective of the amount of Mg being incorporated in the CoFe_2O_4 system. Considering the band gap value of pristine cobalt ferrite, there is a blue shift for all compositions except for $x = 0.2$ and 1, which are red shifted. The results and findings are of profound significance for the design of novel optoelectronic devices.

References

1. Chaves, A.; Azadani, J.; Alsalman, H.; da Costa, D. R.; Frisenda, R.; Chaves, A.; Song, S. H.; Kim, Y.; He, D.; Zhou, J. *npj 2D Materials and Applications* **2020**, 4, (1), 1-21.
2. Regulacio, M. D.; Han, M.-Y. *Accounts of Chemical Research* **2010**, 43, (5), 621-630.
3. Ning, C.-Z.; Dou, L.; Yang, P. *Nature Reviews Materials* **2017**, 2, (12), 1-14.
4. Toufanian, R.; Piryatinski, A.; Mahler, A. H.; Iyer, R.; Hollingsworth, J. A.; Dennis, A. M. *Frontiers in Chemistry* **2018**, 6, 567.
5. Obaidulla, S. M.; Habib, M. R.; Khan, Y.; Kong, Y.; Liang, T.; Xu, M. *Advanced Materials Interfaces* **2020**, 7, (3), 1901197.
6. Zhao, X. G.; Shi, Z.; Wang, X.; Zou, H.; Fu, Y.; Zhang, L. *InfoMat* **2021**, 3, (2), 201-211.
7. Kaner, N. T.; Wei, Y.; Jiang, Y.; Li, W.; Xu, X.; Pang, K.; Li, X.; Yang, J.; Jiang, Y.; Zhang, G. *ACS Omega* **2020**, 5, (28), 17207-17214.
8. Liu, S.; Ma, Q.; Lin, C.; Hong, C.; Yi, R.; Wang, R.; Li, R.; Liu, X.; Nie, A.; Gan, X. *Physical Review Materials* **2020**, 4, (7), 074012.
9. Lei, D.; Shen, Y.; Feng, Y.; Feng, W. *Science China Technological Sciences* **2012**, 55, (4), 903-912.
10. Shen, S.; Wang, Q. *Chemistry of Materials* **2013**, 25, (8), 1166-1178.
11. Swafford, L. A.; Weigand, L. A.; Bowers, M. J.; McBride, J. R.; Rapaport, J. L.; Watt, T. L.; Dixit, S. K.; Feldman, L. C.; Rosenthal, S. J. *Journal of the American Chemical Society* **2006**, 128, (37), 12299-12306.
12. Zimmer, J. P.; Kim, S.-W.; Ohnishi, S.; Tanaka, E.; Frangioni, J. V.; Bawendi, M. G. *Journal of the American Chemical Society* **2006**, 128, (8), 2526-2527.
13. Vladimirova, S.; Prikhodko, K. Y.; Rumyantseva, M.; Konstantinova, E.; Chizhov, A.; Khmelevsky, N.; Gaskov, A. *Journal of Alloys and Compounds* **2020**, 828, 154420.
14. Sanchez-Lievanos, K. R.; Stair, J. L.; Knowles, K. E. *Inorganic Chemistry* **2021**, 60, (7), 4291-4305.
15. Lin, J.; Hu, D.; Yang, H.; Liu, Y.; Xue, C.; Wu, T. *Inorganic Chemistry* **2018**, 57, (8), 4248-4251.
16. Gao, L.; Gao, F. *Applied Physics Letters* **2013**, 103, (5), 053101.
17. Pan, A.; Liu, R.; Sun, M.; Ning, C.-Z. *ACS Nano* **2010**, 4, (2), 671-680.
18. Lovingood, D. D.; Oyler, R. E.; Strouse, G. F. *Journal of the American Chemical Society* **2008**, 130, (50), 17004-17011.

19. Zhong, X.; Feng, Y.; Knoll, W.; Han, M. *Journal of the American Chemical Society* **2003**, 125, (44), 13559-13563.
20. Sung, Y.-M.; Lee, Y.-J.; Park, K.-S. *Journal of the American Chemical Society* **2006**, 128, (28), 9002-9003.
21. Wang, J.-J.; Xue, D.-J.; Guo, Y.-G.; Hu, J.-S.; Wan, L.-J. *Journal of the American Chemical Society* **2011**, 133, (46), 18558-18561.
22. Tan, Y.; Li, C.; Sun, Z.; Bian, R.; Dong, X.; Zhang, X.; Zheng, S. *Chemical Engineering Journal* **2020**, 388, 124386.
23. Das, K. C.; Dhar, S. S. *Journal of Alloys and Compounds* **2020**, 828, 154462.
24. Cheraghi, A.; Davar, F.; Homayoonfal, M.; Hojjati-Najafabadi, A. *Ceramics International* **2021**.
25. Singh, R.; Kumar, S.; Satyapal, H.; Kumar, G. In *A review on magnesium ferrite nanostructure materials: Energy, environment, electronics and biomedical applications*, Abstracts of International Conferences & Meetings, 2021; pp 27-27.
26. Huang, T.; Qiu, Z.; Hu, Z.; Lu, X. *Journal of Energy Storage* **2021**, 35, 102286.
27. Möller, L.; Thauer, E.; Ottmann, A.; Deeg, L.; Ghunaim, R.; Hampel, S.; Klingeler, R. *Journal of Alloys and Compounds* **2020**, 834, 155018.
28. Maitra, S.; Mitra, R.; Nath, T. *Current Applied Physics* **2021**, 27, 73-88.
29. Wang, L.; Wang, Y.; Tian, H.; Qiao, L.; Zeng, Y. *Sensors and Actuators B: Chemical* **2020**, 314, 128085.
30. Priya, R. S.; Chaudhary, P.; Kumar, E. R.; Balamurugan, A.; Srinivas, C.; Prasad, G.; Yadav, B.; Sastry, D. *Ceramics International* **2021**, 47, (11), 15995-16008.
31. He, G.; Wen, Y.; Ma, C.; Li, X.; Gao, L.; Sun, Z. *International Journal of Hydrogen Energy* **2021**, 46, (7), 5369-5377.
32. Kim, K.-H.; Choi, Y.-H. *Electrochimica Acta* **2021**, 395, 139195.
33. Kumar, G. M.; Cho, H.; Lee, D.; Kumar, J. R.; Siva, C.; Ilanchezhian, P.; Kim, D.; Kang, T. *Chemosphere* **2021**, 131134.
34. Mammo, T. W.; Murali, N.; Sileshi, Y. M.; Arunamani, T. *Physica B: Condensed Matter* **2017**, 523, 24-30.
35. Shrestha, D.; Maensiri, S.; Wongpratad, U.; Lee, S. W.; Nyachhyon, A. R. *Journal of Environmental Chemical Engineering* **2019**, 7, (5), 103227.
36. Ounacer, M.; Essoumhi, A.; Sajieddine, M.; Razouk, A.; Fnidiki, A.; Richomme, F.; Juraszek, J.; Dubiel, S.; Sahlaoui, M. *Journal of Physics and Chemistry of Solids* **2021**, 148, 109687.

37. Almessiere, M.; Slimani, Y.; Guner, S.; Sertkol, M.; Korkmaz, A. D.; Shirsath, S. E.; Baykal, A. *Ultrasonics sonochemistry* **2019**, 58, 104654.
38. Liu, B.; Li, J.; Yang, W.; Zhang, X.; Jiang, X.; Bando, Y. *Small* **2017**, 13, (45), 1701998.
39. Zhang, Z.; Yan, X.; Liu, J.; Liu, B.; Gu, Z.-G. *Sustainable Energy & Fuels* **2021**, 5, (10), 2668-2677.
40. Shombe, G. B.; Razzaque, S.; Khan, M. D.; Nyokong, T.; Mashazi, P.; Choi, J.; Bhoyate, S.; Gupta, R. K.; Revaprasadu, N. *RSC Advances* **2021**, 11, (50), 31533-31546.
41. Lewis, E.; Haigh, S.; O'Brien, P. *Journal of Materials Chemistry A* **2014**, 2, (3), 570-580.
42. Shombe, G. B.; Khan, M. D.; Revaprasadu, N.; Alenad, A. M.; Mahmood, R. F., Metal–organic precursors for the solventless synthesis of metallic and metal chalcogenide nanoparticles. *SPR Nanoscience*, **2021**, 213-250.
43. Sujatha, C.; Reddy, K. V.; Babu, K. S.; Reddy, A. R.; Rao, K. *Physica B: Condensed Matter* **2012**, 407, (8), 1232-1237.
44. Zhang, X.; Wang, L. W.; Wang, C. Y.; Wang, W. K.; Chen, Y. L.; Huang, Y. X.; Li, W. W.; Feng, Y. J.; Yu, H. Q. *Chemistry–A European Journal* **2015**, 21, (33), 11872-11877.
45. Vinosha, A.; Jeronsia, E.; Raja, K.; christina Fernandez, A.; Krishnan, S.; Das, J. *Optik* **2016**, 127, (20), 9917-9925.

CHAPTER 7

Summary and future work

7.1 Summary of the work

The work described in this thesis focused on examining the suitability of the solventless thermolysis method for the fabrication of spinel nanoferrite solid solutions from organometallic precursors. A series of spinel ferrite solid solution nanoparticles such as $\text{Ni}_{1-x}\text{Co}_x\text{Fe}_2\text{O}_4$, $\text{Co}_{1-x}\text{Zn}_x\text{Fe}_2\text{O}_4$, $\text{Ni}_{1-x}\text{Mg}_x\text{Fe}_2\text{O}_4$, $\text{Ni}_{1-x}\text{Zn}_x\text{Fe}_2\text{O}_4$, and $\text{Co}_{1-x}\text{Mg}_x\text{Fe}_2\text{O}_4$, were successfully synthesized from their respective metal acetylacetonate precursors. Evaluation of their structural, morphological, compositional, optical and electrochemical properties was performed by a suite of characterization techniques. The effect of composition variation on the physicochemical and electrochemical properties of the synthesized nanostructures was also investigated.

Nanostructured $\text{Ni}_{1-x}\text{Co}_x\text{Fe}_2\text{O}_4$ nanoparticles exhibiting a cubic structure were successfully prepared via a solventless thermolysis method. Evaluation of energy storage behaviour revealed superior charge storage capacity for the $\text{Ni}_{0.4}\text{Co}_{0.6}\text{Fe}_2\text{O}_4$ electrode compared to other electrodes. On the other hand, efficient HER electrocatalysis was showcased by the $\text{Ni}_{0.6}\text{Co}_{0.4}\text{Fe}_2\text{O}_4$ electrode which showed low overpotential of 168 mV and Tafel slope of 120 mV/dec. Similarly, higher OER performance was recorded by $\text{Ni}_{0.8}\text{Co}_{0.2}\text{Fe}_2\text{O}_4$ with a lower overpotential of 320 mV and a low Tafel slope of 79 mV/dec.

The nanofabrication of composition-tuneable spinel $\text{Co}_{1-x}\text{Zn}_x\text{Fe}_2\text{O}_4$ solid solutions was also achieved over the entire composition range. Experimental results revealed that the incorporation of diamagnetic Zn^{2+} in the crystal lattice of CoFe_2O_4 contributed to higher discharge time for $\text{Co}_{0.4}\text{Zn}_{0.6}\text{Fe}_2\text{O}_4$ than the pristine CoFe_2O_4 , which is indicative of higher specific capacitance of the solid solution. Electrocatalytic experiments showed that the $\text{Co}_{0.8}\text{Zn}_{0.2}\text{Fe}_2\text{O}_4$ solid solution exhibited higher OER performance with low overpotential of 317 mV and a small Tafel slope of 56 mV/dec. As for HER in alkaline electrolyte, $\text{Co}_{0.6}\text{Zn}_{0.4}\text{Fe}_2\text{O}_4$ displayed decent performance with low overpotential of 169 mV and Tafel slope of 136 mV/dec compared to other electrode compositions.

It was also demonstrated that by regulating the molar composition of Mg and Ni in the spinel $\text{Ni}_{1-x}\text{Mg}_x\text{Fe}_2\text{O}_4$ solid solutions, the electrochemical performance of the material was tuned. At a current density of 10 mA/cm^2 , the $\text{Ni}_{0.4}\text{Mg}_{0.6}\text{Fe}_2\text{O}_4$ nanoparticles exhibited the best electrocatalytic activity for HER with an overpotential of only 121 mV which is much smaller compared to its analogues, and the electrode exhibited good stability during long-term electrolysis. Meanwhile, $\text{Ni}_{0.2}\text{Mg}_{0.8}\text{Fe}_2\text{O}_4$ showed the best OER activity with an overpotential of 284 mV which was required to deliver the same current density.

The solventless method was also employed to afford a series of $\text{Ni}_{1-x}\text{Zn}_x\text{Fe}_2\text{O}_4$ solid solutions with varying amounts of zinc and nickel. The incorporation of zinc in the crystal lattices of nickel ferrite endowed a larger benefit on HER and OER than on supercapacitance. Specifically, the $\text{Ni}_{1-x}\text{Zn}_x\text{Fe}_2\text{O}_4$ ($x = 0.8$) nanocatalyst displayed excellent HER performance with a small overpotential of 87 mV, whereas $\text{Ni}_{1-x}\text{Zn}_x\text{Fe}_2\text{O}_4$ ($x = 1$) catalyst exhibited superior OER performance with an overpotential of 330 mV.

The synthesis and physicochemical studies of $\text{Co}_{1-x}\text{Mg}_x\text{Fe}_2\text{O}_4$ ($0 \leq x \leq 1$) nanoparticles were also performed. Structural analysis showed that all samples exhibited a cubic spinel ferrite structure with space group $Fd3m$. All samples showed the same morphology irrespective of the amount of Mg being incorporated in the CoFe_2O_4 system. Considering the band gap value of pristine cobalt ferrite, a blue shift was observed for all compositions except for $x = 0.2$ and 1, which were red shifted. These findings are of profound significance for the design of novel electronic and optoelectronic devices.

Overall, it was observed that compared to the parent spinel ferrites, their corresponding solid solutions demonstrated improved physicochemical and electrochemical activity, except for $\text{Ni}_{1-x}\text{Zn}_x\text{Fe}_2\text{O}_4$ where the pristine ZnFe_2O_4 exhibited higher OER activity than the solid solutions. The high performance of the solid solutions is due to elegant combination and synergistic influence of the elements. It was also established that the morphology of nanoparticles in all systems was not affected by variation in dopant composition. This morphological conservation can serve as a straightforward strategy for programming morphological complexity into multi-element nanocrystal systems that require simultaneous control over composition, shape and crystal structure.

The overall work reported in this thesis has demonstrated the suitability of solventless thermolysis approach in the synthesis of semiconductor ferrite solid solutions from metal acetylacetonate precursors.

7.2 Future work

Since the future applications of spinel ferrites are considered to be closely related to environmental and energy issues, future work will continue employing the solventless method in developing new functional materials with advanced properties. The study would extend to the use of metal acetylacetonate complexes to prepare cobaltite, manganite, stannite, gallate, chromate and aluminate solid solution nanoparticles and thin films for potential gas sensing, magnetism, supercapacitance, water splitting and biomedical

applications. The work on $\text{Co}_{1-x}\text{Mg}_x\text{Fe}_2\text{O}_4$ will also be extended to investigate their potential for supercapacitance, HER and OER.

List of publications

1. **Malima, N.M.**, Khan, M.D., Choi, J., Gupta, R.K., Mashazi, P., Nyokong, T. and Revaprasadu, N., 2021. Solventless synthesis of nanospinel $\text{Ni}_{1-x}\text{Co}_x\text{Fe}_2\text{O}_4$ ($0 \leq x \leq 1$) solid solutions for efficient electrochemical water splitting and supercapacitance. *RSC Advances*, 11(49), pp.31002-31014.
2. **Malima, N.M.**, Khan, M.D., Choi, J., Gupta, R.K., and Revaprasadu, N., 2021. Composition-tuneable synthesis of $\text{Co}_{1-x}\text{Zn}_x\text{Fe}_2\text{O}_4$ ($0 \leq x \leq 1$) solid solutions by melt pyrolysis for electrochemical energy conversion and storage (*Under review*).
3. Owonubi, S. J., **Malima, N. M.**, & Revaprasadu, N. (2020). Metal Oxide–Based Nanocomposites as Antimicrobial and Biomedical Agents. In *Antibiotic Materials in Healthcare* (pp. 287-323). Academic Press.
4. Fasiku, V. O., Owonubi, S. J., **Malima, N. M.**, Hassan, D., & Revaprasadu, N. (2020). Metal Oxide Nanoparticles: A Welcome Development for Targeting Bacteria. In *Antibiotic Materials in Healthcare* (pp. 261-286). Academic Press.
5. Owonubi, S. J., Agwuncha, S. C., **Malima, N. M.**, Sadiku, E. R., & Revaprasadu, N. (2021). Development of bacterial resistant acrylamide-polyvinylpyrrolidone-metal oxide hydrogel nanocomposites. *Materials Today: Proceedings*, 38, 982-987.
6. **Malima, N. M.**, Owonubi, S. J., Shombe, G. B., Revaprasadu, N., & Sadiku, E. R. (2020). Bioelectrochemical Technology for Sustainable Energy Production and Waste Treatment. *Bioelectrochemical Systems: Vol. 2 Current and Emerging Applications*, 2, 131.
7. Owonubi, S. J., Agwunca, S. C., **Malima, N. M.**, Makhatha, E. M., & Revaprasadu, N. (2021). Engineering and Surface Modification of Cellulose Nanoparticles and Their Characterization. *Cellulose Nanoparticles: Volume 1: Chemistry and Fundamentals*.
8. Owonubi, S. J., Agwuncha, S. C., **Malima, N. M.**, Shombe, G. B., Makhatha, E. M., & Revaprasadu, N. (2021). Non-woody Biomass as Sources of Nanocellulose Particles: A Review of Extraction Procedures. *Frontiers In Energy Research*, 9.

List of conferences

1. Poster presentation on “Synthesis and characterization of nanostructured $\text{Ni}_{1-x}\text{Co}_x\text{Fe}_2\text{O}_4$ ($0 \leq x \leq 1$) solid solutions via solventless thermolysis of molecular precursors” in the 10th International Conference of the African Materials Research Society (AMRS 2019) on 10th-13th December 2019, Arusha, Tanzania.

2. Oral presentation on “Solventless synthesis of nanospinel $\text{Ni}_{1-x}\text{Co}_x\text{Fe}_2\text{O}_4$ ($0 \leq x \leq 1$) solid solutions for efficient electrochemical water splitting and supercapacitance” in the Nanosciences Young Researchers’ Symposium 2020/2021 on 07th – 08th October 2021, Pretoria, South Africa (Virtual symposium).